



**HAL**  
open science

# Identification de la variabilité des rigidités du bois à l'intérieur de l'arbre par la méthode des champs virtuels : application au P. pinaster dans le plan LR

José Xavier

## ► To cite this version:

José Xavier. Identification de la variabilité des rigidités du bois à l'intérieur de l'arbre par la méthode des champs virtuels : application au P. pinaster dans le plan LR. Sciences de l'ingénieur [physics]. Arts et Métiers ParisTech, 2007. Français. NNT : 2007ENAM0030 . pastel-00003177

**HAL Id: pastel-00003177**

**<https://pastel.hal.science/pastel-00003177>**

Submitted on 17 Dec 2007

**HAL** is a multi-disciplinary open access archive for the deposit and dissemination of scientific research documents, whether they are published or not. The documents may come from teaching and research institutions in France or abroad, or from public or private research centers.

L'archive ouverte pluridisciplinaire **HAL**, est destinée au dépôt et à la diffusion de documents scientifiques de niveau recherche, publiés ou non, émanant des établissements d'enseignement et de recherche français ou étrangers, des laboratoires publics ou privés.



Ecole doctorale n° 432 : Sciences des Métiers de l'Ingénieur

# THÈSE

pour obtenir le grade de

**Docteur**

de

**L'École Nationale Supérieure d'Arts et Métiers**

Spécialité "Mécanique"

*présentée et soutenue publiquement*

*par*

**José XAVIER**

le 27 novembre 2007

**IDENTIFICATION DE LA VARIABILITÉ DES RIGIDITÉS  
DU BOIS À L'INTÉRIEUR DE L'ARBRE  
PAR LA MÉTHODE DES CHAMPS VIRTUELS :  
APPLICATION AU P. PINASTER DANS LE PLAN LR**

*Directeur de thèse : Fabrice PIERRON*

*Co-encadrement de la thèse : Stéphane AVRIL*

Jury :

<b>M. Rémy MARCHAL</b>	Professeur, ENSAM, Cluny	Président
<b>M. Joseph GRIL</b>	Directeur de Recherches CNRS, LMGC, Montpellier	Rapporteur
<b>M. Jérôme MOLIMARD</b>	Maître Assistant HDR, ENSM, Saint-Étienne	Rapporteur
<b>M. Stéphane AVRIL</b>	Maître Assistant HDR, ENSM, Saint-Étienne	Examineur
<b>M. José MORAIS</b>	Professeur, UTAD, Vila Real (Portugal)	Examineur
<b>M. Fabrice PIERRON</b>	Professeur, ENSAM, Châlons-en-Champagne	Examineur
<b>M. Frédéric ROUGER</b>	Directeur de Recherches, FCBA, Paris	Examineur

**Laboratoire de Mécanique et Procédés de Fabrication**

*ENSAM, CER de Châlons-en-Champagne*





Ecole doctorale n° 432 : Sciences des Métiers de l'Ingénieur

# Ph.D. THESIS

to obtain the grade of

**Doctor**

of the

**École Nationale Supérieure d'Arts et Métiers**

Speciality "Mechanics"

*presented by*

**José XAVIER**

the November 27th, 2007

**CHARACTERISATION OF THE WOOD STIFFNESS  
VARIABILITY WITHIN THE STEM  
BY THE VIRTUAL FIELDS METHOD:  
APPLICATION TO *P. PINASTER* IN THE *LR* PLANE**

*Ph.D. Advisors: Fabrice PIERRON*

*Stéphane AVRIL*

Jury:

<b>M. Rémy MARCHAL</b>	Professeur, ENSAM, Cluny	Chairman
<b>M. Joseph GRIL</b>	CNRS Research Director, LMGC, Montpellier	Referee
<b>M. Jérôme MOLIMARD</b>	Assistant Professor, ENSM, Saint-Étienne	Referee
<b>M. Stéphane AVRIL</b>	Assistant Professor, ENSM, Saint-Étienne	Examinator
<b>M. José MORAIS</b>	Professeur, UTAD, Vila Real (Portugal)	Examinator
<b>M. Fabrice PIERRON</b>	Professeur, ENSAM, Châlons-en-Champagne	Examinator
<b>M. Frédéric ROUGER</b>	Research Director, FCBA, Paris	Examinator

**Mechanical Engineering and Manufacturing Research Group**

*ENSAM, CER de Châlons-en-Champagne*



*A Deus e a todos aqueles que  
me ajudam a crescer...*



## *SÍSIFO*

*Recomeça...  
Se puderes,  
Sem angústia e sem pressa.  
E os passos que deres,  
Nesse caminho duro  
Do futuro,  
Dá-os em liberdade.  
Enquanto não alcances  
Não descanses.  
De nenhum fruto queiras só metade.  
E, nunca saciado,  
Vai colhendo  
Ilusões sucessivas no pomar.  
Sempre a sonhar  
E vendo,  
Acordado,  
O logro da aventura.  
És homem, não te esqueças!  
Só é tua a loucura  
Onde, com lucidez, te reconheças.*

*Miguel Torga, Diário, XIII, pág.20.*



# Acknowledgements

*En premier et avant tout, je voudrais remercier chaleureusement Fabrice Pierron et Stéphane Avril, pour l'encadrement de cette thèse. Votre étonnantes connaissances ont été fondamentales pour le bien déroulement de ce travail. Je vous remercie aussi pour l'amitié qui a fleuri entre nous comme résultat de cette thèse.*

*Queria também agradecer a José Morais pelo seu suporte e troca de impressões ao longo de todo este trabalho. E, nomeadamente, por me ter incentivado, já faz algum tempo, para este mundo da investigação.*

*Je tiens aussi a remercier Joseph Gril et Jérôme Molimard d'avoir acceptés d'être rapporteurs de ma thèse, Rémy Marchal d'avoir bien voulu présider le jury lors de ma soutenance de thèse, et Frédéric Rouger d'avoir acceptés d'être parmi les membres du jury.*

*Je voudrais remercier à toutes les personnes du LMPF/ENSAM pour la bonne ambiance qu'a toujours entourée pendant mon séjour au labo. Merci pour votre accueil et ouverture, et pour tous ces champs réels d'amitiés qui resteront gravé dans les beaux souvenirs de ma mémoire.*

*Gostaria de agradecer aos colegas e amigos Marcelo Oliveira e João Luís Pereira do Departamento de Engenharias de Madeiras da Escola Superior de Tecnologia de Viseu pela sua contribuição na preparação dos provetes ensaiados neste trabalho.*

*A special thanks also for our friend Marie Kelly for her advises concerning the thesis writing.*

*Agradeço calorosamente à minha família e amigos pelo seu apoio e encorajamento ao longo de todos estes anos. À Sandra, em particular, agradeço o seu amor e atenção, os ingredientes que adocicaram a minha estadia por estas terras gaulesas.*

*Finalmente, queria agradecer à Fundação para a Ciência e Tecnologia o suporte financeiro sem o qual não me teria sido possível desenvolver este trabalho.*



# Résumé

Le matériau bois est un composite naturel produit par l'arbre. Puisque l'arbre constitue une ressource disponible sur la Terre, historiquement, le bois a toujours joué un rôle important comme matériau (p.-ex., pour la construction). Dans les dernières décennies, de nouveaux produits à base de bois ont été développés, tel que le bois lamellé-collé ou le contre-plaqué. Ces produits ont été spécialement conçus pour répondre à des exigences structurales ([Williamson, 2002](#)). Ainsi, le bois massif et ses produits dérivés sont de nos jours d'une importance considérable, d'autant plus pour les raisons suivantes ([STEP, 1996](#)) : (1) les arbres sont produits par une source d'énergie gratuite (le soleil) et sont renouvelables et recyclables ; (2) il y a des ressources forestières importantes sur Terre ; (3) la sylviculture et la transformation du bois ont un coût relativement faible ; (4) le bois a une rigidité spécifique excellente. Néanmoins, pour une utilisation efficace du bois dans des applications d'ingénierie, les paramètres matériaux figurant dans les lois de comportement (p.-ex., les paramètres de rigidité dans le modèle élastique linéaire anisotrope), de même que d'autres propriétés telles que les résistances, doivent être correctement caractérisées ([ASTM D143, 1994](#); [Bodig and Goodman, 1973](#)).

La grume d'un arbre peut être modélisée comme un matériau orthotrope cylindrique ([Guitard, 1987](#); [Smith et al., 2003](#)). Trois plans de symétrie sont localement définis par les directions longitudinale ( $L, 1$ ), radiale ( $R, 2$ ) et tangentielle ( $T, 3$ ) des cellules du bois (les trachéides pour le bois résineux). Les propriétés mécaniques du bois sont habituellement identifiées dans ce repère matériau. Le comportement mécanique du bois peut être analysé à différentes échelles. À l'échelle macroscopique, le bois sans défaut (c.-à-d., le bois sans noeud ou autres caractéristiques structurelles et avec un fil droit) est normalement considéré comme un matériau continu et homogène. Différentes lois de comportement ont été proposées dans la littérature pour modéliser le bois sans défaut, chacune d'entre elles se limitant à un domaine de validité particulier. Négligeant une possible déformation engendrée par des effets hygro-thermiques, les lois de comportement généralement admises sont les modèles élastiques et viscoélastiques linéaires ([Dinwoodie, 2000](#); [Guitard, 1987](#); [Holmberg et al., 1999](#); [Kollman and Côté Jr., 1984](#); [Smith et al., 2003](#)). Le bois semble être décrit plus exactement par un modèle viscoélastique puisque des observations expérimentales ont indiqué une dépendance de la déformation avec le temps. Cependant, pour la plupart des applications pratiques, la déformation dépendante du temps peut

être négligée et le bois peut simplement être considéré comme élastique linéaire. Cette théorie est valide pour des niveaux relativement bas de contrainte (en dessous de la limite d'élasticité), appliqués sur une période courte (quelques minutes) et à température ambiante.

Pour caractériser les paramètres de comportement de la loi élastique linéaire, on utilise des essais mécaniques quasi-statiques. Cependant, en raison de l'orthotropie de la structure du bois, plusieurs essais indépendants sont habituellement employés pour sa caractérisation mécanique (Guitard, 1987). Ces méthodes se fondent sur des conditions de chargement simples (traction, compression, cisaillement ou flexion) pour lesquelles un état de contrainte simple est supposé s'appliquer sur un élément représentatif de volume du matériau à l'échelle de l'étude. Pour ces essais, une solution analytique peut être obtenue, liant directement les mesures de force et de déformation aux paramètres matériaux inconnus. En raison de l'anisotropie et de l'hétérogénéité, la nécessité d'améliorer les essais mécaniques pour l'identification a depuis longtemps fait l'objet d'études (Jones, 1999; Tarnopol'skii and Kulakov, 1998). Dans ce domaine de recherche, plusieurs essais mécaniques ont été conçus et améliorés (p.-ex., l'essai de traction hors-axes et l'essai de cisaillement d'Iosipescu). Néanmoins, quelques inconvénients ont été indiqués pour ces méthodes, à savoir la difficulté pratique de générer un état simple de déformation sur la totalité de la région d'intérêt en raison des effets de conditions aux limites (Grédiac, 1996; Tarnopol'skii and Kulakov, 1998).

Pour l'identification de paramètres de comportement représentatifs d'une essence de bois, plusieurs éprouvettes, prélevées à différents endroits dans différents arbres, sont nécessaires afin de prendre en compte la variabilité structurale inhérente du matériau (Bodig and Goodman, 1973). Ainsi, en raison de l'anisotropie et de la variabilité du bois, on peut conclure qu'un nombre significatif d'essais est requis, ce qui implique un coût important. Pour simplifier cette procédure, une approche a été proposée depuis les premiers travaux de Bodig and Goodman (1973). Sur le fond, elle consiste à établir des rapports entre les différentes propriétés du bois. Puisque le module élastique longitudinal est connu pour la plupart des essences, ce paramètre a été souvent pris comme variable indépendante (Bodig and Goodman, 1973; Green et al., 1999; Sliker, 1985, 1988; Sliker and Yu, 1993). L'évaluation des paramètres élastiques à partir des propriétés physiques, telles que la densité, a également fait l'objet de plusieurs études (Bodig and Goodman, 1973; Gibson and Ashby, 1997; Guitard, 1987; Sliker and Yu, 1993; Walton and Armstrong, 1986). Un autre type d'approche est proposé dans ce travail.

Grâce au développement des méthodes optiques, permettant de mesurer des grandeurs cinématiques (p.-ex., déplacement, pente, déformation ou courbure) sur toute une région d'intérêt, une nouvelle voie de caractérisation des matériaux s'est développée (Grédiac, 1996, 2004). L'idée fondamentale est qu'une seule éprouvette peut être chargée de telle manière que plusieurs paramètres soient simultanément impliqués dans sa réponse mé-

canique, engendrant des champs de déformation complexes et hétérogènes. En admettant que ces champs soient mesurés par une méthode optique appropriée, l'ensemble des paramètres de comportement peut alors être déterminé par une méthode d'identification adaptée. Cette approche semble être particulièrement intéressante pour un matériau comme le bois. En effet, elle a déjà été appliquée au bois et à ses produits dérivés par quelques auteurs (Cárdenas-García et al., 2005; Foudjet et al., 1982; Jernkvist and Thuvander, 2001; Le Magorou et al., 2002; Rouger, 1988).

Le travail présenté dans cette thèse concerne une approche d'identification inverse permettant la caractérisation des paramètres de rigidité longitudinale-radiale,  $(L, R) \equiv (1, 2)$ , du pin maritime (*Pinus pinaster* Ait.). En particulier, la procédure proposée est basée sur l'application de la méthode des champs virtuels (MCV) à une éprouvette rectangulaire chargée dans le montage d'Iosipescu. Cette méthode est fondée sur les équations fondamentales de la mécanique des solides déformables : le principe des travaux virtuels (PTV) (qui décrit l'équilibre global d'un corps) et la loi de comportement (qui établit le rapport entre les états de contrainte et de déformation en chaque point d'un solide). Des champs virtuels spéciaux par morceaux optimisés (vis-à-vis du critère de sensibilité au bruit) ont été employés. L'essai a été conçu de telle manière que la géométrie et les conditions de chargement génèrent des champs hétérogènes de déformation. Ces champs de déformation, nécessaires dans le problème de caractérisation du matériau, ont été déduits des champs de déplacements mesurés par la méthode de grille, par une approche de régression polynômiale au sens des moindres carrés. Les champs de déformations et la force résultante (mesurée par une cellule de force montée sur la machine d'essai) ont été traités par la MCV pour obtenir l'identification directe des quatre rigidités du bois sans défaut dans le plan  $LR$ :  $Q_{11}$ ,  $Q_{22}$ ,  $Q_{12}$  et  $Q_{66}$ . Ensuite, une contribution à l'évaluation de la variabilité spatiale des paramètres de rigidité au sein de la grume de l'arbre est présentée.

Le mémoire de thèse est composé de six chapitres. Dans le chapitre 1, une étude bibliographique sur le comportement linéaire élastique du bois est présentée, avec un intérêt particulier porté aux essais mécaniques habituellement utilisés pour la caractérisation. Des méthodes optiques de mesure des champs cinématiques utilisées en mécanique expérimentale et leur intérêt pour la mécanique du bois font l'objet du chapitre 2, ainsi qu'une présentation des essais statistiquement indéterminés et le principe général de la MCV. L'approche d'identification inverse proposée dans ce travail est présentée au chapitre 3. La validation numérique et expérimentale de cette approche sont étudiées aux chapitres 4 et 5, respectivement. Le chapitre 6 décrit l'application de la méthodologie proposée pour caractériser la variabilité spatiale des paramètres de rigidité du bois à l'intérieur de la grume de l'arbre. Enfin, les conclusions générales et quelques directions pour les travaux futurs sont données.

Les principaux résultats de cette thèse sont les suivants.

- (i) L'approche d'identification inverse proposée a été premièrement validée d'un point de vue numérique. Les données expérimentales ont été remplacées par des champs de déplacement simulés, obtenus à partir d'un modèle éléments finis de l'essai mécanique développé dans le code ANSYS. Des propriétés élastiques de référence du bois *P. pinaster*, prises dans la littérature, ont été employées dans les simulations numériques. Pour la configuration de l'éprouvette à  $0^\circ$ , une étude a été faite pour calibrer la longueur libre de la zone utile de l'éprouvette. Une longueur de 34 mm a été choisie selon un critère de minimisation où la fonction coût a été définie par rapport aux coefficients de sensibilité au bruit fournis par la routine MCV. Par ailleurs, une étude a été réalisée afin de calibrer le degré du polynôme à employer dans la régression au sens des moindres carrés pour la reconstruction du champ de déformation. Il a été constaté qu'un polynôme de degré 7 était un bon compromis entre l'efficacité du filtrage du bruit et la fidélité de la reconstruction. En outre, une étude paramétrique a été réalisée pour choisir le maillage sur lequel les champs virtuels par morceaux sont définis. On a montré que des résultats stables sont obtenus pour une maille de  $8(x) \times 4(y)$  éléments, même en perturbant les champs de déplacement par l'addition d'un bruit blanc Gaussien.
- (ii) Dans la MCV, les paramètres élastiques ont été supposés constants dans la région d'intérêt de l'éprouvette. Cependant, en raison de la petite taille de cette région (hauteur de 20 mm), la structure des anneaux de croissance des éprouvettes peut contredire cette hypothèse. En conséquence, en développant un modèle matériau multi-couches (composé de couches alternées de bois d'été et de printemps), on a vérifié que la MCV peut fournir des valeurs homogénéisées des paramètres de rigidité. Différents modèles géométriques ont été analysés en changeant les fractions volumiques, le nombre de couches et les propriétés élastiques des bois d'été et de printemps, afin d'accéder à la variabilité inhérente associée à la composition des éprouvettes. À partir de ces modèles, les propriétés moyennes fournies par la loi des mélanges ont pu être retrouvées par la MCV, prouvant la pertinence de l'hypothèse d'homogénéité.
- (iii) Grâce aux coefficients de sensibilité au bruit fournis par la MCV, on a constaté que la réponse mécanique de l'éprouvette à  $0^\circ$  favorise l'identification des paramètres  $Q_{11}$  et  $Q_{66}$  par rapport aux paramètres  $Q_{22}$  et  $Q_{12}$ . Ceci a mené à une étude d'optimisation visant à déterminer la meilleure configuration, c.-à-d., pour laquelle une contribution équilibrée des rigidités pourrait être obtenue. La longueur de la zone utile et l'orientation du fil du bois ont été pris comme variables d'optimisation. Une fonction coût a été définie à partir des coefficients de sensibilité au bruit associés

à la MCV. On a constaté que la rotation de l'angle des fibres augmente la robustesse de l'identification en améliorant la contribution des composantes de déformation  $\varepsilon_1$  et  $\varepsilon_2$ , tout en gardant pour autant une certaine influence de la composante de cisaillement  $\varepsilon_6$ . Une longueur de 35 mm et un angle de  $30^\circ$  se sont avérés maximiser l'identifiabilité de l'ensemble des paramètres de rigidité.

- (iv) L'approche d'identification inverse a été ensuite validée d'un point de vue expérimental. Les mesures des champs de déplacement ont été fournies par la méthode de grille. Trois configurations ont été testées avec des angles de fil du bois à  $0^\circ$ ,  $45^\circ$  et  $30^\circ$ . La longueur libre a été fixée à 34 mm, ainsi une région d'intérêt de  $34 \times 20 \text{ mm}^2$  a été étudiée. La résolution spatiale de la méthode était de l'ordre de grandeur du pas de la grille, c.-à-d. 0.1 mm. La résolution en déplacement a été estimée entre 0.9 et 1.2  $\mu\text{m}$ . Ce paramètre est fortement dépendant de la qualité du transfert de la grille.
- (v) Après traitement des données expérimentales, seuls les paramètres  $Q_{11}$  et  $Q_{66}$  ont pu être identifiés avec une dispersion raisonnable pour la configuration à  $0^\circ$ . La configuration à  $45^\circ$  a apporté quelques améliorations, particulièrement pour l'identification du paramètre  $Q_{22}$ . Cependant, l'identifiabilité du paramètre  $Q_{12}$  est restée faible. Bien qu'on ait montré numériquement que la meilleure configuration correspond à un angle de  $30^\circ$ , expérimentalement, des résultats instables ont été systématiquement obtenus, en raison d'une mauvaise reconstruction des champs de déformation. Par conséquent, la configuration à  $30^\circ$  n'a pas été utilisée dans la suite des expériences.
- (vi) Les paramètres de rigidité identifiés par l'approche inverse proposée étaient systématiquement inférieurs à ceux de référence pour le *P. pinaster* d'environ 30-35%. Comme les éprouvettes utilisées ici et celles de la référence étaient découpées à différents endroits à l'intérieur du même arbre, ces écarts ont été interprétés comme dus à la variabilité longitudinale des propriétés mécaniques du bois dans la grume. En effet, une étude récente ([Machado and Cruz, 2005](#)) pour cette essence de bois a montré qu'une diminution du module élastique longitudinal comprise entre 29% et 35% peut être observée pour des éprouvettes prélevées à différentes hauteurs au sein de l'arbre.
- (vii) La configuration à  $45^\circ$  a été employée pour étudier la variabilité spatiale des paramètres de rigidité  $LR$  du bois *P. pinaster* à l'intérieur de la grume. Les résultats concernant  $Q_{11}$  et  $Q_{12}$  n'étaient pas exploitables en raison de la grande dispersion obtenue. Néanmoins, des résultats intéressants ont été trouvés pour  $Q_{22}$  et  $Q_{66}$ . Il a été constaté que ces deux paramètres diminuent du centre à la moitié du rayon de la grume et augmentent après jusqu'à la périphérie. La variabilité radiale de  $Q_{22}$  est cependant plus importante que celle obtenue pour  $Q_{66}$ , c.-à-d., avec un contraste s'étendant

entre 49%-72% pour  $Q_{22}$  contre 18%-27% pour  $Q_{66}$  (selon l'endroit dans la grume). Cependant, aucune variation longitudinale significative n'a été observée pour  $Q_{22}$  et  $Q_{66}$  entre les deux hauteurs étudiées, séparées d'environ 4 m.

Les points suivants ont été retenus pour améliorer l'approche proposée dans cette thèse et étudier plus avant la variabilité spatiale des propriétés mécaniques du bois.

- Expérimentalement, des difficultés ont été rencontrés en transférant la grille sur le bois. En conséquence, on a souvent observé de petites régions de grille non-transférée où aucune mesure ne peut être obtenue. Bien que la contrainte de résolution spatiale ait menée au choix de la méthode de grille, ces observations suggèrent que les techniques optiques pour lesquelles aucune préparation de surface n'est nécessaire, p.-ex. les techniques de corrélation d'images ou d'interférométrie de speckle, peuvent être préférables pour un matériau biologique comme le bois.
- Étant donné que la régression au sens des moindres carrés employant des polynômes comme fonction de bases a été utilisée, des régions avec de données manquantes ou erronées (p.-ex., de grille non transférée) peuvent avoir un effet global sur la reconstruction des champs de déformation. Par conséquent, une approche plus locale de reconstruction, telle que l'approximation par éléments finis proposée dans ([Avril and Pierron, 2007](#)) peut être préférable.
- La méthodologie proposée dans ce travail pourrait être reliée à une étude focalisée sur la structure du matériau (p.-ex., l'angle de microfibril, pourcentage du bois juvénile et mûr des spécimens...), afin de fournir des informations appropriées au sujet des causes dans l'origine de la variation spatiale des propriétés de rigidité du bois. Dans la littérature seulement quelques études ont abordé cette question (p.-ex., [Xu et al., 2004](#)).
- Il serait souhaitable de s'interroger sur les configurations d'essais elles-mêmes. Des essais non standards (soit en membrane soit en flexion) permettant l'identification de toutes les composantes de rigidité ( $\{\sigma\} = [C]\{\varepsilon\}$ ) du bois sans défaut, c.-à-d., l'identification des neuf paramètres de rigidité indépendants, dans le repère du matériau, restent à concevoir. Il serait ainsi possible de tout identifier avec seulement trois essais, au lieu de six habituellement utilisés (p.-ex., essais de traction ou compression et essais de cisaillement).
- L'utilisation d'un essai de flexion sur une plaque mince prélevée du centre jusqu'à la périphérie de la grume pourrait permettre d'identifier directement, à partir d'un seul essai, la variabilité radiale des rigidités du bois par la MCV. Une application similaire de la MCV a déjà été mise en œuvre ([Kim et al., 2007](#)).

- 
- À l'échelle mésoscopique, l'identification des rapports de rigidité entre les bois d'été et de printemps en utilisant la MCV est une autre perspective.
  - Enfin, l'application de la MCV à des lois de comportements plus complexes, p.-ex., visco-élastiques en employant des champs virtuels spéciaux complexes constituerait une extension intéressante de la méthode ([Giraudeau et al., 2006](#)).



# Contents

<b>Résumé</b>	<b>vii</b>
<b>Table of contents</b>	<b>xviii</b>
<b>List of figures</b>	<b>xxii</b>
<b>List of tables</b>	<b>xxiv</b>
<b>General Introduction</b>	<b>1</b>
<b>1 The linear elastic behaviour of clear wood: a review</b>	<b>5</b>
1.1 Hierarchical structure and modelling of wood . . . . .	5
1.1.1 Introduction . . . . .	5
1.1.2 Massive scale: structural wood . . . . .	5
1.1.3 Macro scale: clear wood . . . . .	7
1.1.4 Meso scale: growth ring . . . . .	9
1.1.5 Micro scale: cell level . . . . .	9
1.1.6 Conclusions . . . . .	10
1.2 Constitutive behaviour of clear wood . . . . .	10
1.2.1 Introduction . . . . .	10
1.2.2 Anisotropic linear elastic constitutive behaviour . . . . .	11
1.2.2.1 Constitutive equations for an orthotropic material . . . . .	11
1.2.2.2 Plane stress assumption . . . . .	12
1.2.2.3 Engineering constants . . . . .	12
1.2.3 Conclusions . . . . .	13
1.3 Characterisation of elastic properties of clear wood using quasi-static me- chanical tests . . . . .	14
1.3.1 Introduction . . . . .	14
1.3.2 Tensile tests . . . . .	14
1.3.2.1 Parallel to grain . . . . .	14
1.3.2.2 Perpendicular to grain . . . . .	15
1.3.3 Compression tests . . . . .	16

---

1.3.3.1	Parallel to grain	16
1.3.3.2	Perpendicular to grain	17
1.3.4	Shear tests	17
1.3.4.1	Torsional test	17
1.3.4.2	Off-axis tensile test	18
1.3.4.3	Iosipescu shear test	20
1.3.4.4	Arcan test	23
1.3.4.5	Other shear tests	24
1.3.5	Bending tests	24
1.3.5.1	Three-point bending test	25
1.3.5.2	Four-point bending test	27
1.3.6	Conclusions	27
1.4	About the elastic properties of clear wood	29
1.4.1	Introduction	29
1.4.2	Relationships among elastic properties	29
1.4.3	Factors affecting the elastic properties of clear wood	30
1.4.3.1	Moisture content	30
1.4.3.2	Density	31
1.4.4	Spatial variation of elastic properties within the stem	32
1.4.4.1	Radial variation	33
1.4.4.2	Longitudinal variation	33
1.4.5	Conclusions	34
<b>2</b>	<b>Material characterisation from kinematic full-field measurements</b>	<b>35</b>
2.1	A classification of optical methods	35
2.1.1	Introduction	35
2.1.2	Metrological aspects	38
2.1.3	White-light techniques	39
2.1.3.1	Digital speckle photography	39
2.1.3.2	Digital image correlation	40
2.1.3.3	Stereo-correlation	41
2.1.3.4	Geometrical moiré and grid methods	41
2.1.4	Interferometric techniques	43
2.1.4.1	Moiré interferometry	43
2.1.4.2	Electronic speckle pattern interferometry	44
2.1.4.3	Shearography	45
2.1.5	Conclusions	45
2.2	Application of optical methods to wood characterisation	46
2.2.1	Introduction	46

2.2.2	Mechanical testing	46
2.2.3	Influence of the anisotropy and heterogeneity of wood on its mechanical behaviour	47
2.2.4	Crack characterisation	48
2.2.5	Parameter identification from full-field measurements	49
2.2.6	Conclusions	50
2.3	Inverse identification methods	50
2.3.1	Introduction	50
2.3.2	Statistically undetermined tests	51
2.3.3	The virtual fields method: general principle	52
2.3.4	Conclusions	54
<b>3</b>	<b>Inverse identification approach</b>	<b>55</b>
3.1	Introduction	55
3.2	Unnotched Iosipescu test	55
3.3	Grid method: principle	56
3.4	Image processing	58
3.4.1	Phase-evaluation algorithm	58
3.4.2	Strain field reconstruction	61
3.4.2.1	Least-squares polynomial approximation	62
3.5	Stiffness identification by the virtual fields method	64
3.5.1	Principle	64
3.5.2	Determination of the special virtual fields	67
3.5.2.1	Piecewise expansion	67
3.5.2.2	Prescribed conditions	68
3.5.2.3	Optimal solution	70
3.6	Conclusions	71
<b>4</b>	<b>Characterisation of the longitudinal-radial stiffness of <i>P. pinaster</i> wood by a single test. I: Numerical study</b>	<b>73</b>
4.1	Introduction	73
4.2	0° configuration	73
4.2.1	Homogeneous material model	74
4.2.1.1	Finite element model	74
4.2.1.2	Numerical results	76
4.2.1.2.1	Gauge length	76
4.2.1.2.2	Polynomial degree	78
4.2.1.2.3	Virtual mesh size	81
4.2.1.2.4	Stiffness identification	83
4.2.2	Layered material model	84

4.2.2.1	Finite element model . . . . .	85
4.2.2.2	Numerical results . . . . .	87
4.3	Optimal specimen configuration: sensitivity study . . . . .	90
4.3.1	Optimisation scheme . . . . .	90
4.3.2	Numerical results . . . . .	93
4.4	Conclusions . . . . .	94
<b>5</b>	<b>Characterisation of the longitudinal-radial stiffness of <i>P. pinaster</i> wood by a single test. II: Experimental validation</b>	<b>97</b>
5.1	Introduction . . . . .	97
5.2	Experimental work . . . . .	97
5.2.1	Tree and specimens . . . . .	97
5.2.2	Pitch evaluation and grid transfer . . . . .	99
5.2.3	Photomechanical set-up and measurement details . . . . .	101
5.3	Results and discussion . . . . .	107
5.3.1	0° configuration . . . . .	107
5.3.2	45° configuration . . . . .	114
5.3.3	30° configuration . . . . .	119
5.4	Conclusions . . . . .	121
<b>6</b>	<b>On the spatial variability of the longitudinal-radial stiffness of <i>P. pinaster</i> wood within the stem</b>	<b>123</b>
6.1	Introduction . . . . .	123
6.2	Experimental work . . . . .	124
6.3	Results and discussion . . . . .	126
6.3.1	Stiffness variation along the radial direction . . . . .	126
6.3.2	Stiffness variation along the longitudinal direction . . . . .	130
6.4	Conclusions . . . . .	133
	<b>General conclusions and future work</b>	<b>137</b>
	<b>References</b>	<b>151</b>

# List of Figures

1.1	Hierarchical scales of wood. . . . .	6
1.2	Macrostructure features of the softwood stem: (1) cross-section; (2) radial-section; (3) tangential-section; (4) pith; (5) heartwood; (6) sapwood; (7) growth ring; (8) cambium; (9) bark; (10) rays ( $L$ -longitudinal, $R$ -radial and $T$ -tangential). . . . .	8
1.3	Schematic representation of tensile tests using two specimen configurations.	15
1.4	Specimens for tensile tests carried out perpendicularly to the grain along the (a) radial and (b) tangential directions. . . . .	16
1.5	Schematic representation of specimens for compression testing. Parallel to grain longitudinal compression (ASTM D143, 1994): $l = 200$ mm, $w = t = 50$ mm ( $1 - 2 \equiv L - R$ ). . . . .	17
1.6	Off-axis tensile test: (a) schematic representation ( $l = 200$ mm, $w = 20$ mm, $t = 5$ mm, $\alpha = 15^\circ$ ); (b) rectangular and oblique end tabs. . . . .	19
1.7	Schematic representations of: (a) the Iosipescu shear test; (b) the Iosipescu fixture. . . . .	21
1.8	Schematic representations of: (a) the Arcan shear test (for clear wood specimen: $l = 70$ mm, $w = 50$ mm, $t = 8$ mm, $d = 30$ mm, $r = 2$ mm and $\theta = 110^\circ$ ); (b) the Arcan fixture. . . . .	23
1.9	Schematic representations of the shear tests: (a) the in-plane shear test (Yoshihara and Matsumoto, 2005); (b) the quasi-simple shear test (Naruse, 2003); (c) the square-plate twist test (Yoshihara and Sawamura, 2006). . . . .	25
1.10	Schematic representation of: (a) the 3 point bending test (for clear wood specimen: $d \geq 420$ mm, $L = \{107, 129, 173, 400\}$ mm, $w = 20$ mm, $t = 20$ mm and $r = 15$ mm); (b) the variable span method for the identification of the longitudinal and shear moduli ( $\beta = R, T$ ). . . . .	26
1.11	Schematic representation of the four-point bending test (EN 408 (2002): $d = 380$ mm, $a = 120$ mm, $b = 120$ mm, $w = t = 20$ mm, and $r = 15$ mm).	26
3.1	Schematic representation of the unnotched Iosipescu test. $x - y$ is the specimen coordinate system; $1 - 2$ is the material coordinate system. . . . .	56

3.2	(a) Schematic representation of the grid principle: (a) imaging system (b) grid deformation. . . . .	57
3.3	Image processing and identification flowchart. . . . .	59
3.4	Images of the: (a) crossed grid, $I(x, y)$ ; (b) vertical lines grid, $I_x(x, y)$ ; (c) horizontal lines grid, $I_y(x, y)$ . . . . .	60
3.5	Weighting matrix: (a) first iteration (3.5% of invalid pixels over the region of interest); (b) second iteration (8.3% of invalid pixels over the region of interest). . . . .	64
3.6	Schema of the unnotched Iosipescu test illustrating the application of the virtual fields method. $x - y$ and 1 - 2 are the specimen and material coordinate systems, respectively. . . . .	65
4.1	Algorithm implemented in the validation of the material characterisation approach ( $\beta = x, y, i, j = 1, 2, 6$ ). . . . .	74
4.2	(a) Finite element model of the unnotched Iosipescu test, with $L = 34$ mm ( $\delta = 0.4$ mm, FE size = 0.6 mm); (b) meshing refinement study - $Q_{ij}^r$ and $Q_{ij}$ are, respectively, the reference and identified stiffness parameters. . . . .	75
4.3	(a) Variation of the sensitivity coefficients, $\xi_{ij} = \eta_{ij}/Q_{ij}$ , with regard to the gauge length $L$ ; (b) evaluation of the objective function $\phi(L)$ . . . . .	78
4.4	(a) Simulated, (b) approximated (7th-degree polynomial) and (c) residual $u_x$ displacement component obtained for the $0^\circ$ specimen (without and with adding a Gaussian white noise with $\sigma_u = 2 \mu\text{m}$ ) (unit: $\mu\text{m}$ ). . . . .	79
4.5	(a) Simulated, (b) approximated (7th-degree polynomial) and (c) residual $u_y$ displacement component obtained for the $0^\circ$ specimen (without and with adding a Gaussian white noise with $\sigma_u = 2 \mu\text{m}$ ) (unit: $\mu\text{m}$ ). . . . .	80
4.6	Evaluation of the residual ( $\Delta u_\beta$ , $\beta = x, y$ ) of the difference between simulated ( $u_\beta$ ) and approximated ( $\bar{u}_\beta$ ) displacement fields, with the increase of the degree ( $d$ ) of the fitting polynomial (unit: $\mu\text{m}$ ). . . . .	81
4.7	Typical strain fields ( $P = -261.8$ N): (a) $\varepsilon_1$ , (b) $\varepsilon_2$ , (b) $\varepsilon_6$ , obtained for the $0^\circ$ specimen by differentiating (finite difference scheme) 2D polynomial displacements with degrees ( $d$ ) ranging from 5 to 11 (unit: $\times 10^{-3}$ ). . . . .	82
4.8	Relative differences of the (a) $Q_{11}$ , (b) $Q_{22}$ , (c) $Q_{12}$ and (d) $Q_{66}$ stiffness components, with regard to reference values, identified using piecewise virtual fields defined over a mesh of $N_X = \{2, 3, \dots, 14\}$ and $N_Y = \{2, 3, \dots, 8\}$ elements (using a 7th-degree polynomial displacement without noise). . . . .	83
4.9	Graphical display of the mesh deformation corresponding to each optimised special virtual field used in the identification of: (a) $Q_{11}$ ; (b) $Q_{22}$ ; (c) $Q_{12}$ ; (d) $Q_{66}$ . . . . .	84

4.10	Layered material model of the unnotched Iosipescu wood specimen. . . . .	86
4.11	(a) Simulated, (b) approximated (7th-degree polynomial) and (c) residual $x$ and $y$ displacement components obtained for the layered material model ( $n = 10$ , $w^l = 0.4$ and $k = 2$ ) (unit: $\mu\text{m}$ ). . . . .	88
4.12	Strain field components ( $\varepsilon_1$ , $\varepsilon_2$ and $\varepsilon_6$ ) of the layered material model ( $P = -261.2$ N): (a) obtained from numerical differentiation of the polynomial displacement fields; (b) delivered directly from ANSYS (unit: $\times 10^{-3}$ ). . . . .	89
4.13	Elastic constants: (a) $E_1$ , (b) $E_2$ , (c) $\nu_{12}$ and (d) $G_{12}$ , identified from the layered material models by the virtual fields method (parametric data: $(w^l, k)$ ). . . . .	90
4.14	Algorithm used in the optimisation scheme of the configuration of the unnotched Iosipescu specimen. . . . .	92
4.15	The cost function pattern as function of the $L$ and $\theta$ design variables. . . . .	94
4.16	Strain field maps ( $\varepsilon_1$ , $\varepsilon_2$ and $\varepsilon_6$ ), along with their histograms plots, obtained for the ( $L = 35$ mm): (a) $0^\circ$ configuration, (b) $30^\circ$ configuration (unit: $\times 10^{-3}$ ). . . . .	95
5.1	<i>P. pinaster</i> tree from where the specimens were manufactured. . . . .	98
5.2	Illustration of the steps in the grid transfer ( $p = 0.1$ mm). . . . .	100
5.3	(a) Photo and (b) schematic of the mechanical set-up ( $WD$ (working distance) $\sim 450$ mm). . . . .	102
5.4	(a) Grid image; (b) moiré effect used in the calibration of the optical system magnification; (c) histogram of the grid image. . . . .	103
5.5	(a) Residual maps of the displacement typically obtained from experimental measurements; (b) Verification of the Gaussian distribution of the residual values of the displacement ( $- \cdot - : 2\sigma$ ) (unit: $\mu\text{m}$ ). . . . .	106
5.6	Variation of the stiffness parameters with respect to the degree of the fitting polynomial for $0^\circ$ (■) and $45^\circ$ (□) specimens: (a) $Q_{11}$ , (b) $Q_{12}$ , (c) $Q_{22}$ , (d) $Q_{66}$ . . . . .	108
5.7	(a) Measured, (b) approximated (7th-degree polynomial) and (c) residual for $u_x$ and $u_y$ obtained for a $0^\circ$ specimen ( $P = -139.4$ N) (unit: $\mu\text{m}$ ). . . . .	110
5.8	Typical (I) experimental and (II) numerical strain fields obtained for a $0^\circ$ specimen ( $P = -139.4$ N): (a) $\varepsilon_1$ , (b) $\varepsilon_2$ , (b) $\varepsilon_6$ . . . . .	111
5.9	Variation of the identified stiffness components with respect to the number of elements used to set up the <i>virtual</i> mesh of the $0^\circ$ specimen: (a) $Q_{11}$ , (b) $Q_{12}$ , (c) $Q_{22}$ , (d) $Q_{66}$ . . . . .	111
5.10	Identified stiffness parameters as a function of the applied load for a $0^\circ$ (■) and $45^\circ$ (□) specimens: (a) $Q_{11}$ , (b) $Q_{22}$ , (c) $Q_{12}$ , (d) $Q_{66}$ . . . . .	112

5.11	(a) Measured, (b) approximated (7th-degree polynomial) and (c) residual for $u_x$ and $u_y$ obtained for a 45° specimen ( $P = -143.0 N$ ) (unit: $\mu\text{m}$ ). . . . .	116
5.12	Typical (I) experimental and (II) numerical strain fields obtained for a 45° specimen ( $P = -143.0 N$ ): (a) $\varepsilon_1$ , (b) $\varepsilon_2$ , (b) $\varepsilon_6$ . . . . .	117
5.13	Variation of the identified stiffness components with regard to the number of elements used to set up the <i>virtual</i> mesh of the 45° specimen: (a) $Q_{11}$ , (b) $Q_{12}$ , (c) $Q_{22}$ , (d) $Q_{66}$ . . . . .	117
5.14	Typical (I) experimental and (II) numerical strain fields obtained for a 30° specimen ( $P = -176.5 N$ ): (a) $\varepsilon_1$ , (b) $\varepsilon_2$ , (b) $\varepsilon_6$ . . . . .	120
5.15	Identified stiffness parameters as function of the applied load for a 30° specimen: (a) $Q_{11}$ , (b) $Q_{22}$ , (c) $Q_{12}$ , (d) $Q_{66}$ . . . . .	120
6.1	(a) Logs (1, 2, 3 and 4) of the <i>P. pinaster</i> tree from where specimens were manufactured; (b) schematic representation of the specimen sampling within the stem. . . . .	125
6.2	Curves of load versus cross-head displacement obtained at vertical location 1 for the radial positions : (a) $r_1$ ; (b) $r_2$ ; (c) $r_3$ ; (d) $r_4$ ; (e) average curves (displacement rate of 1 mm/min). . . . .	127
6.3	Curves of load versus cross-head displacement obtained at vertical location 2 for the radial positions: (a) $r_1$ ; (b) $r_2$ ; (c) $r_3$ ; (d) average curves (displacement rate of 1 mm/min). . . . .	128
6.4	Variation of the oven-dry density ( $\rho$ ) at vertical locations 1 (■) and 2 (□) with the radial positions. . . . .	128
6.5	Identified stiffness parameters at vertical location 1 as a function of the applied load: (a) $Q_{22}$ ; (b) $Q_{66}$ . . . . .	131
6.6	Identified stiffness parameters at vertical location 2 as a function of the applied load: (a) $Q_{22}$ ; (b) $Q_{66}$ . . . . .	131
6.7	Stiffness values: (a) $Q_{22}$ ; (b) $Q_{66}$ , identified at vertical position 1 for the radial positions $r_1$ , $r_2$ , $r_3$ and $r_4$ (unit: $\rho$ - $\text{g}\cdot\text{cm}^{-3}$ ; $Q_{ij}$ - GPa). . . . .	134
6.8	Stiffness values: (a) $Q_{22}$ ; (b) $Q_{66}$ , identified at vertical position 2 the radial positions $r_1$ , $r_2$ and $r_3$ (unit: $\rho$ - $\text{g}\cdot\text{cm}^{-3}$ ; $Q_{ij}$ - GPa). . . . .	135
6.9	Variation of the stiffness parameters: (a) $Q_{22}$ ; (b) $Q_{66}$ , identified at the two vertical locations 1 (■) and 2 (□) as a function of the radial position ( $r/R$ ). . . . .	136
6.10	Comparison of the stiffness parameters: (a) $Q_{22}$ ; (b) $Q_{66}$ , identified at the two vertical locations 1 (■) and 2 (□) at the outmost radial position, $r_4$ and $r_3$ , respectively, with regard to reference values (○). . . . .	136

# List of Tables

2.1	Optical methods in experimental mechanics. . . . .	36
2.2	Some heterogeneous mechanical tests for the identification of constitutive parameters. . . . .	53
4.1	Reference elastic engineering properties of <i>P. pinaster</i> wood used in the finite element analyses (Pereira, 2005; Xavier et al., 2004) ( $1 - 2 \equiv L - R$ ). . . . .	75
4.2	Stiffness parameters identified by the virtual fields method (with a mesh of $8(x) \times 4(y)$ elements) from the finite element strains, without (Ident. 1) and with (Ident. 2) noise ( $\sigma_\varepsilon = 10^{-4}$ , 30 iterations), and from the finite element displacements, without (Ident. 3) and with (Ident. 4) noise ( $\sigma_u = 2 \mu m$ , 30 iterations) (unit: GPa) ( $1 - 2 \equiv L - R$ ). . . . .	85
4.3	Earlywood and latewood elastic engineering properties used in the finite element analyses ( $k = 2$ , $w^l = 0.4$ ) ( $1 - 2 \equiv L - R$ ). . . . .	87
4.4	Identification of homogenised elastic engineering properties of the layered material model of the unnotched Iosipescu wood specimen by the virtual fields method: (1) directly from the finite element strain fields without noise (Ident. 1); (2) from the finite element displacement maps without noise (Ident. 2). Ident. 3: identification results obtained from the homogeneous material model (from Ident. 1 in Table 4.2) ( $1 - 2 \equiv L - R$ ). . . . .	91
5.1	Reference stiffness values of <i>P. pinaster</i> wood identified using standard tests (moisture content of about 11%) (Pereira, 2005; Xavier et al., 2004) ( $1 - 2 \equiv L - R$ ). . . . .	112
5.2	Stiffness properties of <i>P. pinaster</i> wood identified by the virtual fields method ( <i>virtual</i> mesh of $8(x) \times 4(y)$ elements) from the $0^\circ$ specimens (moisture content about 9–10%) ( $1 - 2 \equiv L - R$ ). . . . .	113
5.3	Stiffness properties of <i>P. pinaster</i> wood identified by the virtual fields method ( <i>virtual</i> mesh of $5(x) \times 3(y)$ elements) from the $45^\circ$ specimens (moisture content about 9–10%) ( $1 - 2 \equiv L - R$ ). . . . .	118

6.1	Comparison of mean values between the different radial positions at vertical location 1 by the Student's $t$ -test of equality of means of two samples at a 95% of confidence level ( $1 - 2 \equiv L - R$ ). . . . .	132
6.2	Comparison of mean values between the different radial positions at vertical location 2 by the Student's $t$ -test of equality of means of two samples at a 95% of confidence level ( $1 - 2 \equiv L - R$ ). . . . .	132

# General Introduction

Wood is a natural composite material formed by trees. Since trees are a valuable resource on earth, historically, wood has always played an important role as a material (*e.g.*, in construction). In more recent decades, manufacturing developments have led to new engineering products based on raw wood material – such as glued laminated timber, structural plywood, oriented strand board (OSB), laminated veneer lumber (LVL) and wood I-joists – specifically designed to fit structural requirements ([Williamson, 2002](#)). Both solid wood and its derivative products constitute nowadays important engineering materials owing to the following reasons ([STEP, 1996](#)): (1) trees are produced by a free source of energy (the sun) and they are renewable and recyclable; (2) there are important forestal resources on earth; (3) the silviculture and wood transformation have a relatively low cost; (4) the wood material has good stiffness to weight and strength to weight ratios. Nevertheless, for the efficient utilisation of wood in engineering applications, the material parameters governing relevant constitutive equations (*e.g.*, the stiffness parameters in the linear elastic anisotropic model) as well as other properties such as strength values, must be properly characterised for each species ([ASTM D143, 1994](#); [Bodig and Goodman, 1973](#)).

As a rough approximation, the stem of a tree can be conceptualised as a cylindrical orthotropic material ([Guitard, 1987](#); [Smith et al., 2003](#)). Three planes of symmetry are locally defined by the longitudinal ( $L, 1$ ), radial ( $R, 2$ ) and tangential ( $T, 3$ ) principal directions of the longitudinal wood cells (tracheids in softwood). The mechanical properties of wood are usually identified in this material coordinate system; properties along different directions can be determined from standard transformation equations afterwards. The mechanical behaviour of wood can be analysed hierarchically over a spectrum of length scales. At the macroscopic scale, clear wood (*i.e.*, defects-free and straight-grained wood) is normally assumed as a solid (continuous) and homogeneous material. Different constitutive equations have been proposed in the literature for clear wood modelling, each of them with a specific domain of validity. Neglecting any deformation generated by hygro-thermal effects, the constitutive equations generally accepted are the linear elastic and viscoelastic models ([Dinwoodie, 2000](#); [Guitard, 1987](#); [Holmberg et al., 1999](#); [Kollman and Côté Jr., 1984](#); [Smith et al., 2003](#)). Wood seems to be more accurately described by the viscoelastic theory since experimental observations have revealed a strain-rate dependence

on its mechanical response. However, for most practical applications, the time dependent deformation may be neglected and wood can simply be considered as a linear elastic solid. This theory assumes relatively low levels of stress (below the elastic limit), applied over a short period of time (a few minutes) and at room temperature. The elastic parameters governing the linear elastic constitutive equation have been recognised as fundamental data in the following applications: (1) for the comparison of properties among trees and species (ASTM D143, 1994; Dinwoodie, 2000); (2) for understanding the effects on wood mechanical properties of factors such as density, moisture content, geographical origin and positions within the stem (ASTM D143, 1994; Dinwoodie, 2000; Guitard, 1987; Kollman and Côté Jr., 1984; Machado and Cruz, 2005); (3) for the numerical and experimental analyses of the deformation of structural wood members (Bodig and Goodman, 1973; Sliker, 1985); (4) for capturing genetic breeding opportunities and also for improving the stiffness properties of juvenile wood in fast grown conifers (Lindström et al., 2002).

Furthermore, one major advantage of the assumption of linear elasticity is that quasi-static mechanical tests can be carried out for the characterisation of the elastic properties of wood. However, because of the orthotropy of the wood structure, several independent tests are usually required (Guitard, 1987). Such methods rely on simple loading conditions (tension, compression, shear or bending) for which a simple state of stress is assumed over a representative volume element of the material at the scale of analysis. In these cases, an analytical (closed-form) solution can be derived, directly linking the load and strain measurements to the unknown material parameters. Owing to anisotropy and heterogeneity, the requirement for improved mechanical test methods has soon emerged (Jones, 1999; Tarnopol'skii and Kulakov, 1998). In this field of research, several mechanical tests have been designed and improved for this type of material (*e.g.*, the off-axis tensile test and the Iosipescu shear test). Nevertheless, some drawbacks have been pointed out to these methods, namely, the practical difficulty of generating a uniform stress/strain field across the region of interest because of both end and edge effects (Grédiac, 1996; Tarnopol'skii and Kulakov, 1998).

For the identification of representative parameters of a given species of wood, several specimens, cut at random locations within the stem and from different trees, need to be tested in order to account for the inherent structural variability of wood (Bodig and Goodman, 1973). Hence, owing to the anisotropy and variability of wood, it can be concluded that a significant amount of tests are required, which is quite expensive and time consuming. To simplify this procedure, an approach has been proposed since the early work of Bodig and Goodman (1973). Basically, it consists in deriving relationships among wood properties. Since the longitudinal elastic modulus is known for most species, this parameter has been often taken as the independent variable (Bodig and Goodman, 1973; Green et al., 1999; Sliker, 1985, 1988; Sliker and Yu, 1993). The prediction of the elastic parameters from physical properties such as the density has also been the object of

research in several studies (Bodig and Goodman, 1973; Gibson and Ashby, 1997; Guitard, 1987; Sliker and Yu, 1993; Walton and Armstrong, 1986). An alternative approach is used in this work.

Thanks to the advent of full-field optical methods, which provide the measurement of kinematic quantities (*e.g.*, displacement, slope, strain or curvature) over a whole region of interest, a new perspective on mechanical testing for material characterisation has been progressively introduced (Grédiac, 1996, 2004). The basic idea is that a single specimen can be loaded in such a way that several parameters are simultaneously involved in its mechanical response, yielding complex and heterogeneous stress/strain fields. Providing that these fields are measured by a suitable optical method, the whole set of active parameters can be determined afterwards by an appropriate identification strategy. This approach seems to be particularly convenient for a material like wood. Indeed, it has been already applied to wood or wood based products by a few authors (Cárdenas-García et al., 2005; Foudjet et al., 1982; Jernkvist and Thuvander, 2001; Le Magorou et al., 2002; Rouger, 1988).

The aim of this work is to apply this inverse identification approach to the characterisation of the longitudinal-radial,  $(L, R) \equiv (1, 2)$ , stiffness parameters ( $Q_{11}$ ,  $Q_{22}$ ,  $Q_{12}$  et  $Q_{66}$ ) of maritime pine (*Pinus pinaster* Ait.) wood. Particularly, the proposed procedure is based on the application of the virtual fields method (VFM) to a rectangular specimen loaded in the Iosipescu fixture. Displacement fields are measured by the optical grid method. Eventually, a contribution to the spatial variability of the  $LR$  stiffness parameters within the stem is proposed.

This report consists of six chapters. In chapter 1, the linear elastic behaviour of wood is reviewed, with emphasis being placed on the standard mechanical tests usually employed for its characterisation. The full-field optical methods most commonly used in experimental mechanics and their interest to wood mechanics are outlined in Chapter 2, along with a presentation of statistically undetermined tests and the general principle of the VFM. Chapter 3 presents the inverse identification approach proposed in this work. The numerical and experimental validation of this approach are studied in Chapters 4 and 5, respectively. Chapter 6 describes the application of the proposed methodology in accessing the spatial variability of the stiffness parameters within the stem. Finally, the general conclusions and some directions for future work are given.



# Chapter 1

## The linear elastic behaviour of clear wood: a review

### 1.1 Hierarchical structure and modelling of wood

#### 1.1.1 Introduction

Trees can be classified, into two main groups, according to their anatomy: softwoods (*Gymnospermae*) and hardwoods (*Angiospermae*). Although the nature and composition of wood is basically the same for all trees, this classification is justified because the types of cells, their proportions and arrangements greatly differ from one species to another. As maritime pine wood (*Pinus pinaster* Ait.) was used as tested material in this work, this section will focus specifically on softwood species.

A tree is a vascular woody plant which contains three main parts: the root system, the stem and the crown system. Only the stem of the tree will be considered. The wood within the stem has a heterogeneous structure which can be observed hierarchically over a spectrum of length scales as illustrated in Figure 1.1.

In understanding the mechanical behaviour of wood it is important to be acquainted with its morphology. The main features of the wood structure are reviewed below, based on the following references: [Dinwoodie \(2000\)](#); [Guitard \(1987\)](#); [Kollman and Côté Jr. \(1984\)](#); [Smith et al. \(2003\)](#).

From a mechanical point of view, different models along with test methods are usually applied along the hierarchical scales. At each relevant scale of observation, the basic assumptions on which wood modelling relies on are also summarised in this section.

#### 1.1.2 Massive scale: structural wood

At the structural scale ( $> 1\text{ m}$ ), several growth features can be distinguished within the stem such as juvenile and mature wood, knots, reaction wood and spiral grain (Fig-

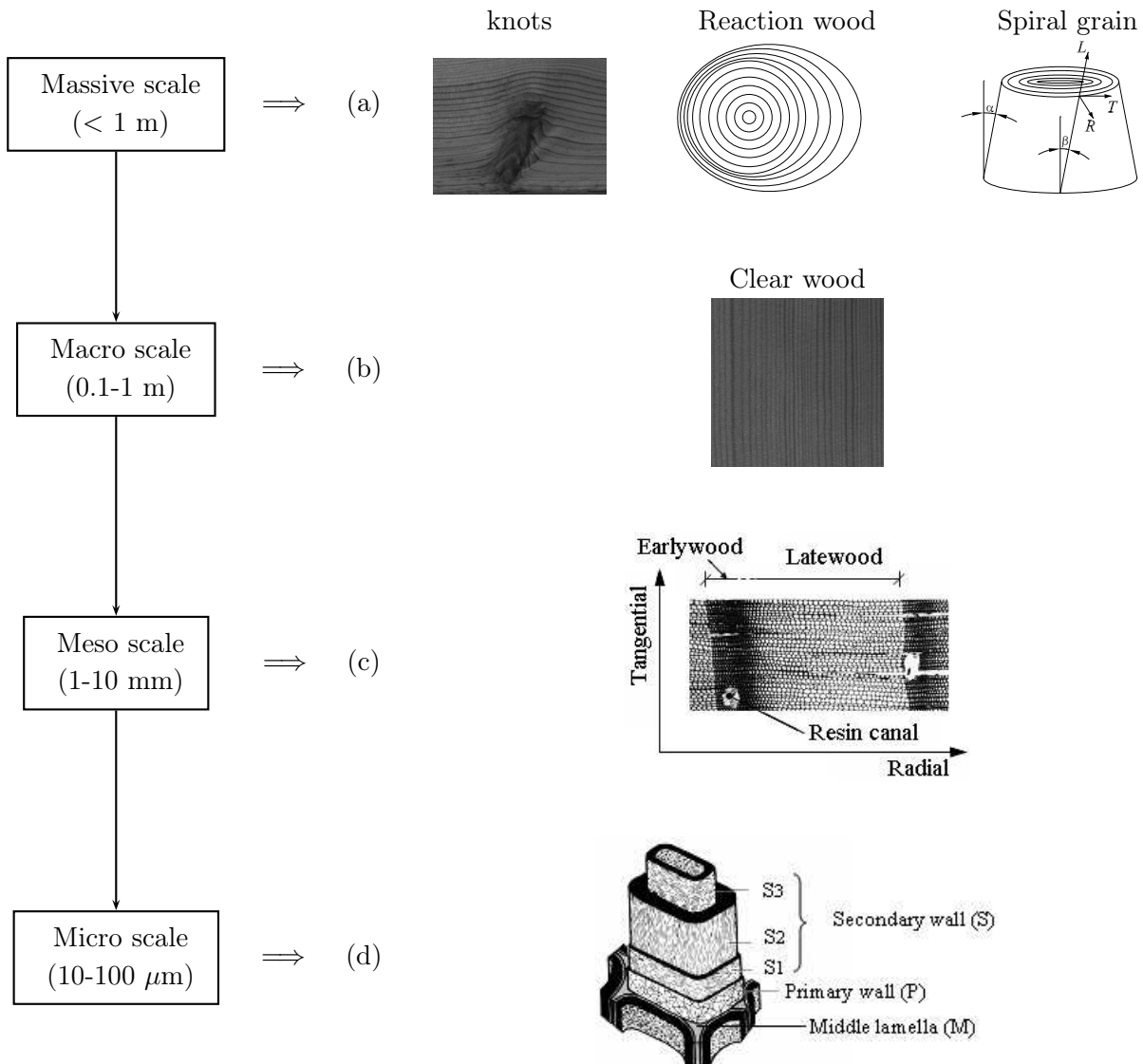


Figure 1.1: Hierarchical scales of wood.

ure 1.1(a)). Juvenile wood is a layer of wood surrounding the pith typically formed within the first 5-20 annual growth rings. This wood consists of cells formed by juvenile cambium and exists in all trees. Compared with mature wood, which is formed later in the growing process, juvenile wood is characterised by short cells with large diameter lumen (hollow of the cell), thin cell walls, and usually has more knots. Furthermore, the physical and mechanical properties of juvenile wood are spatially less uniform than the ones of mature wood. Knots (Figure 1.1(a)) are sections of the tree branches that are embedded in the wood of the stem. They create localised disturbances in the orientation of the longitudinal wood cells, resulting in wood structure, and therefore wood properties, variations. Reaction wood (Figure 1.1(a)) is another component of the tree, associated with the ec-

central location of the pith and abnormal growth rings formed by trees as a reaction to adverse external forces (*e.g.*, the wind). In softwood, the growth rings are abnormally wide on the underside of an inclined stem, leading to what is called compression wood. Key disadvantages of reaction wood, compared to normal wood, are the reduction of the strength and the augmentation of shrinkage along the grain. Another important feature about the wood architecture is the alignment of the longitudinal wood cells with regard to the long axis of the stem, called spiral grain (Figure 1.1(a)). The grain is usually arranged either in a right- or left- handed helical or spiral pattern around the stem. This pattern usually changes during the growing of the tree. The local orientation of the grain can be defined by the radial ( $\alpha$ ) and tangential ( $\beta$ ) angles formed with regard to the longitudinal direction of the stem (Figure 1.1(a)). The spiral grain can lead to the reduction of the mechanical properties of wood and the enhancement of its tendency to twist during drying.

Conceptually, the wood of a tree can be modelled as a cylindrical orthotropic material having three planes of symmetry (sections 1, 2 and 3 in Figure 1.2) along its longitudinal ( $L, 1$ ), radial ( $R, 2$ ) and tangential ( $T, 3$ ) directions. At the structural scale and for engineering design purposes, the cylindrical orthotropy of wood is usually turned into transverse isotropy, *i.e.*, the mechanical properties of wood are assumed identical across the radial-tangential ( $R-T$ ) plane (ASTM D143, 1994; EN 408, 2002; STEP, 1996). This assumption is based on the observation that the anisotropy ratio  $E_R/E_T$  is usually close to unity – *e.g.*,  $E_R/E_T = 1.9$  for *P. pinaster* wood (Pereira, 2005). The properties of wood along the transversal cross-section are usually referred in the literature as perpendicular to grain, whereas along the longitudinal direction they are referred to as parallel to grain.

### 1.1.3 Macro scale: clear wood

The features of wood at the macroscopic level (0.1-1 m) can be observed by considering the cross-section (1), the radial-section (2), and the tangential-section (3) of the stem (Figure 1.2). In the cross-section the following layers can be distinguished: pith (4), heartwood (5), sapwood (6), cambium (8) and bark (9) (Figure 1.2). The pith consists of soft spongy cells with low strength and durability, located in the centre part of the stem. Typically its diameter is of a few millimeters. Surrounding the pith there are the heartwood and sapwood layers, which are the inward and outward parts of the stem, respectively. The heartwood is typically darker than sapwood. The width and colour of these layers can vary significantly between species. The cells in the heartwood are dead and they contribute mostly to the structural support of the tree. Also, this region accumulates the function of storage of the excess of nutrients, that are metabolised into extractives such as resin and tannins. Sapwood is used by the tree for conducting water and nutrients, necessary for its growing process. After these layers, which constitute the

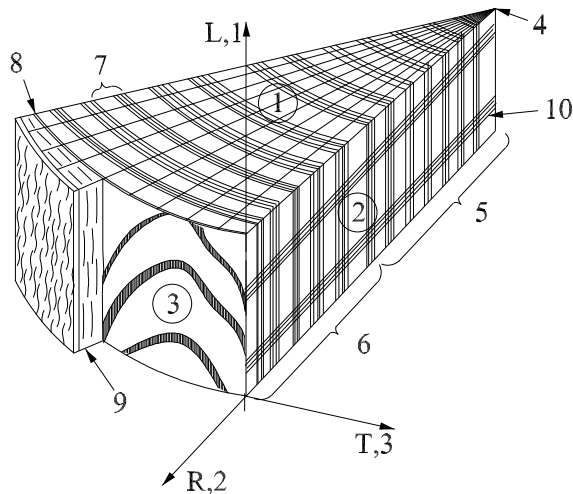


Figure 1.2: Macrostructure features of the softwood stem: (1) cross-section; (2) radial-section; (3) tangential-section; (4) pith; (5) heartwood; (6) sapwood; (7) growth ring; (8) cambium; (9) bark; (10) rays ( $L$ -longitudinal,  $R$ -radial and  $T$ -tangential).

wood material of the stem or xylem, follows the vascular cambium, which is a thin layer located just beneath the bark where the formation of new cells takes place. The cells of the cambium divide, forming wood (xylem) to the inside and bark (phloem) to the outside. Thus, the stem of the tree increases radially and longitudinally. Finally, the bark is the outermost layer of the stem whose function is the protection of the tree from its surrounding environment.

For species growing in temperate climates, alternately concentric regions are visible (7), corresponding to the annual growth increments of wood (Figure 1.2). The wood rays (10), consisting of parenchyma cells, can be observed in the radial section and they represent only a small percentage (5-10%) of the entire wood in the stem (Figure 1.2). They are organised in tissues disposed from the pith to the bark, and their main function is the storage of nutrients. These cells are perpendicular to the longitudinal ones (tracheids), and give some strength and stiffness to wood in the radial direction.

At this scale, wood is called clear wood because it is assumed free from structural defects such as knots and gross grain deviation. A sample of clear wood is usually assumed to be homogeneous, *i.e.*, an elementary representative volume of material with uniform mechanical properties. In addition, as the characteristic dimensions of the sample are much larger than the microscopic cellular structure of wood (a few tenths of a micrometre), the assumption of a continuum medium is justified. The wood cells formed in the growing process of a tree are roughly arranged longitudinally in concentric circles within the stem. If a sample of wood is cut at a sufficient distance from the pith (*i.e.*, in the outward part of the stem), such as the curvature of the growth rings can be neglected, wood may be simply modelled assuming rhombic orthotropy. Locally at each material point within the stem, three principal material directions of wood are defined: the longitudinal direction ( $L, 1$ ) along the grain; the radial direction ( $R, 2$ ) perpendicular to the longitudinal cells and parallel to the rays; and the tangential direction ( $T, 3$ ) tangent to the growth ring and

perpendicular to  $L$  and  $R$  (Figure 1.2). These directions define the material coordinate system.

#### 1.1.4 Meso scale: growth ring

At this scale of magnification (1-10 mm) the cellular structure of wood can be observed (Figure 1.1(c)). It consists of an aggregate of cells, often with an hexagonal shape, aligned with the direction of the stem. At this level, an individual annual growth ring can be assumed consisting of two principal layers called, respectively, earlywood (springwood) and latewood (summerwood) (Figure 1.1(c)). The early and late woods are formed at the beginning and at the end of the growing season (spring) respectively. The transition from earlywood to latewood occurs gradually (a transition zone may be distinguished), as opposed to the latewood to earlywood one which is rather abrupt. The cells in the earlywood are characterised by thin walls and large diameters, whilst it is the converse for the latewood, where the cells are smaller in diameter and have thick walls. The growth rate of the tree is different throughout the years, resulting in the radial variation of the width of the annual rings within the stem. As a typical pattern, founded for instance in *P. pinaster* wood, the annual rings are wider in the centre and thinner at the periphery; besides, the width of the latewood layer tends to be constant. Furthermore, although the cross-section of the stem is roughly circular, the annual rings do not necessarily develop uniformly in all the radial directions due to effects such as the direction of sunlight, the shade and the topography of the growth site. This can induce, for instance, the formation of reaction wood (§ 1.1.2).

At the meso scale, wood is usually analysed and modelled as a cellular solid material. Honeycomb models of the aggregate of wood cells (unit cell method) have been proposed for estimating the stiffness of the cellular wood material from the cell geometry, cell wall properties and applied beam theory.

#### 1.1.5 Micro scale: cell level

The wood cell wall (10-100  $\mu m$ ) is a layered structure consisting of middle lamella (M), primary wall (P) and secondary wall (S) (Figure 1.1(d)). Each layer consists of an amorphous matrix made up of hemicelluloses and lignin, reinforced by highly ordered bundles of cellulose chains called microfibrils. The orientation of the microfibrils, with regard to the long cell axis, is called the microfibril angle (MFA). Cells are joined together by the middle lamella. The primary wall is usually very thin, about 0.1  $\mu m$ , and has randomly distributed microfibrils. Their distribution is more organised within the secondary wall. In both S1 and S3 secondary-wall layers, the microfibrils are oriented almost perpendicular to the cell axis. However, in the S2 layer, the thickest of the three (about 80% of the cell wall thickness), the microfibrils form a right-handed spiral and are nearly oriented

parallel to the cell axis.

At this scale, wood can be modelled as a natural fibre-reinforced composite laminated material. The lay-up of the cellulose microfibrils within the cell wall (*i.e.*, the variation of the MFA across the cell wall thickness, especially in the S2 secondary layer) as well as the elongated geometry of the cell (the length of the cell is about 100-fold greater than the dimensions of its cross-section), play an important role in the stiffness and anisotropy of the wood cell wall.

### 1.1.6 Conclusions

Trees can be distinguished by their anatomical structure into softwood and hardwood species. Maritime pine wood (*Pinus pinaster* Ait.), which belongs to softwoods species, was selected as the material for this work. *P. pinaster* wood is an important species in Southern Europe. In Portugal, it represents about 23% (almost 1 hectare) of the total forest area of the country and 88% of the volume of raw material consumed in wood-based industries (*e.g.*, sawmill, plywood, particle board, pulp and paper) (DGF, 2007).

The structure and the mechanical behaviour of wood can be analysed hierarchically at several length scales. At each level, different assumptions and models are usually assumed. In this work, wood will be analysed at the macroscopic scale. At this scale, wood is modelled as a continuous (solid) and homogeneous material, with three plane of orthotropic symmetry defined by the longitudinal ( $L$ ), radial ( $R$ ) and tangential ( $T$ ) directions of the wood cells (tracheids).

## 1.2 Constitutive behaviour of clear wood

### 1.2.1 Introduction

Owing to the biological nature of wood, its deformation process can be quite complex. At low levels of stresses, experimental observations have suggested that wood can be modelled as an anisotropic, viscoelastic and hygroscopic material. The anisotropy nature of wood means that the mechanical properties at a given material point are directionally dependent (Guitard, 1987, p. 57). The viscoelasticity of wood implies that its mechanical properties are sensitive to strain rate (Widehammar, 2006). In the hygroscopic domain, defined between the anhydrous and cell wall saturation states (§ 1.4.3.1), the ability of wood to exchange humidity with its surrounding environment can be responsible for an additional free shrinkage or swelling deformation (Badel and Perré, 2001). Moreover, when wood is simultaneously subjected to loading and moisture content changes below the fiber saturation point (§ 1.4.3.1), the mechano-sorptive effect may be observed as an additional deformation (Muszyński et al., 2005).

Consequently, it can be concluded that the constitutive modelling of all different contributions on the mechanical behaviour of wood can be quite complex. Particularly, from the experimental point of view, the parameter identification can be a rather difficult task (Muszyński, 2006; Muszyński et al., 2005). Based on the fact that the constitutive behaviour of wood depends on the actual application, *i.e.*, on the type and duration of load and on environmental effects (moisture and temperature variations) to be considered, hypothesis and assumptions are usually postulated, restricting the analyses to particular mechanical responses. In the simplest case, involving low levels of stress (below the elastic limit), short periods of time (a few minutes) and minor variations of moisture content and temperature (absence of hygro-thermal environment effects), it should be sufficient to simply assume wood as a linear elastic anisotropic material (Dinwoodie, 2000, p. 94). In other cases, however, such as in wood drying, it is necessary to include mechano-sorptive effects and creep in the model (Holmberg et al., 1999). Besides, under conditions of very heavy loading, such as in defibration or wood machining, account must be taken of large deformations and fracture (Holmberg et al., 1999; Reiterer and Stanzl-Tschegg, 2001).

In this work, anisotropic linear elastic behaviour is assumed. A brief summary of linear orthotropic elasticity is presented in the following subsection.

## 1.2.2 Anisotropic linear elastic constitutive behaviour

### 1.2.2.1 Constitutive equations for an orthotropic material

At a given material point, the linear elastic constitutive law is defined by a linear relationship between the stress ( $\sigma$ ) and strain ( $\varepsilon$ ) tensors:

$$\sigma_{ij} = C_{ijkl}\varepsilon_{kl} \quad (i, j, k, l = 1, 2, 3) \quad (1.1)$$

where  $C_{ijkl}$  is the fourth order stiffness tensor whose components are the elastic parameters of the material. Using Voigt notation and assuming orthotropy, Eq. (1.1) can be written in the axes of orthotropy ( $O, \mathbf{e}_1, \mathbf{e}_2, \mathbf{e}_3$ ) as:

$$\begin{Bmatrix} \sigma_1 \\ \sigma_2 \\ \sigma_3 \\ \sigma_4 \\ \sigma_5 \\ \sigma_6 \end{Bmatrix} = \begin{bmatrix} C_{11} & C_{12} & C_{13} & 0 & 0 & 0 \\ C_{21} & C_{22} & C_{23} & 0 & 0 & 0 \\ C_{31} & C_{32} & C_{33} & 0 & 0 & 0 \\ 0 & 0 & 0 & C_{44} & 0 & 0 \\ 0 & 0 & 0 & 0 & C_{55} & 0 \\ 0 & 0 & 0 & 0 & 0 & C_{66} \end{bmatrix} \begin{Bmatrix} \varepsilon_1 \\ \varepsilon_2 \\ \varepsilon_3 \\ \varepsilon_4 \\ \varepsilon_5 \\ \varepsilon_6 \end{Bmatrix} \quad (1.2a)$$

or in compact matrix notation

$$\{\sigma\} = [C]\{\varepsilon\} \quad (1.2b)$$

where  $\{\sigma\}$  and  $\{\varepsilon\}$  are, respectively, the stress and strain pseudo-vectors and  $[C]$  the stiffness matrix, which is symmetric and positive definite. The complete identification of the nine independent stiffness components of matrix  $[C]$  requires classically several independent tests: three uniaxial tensile/compression tests along the material principal directions and three shear tests along the planes of symmetry.

### 1.2.2.2 Plane stress assumption

An important issue in the experimental characterisation of materials is the plane stress assumption. This approach is verified when the shape of the test specimen is reduced to a plane. In this case, only the in-plane stress components are significant and they are assumed to be constant across the thickness. Accordingly and considering the 1–2 plane of symmetry, Eq. (1.2) can be reduced to ( $\sigma_3 = \sigma_4 = \sigma_5 = 0$ ):

$$\begin{Bmatrix} \sigma_1 \\ \sigma_2 \\ \sigma_6 \end{Bmatrix} = \begin{bmatrix} Q_{11} & Q_{12} & 0 \\ Q_{12} & Q_{22} & 0 \\ 0 & 0 & Q_{66} \end{bmatrix} \begin{Bmatrix} \varepsilon_1 \\ \varepsilon_2 \\ \varepsilon_6 \end{Bmatrix} \quad (1.3a)$$

or

$$\{\sigma\} = [Q]\{\varepsilon\} \quad (1.3b)$$

where  $[Q]$  is the reduced stiffness matrix, which can be determined directly from  $[C]$  (Eq. 1.2) according to:

$$Q_{ij} = C_{ij} - \frac{C_{i3}C_{j3}}{C_{33}} \quad (i, j = 1, 2, 6). \quad (1.3c)$$

The constitutive equations given in (Eq. 1.3a) can be written for an arbitrary orientation between the specimen ( $x-y$ ) and material (1–2) coordinate systems using classical formulas of matrix transformation (Jones, 1999, §2.6).

### 1.2.2.3 Engineering constants

The stiffness matrix in the constitutive equations (1.3) is determined experimentally from appropriate mechanical test methods. Historically, in the interpretation of these tests engineering constants have been introduced, linked directly to the load and strain measurements. The stiffness and engineering constants can be related by the following equalities (Jones, 1999, p. 72):

$$\left\{ \begin{array}{l} Q_{11} = E_1/(1 - \nu_{12}\nu_{21}) \\ Q_{22} = E_2(1 - \nu_{12}\nu_{21}) \\ Q_{12} = -\nu_{21}E_1/(1 - \nu_{12}\nu_{21}) \\ Q_{21} = -\nu_{12}E_2/(1 - \nu_{12}\nu_{21}) \\ Q_{66} = G_{12} \end{array} \right. \quad \text{or} \quad \left\{ \begin{array}{l} E_1 = Q_{11} - Q_{12}^2/Q_{22} \\ E_2 = Q_{22} - Q_{12}^2/Q_{11} \\ \nu_{12} = Q_{12}/Q_{22} \\ G_{12} = Q_{66} \end{array} \right. \quad (1.4)$$

along with  $\nu_{12}/E_1 = \nu_{21}/E_2$ . In Eqs. (1.4),  $E_i = \sigma_i/\varepsilon_i$  is the elastic modulus along the  $i$  direction,  $\nu_{ij} = -\varepsilon_j/\varepsilon_i$  is the Poisson's ratio in the  $j$  direction when an uniaxial stress is applied in the  $i$  direction and  $G_{ij} = \sigma_{ij}/\varepsilon_{ij}$  is the shear modulus identified when a shear stress is applied in the  $ij$  plane of symmetry.

The engineering constants of wood along its principal directions of symmetry can be significantly different (Guitard, 1987, pp. 116-118):

$$\left\{ \begin{array}{l} E_L \gg E_R > E_T \\ \nu_{RT} > \nu_{LT} > \nu_{LR} \simeq \nu_{TR} \gg \nu_{RL} > \nu_{TL} \\ G_{LR} > G_{LT} \gg G_{RT} \end{array} \right.$$

Furthermore, reference anisotropy ratios of softwood species are of the order of (Guitard, 1987, pp. 116-118):  $E_L/E_R = 13$ ;  $E_L/E_T = 21$ ;  $E_R/E_T = 1.6$ ;  $G_{LR}/G_{RT} = 10.3$ ;  $G_{LT}/G_{RT} = 8.9$  (these ratios correspond to wood with density of about  $\rho = 450 \text{ kg/m}^3$ ).

The anisotropy of wood can be explained by its morphology. The longitudinal elastic modulus ( $E_L$ ) is larger than the transverse ones ( $E_R$  and  $E_T$ ) owing to: (1) the elongated shape of the majority (about 90-95%) of the wood cells (tracheids) along the stem; (2) the reinforcement by the cellulose microfibrils within the wood cell walls, which are nearly aligned with the long cell axis in the S2 thicker layer (§ 1.1.5). Furthermore, the slightly anisotropy of wood in the radial-tangential plane ( $E_R > E_T$ ) may be explained by the reinforcement added by the wood ray cells oriented radially across the stem (Ljungdahl et al., 2006), as well as by the difference in the structural arrangement of the cells in the radial and tangential directions (Persson, 2000, p. 107).

### 1.2.3 Conclusions

Several constitutive equations are proposed in the literature for modelling clear wood. Generally, these models have a particular domain of validity and are restricted to the description of specific aspects of the complex behaviour of wood. Linear elastic orthotropic behaviour is considered in this work. Neglecting hygro-thermal effects, this model assumes relatively low levels of stresses, applied over a short period of time and at room temperature.

## 1.3 Characterisation of elastic properties of clear wood using quasi-static mechanical tests

### 1.3.1 Introduction

The complete characterisation of the linear elastic orthotropic behaviour of clear wood requires the determination of nine independent parameters. In identifying these material parameters, the conventional experimental approach consists in carrying out several mechanical tests, in which both loading and specimen geometry are most often oriented along the material directions. Moreover, these tests are based on the assumption that the boundary conditions generate a simple and homogeneous stress/strain state across the elementary representative volume of the material at the scale of observation.

The tests usually employed for the characterisation of the mechanical properties of wood can be separated into two main groups: (1) at the macroscopic scale, the methods using clear wood specimens containing radially a few annual growth rings ([ASTM D143, 1994](#)); (2) at the structural scale, the procedures employing timber with structural size that may contain features such as knots and gross grain deviation ([ASTM D198, 1994](#); [EN 408, 2002](#)).

The choice of the specimen size and consequently the mechanical test will be determined by the type of information needed ([ASTM D143, 1994](#); [Dinwoodie, 2000](#)). On the one hand, in determining design stresses it may be desirable to directly test structural elements for which actual service conditions can be reproduced. On the other hand, for the comparison of wood properties, among different trees and species, tests on clear wood specimens may be preferable. Besides, when testing small clear wood specimens, safety coefficients can be specified in order to take into account structural factors (*e.g.*, knots and distortion grain) in the derivation of service stresses for timber ([Dinwoodie, 2000](#); [STEP, 1996, 1997](#); [Williamson, 2002](#)).

In this section, the quasi-static mechanical tests (tension, compression, shear and bending) usually carried out for the determination of the elastic properties of clear wood at the macroscopic scale are reviewed.

### 1.3.2 Tensile tests

#### 1.3.2.1 Parallel to grain

The tensile test parallel to grain is schematically shown in [Figure 1.3](#) using two different specimen geometries. It is worth mentioning that other configurations can be found in the literature (*e.g.*, [Kollman and Côté Jr., 1984](#), [Figure 7.40, p.324](#)). The specimens are prismatic bars oriented along the grain, mostly with a gauge region having a reduced cross-section area ([Figure 1.3\(a\)](#)), in order to allow the stress to be larger in this region.

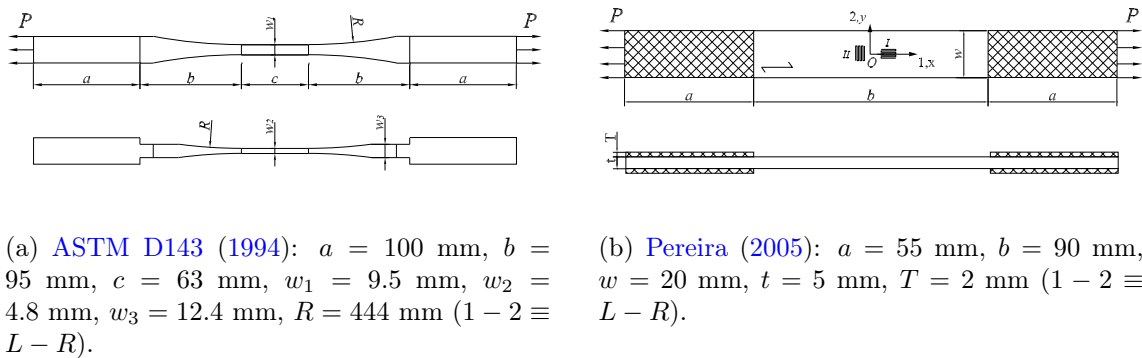


Figure 1.3: Schematic representation of tensile tests using two specimen configurations.

The width of the specimens is oriented in the radial direction and its dimension is chosen in order to embrace several annual growth rings ( $1 - 2 \equiv L - R$ ) (Figure 1.3). The gripping region of the specimen can be reinforced by end tabs made of denser wood to protect the specimen from the pressure induced by the grips of the testing machine (Figure 1.3(b)).

In a tensile test, the experimental measurements are the applied force ( $P$ ), measured by the load cell of the testing machine, and the longitudinal and transverse strains (respectively,  $\varepsilon_1$  and  $\varepsilon_2$ ), measured by strain gauges. Strains are measured in the region of interest where both the strains and stresses are assumed to be homogeneous (Figure 1.3). From the constitutive equations, these measurements are directly linked, respectively, to the longitudinal elastic modulus and to Poisson's ratio by the following equations:

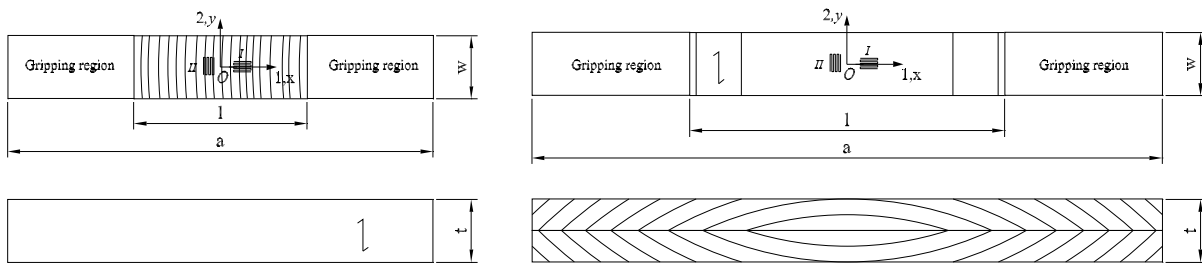
$$E_1 = \frac{P/A}{\varepsilon_1} \quad \text{and} \quad \nu_{12} = -\frac{\varepsilon_2}{\varepsilon_1}. \quad (1.5)$$

where  $A$  is the initial area of the cross-section perpendicular to the applied load.

Typical stress-strain curves obtained in tensile tests carried out parallel to the grain on clear wood specimens are practically linear up to failure (see [STEP, 1996](#), Figure 2, p.IV-2-2). This is characteristic of a linear elastic brittle behaviour.

### 1.3.2.2 Perpendicular to grain

The stiffness properties of wood perpendicular to grain ( $E_R$  and  $E_T$ ) are significantly lower than the ones parallel to grain. Although tensile tests perpendicular to grain are proposed by standards (*e.g.*, [ASTM D143, 1994](#)), these methods only consider the characterisation of strength. Alternatively, other methods have been suggested in the literature, most often taking into account the orthotropic character of wood ([Aicher et al., 2001](#); [Pereira, 2005](#)). An example, proposed by [Pereira \(2005\)](#), of radial and tangential specimens loaded in tension perpendicular to grain is shown in Figure 1.4(a) and (b) respectively. The tangential specimen is obtained by bonding two parts in order to obtain a



(a) (Pereira, 2005):  $a = 135$  mm,  $l = 55$  mm,  $w = t = 20$  mm ( $1 - 2 \equiv R - T$ ).  
 (b) (Pereira, 2005):  $a = 200$  mm,  $l = 100$  mm,  $w = t = 20$  mm ( $1 - 2 \equiv T - L$ ).

Figure 1.4: Specimens for tensile tests carried out perpendicularly to the grain along the (a) radial and (b) tangential directions.

double symmetry specimen (Figure 1.4(b)). The engineering constants provided by these tests can be determined from Eqs. (1.5), where  $1 - 2 \equiv R - T$  and  $1 - 2 \equiv T - L$ , respectively, for the tensile tests carried out perpendicularly to the grain along the radial and tangential directions.

Several authors have pointed out that, in spite of the simple uniaxial loading, a heterogeneous stress/strain field can occur if the curvature of the annual growth rings (annual rings pattern) is not negligible across the region of interest of the specimen (Aicher et al., 2001; Pedersen et al., 2003). The degree of inhomogeneity increases when the anisotropy ratio  $E_R/E_T$  increases. Moreover, it is also dependent on the shear modulus of the material; a lower value of the shear modulus will enhance the effect of the  $E_R/E_T$  ratio (Aicher et al., 2001; Pedersen et al., 2003). Pereira (2005) has proposed a numerical factor for correcting the properties determined directly from Eqs. (1.5), in order to take into account both stress and strain inhomogeneous distributions.

### 1.3.3 Compression tests

#### 1.3.3.1 Parallel to grain

The standard ASTM D143 (1994) recommends a prismatic specimen with dimensions of  $R(50) \times T(50) \times L(200)$  mm<sup>3</sup> (primary method) for compression tests carried out parallel to the grain (Figure 1.5). The height to width ratio is chosen in order to avoid premature buckling of the sample.

The behaviour of wood in compression parallel to grain has been thoroughly studied by several authors (Gibson and Ashby, 1997; Poulsen et al., 1997; Reiterer and Stanzl-Tschegg, 2001). Usually, the stress-strain response is non-linear. The elastic limit is an intrinsic material parameter. Failure occurs gradually by a local buckling process which initiates in the cell walls. Therefore, for this type of loading, wood behaves as a ductile

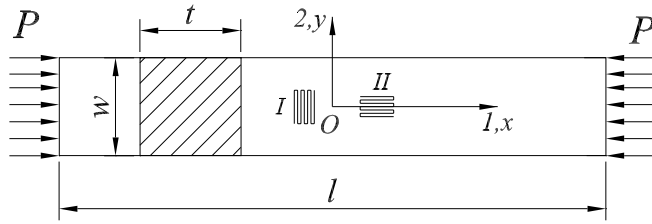


Figure 1.5: Schematic representation of specimens for compression testing. Parallel to grain longitudinal compression (ASTM D143, 1994):  $l = 200$  mm,  $w = t = 50$  mm ( $1 - 2 \equiv L - R$ ).

material.

Similarly to the tensile tests, the elastic properties of wood in compression tests carried out parallel to the grain (elastic modulus and Poisson's ratio) can be determined from the load and strain measurements using Eqs. (1.5). It is assumed that the strain and stress are uniform and the stress is uniaxial in the gauge area of the specimen. The longitudinal elastic modulus in tension ( $t$ ) or compression ( $c$ ), namely for softwoods, are generally assumed to be equivalent:  $E_L^t = E_L^c$  (Connors and Medvecz, 1992).

### 1.3.3.2 Perpendicular to grain

The behaviour of wood in compression perpendicular to grain has been studied by several authors (Gibson and Ashby, 1997; Nairn, 2007; Shipsha and Berglund, 2007). Different specimen dimensions and loading cases, leading to different stress distributions and stress-strain responses have been employed (see STEP, 1996, Figure 4, p. IV-2-4). Similarly to the case of tensile tests carried out perpendicularly to the grain, the elastic properties of wood in transverse compression can be influenced by both shear coupling effects and by the cylindrical symmetry of the annual rings pattern.

## 1.3.4 Shear tests

Because of the anisotropic structure of wood, three independent shear tests must be carried out for the evaluation of the shear modulus. Therefore, special attention has been paid to the investigation of appropriate shear test methods for clear wood whose review is presented in the following.

### 1.3.4.1 Torsional test

The shear moduli of a wooden rectangular prismatic bar can be evaluated from the torsional stiffness, when the bar is submitted to a torque around its longitudinal ( $L \equiv 1$ ) orthotropic axis. In practice, a simplified torsional stiffness formula can be used outlined by (Janowiak and Pellerin, 1992):

$$\left(\frac{3}{tw^3}\right) K_1 = G_{12} - 0.63025G_{12}\sqrt{\frac{G_{12}}{G_{13}}}\left(\frac{w}{t}\right) \quad (1.6)$$

where  $(3/tw^3)K_1$  is the reduced torsional stiffness term,  $t$  is the specimen thickness,  $w$  is the specimen width, and  $G_{12}$  and  $G_{13}$  are, respectively, the in-plane and transverse shear moduli. Eq. (1.6) is valid for width-to-thickness ratios satisfying the condition of:  $t/w < (\pi/4)(\sqrt{G_{12}/G_{23}})$ .

The test procedure requires the evaluation of  $K_1$  for several  $w/t$  values. For each measurement, the torsional stiffness is determined as:  $K_1 = TL/\Theta$ , where  $T$  is the applied torque,  $L$  the torsional gauge length and  $\Theta$  the measured twist angle. A least-squares linear regression is then applied to the data, plotted in the form of  $(3/tw^3)K_1$  against the  $w/t$  ratios (Eq. 1.6). The modulus  $G_{12}$  is defined as the intersection of the fitting line with the ordinate axis ( $w/t = 0$ ). The transverse shear modulus is deduced according to:  $G_{13} = (0.3972G_{12}^3)/k_s^2$ , where  $k_s$  is the slope of the fitting line. Accuracy in the identification of  $G_{13}$  is significantly affected by the evaluation of  $G_{12}$  as the former is a cubic function of the latter. In practice, care must be taken regarding the measurement of the twisting angle, because of restrictions usually imposed by the torsional loading grips (Janowiak and Pellerin, 1992).

#### 1.3.4.2 Off-axis tensile test

The off-axis tensile test is a method proposed for the characterisation of the shear behaviour of anisotropic materials. Major developments were achieved in the field of fibrous composite materials (Chamis and Sinclair, 1977; Kawai et al., 1997; Pierron and Vautrin, 1996; Pierron et al., 1998; Pindera and Herakovick, 1986; Sun and Berreth, 1998; Sun and Chung, 1993). The application of this test to clear wood was also investigated by several authors (Ebrahimi and Sliker, 1981; Liu, 2002; Sliker and Yu, 1993; Xavier et al., 2004; Zhang and Sliker, 1991).

A schematic representation of the off-axis tensile test is shown in Figure 1.6(a). In this test, no special fixtures or specimen preparation is required. The specimen consists of a rectangular coupon with a high length/width ( $l/w$ ) ratio. The (1, 2) orthotropic directions of the material are rotated at an angle of  $\alpha$  with regard to the ( $x, y$ ) geometrical directions of the specimen. A uniaxial and uniform load is applied at the ends of the specimen along its horizontal direction. Thus, in the ( $x, y$ ) specimen coordinate system, the in-plane stress state in a central cross-section of the specimen is equal to (using the following contraction of indices:  $xx \rightarrow x, yy \rightarrow y, xy \rightarrow s$ ):

$$\sigma_x = \frac{P}{A}, \quad \sigma_y = \sigma_s = 0 \quad (1.7)$$

where  $P$  is the applied load measured by the load cell of the testing machine and  $A$  the

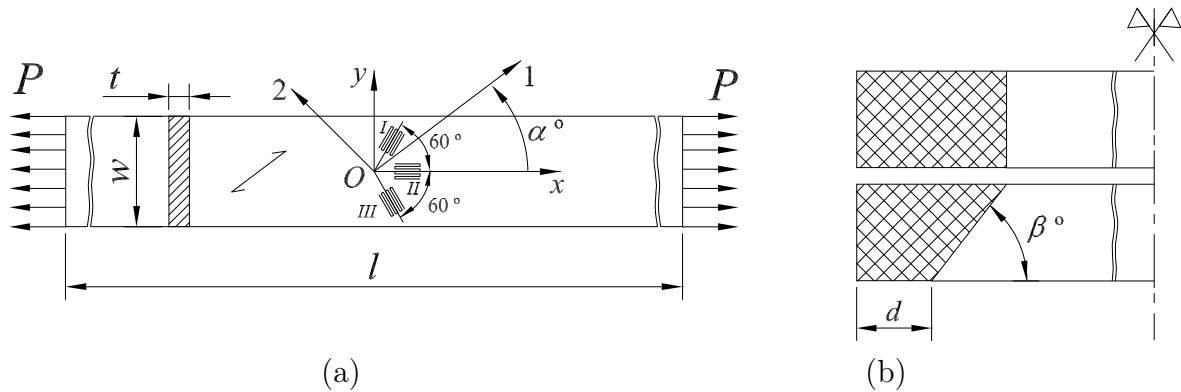


Figure 1.6: Off-axis tensile test: (a) schematic representation ( $l = 200$  mm,  $w = 20$  mm,  $t = 5$  mm,  $\alpha = 15^\circ$ ); (b) rectangular and oblique end tabs.

cross-section area of the specimen ( $A = w \times t$ , using notations of Figure 1.6(a)). Using both Eq. (1.7) and classical formulae of matrix transformation, the stress components in the (1, 2) material coordinate system can be written as:

$$\sigma_1 = \frac{P}{A} \cos^2 \alpha, \quad \sigma_2 = \frac{P}{A} \sin^2 \alpha, \quad \sigma_6 = \frac{P}{A} \cos \alpha \sin \alpha. \quad (1.8)$$

Eq. (1.8) shows that the application of a uniaxial state of stress to the off-axis specimen results in a biaxial state of stress in the material axes, that is dependent on the off-axis angle  $\alpha$ .

In order to enhance the shear behaviour (minimising the effect of longitudinal and transverse tensile stress components), the angle  $\alpha$  must be calibrated. This preliminary study consists in finding the most appropriate angle for generating predominant shear in the material coordinate system. This analysis can be achieved with regard to either the stiffness or strength properties of the material. On the one hand, the off-axis angle can be evaluated as the one corresponding to the maximum  $\varepsilon_6(\alpha)/\varepsilon_x$  ratio, where  $\varepsilon_6$  is the shear strain in the material axes and  $\varepsilon_x$  the strain along the load direction (Chamis and Sinclair, 1977); this ratio depends on the material properties. On the other hand, the stress components (Eq. 1.8) can be normalised with respect to the material strength parameters and their variation evaluated from the off-axis angle:  $\sigma_1(\alpha)/X^+$ ,  $\sigma_2(\alpha)/Y^+$  and  $\sigma_6(\alpha)/S$ , where  $X^+$  and  $Y^+$  are the longitudinal and transverse tensile strengths, respectively, and  $S$  is the shear strength (Alloba, 1997). Although the value of the shear modulus or shear strength of the material is required to determine the off-axis angle, it can be shown that its initial estimate does not have a significant effect on the angle evaluation.

The shear strain component can be measured by a rosette bonded at the centre of the specimen. Among different possible configurations (Dally and William, 1991, Chapter 9), a three-element (60-deg) rosette can be used (Figure 1.6(a)). In this case, the gauge

strains ( $\varepsilon_I$ ,  $\varepsilon_{II}$ ,  $\varepsilon_{III}$ ) and the engineering shear strain in the material coordinate system ( $\varepsilon_6$ ) are linked by the following equation:

$$\varepsilon_6 = (\varepsilon_I - 2\varepsilon_{II} + \varepsilon_{III}) \sin \alpha + (\varepsilon_I - \varepsilon_{III}) \cos \alpha \quad (1.9)$$

Finally, the shear modulus in the material axes is determined as:

$$G_{12} = \frac{\sigma_6}{\varepsilon_6}. \quad (1.10)$$

Experimentally, the application of a uniaxial stress as shown in Figure 1.6(a) is not possible. Instead, the specimen is clamped to the testing machine. The clamping forces at the ends of the specimen prohibits localised rotation (end effects). This constraint can generate a nonuniform strain field at the centre of the specimen. The gripping regions of the specimen are usually reinforced by either rectangular or oblique end tabs (Figure 1.6(b)). When rectangular end tabs are used, these end effects are at the origin of a *S*-shape deformation of the off-axis specimen, rather than its theoretical parallelogram deformation (Pierron and Vautrin, 1996; Pindera and Herakovick, 1986). Moreover, these effects are enhanced for specimens with a low length/width ratio or having a high anisotropy ratio. This type of response can affect the measurements and consequently the determination of both stiffness and strength properties. The use of correcting factors for evaluating the shear modulus were proposed to overcome this problem (Pindera and Herakovick, 1986). Furthermore, an alternative method consists in using oblique end tabs (Figure 1.6(b)). In this case, it has been proved that a uniform state of stress can be obtained across a larger region of the specimen (Kawai et al., 1997; Pierron and Vautrin, 1996; Pierron et al., 1998; Sun and Berreth, 1998; Sun and Chung, 1993). Accordingly, the correct identification of the shear modulus can be reached directly from Eq. (1.10). The angle of the end tabs  $\beta$  corresponds to the theoretical lines of iso-displacement and can be deduced by the following equation:

$$\cot \beta = -\frac{\overline{S}_{16}}{\overline{S}_{11}} \quad (1.11)$$

where the  $\overline{S}_{ij}$  are components of the reduced compliance tensor  $[\overline{S}]$  written in the specimen coordinate system (Jones, 1999, p. 78).

It follows that the shear modulus of an anisotropic material can be directly identified by the off-axis tensile test, providing that a convenient choice of the whole set of  $l$ ,  $w$ ,  $\alpha$  and  $\beta$  geometric parameters is made.

### 1.3.4.3 Iosipescu shear test

The Iosipescu shear test is a standard method for the characterisation of the shear behaviour of fibrous composite materials (ASTM D5379, 1993). Several studies have been

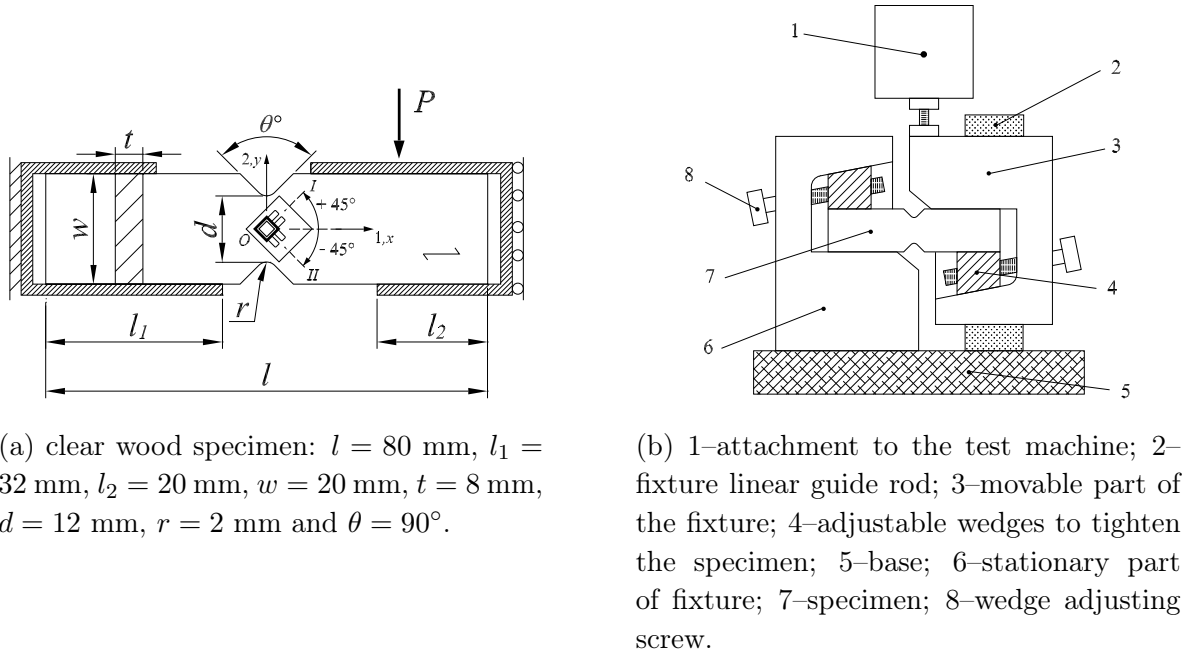


Figure 1.7: Schematic representations of: (a) the Iosipescu shear test; (b) the Iosipescu fixture.

undertaken regarding this test method (Adams and Walrath, 1987; Ho et al., 1993; Ifju, 1994; Morton et al., 1992; Pierron, 1998; Pierron and Vautrin, 1994; Pindera et al., 1987, 1990; Walrath and Adams, 1983). The application of the Iosipescu test to clear wood, for different species and material planes, was also investigated by several authors (De Magistris and Salmén, 2005; Dumail and Salmén, 2001; Dumail et al., 2000; Liu, 2000; Xavier et al., 2004; Yoshihara et al., 1999).

A schematic representation of the Iosipescu test method is shown in Figure 1.7(a). The Iosipescu specimen consists of a straight coupon of small dimensions with two symmetric V-notches at its centre. A specific fixture is used to transfer the vertical cross-head movement of the testing machine into a predominant shear loading at the smallest cross-section of the specimen (Figure 1.7(b)). The V-notches configuration allows a quasi-uniform distribution of the shear stress between the notches. Assuming that the stress distribution is perfectly uniform between the notches and across the thickness of the specimen, the (theoretical) shear stress ( $\sigma_6$ ) is measured by:

$$\sigma_6 = \frac{P}{A} \quad (1.12)$$

where  $P$  represents the resultant of the vertical load measured by the load cell of the testing machine, and  $A$  is the area of the smallest cross-section between the notches ( $A = d \times t$ , in Figure 1.7(a)).

The engineering shear strain ( $\varepsilon_6$ ) is usually measured by a two-element rectangular rosette, bonded at the centre of the specimen at  $\pm 45^\circ$  with respect to the specimen

longitudinal axis (Figure 1.7(a)), according to the following equation:

$$\varepsilon_6 = \varepsilon_I^{+45^\circ} - \varepsilon_{II}^{-45^\circ} \quad (1.13)$$

where  $\varepsilon_{I,II}^{\pm 45^\circ}$  represent the gauge strains. According to the anisotropic linear elastic constitutive equations, the shear modulus, in the material coordinate system, can be determined from the experimental measurements as:

$$G_{12}^a = \frac{\sigma_6}{\varepsilon_6}. \quad (1.14)$$

Different studies (Ho et al., 1993; Morton et al., 1992; Pierron, 1998; Pindera et al., 1987) have shown that neither the stress distribution between V-notches nor the strain distribution over the area covered by the rosette, are uniform. Besides, the measurement of the shear strain is sensitive to the size of the strain gauge. Therefore the shear modulus identified directly from Eq. (1.14) can be under- or over- estimated, depending on the orientation of the orthotropy axes with regard to the specimen directions ( $0^\circ$  or  $90^\circ$  configuration). To overcome this drawback numerical correction factors have been proposed for the correct determination of the shear modulus (Pierron, 1998):

$$G_{12}^c = \frac{\sigma_6^O}{P/A} \frac{\varepsilon_6^{sg}}{\varepsilon_6^O} G_{12}^a = CS G_{12}^a, \quad (1.15)$$

where  $G_{12}^c$  is the corrected shear modulus,  $\sigma_6^O$  the shear stress value at the centre of the specimen,  $P/A$  the average shear stress between the V-notches,  $\varepsilon_6^{sg}$  the shear strain measured by the rosette,  $\varepsilon_6^O$  the shear strain at the centre of the specimen,  $C$  the shear stress correction factor and  $S$  the shear strain correction factor. The  $C$  factor quantifies the degree of heterogeneity of the shear stress distribution between the V-notches, whereas the  $S$  factor takes into account the heterogeneity of the shear strain distribution over the gauge area. These factors are determined by finite element analyses. The testing conditions remaining unchanged, the  $CS$  correction factor (Eq. 1.15) is mostly affected by the elastic material properties. For specimens of *P. pinaster* wood oriented in the  $LR$ ,  $LT$  and  $RT$  planes of symmetry, the  $CS$  correction factor was determined respectively equal to 0.96 ( $-4\%$ ), 0.91 ( $-9\%$ ) and 1.02 ( $2\%$ ) (Xavier et al., 2003, 2004). Thus, it can be concluded that the error in the shear modulus evaluation by using Eq. (1.14), is smaller or of the same order of magnitude of the scatter usually found experimentally in the characterisation of wood mechanical properties due to its inherent structural variability.

The data reduction method presented above assumes that both stress and strain distributions are constant through the thickness of the specimen. However, some authors (Ifju, 1994; Morton et al., 1992; Pierron, 1998) have pointed out that strain measurements on both front and back surfaces of the specimen can be significantly different, thus leading to an additional scatter in the identification of the shear modulus. A consistent

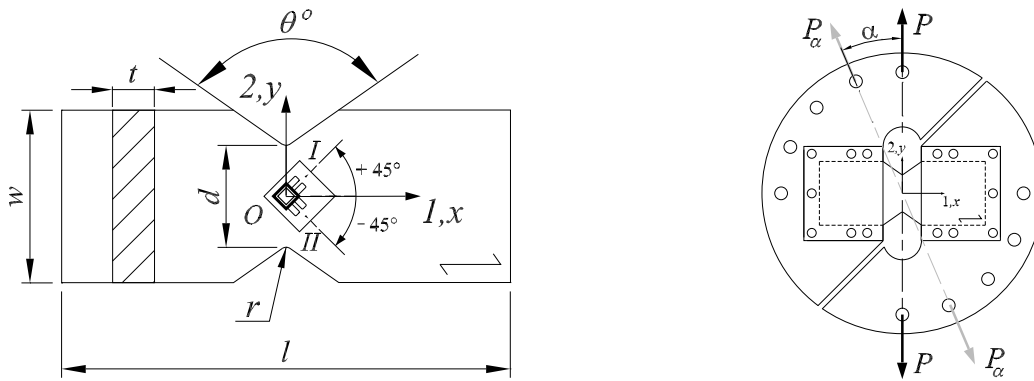


Figure 1.8: Schematic representations of: (a) the Arcan shear test (for clear wood specimen:  $l = 70$  mm,  $w = 50$  mm,  $t = 8$  mm,  $d = 30$  mm,  $r = 2$  mm and  $\theta = 110^\circ$ ); (b) the Arcan fixture.

explanation of these observations was proposed by Pierron (1998) based on Saint-Venant effects, in which the strain variation through the thickness is a consequence of the uneven load distribution over the loading surfaces of the specimen due to geometric imperfections. This effect is more critical when testing thick specimens or when the fibres direction is oriented parallel to the loading direction ( $90^\circ$  specimen). Nevertheless, it has been shown (Pierron, 1998) that this effect can be minimised by measuring the shear strain on both faces of the specimen and take their average for the determination of the shear modulus of the material.

#### 1.3.4.4 Arcan test

The Arcan test was first proposed for the shear characterisation of plastic materials (Goldenberg et al., 1958). Several developments were achieved afterwards in the field of fiber-reinforced composite materials (Arcan et al., 1976; El-Hajjar and Haj-Ali, 2004; Hung and Liechi, 1997; Mohr and Doyoyo, 2003; Voloshin and Arcan, 1980) as well as for clear wood species (Liu and Ross, 2005; Oliveira, 2004; Rammer and Hernandez, 1988).

The Arcan shear test is shown in Figure 1.8. Conceptually, this test is rather close to the Iosipescu shear test. The configuration of the Arcan wooden specimen employed by Oliveira (2004) is shown in Figure 1.8(a). A specific fixture, consisting of two separated supports mounted in a *butterfly* shape (Figure 1.8(b)), is used to impose a predominant shear stress across the central part of the specimen. Several studies have emphasised the gripping system (El-Hajjar and Haj-Ali, 2004; Hung and Liechi, 1997; Mohr and Doyoyo, 2003; Oliveira, 2004), since it has important effects on the specimen mechanical response. Both the applied load and the gauge strains at the central region of the specimen are measured (Figure 1.8). Subsequently, the average shear stress and the average shear strain are determined from these measurements. Finally, the shear modulus in the material coordinate system is simply determined through Eq. (1.15).

### 1.3.4.5 Other shear tests

Other shear tests have been applied in the literature on clear wood specimens, as for instance: (1) the in-plane shear test using a thin specimen (Yoshihara and Matsumoto, 2005) (Figure 1.9(a)); (2) the quasi-simple shear test (Naruse, 2003) (Figure 1.9(b)); (3) the square-plate twisting test (Janowiak and Pellerin, 1992; Yoshihara and Sawamura, 2006) (Figure 1.9(c)).

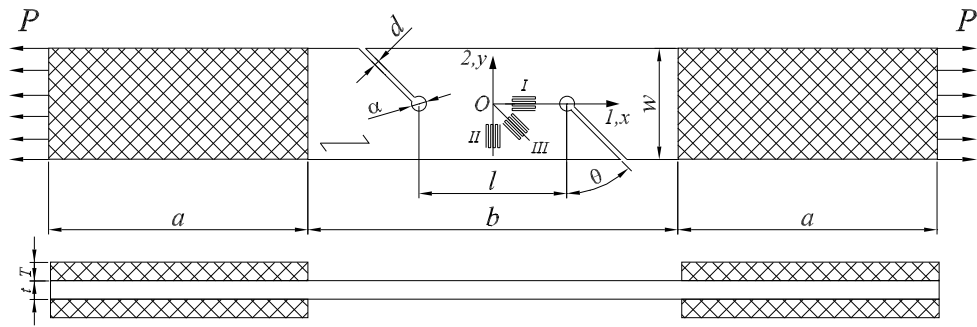
The test in Figure 1.9(a) employs a specimen with two slots cut asymmetrically on both sides of the specimen, between which a shear stress is generated by the application of a tensile load. In the data reduction, the shear stress is determined by  $\sigma_6 = P/tl$  and the shear strain is measured from a three-element rosette according to  $\varepsilon_6 = 2\varepsilon_{III} - \varepsilon_I - \varepsilon_{II}$ . The shear modulus is determined afterwards from the shear stress-strain ( $\sigma_6 - \varepsilon_6$ ) curve.

Naruse (2003) proposed the shear test presented in Figure 1.9(b), where two predominant shear zones ( $l \times c$ ) are assumed to exist, providing that the distance  $c$  is sufficiently small. A special fixture is used for loading the specimen in a universal testing machine (Naruse, 2003). The stress and strain values during the test are measured, respectively, by the load cell of the testing machine and strain gauges. An apparent shear modulus is determined from the initial linear part of the shear stress-strain curve. Numerical correction factors, estimated by finite element analyses, are proposed for evaluating the correct shear modulus. They take into account the uneven stress distribution in the region of measurement. The author has determined a factor of 1.45 (for  $c = 10$  mm in Figure 1.9.b) for a specimen of Bruna (*Fagus crenata* Blume) cut in the  $LR$  plane.

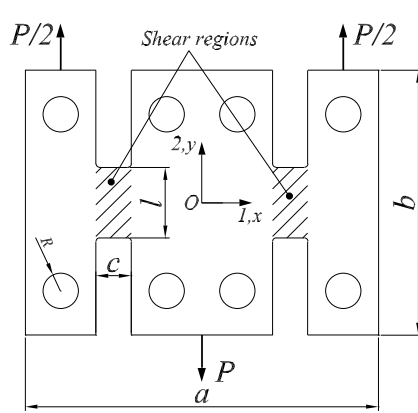
The square-plate twisting test was originally proposed by the ASTM D3044 (1994) for determining the shear modulus of plywood (a wood-based product). When applied to clear wood, this test has, however, some drawbacks owing to its inherent high longitudinal/transverse anisotropy (Mamada et al., 1959). Recently, Yoshihara and Sawamura (2006) have proposed some improvements to this test for clear wood specimens. Among other variants, tests were performed under the modified NPL square-plate twisting configuration (ISO 15310, 1999) (Figure 1.9(c)). The specimen consists of a plate (oriented in the  $LR$  plane) simply supported on two opposite corners of a diagonal, and submitted to transverse loads applied at the opposite ends. In this case, the shear modulus ( $G_{12}$ ) can be determined from the measurements of both the applied load and the deflection of its point of application, and from the dimensions of the plate (length, width and thickness). A correction factor is used for taking into account the shifted position of the loading points (Eq. 1 in Yoshihara and Sawamura, 2006).

### 1.3.5 Bending tests

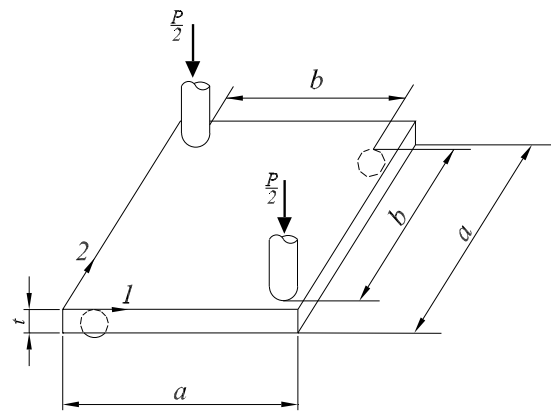
Bending tests are widely used for the identification of both the longitudinal elastic modulus and the tensile strength of wood parallel to grain (ASTM D198, 1994; EN 408,



(a)  $a = 75$  mm,  $b = 90$  mm,  $w = 30$  mm,  $t = T = 5$  mm,  $l = 30$  mm,  $d = 1$  mm,  $\alpha = 4$  mm and  $\tan \theta = \{-1.5, -1, -0.5, 0, 0.5, 1, 1.5\}$  ( $1 - 2 \equiv L - T$ ).



(b)  $a = 100$  mm,  $b = 75$  mm,  $c = \{10, 15\}$  mm,  $l = 20$  mm,  $R = 5$  mm,  $t = 5$  mm ( $1 - 2 \equiv R - L$ ).



(c)  $a = \{140, 240\}$  mm,  $b/a = \{0.7, 0.75, 0.8, 0.85, 0.9, 0.95\}$  mm,  $t = \{3, 4, 5, 10\}$  mm ( $1 - 2 \equiv L - R$ ).

Figure 1.9: Schematic representations of the shear tests: (a) the in-plane shear test (Yoshihara and Matsumoto, 2005); (b) the quasi-simple shear test (Naruse, 2003); (c) the square-plate twist test (Yoshihara and Sawamura, 2006).

2002). This is certainly due to the simplicity of both specimen manufacturing and testing.

### 1.3.5.1 Three-point bending test

The longitudinal elastic modulus can be determined by measuring the bending stiffness of a prismatic beam subjected to a three-point bending test (Figure 1.10). The Euler-Bernoulli beam theory gives an analytical solution according to the following equation:

$$E_1^a = \frac{1}{4t} \left( \frac{L}{w} \right)^3 \frac{F}{f}, \quad (1.16)$$

where  $L$ ,  $w$  and  $t$  are, respectively, the span, the width and the thickness of the beam, and  $F/f$  represents the slope in the linear elastic domain of the load-deflection curve

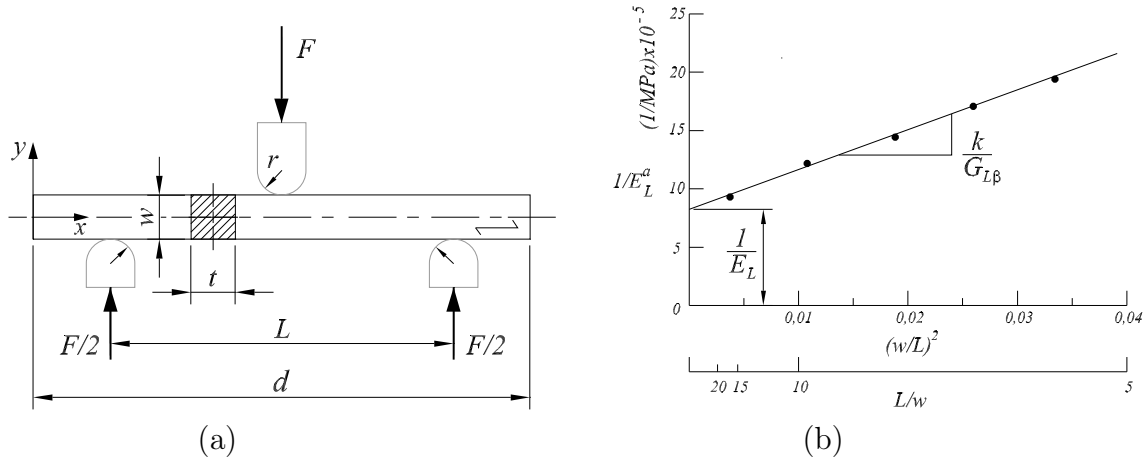


Figure 1.10: Schematic representation of: (a) the 3 point bending test (for clear wood specimen:  $d \geq 420$  mm,  $L = \{107, 129, 173, 400\}$  mm,  $w = 20$  mm,  $t = 20$  mm and  $r = 15$  mm); (b) the variable span method for the identification of the longitudinal and shear moduli ( $\beta = R, T$ ).

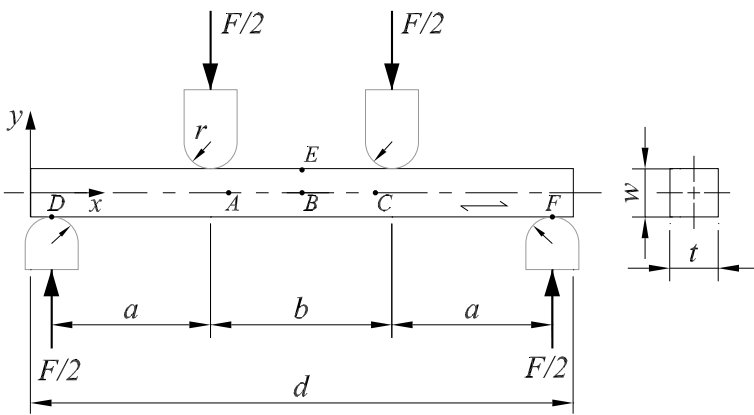


Figure 1.11: Schematic representation of the four-point bending test (EN 408 (2002):  $d = 380$  mm,  $a = 120$  mm,  $b = 120$  mm,  $w = t = 20$  mm, and  $r = 15$  mm).

measured experimentally for a given  $L/w$  ratio. The value determined from Eq. (1.16) is actually an apparent estimate of the longitudinal elastic modulus ( $E_1^a$ ). It is exact only for high  $L/w$  ratios. The deviation observed for shorter  $L/w$  ratios is caused by the generation of transverse shear strains in the region of interest that are not considered by the Euler-Bernoulli theory. To overcome this problem, the variable span method has been proposed (ASTM D198, 1994; EN 408, 2002). It is based on the Timoshenko beam theory from which the effect of transverse shear is taken into account. Thus, the variable span method allows the simultaneous identification of both the longitudinal ( $E_1$ ) and shear ( $G_{1\beta}$ ,  $\beta = 2, 3$ ) moduli according to the following equation (Figure 1.10(b)):

$$\frac{1}{E_1^a} = \frac{1}{E_1} + \frac{k}{G_{1\beta}} \left(\frac{w}{L}\right)^2, \tag{1.17}$$

where  $k$  is a constant. For a rectangular cross-section,  $k$  is equal to 1.2 or 1.5 depending on the theory used for its estimation (EN 408, 2002).

The standards (ASTM D198, 1994; EN 408, 2002) recommend the use of a beam with a square cross-section of  $w \times t = 400 \text{ mm}^2$  and a total length of  $d \geq 21 \times w = 420 \text{ mm}$  (Figure 1.10(a)). The load must be applied at a rate not higher than  $5 \times 10^{-5} L^2/6w \text{ mm/s}$  and repeated for, at least, four different span values ( $L$ ). The span values should be evenly distributed within the limits of validity of the method:  $w^2/L^2 = [0.0025, 0.035]$  (Figure 1.10(b)). For each  $w/L$  ratio, the  $E_1^a$  value is determined from the load-deflection curve according to Eq. (1.16). The  $1/E_1^a - (h/L)^2$  curve is obtained afterwards (Figure 1.10(b)). A straight line is adjusted to the experimental points by linear regression. The intersection of this line with the abscissa axis gives the inverse of  $E_1$ , whereas its slope gives the  $k/G_{1\beta}$  term (Figure 1.10(b)). Owing to the low stiffness and strength properties of wood in compression perpendicularly to grain, the standards (ASTM D198, 1994; EN 408, 2002) propose the use of steel plates between the specimen and the supports for avoiding indentation effects.

### 1.3.5.2 Four-point bending test

The longitudinal elastic modulus can be determined by measuring the bending stiffness of a prismatic beam subjected to a four-point bending test according to the following equation (Figure 1.11) (EN 408, 2002):

$$E_1^a = \frac{3}{64t} \left( \frac{L}{w} \right)^3 \frac{F}{f} \quad (1.18)$$

In comparison to the three-point bending test, this test has the advantage of having a central region of interest where the stress distribution is uniform along the longitudinal axis of the beam. However, some ambiguity exists concerning the reference points for the measurement of deflection. The standard EN 408 (2002) recommends a deflection measurement over a length equal to five times the beam depth (100 mm) centred within the specimen span (points  $A$ ,  $B$  and  $C$  in Figure 1.11). This procedure yields a local elastic modulus as opposed to a global one, determined over the entire length of the beam (*e.g.*, points  $D$ ,  $E$  and  $F$  in Figure 1.11) (Boström, 1999). Boström (1999) found, for both spruce and pine timber, that the results obtained from the two aforementioned procedures can be different. Moreover, the ratio between the local and global elastic moduli is affected by shear effects as well as by timber quality (position and size of defects).

### 1.3.6 Conclusions

The following conclusions can be drawn about the mechanical tests proposed in the literature for the characterisation of clear wood elastic properties.

- (i) A spectrum of different mechanical tests has been applied for the identification of the elastic properties of clear wood. Generically, these tests are based on simple loading

conditions (*e.g.*, tension, compression, shear or bending) and specimen geometries. A few parameters are identified from each test. Therefore, several independent tests are needed for the complete identification of all the elastic properties of wood. In this framework, however, the advantage is that an analytical (closed-form) solution ties both load and strain measurements to the unknown parameters.

- (ii) These tests are not usually applicable for the determination of wood properties in directions perpendicular to grain: (1) the off-axis tensile test may not be adapted for the measurement of the shear modulus in the  $RT$  plane because of both specimen size requirements and low anisotropy ratio of wood in this plane; (2) a beam with proper dimensions oriented in the transversal section of the stem is also not machinable for bending tests.
- (iii) The transverse dimensions of the specimens employed in the determination of the elastic properties of clear wood have to satisfy contradictory conditions. On the one hand, the volume of the region of interest must integrate the heterogeneity associated to the earlywood and latewood layers, in such a way that homogenised material parameters would be identified at the macro scale of analysis. This requirement imposes that, radially, the specimen should contain several annual rings. On the other hand, the tangential dimension of the specimen must be small enough when compared to the average radius of curvature of the annual rings intercepted by the specimen. Most often, this means that the specimen has to be cut in the outer part of the stem far away from the pith (cylindrical origin). Moreover, the properties of wood are accepted to be more stable in this region of the stem, which corresponds to mature wood. When the above requirements are fulfilled, wood is usually modelled as a rhombic orthotropic material and the strain field is assumed uniform over the material transverse directions. Otherwise, a too large curvature of the annual rings in the region of interest imposes the use of polar coordinates for modelling the local behaviour, which means that the strain field may vary with the local orientation of the radial and tangential directions.
- (v) The test methods usually employed on the evaluation of clear wood properties (*e.g.*, tension, compression and shear) are based on the concept of pure and uniform state of stress in the volume of material representing the region of interest. However, such a state is very difficult to obtain in practice. Therefore, the presence of parasitic effects inherent to many tests complicates the analysis of the data and the comparison between different tests.

Several drawbacks have been summarised concerning the mechanical test methods usually employed in wood characterisation. It should be noticed that these shortcomings are also to be found in other anisotropic materials such as fibre composites. The recent

development of optical methods, for which kinematic quantities are measured over a whole region of interest, has given rise to a new approach for material characterisation (Grédiac, 1996, 2004). In this approach several material parameters are identified from a single test, providing that they all contribute to the mechanical response of the material. This new way of testing has turned into a novel topic of research in experimental mechanics, aiming at overcoming some of the limitations of classical (homogeneous) test methods. This procedure seems particularly interesting for an anisotropic and heterogeneous material like wood. This constitutes the motivation of this work. The basis of this approach is presented later in § 2.3 of Chapter 2.

## 1.4 About the elastic properties of clear wood

### 1.4.1 Introduction

Issues regarding the variability of the elastic properties of wood are presented in this section, due to their importance when testing wooden specimens.

### 1.4.2 Relationships among elastic properties

Reported in the previous section, owing to the orthotropic nature of wood, several independent mechanical tests should be carried out for the complete identification of its elastic parameters. This characterisation has to be done for each individual species of wood. Moreover, for the identification of representative parameters of a given species of wood, several specimens, cut at random locations within the stem and from different trees growing at different locations, should be tested in order to take into account the inherent structural variability of wood from a statistical point of view. Therefore, because of the anisotropy and variability of wood, one can conclude that a significant effort in terms of testing and equipment is required for the characterisation of the elastic parameters of wood. In other words, this approach is quite expensive and time consuming. To overcome this problem an approach has been proposed since the early work of Bodig and Goodman (1973), which consists of studying relationships among mechanical properties. The idea is to define some proper independent variables and then to relate the remaining elastic parameters in function of them. Most often, the longitudinal elastic modulus is chosen because this parameter is known for most of the species of wood (Bodig and Goodman, 1973; Green et al., 1999; Sliker, 1985, 1988; Sliker and Yu, 1993). Average ratios between  $E_L$  and the elastic properties ( $E_R$ ,  $E_T$ ,  $G_{LR}$ ,  $G_{LT}$ ,  $G_{RT}$ ) of several hardwood and softwood species can be found in Green et al. (1999, Table 4-1, p.4-2).

In this work this same problem is considered, although from a different point of view. Here, the minimisation of the total number of mechanical tests required for the identifi-

cation of the elastic properties of wood is investigated. This approach is based on more complex mechanical tests for which the identification of several parameters by a single test may be feasible.

### 1.4.3 Factors affecting the elastic properties of clear wood

Several factors have been identified to affect the mechanical properties of wood (*e.g.*, [Smith et al., 2003](#), pp. 27-33). In particular, from a mechanical point of view, key factors are the moisture content and density ([Dinwoodie, 2000](#); [Gibson and Ashby, 1997](#); [Guitard, 1987](#); [Sliker and Yu, 1993](#); [Walton and Armstrong, 1986](#)). Below, the definition of these two parameters and their influence on the elastic properties of wood is presented.

#### 1.4.3.1 Moisture content

The moisture content ( $\mu$ , %) of a sample of wood is defined as the amount of water held in it, expressed as a percentage of its anhydrous or dry mass:

$$\mu = \frac{m_{\mu} - m_0}{m_0} \times 100\% \quad (1.19)$$

where,  $m_{\mu}$  represents the mass of the sample at the moisture content of  $\mu$  and  $m_0$  the dry mass. The dry mass of wood can be determined according to the oven-dry method ([ASTM D4442, 2003](#)), which consists in drying the wooden sample at a temperature of  $103^{\circ} \pm 2^{\circ}\text{C}$  until constant mass is reached.

In most species, when trees are felled, wood has a moisture content of about 60%; moreover, the percentage of water in sapwood is greater than the one in heartwood ([Williamson, 2002](#), Table 1.9, p.1.11). Owing to the cellular structure of wood, water can be held in two ways: (1) free (liquid or vapour) water in the cell cavities, and (2) chemically bound water in the cell walls. When transforming harvested wood, this water must be removed to a certain extent in order to provide wood in equilibrium with in-service or end-user moisture conditions. The removal of free-water occurs first, with no change either in dimension or in mechanical properties of wood. At the state where no free-water is present in the cell cavity and the cell wall is fully saturated with bounded water, the cell is said to be at the fiber saturation point (FSP). For practical purposes, this level of moisture content is generally considered around 25%-30%. The variation of moisture content below the FSP is accompanied by dimensional variations. During the desorption, *i.e.*, when wood loses moisture, the specimen undergoes shrinkage. Conversely, during absorption, *i.e.*, when wood gains moisture into its cell walls, the specimen swells. Macroscopically, this process is quantified by the volumetric shrinkage coefficient ( $\alpha$ ), which is defined as the percentage of reduction of the swollen dimension, associated to the loss of moisture, with regard to the dry or saturate (FSP) condition ([Guitard, 1987](#), p. 41). This shrinkage

process is directional dependent:  $\alpha_T > \alpha_R \gg \alpha_L$ . Furthermore, variations in the moisture content below the FSP also result in variations in the mechanical properties of wood. For example, the effect of moisture content on the elastic constants of Sitka spruce can be found in (Dinwoodie, 2000, p. 114). As it can be seen from this reference, a roughly linear decrease in the elastic properties is observed as the moisture content increases from dry condition to about the FSP. The only exceptions are the three Poisson's ratios, that remain constant. In practice, a linear relationship between the elastic moduli of wood and the moisture content can be assumed within a range of 8-20% (STEP, 1996, p. III-1-19). Besides, laws of variation of the elastic properties of wood at different moisture contents (within the interval of 6-20%), with regard to their values at 12%, are proposed in (Guitard, 1987, p. 127).

Wood constantly exchanges water with its surrounding environment in order to be in a state of equilibrium, called the equilibrium moisture content (EMC). This exchange depends on the relative humidity and, in a smaller degree, on the temperature of the surrounding climate. For instance, with a relative humidity of 65% and a temperature of 20°C, the EMC is about 12% for most species (Smith et al., 2003, p. 24). Other correspondences can be found in abacus (Dinwoodie, 2000, p.50).

### 1.4.3.2 Density

The density ( $\rho$ , kg/m<sup>3</sup>) of a material is defined as the mass ( $m$ , kg) per unit volume ( $V$ , m<sup>3</sup>). However, because wood is hygroscopic, both the mass and the volume of a wood sample may significantly vary due to the presence of moisture. Besides, wood density can also be affected by the presence of extractives, although their influence is lower since they normally exist in a small percentage of the dry mass of wood. Therefore, measurements of wood density must be achieved at a specified moisture content ( $\mu$ , %):

$$\rho_\mu = \frac{m_\mu}{V_\mu}. \quad (1.20)$$

Different combinations of moisture content can be used to define wood density. In practice, a common measurement is the basic (engineering) density determined as the ratio between the oven-dry weight and green volume (volume of the sample at a certain moisture content). The calculation of density according to Eq. (1.20) represents an average measurement, which assumes integration over the local earlywood and latewood densities. In the literature, the density of wood is often expressed as specific gravity, which is defined as the ratio between wood and water densities (the density of water, denoted  $\rho_w$ , is usually taken equal to 1000 kg/m<sup>3</sup> at 4 °C):

$$G_\mu = \frac{\rho_\mu}{\rho_w}. \quad (1.21)$$

The density of wood has a significant influence on its mechanical properties. In general, the greater the density the greater the stiffness and strength. The relationship between specific gravity and mechanical properties can be modelled by the following equation (*e.g.*, [Williamson, 2002](#), p. 1.9):

$$P = kG^n, \quad (1.22)$$

where  $P$  represents the mechanical property,  $G$  is the specific gravity, and  $k$  and  $n$  are constants to be determined.

The relationship between density and stiffness properties has been widely investigated ([Dinwoodie, 2000](#); [Guitard, 1987](#)). A general survey of the variation of the longitudinal elastic modulus with regard to specific gravity for several species of wood, tested in the green and dry conditions, can be found in ([Dinwoodie, 2000](#), p. 111). Moreover, analytical expressions linking the elastic engineering constants of wood with density can be found either in ([Guitard, 1987](#), p. 123) or in ([Gibson and Ashby, 1997](#), p. 418).

The density of the cell wall of wood (either for softwood or hardwood species), whose major constituents are the cellulose, hemicellulose and lignin, is roughly constant of about  $1500 \text{ kg/m}^3$  ([Gibson and Ashby, 1997](#), p. 394). This means that any variation of density in wood is mainly a consequence of the variation of proportions among solid wood, extractives and cell lumen volume (air or water). In other words, the density of a wood sample can be interpreted as a measurement of its gross porosity. Therefore, the density of wood can vary significantly between wood species because of their morphological differences. Besides, the wood density also varies within wood species, mainly in consequence of different conditions of growing (climate, nature of the ground and silviculture). Furthermore, in a single tree, density varies spatially within the stem according to the following patterns: (i) longitudinally, usually decreasing from bottom to top because of the greater percentage of juvenile wood; (ii) radially, increasing or decreasing from pith to bark depending on the species (*e.g.*, [Smith et al., 2003](#), p. 18).

#### 1.4.4 Spatial variation of elastic properties within the stem

The structure of the wood cells formed by the tree varies during its growing process over the years, namely because of cambium age and environmental conditions. This accounts for the rough distinction between juvenile and mature wood within the stem (§ 1.1.2). As a main consequence of this inherent anatomical variability, the physical and mechanical properties of wood vary spatially within the stem, both radially (horizontal variability) and longitudinally (vertical variability). Most of the studies about this topic are concerned with the anatomical and physical properties of wood ([Zobel and Buijtenen, 1989](#)). However, the spatial variability of the mechanical properties of wood within the stem has scarcely been investigated.

#### 1.4.4.1 Radial variation

Pearson and Gilmore (1980) have studied the radial spatial variation of the mechanical properties of Loblolly pine, showing an average increase from pith to bark of 42% and 82%, respectively, for 41- and 15- years old trees. Tsehaye et al. (1995) observed on Radiata pine an average increase of 90% of the elastic modulus parallel to grain from inward to outward of the stem, with a clear distinction of properties between juvenile and mature wood. Kliger et al. (1998) studied Norway spruce from fast and slow-grown stands. They have concluded that the longitudinal elastic modulus in bending was 30% higher on mature wood than in wood near the pith. Ormarsson et al. (1998) reported for Norway spruce a correlation between the distance to pith and the elastic modulus parallel to grain. The stiffness near the bark was found to be four times higher than that determined closer to the pith. Machado and Cruz (2005) have studied the radial variation of the longitudinal elastic modulus of *P. pinaster* wood by standard bending test. Specimens were cut at distances from the pith of 10%, 50% and 90% of the radius of the stem. The authors have concluded that the modulus has an average increase of 87% and 99%, respectively, between the positions 10%-50% and 10%-90%. Different authors (Machado and Cruz, 2005; Ormarsson et al., 1998) have reported that orientation (North/South) of the specimen within the stem has no significant influence on the stiffness properties.

A common conclusion of all studies is the existence of a clear increase of mechanical properties from pith to bark, strongly connected to the transition from juvenile to mature wood. Nevertheless, in terms of elastic parameters, the data are only concerned with to the variations of the longitudinal elastic modulus. To our knowledge, no information is typically available about the radial variability of other elastic properties of wood.

#### 1.4.4.2 Longitudinal variation

Tsehaye et al. (1995) found a marginal variation of the elastic modulus parallel to grain from bottom to top logs. Kliger et al. (1992) working on Norway spruce showed an increase of 20% of the longitudinal elastic modulus from bottom to top in beams close to the pith. For *P. pinaster* wood grown in France, Castéra and Morlier (1993) observed a decrease of the longitudinal elastic modulus from bottom to top. On the same species but grown in Portugal, Machado and Cruz (2005) reported a vertical decrease of the elastic modulus parallel to grain of 14%, 35% and 28.5%, respectively, for specimens cut radially at 10%, 50% and 90% of the local stem radius, corresponding to a variation of the tree height of 65% with regard to the tree bottom (*i.e.*, for distances higher than about 10 m from the tree bottom). Moreover, the decrease of the elastic modulus, especially for the outer specimens (50% and 90%), was more significant for higher locations within the stem, *i.e.*, from 35% to 65% of tree height (*i.e.*, up than about 5.6 m from the tree bottom).

A general conclusion from these studies is that the longitudinal variation of the elastic

modulus parallel to grain is less pronounced than that observed radially. As mentioned above, no information could be found in the literature about the pattern variation of other elastic properties of wood.

### 1.4.5 Conclusions

From this survey about the elastic properties of wood, the following conclusions can be drawn.

- (i) In the evaluation of statistical representative properties of wood, several specimens, cut at different locations within the stem and from different trees, should be tested in order to take into account the inherent heterogeneity and variability of wood. However, this requires considerable testing and instrumentation which is quite expensive and time consuming.
- (ii) When studying the applicability of a given test to wood, special attention must be paid to the selection of specimens in order to minimise the scatter on the identified properties due to material variability. Coefficients of variation of 15% to 30% are usually reported for wood properties ([Green et al., 1999](#)). The following guidelines may be considered in the selection of matched clear wood specimens: (1) at a given height of the tree, specimens must be cut in the outer part of the stem (mature wood); (2) the specimens must be free of structural defects such as knots and have straight grain.
- (iii) For comparison among different tests or species, the mechanical properties of wood must be reported along with the moisture content and the density of the tested specimens, owing to their significant influence on wood properties.
- (iv) The mechanical properties of wood can vary significantly within a single stem. This variation is more important from pith to bark (radial variation) than from bottom to top (vertical variation).

# Chapter 2

## Material characterisation from kinematic full-field measurements

### 2.1 A classification of optical methods

#### 2.1.1 Introduction

Photomechanics is a discipline that has been developing over the last decades thanks to the progress of computer science, automated image processing and digital cameras. It relies on the use of photonics (the science and technology of generating, controlling and detecting radiant energy) for the measurement of kinematic quantities in the branch of mechanics. Within this domain of research, several optical methods have been proposed in the literature (Grédiac, 2004; Surrel, 2004a); they are classified in Table 2.1. A first criterion of classification is the nature of the physical phenomenon involved, sorting the optical methods into white-light (non-interferometric) and interferometric techniques. Other criteria can be the nature of the measurand (displacement, slope or strain), the characteristic pattern of the surface analysed in white-light based techniques (periodic or random), and the way light is reflected by the object surface in interferometric techniques (diffuse or diffracted light).

White-light techniques are based on the analysis of a pattern that follows the deformation of a surface of interest of a material, which has been subjected to an external load. It is assumed that the local luminance coming from each source point of the pattern is kept constant throughout the material deformation. The analysis is then focussed on the spatial variation of the light intensity distribution reflected from it. This class of methods can still be sorted with regard to the type of characteristic pattern. It can be either periodic (phase-measuring techniques) or random (image correlation techniques) (Table 2.1). A periodic pattern is usually a network of parallel and evenly spaced lines or dots. It is used either in geometrical moiré methods (in-plane, shadow, projection and reflection moiré) and in grid methods (grid method and deflectometry). A random

Table 2.1: Optical methods in experimental mechanics.

White-light techniques		
Measurand <sup>(a)</sup>	Period pattern	Speckle pattern
$u_x, u_y$ <sup>(b)</sup>	in-plane geometrical moiré (Cloud, 1995; Post et al., 1994) grid method (Surrel, 1999, 2004b) point tracking method (Doumalin, 2000)	digital speckle photography (Sjödahl, 1998) digital image correlation (Sutton et al., 1999)
$u_z$	shadow and projection moiré (Cloud, 1995; Post et al., 1994) grid projection (Le Magorou et al., 2002)	–
$u_x, u_y, u_z$ <sup>(c)</sup>	–	stereo-correlation (Synnergren and Sjödahl, 1999)
$\theta_x, \theta_y$ <sup>(d)</sup>	reflection moiré (Cloud, 2006) deflectometry (Surrel, 2004c)	–
Interferometric techniques		
Measurand	Diffuse light	Diffracted light
$u_x, u_y, u_z$	speckle interferometry (Cloud, 1995)	moiré interferometry (Post et al., 1994)
$\varepsilon_x, \varepsilon_y, \varepsilon_{xy}$	speckle shearography (Hung and Ho, 2005)	grating shearography (Lee et al., 2004a)

<sup>(a)</sup>  $u$  - displacement;  $\theta$  - slope;  $\varepsilon$  - strain

<sup>(b)</sup> the in-plane ( $u_x, u_y$ ) measurements are coupled with the out-of-plane ( $u_z$ ) displacement

<sup>(c)</sup> the camera calibration is needed

<sup>(d)</sup> the slope measurements are coupled with position coordinates

pattern can be imaged by a detector (*e.g.*, a CCD<sup>1</sup> camera) when a rough diffuse surface (roughness  $>$  wavelength  $\lambda$ ) is illuminated by coherent light (*e.g.*, a laser). In this case, the light is scattered in all directions. Its spatial interference forms a granular pattern, called speckle, which is used as a metrological carrier in digital speckle photography. In digital image correlation, white-light is used and the speckle pattern can be either the natural contrasted texture of the surface of interest, or an artificial texture obtained by spraying a black (white) paint over a white (black) background. The image correlation technique can also be used with period regular patterns (point tracking method). For most of the non-interferometric techniques, the optical aspects are reduced to the image

<sup>1</sup>Charge Coupled Device (CDD)

formation by the camera-lens system.

The interferometric techniques are based on the phenomenon of interference of light waves. These techniques use a monochromatic and coherent light source (*e.g.*, a laser) to illuminate the material surface. Considering the way light interacts with this surface, these methods can be sorted into diffused light (speckle) and diffracted light (grating) interferometric techniques (Table 2.1). Speckle interferometry is based on the diffuse reflection of light from an optical rough surface, whereas grating interferometry is based on the diffraction of light by a grating attached to the object surface. Several configurations can be set-up with regard to the directions of illumination and observation. These directions define the sensitivity vector, giving the component of the measurand to which the measured phase is sensitive to. Thus, there are speckle interferometry techniques for both in-plane and out-of-plane displacement measurements. The moiré interferometry is a technique based on grating metrology allowing the measurement of both in-plane and out-of-plane displacements. Finally, there are also different shearography set-ups (Table 2.1) that provide directly the measurement of the (optical) derivatives of the displacement.

The white-light techniques require simpler experimental set-ups than the interferometry counterparts since no special equipment, such as lasers and anti-vibration tables, is needed. Therefore, they can be easily coupled with more conventional apparatus such as universal testing machines.

The choice of an optical method for a particular application may not be straightforward (Grédiac, 2004). Nevertheless, several criteria can be considered such as: the cost, the simplicity of execution, the performances (resolution, spatial resolution...), the desired measurand (displacement, strain...), the expected range of variation of the measurand (*e.g.*, small or high deformations), the sensitivity to vibrations and the size of the region of interest (macro, micro or nano).

In contrast to classical techniques more frequently used in experimental mechanics, *e.g.*, strain gauges or extensometers (Dally and William, 1991, Part II, pp.129-340), optical methods provide an array of measurements over a whole surface of interest. Besides, although strain gauges still have a higher resolution than that usually reached nowadays by optical methods (especially white-light techniques), the latter have generally the advantage of being non-contact.

Most of the optical methods provide the measurement of the displacements across a whole surface of interest (Table 2.1). In the applications where the important kinematic quantity is the strain field, as, for instance, in the characterisation of material constitutive parameters, these techniques can still be used. In this case, the strain field components are computed from the full-field displacements by some suitable numerical denoising and differentiation procedure. This step is not straightforward because the measurements are always performed with some amount of noise and, in addition, data may be missing at some points. Alternatively, a few methods exist for which this differentiation is achieved

optically and thus delivering directly the gradient field of the surface deformation (shearography techniques) (Table 2.1).

The purpose of this section is to give an overview of the optical methods used in experimental mechanics.

### 2.1.2 Metrological aspects

Let us introduce a set of metrological quantities suitable for the characterisation of the kinematic full-field measurements provided by the optical methods. Moreover, these quantities can be systematically used for the evaluation and comparison of the techniques (Surrel, 2002, 2004a):

- Field of view: this is the total area covered by the camera-lens optical system.
- Sensitivity: this is the change in the response of a measuring instrument divided by the corresponding change of the stimulus. For the optical methods based on processing fringe images (*e.g.*, interferometry techniques) or line images (grid methods), the sensitivity can be defined at the phase level by:  $S = \partial\phi/\partial M$ , where  $M$  represents the measurand quantity (*e.g.*, displacement) and  $\phi$  the measured phase. Let us consider, for example, the case of the grid method (Table 2.1). In this technique the in-plane displacement field is measured through a pattern of alternating black and white lines separated by a distance  $p$ . Therefore, the phase of the periodic signal of the pattern varies of  $2\pi$  when the grid is moved (orthogonally to the lines direction) by an amount equal to its pitch ( $p$ ). Thus, in this case the sensitivity is given by:

$$S = \frac{2\pi}{p} \quad (\text{rad/mm}). \quad (2.1)$$

- Spatial resolution: this is the smallest distance separating two successive independent measurements. In the theory of image formation, owing to diffraction effects, the optical system acts as a low pass filter with a finite optical resolution (the smallest object resolutibility reached by an optical system), which can be globally quantified by the modulation transfer function (Smith, 2000, Chap. 11). Therefore, the highest frequencies reflected by an object will not be imaged beyond a certain spatial cutoff frequency,  $f_c$ . The spatial resolution,  $\Delta u$ , can then be defined as the inverse of this frequency:  $\Delta u = 1/f_c$  (mm). Besides, it should be noticed that further image processing, *e.g.* spatial phase-evaluation in which a set of adjacent pixels is used for sampling an entire period of the carrier grating, sub-image division in digital image processing, or field denoising by convolution methods, will degrade the spatial resolution.
- Resolution: this is the smallest measurand value that can be detected. In practice,

this value can be quantified by the amount of noise in the measurements. This noise is usually assumed as a Gaussian white noise (which has zero mean), so that the resolution can be defined as a function of its standard deviation ( $\sigma$ ). The noise can be globally characterised by calculating the difference between two independent consecutive measurements of the same kinematic state of the specimen:  $\Delta m(i, j) = n_2(i, j) - n_1(i, j)$ , where  $n_k(i, j)$  is the noise added to the signal at the instant  $k$  ( $k = 1, 2$ ), and  $(i, j)$  are the spatial coordinates of the 2D array of data. In the subtraction operation the signal is cancelled out because it is assumed to be constant. Assuming that:  $\sigma_{\Delta m}^2 = \sigma_{n_1}^2 + \sigma_{n_2}^2 = 2\sigma_n^2$ , *i.e.*, the noise is statistically identical between two successive acquisitions, the standard deviation of the measured noise is determined by:  $\sigma_n = \sigma_{\Delta m}/\sqrt{2}$ . Let us consider again the grid method as an example. In this technique  $\sigma_n$  is evaluated at the phase level. Thus, the phase resolution,  $\sigma_\phi$ , can be quantified from the difference of two successive phase measurements,  $\phi_1(i, j)$  and  $\phi_2(i, j)$ , of the same measurand field by:

$$\sigma_\phi = \frac{\sigma_{\phi_1} - \sigma_{\phi_2}}{\sqrt{2}} = \frac{\sigma_{\Delta\phi}}{\sqrt{2}} \quad (\text{rad}). \quad (2.2)$$

The displacement resolution,  $\sigma_u$ , can then be determined with regard to the sensitivity (Eq. 2.1) of the method as:

$$\sigma_u = \frac{\sigma_{\Delta\phi}}{S} = \frac{\sqrt{2}\sigma_\phi}{S} \quad (\text{mm}). \quad (2.3)$$

Hence, by this definition, the resolution is presented as a discrimination threshold, *i.e.*, the smallest variation of the measurand that induces a detectable signal.

## 2.1.3 White-light techniques

### 2.1.3.1 Digital speckle photography

In speckle photography an optically rough surface (*i.e.*, with a roughness  $>$  wavelength) of a material under investigation is illuminated by coherent light (*e.g.*, with a laser). Thus, the light intensity will be randomly scattered from the surface in all directions. The multiple interference of light, issued from different parts of the surface, is imaged and recorded by a detector as a granular pattern of bright and dark spots called speckle. The pattern of the speckle (subjective speckle), *i.e.* the size and contrast of the spots, is dependent on the coherence of the incident radiation, on the surface roughness and on the magnification and aperture of the imaging system. The speckle pattern represents a marker of the actual state of the diffuse surface, such that, when the material undergoes a deformation, the position of the pattern will also change correspondingly.

In digital speckle photography (DSP) an electronic camera (*e.g.* a CCD camera)

is used for image grabbing. The DSP has several advantages over the classical speckle photography (Sjödahl, 1998). In the DSP technique, speckle images are recorded before and after the surface deformation. These images are divided into a mosaic of sub-images, with dimensions of  $(2n + 1) \times (2n + 1)$  pixels, within which an independent measurement of the in-plane displacement is performed by a matching strategy between them (cross-correlation approach). The accuracy of the displacement measurement by DSP is affected by speckle correlation, speckle size, sub-image size, and displacement gradients (Sjödahl and Benckert, 1994); a typical value of about 1/100 of a pixel can be reached (Sjödahl, 1997).

### 2.1.3.2 Digital image correlation

Digital image correlation (DIC)<sup>2</sup> is a technique merged from the same principles of the speckle photography, but using incoherent light (white-light). The speckle pattern in this method is physically attached to the material surface, either naturally by the own texture of the surface (*e.g.*, in most materials imaged at a high magnification) or artificially by black and white randomly sprayed paint. In strain field measurements, DIC may have several advantages over DSP (Brillaud and Lagattu, 2002; Sjödahl, 1997). White-light speckle is more robust to decorrelation. In addition, neither a laser nor specific optical devices are required in the practical implementation of DIC, although both lenses (minimum aberrations) and white-light speckle patterns of high-quality are usually necessary. Similarly to the DSP, the 2D displacement field in the DIC technique is obtained by matching regions of images recorded successively at different load steps. The image processing is performed using the same type of algorithms as in DSP. The spatial resolution of these techniques is dependent on the size of the sub-images chosen throughout the processing. Therefore, although simpler in concept and execution, they have usually a lower spatial resolution than other counterpart optical methods.

The main advantage of these spatial cross-correlation based techniques is their ability to measure large deformations and strains (Parsons et al., 2004). Furthermore, they are advantageous in applications where the use of strain gauges may not be suitable, as, for instance, due to the difficulty of bonding or because it may disturb the mechanical response of a soft material owing to local stiffness variation (Hild et al., 2002). Regarding the details of the DIC technique, further information can be found for instance in (Sutton et al., 1999).

The image correlation algorithm can also be applied to images of regular surface patterns. Such a technique is called point tracking method. Its principle consists in following the displacements of point markers, regularly distributed across the region of interest with a given spatial resolution, when the material is deformed by an external load. Details

---

<sup>2</sup>Some authors call this technique white-light digital speckle photography.

about this technique are found in (Doumalin, 2000).

### 2.1.3.3 Stereo-correlation

The DSP and DIC techniques described above provide the measurement of the in-plane displacement of (quasi-)planar specimens with a single camera. Therefore, in these techniques attention must be paid to avoid the out-of-plane motion of the specimen (in the direction towards the camera), since this displacement can disturb the in-plane measurements. To overcome this limitation these techniques can be extended to binocular vision. Such technique is commonly called stereo-correlation or stereo-vision. In this case, the measurements can be achieved, for instance, by two cameras imaging the material surface from different directions, such that their optical axes intersect at the geometrical midpoint of the field of view; this configuration is called the angular-displacement method (Prasad and Jensen, 1995). The advantage is that the measurement of the 3D shape of a static object or the 3D deformation of a material submitted to external loads can be performed (Garcia et al., 2002; Synnergren and Sjö Dahl, 1999). In this latter type of application, the two cameras record the images of the specimen before and after deformation. These two sets of images are then compared (cross-correlation approach) in order to retrieve the three components of the displacement. However, before testing, a camera calibration process is needed for the accurate determination of the parameters of the vision model. Further information about this technique can be found in (Sutton et al., 1999).

### 2.1.3.4 Geometrical moiré and grid methods

When (quasi-)periodic structures such as line gratings or dot screens are superimposed, fringes are generated by geometrical interference. This effect is called moiré and is at the origin of the moiré methods. The analysis of the interference pattern allows the quantification of differences of pitch and/or orientation between the superimposed structures.

In the in-plane geometrical moiré (Cloud, 1995; Gåsvik, 2002; Post et al., 1994), the specimen grating (a uniform cross-line pattern) is attached to the material surface under investigation, whilst the reference one (a linear-line pattern perpendicular to the direction of interest) is kept motionless. In the undeformed state of the material these gratings are usually identical, *i.e.*, they have the same frequency ( $f$ ) (number of lines per unit length), and they are set to provide no moiré fringes (exceptions are the mismatch reference grating or reference grating shifting procedures (Post et al., 1994, p. 115-117)). When the material is submitted to an external loading, a visual interference pattern can be generated by the interaction between the gratings, encoding information about the undergoing deformation. Therefore, relative displacements are measured along the direction perpendicular to the lines of the reference grating. The value of the displacement at a point is simply obtained

by multiplying the pitch of the reference grating by the order of the moiré fringe at this location. The other component of the in-plane displacement can be measured by rotating the reference grating by  $90^\circ$ . The specimen grating can be transferred onto the material surface by several procedures such as printing, stamping, etching, scribing, coating or lithography (Parks, 1993; Takeda, 1998).

The moiré method can also be used for the measurement of out-of-plane displacements (*e.g.*, the deflection field obtained from bent or vibration plates). These techniques are called shadow moiré and projection moiré (Cloud, 1995; Gåsvik, 2002; Post et al., 1994). They are based on the triangulation principle (Gåsvik, 2002, p. 190) and therefore only a reference grating may be needed. In shadow moiré a reference grating, at least as large as the region of analysis, is installed close to the object surface, which has to be prepared with matt white paint. The grating and specimen are illuminated at an appropriate angle. An interference pattern can then be generated by the interaction between the reference grating and the grating made by its shadow (the shadow being the specimen grating). The orientation of the light source has a significant influence on the contrast of the moiré fringes. The relative height profile of the object surface can then be measured in function of the angles of illumination and observation, the pitch of the reference grating and the fringe order. In projection moiré a reference grating is projected onto the surface of interest by means, for instance, of a slide projector. The pattern reflected from the material surface can be interfered with a detection grating set in front of the observation system for the generation of the moiré fringes. Alternatively, the moiré fringes can be obtained by digital superposition of the images of the reference grating before and after the material deformation. The shape of the object surface can be measurement from the angle of projection, the pitch of the reference grid and the fringe order.

There is also a variant of the moiré method called the reflection moiré (Cloud, 2006; Gåsvik, 2002), which allows the measurement of the slope field providing that the specimen has a mirror-like surface. In this case, the reference grating is imaged by reflection from the specimen surface. The moiré fringe pattern is formed by superimposing the images recorded before and after loading. The moiré fringes obtained by this technique carry information about the derivative of the deflection field, *i.e.* the slope of the surface. The slope field can be calculated from the pitch of the grating, the fringe order and the distance separating the grating and the specimen (this distance should be large enough to minimise the effects of the out-of-plane displacement on the slope measurement). Both  $x$  and  $y$  components of the slope field can be measured by rotating the grating by  $90^\circ$ . The numerical differentiation of these slope fields can provide afterwards the measurement of the curvature field, needed in plate bending problems. This technique is very sensitive: it can have a maximum resolution of the order of  $7 \times 10^{-3}$  rad (Gåsvik, 2002, p. 190).

The application of geometrical moiré methods in material deformation problems is limited by its low sensitivity (the number of fringes generated per unit displacement). In

order to overcome this shortcoming, methods such as fringe multiplication, fringe interpolation and mismatch have been introduced to enhance their sensitivity (Gåsvik, 2002, p. 177).

The grid method is a development of the in-plane geometrical moiré method which does not actually require moiré processing since the analysis is performed directly on the image of the grid (Surrel, 1999, 2004b). The resolution of this method, expressed as a fraction of the pitch of the grid ( $p$ ), is in the range of  $p/100 - p/200 \mu\text{m}$ . The spatial resolution can be the equivalent of 1 pixel or several pixels depending on the method employed in the phase evaluation (temporal or spatial phase-shifting methods, respectively).

The version of the grid method for reflection moiré is called the deflectometry method by grid reflection (Surrel, 2004c). This technique provides the measurement of the slope fields, providing the material surface has a sufficient specular reflection. Surrel (2004c) reported for this technique a sensitivity of 1728 and a slope resolution of  $7.3 \mu\text{rad}$ . Moreover, the value of the resolution was found dependent on the quality of the reflected image.

The version of the grid method for projected moiré is called grid projection (Le Magorou et al., 2002). In this technique the image of a linear grid is projected onto the surface of interest with an appropriate angle. This image is recorded by a digital camera set orthogonal to the planar (undeformed) specimen. The local phase of the grid profile varies as function of a given out-of-plane deformation of the specimen. Thus, the phase difference between the undeformed and deformed states of the material can afterwards provide the measurement of the out-of-plane displacement field, in terms of the pitch of the grid, the angle of projection and a scaling factor. In order to improve the spatial resolution of the method, the temporal phase-shifting technique can be used, consisting in introducing a constant phase shifting by displacing the projected grid image (Le Magorou et al., 2002).

## 2.1.4 Interferometric techniques

### 2.1.4.1 Moiré interferometry

Moiré interferometry (Dally and William, 1991; Post et al., 1994) is based on the same physical phenomenon as the geometrical moiré, *i.e.*, the interference between specimen and reference gratings. However, in moiré interferometry the frequency ( $f$ ) of the specimen grating is usually greater than 1000 or 2000 lines/mm (the theoretical limit is about 4000 lines/mm), compared to a maximum of 80 lines/mm employed in the geometrical moiré (Dally and William, 1991, p. 415). This high-frequency grating is usually transferred to the surface of the specimen by a replication process (Post et al., 1994, p. 175). Besides, in moiré interferometry the illumination must be achieved with coherent light. Moreover, the reference grating is not a real array of lines as in geometrical moiré, but instead it consists of a virtual image optically formed by an interference pattern generated by

mirrors. A four-beam interferometer combined with a crossed diffraction grating can be used to produce the moiré fringe patterns for the measurement of the two components of the in-plane displacement (Post et al., 1994, p. 152).

Moiré interferometry is a high sensitivity method, since high-frequency gratings are used and the sensitivity increases with the grating frequency. For the case of  $f = 2400$  lines/mm the sensitivity is 2.4 fringes/ $\mu\text{m}$  displacement (Post et al., 1994, p. 152). The inverse of the sensitivity defines the contour interval,  $1/f$ , which represents displacement per fringe order. For  $f = 2400$  lines/mm the displacement per fringe order is  $0.417 \mu\text{m}$ . The displacement resolution, which is proportional to the uncertainty of the fringe order, can be of the order of  $1/(5f)$  or  $1/(10f)$ ; thus, when  $f = 2400$  lines/mm the resolution is  $0.08$  or  $0.04 \mu\text{m}$  (Post et al., 1994, pp. 152, 265). Besides, this technique has an excellent fringe contrast and spatial resolution (Post et al., 1994, p. 264). Nevertheless, the surface preparation is non-trivial and the dimensions of the specimen grating can limit the region of interest to be analysed. A field of view of 30 to 40 mm is recommended for general engineering applications (Post et al., 1994, p. 156).

#### 2.1.4.2 Electronic speckle pattern interferometry

Electronic speckle pattern interferometry (ESPI)<sup>3</sup> (Cloud, 1995) is based on the interference of specimen and reference light waves. Speckle patterns are obtained since optically rough surfaces are illuminated by a laser beam. The light intensity field, formed by the interference of specimen and reference beams, are recorded before and after the specimen deformation. The phase of the speckle pattern (primary interference) in each state of the specimen, can be determined from the temporal (Kao et al., 2002) or spatial (Bothe et al., 1997) phase-shifting method. Correlation fringes (secondary interference) are obtained by subtracting the two speckle intensity fields. They correspond to the change of phase of the speckle pattern generated by the specimen deformation between the two exposures, the fringes representing lines of constant displacements in the direction of the sensitivity vector (defined by the optical setup) (Cloud, 1995, p. 365). A phase-shifting method can then be used to compute this phase difference (Creath, 1985). This calculation yields the phase modulo  $2\pi$ . A phase-unwrapping algorithm is used afterwards to eliminate the  $2\pi$  ambiguities and therefore to provide the continuous displacement field (Vrooman and Maas, 1991).

The advantages of this technique are that neither grating nor smooth surface is necessary. However, the system is sensitive to vibration disturbances and only small deformation (of the order of the average speckle diameter) can be measured between two successive exposures because of the decorrelation of the speckle pattern. The object size that can be studied depends on the lenses used in the imaging system and laser power,

---

<sup>3</sup>it is also known, among others, as Digital speckle pattern interferometry (DSPI), speckle correlation interferometry or TV-holography.

but it is typically higher than in moiré interferometry.

### 2.1.4.3 Shearography

The basic principle of shearography methods is to create interferences between the waves coming from two adjacent points of the object surface. The resulting fringes are related to the gradient of the optical phase, from which the gradient of the displacement can be deduced. Therefore, strain components or local rotations can be directly obtained. Moreover, compared to classical interferometry, shearography has some advantages since simple optical set-ups are needed and both the vibration sensitivity and the coherence length requirements are greatly reduced, leading to fringes of better quality (Hung and Ho, 2005). Shearing interferometry methods can be classified into two techniques: speckle shearography (SS) (Hung and Ho, 2005) and grating shearography (GS) (Lee et al., 2004a). The SS has the advantage of being non-contact, thus no particular surface preparation (white-color painting) is required, compared with a non-trivial preparation of the surface in GS, consisting in the specimen grating replication. The images of the phase maps typically obtained in SS contain spatial noise which requires a filtering or fitting process for quantitative measurements, inducing, therefore, a degradation of the spatial resolution. In GS the use of the specimen grating provides phase map images with a high signal-to-noise ratio, where the speckle noise is negligible; thus a very high spatial resolution is conserved. Due to the decorrelation of the speckle, the application of SS is limited to relatively small deformations between two successive exposures. In GS the deformation of the specimen grating is limited by its delamination. A further comparison between these two methods is reported in (Lee et al., 2004b).

### 2.1.5 Conclusions

Several optical techniques for full-field kinematic measurements are proposed in the literature. Among them, the grid method has been chosen. Key advantages of this technique are:

- it may be applied to any sort of solid material;
- it can be adapted to study regions of interest with different size (*e.g.*, by changing the pitch of the grid);
- it has a better spatial resolution than equivalent white-light techniques such as digital image correlation;
- it is less sensitive to object vibrations than interferometric techniques, thus more readily coupled with a universal testing machine in a photo-mechanical set-up.

A major disadvantage of this method is, however, the transfer of the grid onto the surface of interest of the specimen by a suitable procedure.

Since the measurement of complex inhomogeneous strain fields is needed in the identification procedure used throughout this work (§2.3), and considering the possible localisation of strains in small regions of the tested specimen, the grid method has been chosen as a compromise between good spatial resolution and simplicity of execution.

## 2.2 Application of optical methods to wood characterisation

### 2.2.1 Introduction

The interest of optical methods in experimental solid mechanics has been underlined in the course of the last number of decades (Grédiac, 1996, 2004). These techniques have been progressively applied to wood mechanics in several studies. This is the topic of review in this section.

### 2.2.2 Mechanical testing

Dumail et al. (2000) used the DIC technique coupled with the Iosipescu shear test on Norway spruce wood (*Picea abies*) oriented in the radial-tangential plane. Accordingly, a mean value of the shear strain between the V-notches could be determined, instead of a local measurement at the centre of the specimen obtained by strain gauge measurements. This approach has the advantage of needing no correction factor for taking into account the inhomogeneity of the shear strain across the area of measurement (the  $S$  correction factor in Eq. 1.15, § 1.3.4.3). Besides, in this plane of symmetry, owing to the cellular structure of wood, strain gauge bonding is generally more difficult (Xavier et al., 2004). Moreover, due to the low stiffness properties of wood in the radial-tangential plane (perpendicular to the grain), the use of a contactless technique is recommended in order to prevent local stiffening.

De Magistris and Salmén (2004) have investigated the use of a modified Iosipescu test fixture in order to study the combined shear and compression behaviour of anisotropic materials using DIC. The tests were performed using medium-density fiberboards. Finite element analyses have shown that for a rotation of the fixture of an angle of  $45^\circ$ , both shear and compression fields were almost uniform in the gauge area. This was ascertained by comparing the full-field numerical and experimental response of the material. Thus, the use of this technique allowed the verification of the reliability of this test for the purpose of the study.

Muszyński et al. (2003) have studied the reliability of an experimental protocol for the determination of the basic mechano-sorptive parameters of Red spruce (*Picea Rubra*) wood in uniaxial loading parallel to grain. In order to enable the separation of strain components, which were expressed as a linear superposition of visco-elastic deformation ( $\varepsilon_{ve}$ ), free shrinkage and swelling ( $\varepsilon_{\alpha}$ ) and mechano-sorptive deformation ( $\varepsilon_{MS}$ ), three groups of tests were carried out on matched clear wood specimens. In this study, the DIC technique was used for the measurement of the specimen deformation during the tests. One of the advantages of this technique versus strain gauges or extensometers was the significant simplification of the specimen handling procedure and reduction of time in the specimen set-up, which was important because of the climatic conditioning of the specimens.

Serrano and Enquist (2005) have investigated the mechanical behaviour of wood-adhesive bonds using the DIC technique. Conventionally, testing wood-adhesive bonds is based on standard methods, where the load and the displacement are measured for the evaluation of the strength of the bond line. Moreover, small clip-gauges or linear variable differential transformers (LVDTs) can be attached to selected parts of the specimen for gathering data on crack opening modes for the determination of strain energy release rates. However, these systems are difficult to incorporate into the bond line, and, besides, they can disturb the strain distribution in the gauge section. Therefore, the use of a non-contact technique such as DIC for measuring the strain distribution over the bond was found convenient. In this study, the full-field measurements allowed the comparison among three different adhesives in terms of their strain distribution at a given load.

The moiré technique has been used by Wolfe et al. (1994) for evaluating wood-frame truss connections. The technique has been shown to be appropriate in detecting variations of stress along the length of the joint plates as well as stress concentration regions.

Eberhardsteiner (1995) has developed a new biaxial testing equipment for the experimental determination of the mechanical properties of a cruciform wooden specimen. The author employed the ESPI technique for the measurement of the displacement field at the surface of the specimen. The investigated metrological problem enhanced the importance of using this full-field optical technique. The ESPI technique was also used by Konnerth et al. (2006) for studying the deformation of timber finger joints loaded in tension. Quantitative analyses have been possible concerning the strain distribution in the adhesive bound line. Similar analyses have been carried out by Hernandez (1998) using moiré interferometry.

### 2.2.3 Influence of the anisotropy and heterogeneity of wood on its mechanical behaviour

Shipsha and Berglund (2007) have applied the DIC technique for measuring the dis-

placement/strain distribution over a whole region of interest in transverse compression tests with specimens having different annual ring patterns. With this full-field technique the local strain/stress inhomogeneity due to the annual ring structure and anisotropy could be quantified. This study would not have been possible with more traditional methods using strain gauges.

Although the mechanical behaviour of clear wood is usually analysed based on the homogeneity assumption (continuous and orthotropic material), its structure is actually highly heterogeneous. In the past, because of the lack of appropriate instrumentation, detailed studies on the effect of the variable structure of wood on its mechanical behaviour were very limited. Recent studies (Choi et al., 1996; De Magistris and Salmén, 2005; Ljungdahl et al., 2006; Samarasinghe and Kulasiri, 2000; Zink et al., 1995), however, brought important progress in this topic of research thanks to the utilisation of optical methods. For instance, Ljungdahl et al. (2006) studied the mechanical behaviour of European oak (*Quercus robur* L.) in transverse compression using the DIC technique for the evaluation of the strain field in the region of interest. The strain components and the effective Poisson's ratio ( $\nu_{RT} = -\varepsilon_T/\varepsilon_R$ ) could be determined separately in the earlywood and latewood layers. The full-field data allowed a better interpretation of the stress-strain curve in terms of the progressive deformation and failure of the structural elements of the material. Owing to the hierarchical structure of wood, the authors pointed out that, in certain cases (tangential compression), it is necessary to measure the deformation of wood at different scales of observation in order to identify the critical failure events. Besides, the full-field strain measurements provided direct evidence that the rays are the main microstructural factor controlling transverse anisotropy for this species of wood.

De Magistris and Salmén (2005) have applied a modified Iosipescu test fixture (De Magistris and Salmén, 2004) in order to study the combined shear and compression behaviour of Norway spruce wood in the radial-tangential plane. In this case, the DIC method allowed the visualisation of a non-uniform distribution of the shear strain field associated to the earlywood and latewood structure of the annual rings. A finite element model was developed to take into account the annual ring structure. Thus, the comparison between experimental and numerical fields could also be analysed.

#### 2.2.4 Crack characterisation

For a better understanding of crack growth in the radial-tangential plane of *P. sylvestris* L. wood, Thuvander et al. (2000) have used the DIC technique for measuring the strain field around the crack tip at the growth ring level. Samarasinghe and Kulasiri (2004) have also employed this technique to measure the displacement fields near the crack tip in the tangential-longitudinal opening mode, in pinus radiata wood subjected to tension. Coupling these measurements with the linear elastic orthotropic fracture theory and using

representative material properties, the stress intensity factor ( $K_{I_{TL}}$ ) of this species could be determined.

### 2.2.5 Parameter identification from full-field measurements

A small number of studies (Cárdenas-García et al., 2005; Foudjet et al., 1982; Jernkvist and Thuvander, 2001; Le Magorou et al., 2002; Rouger, 1988) have addressed the topic of wood parameter identification using full-field kinematic measurements.

Foudjet et al. (1982) proposed an inverse identification approach to determine the elastic constants of wood plates from bending and torsion tests. However, since a mixed numerical-experimental approach (§ 2.3) has been used, full-field data provided by a suitable optical method were not really necessary. Indeed, the authors measured the deflections only at several points over the plate with inductive gauges, and they compared these data with numerical ones provided by a finite element model. They eventually set up a cost function figuring the deviation between both types of data, and minimized this cost function for identifying the constitutive parameters.

Rouger (1988) developed an approach for characterizing the linear elastic behaviour of wood using a statically undetermined bending test. The approach was aimed at identifying the four in-plane stiffness parameters by minimising the difference between experimental and numerical data. The length to width ratio of the beam was chosen in order to enhance the contribution of all stiffness components in the mechanical response. Points across the surface of the beam were judiciously selected for the parameter identification. Although, no experimental validation was provided.

Jernkvist and Thuvander (2001) employed the DIC technique to measure the radial and tangential displacements in a single growth ring of Norway spruce subjected to a tensile test in the radial direction. The strain fields were determined from these measurements. A finite element modelling strategy (equilibrium of computed stresses) was set up for identifying the orthotropic elastic properties of the material. In spite of the uniaxial tensile loading, the authors claimed that the identification of all the in-plane engineering constants was possible because of the abrupt stiffness variation from latewood to earlywood constituents, inducing a biaxial variation of the strain and stress within the growth ring. Thanks to the sharp spatial resolution achieved in the measurements, it was also possible to determine the radial variation of the elastic properties across the growth ring. Even though the authors obtained consistent results about the mechanical properties of earlywood and latewood, they provided only few details about the numerical procedure used for solving the inverse problem. Moreover, they did not explain how the noise contained in their measurements was handled. This point is essential because, as they identified the spatial variations of properties, they had to deal with a large number of unknown, causing the inverse problem to be ill-posed.

[Le Magorou et al. \(2002\)](#) simultaneously determined the bending and torsion rigidities of wood-based panels (Okoume plywood panels) by a mixed numerical-experimental identification method. In this study, the deflection fields across the bent plate was measured by the grid projection method. The numerical displacements obtained from a finite element model of the test were compared with the experimental data, through an iterative optimisation scheme, in order to recover the material properties. Although full-field measurements are not strictly necessary in this approach, the huge amount of data provided by the optical method improves the robustness of the methodology.

[Cárdenas-García et al. \(2005\)](#) used the moiré “pre-existing hole” method for identifying the elastic constants of different species of wood: oak, birch and spruce. In this approach, biaxial stresses were applied to a thin wood open-hole plate. The moiré fringes around the hole were processed in order to identify the four independent orthotropic elastic constants of the material. The robustness of the procedure was tested numerically by means of computer generated moiré images, but no experimental validation was provided.

## 2.2.6 Conclusions

The importance of optical methods in the investigation of wood mechanics has been underlined. Several topics of interest were identified: (i) mechanical testing; (ii) influence of the anisotropy and heterogeneity of wood on its mechanical behaviour; (iii) crack characterisation; (iv) parameter identification from full-field measurements.

Among the above applications, the topic of research of the present work is inserted in the identification of constitutive parameters of wood from full-field measurements. Only a few studies ([Cárdenas-García et al., 2005](#); [Foudjet et al., 1982](#); [Jernkvist and Thuvander, 2001](#); [Le Magorou et al., 2002](#); [Rouger, 1988](#)) have addressed this subject in the literature, although it seems of great interest for characterising wood mechanical properties owing to its inherent heterogeneity and anisotropy.

In this approach no closed-form solution exists, thus, specific identification strategies are needed for the identification of the constitutive parameters, coupled with a suitable testing configuration. These are the topics of review in the following section.

## 2.3 Inverse identification methods

### 2.3.1 Introduction

The effective parameters governing the constitutive equations of materials are determined experimentally through suitable mechanical tests. In the field of solid mechanics, this issue is presented as an inverse problem where the material parameters are to be determined from the knowledge of the specimen geometry, the boundary conditions and the

strains (or displacements). Conventionally, this identification is achieved by carrying out mechanical tests for which the geometry of the specimen and loading system are designed in such a way that a homogeneous and simple state of strain/stress is generated across the gauge area. The concept behind this assumption is useful for theoretical analyses because a closed-form solution can be found, relating the unknown material parameters to the load and strain measurements (statically determined tests). However, as pointed out in Chapter 1, the practical implementation of these tests can be difficult, especially for anisotropic and heterogeneous materials.

The recent development of full-field optical techniques has enabled a new glance on the mechanical tests for material characterisation (Grédiac, 1996, 2004). The basic idea driving this new approach is that a single specimen – with a convenient geometry – can be loaded in order that several parameters are involved in its mechanical response, yielding heterogeneous and complex strain fields (statically undetermined tests). By means of a suitable identification strategy all the active parameters can be determined afterwards.

A few approaches exist in the literature for addressing this problem. The most familiar may be the finite element model updating method (FEMUM) (Le Magorou et al., 2002; Lecompte, 2007; Molimard et al., 2005). It consists in building a finite element model of the mechanical test and considering a cost function of the difference between numerical and experimental data (displacement or strain) over the region of interest. The minimisation of this cost function with respect to the unknown material parameters (design variables), iteratively updated in the model, provides the solution to the problem. This method is flexible and does not specifically require full-field measurements. However, as it is iterative, it can be time consuming and the convergence dependent on the initial guess of the parameters. Moreover, accurate boundary conditions need to be modelled to avoid a bias on the identified parameters. The presence of noise in the measurements will also affect the robustness of the updating routine. To overcome the drawbacks associated to the FEMUM, an alternative approach called the virtual fields method (VFM) has been gradually developed since the early work of Grédiac (1989). One of its advantages is the fact that it directly provides the unknown constitutive parameters in the case, for instance, of linear elasticity. All the advances of the VFM have been recently reviewed in (Grédiac et al., 2006).

In this section, the mechanical tests proposed in the literature for the identification of several constitutive parameters from full-field heterogeneous strain measurements are reviewed. Moreover, the general principle of the VFM is also recalled.

### 2.3.2 Statistically undetermined tests

The design of statically determined mechanical tests, for which the actual state of stress across the gauge area can be deduced directly from the applied load, is most often

restricted to simple geometries and loadings (Chapter 1). The main advantage is that simple data reduction can be achieved in these cases. Conversely, more complex tests giving rise to heterogeneous mechanical responses can be carried out for material characterisation, providing that full-field measurements are available via an optical method. However, a redesign of the mechanical test methods usually employed in the parameter identification is necessary. The purpose is to choose a geometry and loading conditions yielding strain fields that involve all the unknown constitutive parameters.

Regarding the design of mechanical tests, this new approach opens a huge spectrum of possibilities. Several test configurations have already been proposed in the literature (Table 2.2). Most of these tests aim at identifying the linear elastic properties of orthotropic materials through either in-plane or bending tests. Only some attempts were made to redesign the tests used for identifying elasto-plastic constitutive parameters (Table 2.2).

Classically in test design, the configurations must be optimised with regard to the identifiability of the whole set of constitutive parameters to be determined (Le Magorou et al., 2002; Pierron et al., 2007). A general procedure is to build up a cost function that penalises unbalanced strain components. Generically, this condition may be considered as sufficient to guarantee that several (or all) parameters contribute to the global response of the specimen. Consequently, they can be recovered afterwards by a suitable identification strategy.

### 2.3.3 The virtual fields method: general principle

The VFM is based on the fundamental equations of solid mechanics: the equilibrium equation, through the principle of virtual work (PVW), and the constitutive equations. Generically, the PVW can be written for an arbitrary solid as:

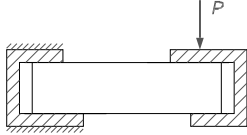
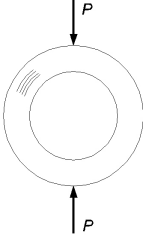
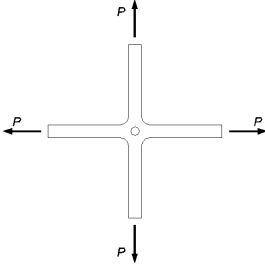
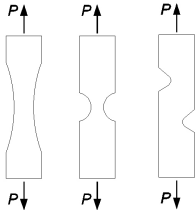
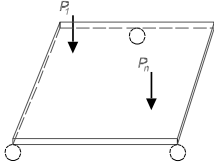
$$\int_V \sigma : \varepsilon^* \, dV = \int_{S_f} \mathbf{T} \cdot \mathbf{u}^* \, dS + \int_V \mathbf{f} \cdot \mathbf{u}^* \, dV + \int_V \rho \gamma \cdot \mathbf{u}^* \, dV \quad (2.4)$$

where  $\sigma$  is the stress tensor,  $\varepsilon^*$  the virtual strain tensor,  $V$  the volume of the solid,  $\mathbf{T}$  the distribution of external tractions applied over  $S_f$ ,  $\mathbf{u}^*$  the virtual displacement vector,  $\mathbf{f}$  the distribution of volume forces acting over  $V$ ,  $\rho$  the mass per unit volume and  $\gamma$  the acceleration. Eq. (2.4) is valid for any kinematically admissible (K.A.) virtual field  $(\mathbf{u}^*, \varepsilon^*)$ , *i.e.*, continuous, differentiable and equal to the prescribed displacements at the displacement boundary conditions. A macroscopic constitutive model of the material must be assumed at this point. In a general case this equation may be written as:

$$\sigma = g(\varepsilon, p) \quad (2.5)$$

where  $g$  is a given function of the actual strain components ( $\varepsilon$ ) and of the constitutive parameters ( $p$ ). If the body forces and the accelerations are negligible, the PVW (Eq. 2.4)

Table 2.2: Some heterogeneous mechanical tests for the identification of constitutive parameters.

Mechanical test	Constitutive equations
1. Unnotched Iosipescu test <sup>(a)</sup> 	<ul style="list-style-type: none"> <li>– Anisotropic linear elastic model: <math>\sigma_i = Q_{ij}\varepsilon_j</math></li> <li>– Shear damage model: <math>\sigma_s = Q_{ss}^0\varepsilon_s - K\varepsilon_s\langle\varepsilon_s - \varepsilon_s^0\rangle^+</math></li> </ul>
2. Open-hole tensile test <sup>(b)</sup> 	<ul style="list-style-type: none"> <li>– Anisotropic linear elastic model: <math>\sigma_i = Q_{ij}\varepsilon_j</math></li> </ul>
3. Ring compression test <sup>(c)</sup> 	<ul style="list-style-type: none"> <li>– Anisotropic linear elastic model: <math>\sigma_i = Q_{ij}\varepsilon_j</math> (polar coordinates)</li> </ul>
4. Biaxial tensile tests on cruciform specimen <sup>(d)</sup> 	<ul style="list-style-type: none"> <li>– Anisotropic linear elastic model: <math>\sigma_i = Q_{ij}\varepsilon_j</math></li> <li>– Elasto-plastic model</li> </ul>
5. Tensile test on flat dog-bone like specimens <sup>(e),(f),(g)</sup> 	<ul style="list-style-type: none"> <li>– Elasto-plastic behaviour – Voce's hardening model: <math>\sigma = \sigma_0 + R_0\varepsilon^p + R_{\text{inf}}[1 - \exp(-b\varepsilon^p)]</math></li> </ul>
6. Bending test on a plate <sup>(h)</sup> 	<ul style="list-style-type: none"> <li>– Anisotropic linear elastic model: <math>\sigma_i = Q_{ij}\varepsilon_j</math></li> </ul>

<sup>(a)</sup> (Chalal et al., 2006; Grédiac et al., 2002; Pierron and Grédiac, 2000)<sup>(b)</sup> (Molimard et al., 2005)<sup>(c)</sup> (Moulart et al., 2006)<sup>(d)</sup> (Lecompte, 2007)<sup>(e)</sup> (Pannier et al., 2006); <sup>(f)</sup> (Kajberg and Lindkvist, 2004); <sup>(g)</sup> (Meuwissen et al., 1998)<sup>(h)</sup> (Bruno et al., 2002; Grédiac, 1989; Le Magorou et al., 2002)

can be written as:

$$\int_V g(p, \varepsilon) : \varepsilon^* \, dV = \int_{S_f} \mathbf{T} \cdot \mathbf{u}^* \, dS. \quad (2.6)$$

The VFM consists in writing Eq. (2.6) with as many independent virtual fields as there are unknown parameters. In some cases, as for instance in linear elasticity, this procedure leads to a linear system of equations whose solution yields directly the constitutive parameters, providing that the response is sensitive to all of them.

A key issue of the VFM is the selection of the virtual fields. In the recent past significant efforts have been put into this topic which has led to the following developments:

- the automatic construction of virtual fields (Grédiac et al., 2002);
- the piecewise construction of virtual fields (Toussaint et al., 2006);
- the selection of virtual fields that minimise the sensitivity of the VFM to noisy data (Avril and Pierron, 2007; Avril et al., 2004b).

### 2.3.4 Conclusions

Mechanical tests generating heterogeneous and multiaxial strain fields can be carried out for the characterisation of the several constitutive parameters of anisotropic materials. The unnotched Iosipescu test (test 1 in Table 2.2) has been chosen in this work. It consists in loading a straight rectangular specimen using the Iosipescu fixture. In contrast with the standard Iosipescu shear test (ASTM D5379, 1993), suitable for the characterisation of the shear behaviour of anisotropic materials, this test has been designed for the purpose of the identification of all the in-plane orthotropic properties. A heterogeneous strain field can be obtained over the central part of the specimen by eliminating the V-notches from the classical geometry of the specimen, and choosing, judiciously, the length between the inner supports ( $L$ ) and the grain (fibre) angle ( $\theta$ ).

For this test, however, a specific identification method, dealing with full-field kinematic measurements, is needed for the material characterisation, since no closed-form solution exists in this case. A few identification methods have been proposed in the literature for solving this type of problem. In this work the so-called virtual fields method has been chosen. Up to now, it has been successfully applied in the case of linear elastic anisotropy. This method has to be coupled with full-field displacement measurements provided by the grid method, for retrieving the wood stiffness properties from the unnotched Iosipescu test.

# Chapter 3

## Inverse identification approach

### 3.1 Introduction

The aim of this chapter is to present the material characterisation approach used in this work for the simultaneous identification of the longitudinal-radial ( $LR$ ) stiffness parameters of *P. pinaster* wood from a single test. The procedure is based on the virtual fields method (VFM) coupled with full-field displacement measurements provided by the grid method. All the involved in-plane orthotropic properties are identified using a single rectangular specimen loaded in the Iosipescu fixture.

### 3.2 Unnotched Iosipescu test

The mechanical test proposed in this work was the unnotched Iosipescu test (Figure. 3.1) (§ 2.3.2). This test has been designed in such a way that a complex and inhomogeneous strain field is generated across the central part of the specimen. This mechanical response can be achieved by removing the V-notches from the classical geometry of the Iosipescu specimen, such that all the in-plane strain components can eventually contribute to the material deformation thanks to the shear/bending/compression stress distribution applied by the fixture. A  $L \times W$  mm<sup>2</sup> gauge area was considered (Figure. 3.1), because the magnitude of the strain gradients are expected to be more important in this region and the length to width ratio is not too enhanced with regard to the typical format of digital camera sensors.

In order to balance out the contribution of the different strain field components, and consequently enhance the identifiability of all the in-plane constitutive parameters, an optimisation study can be undertaken for calibrating the design parameters consisting of the length between the inner supports ( $L$ ) and the grain (fibre) angle ( $\theta$ ) (Figure. 3.1). This optimisation scheme will be presented in Chapter 4.

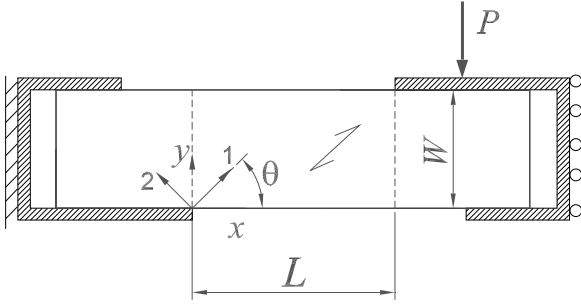


Figure 3.1: Schematic representation of the unnotched Iosipescu test.  $x - y$  is the specimen coordinate system;  $1 - 2$  is the material coordinate system.

### 3.3 Grid method: principle

The grid method provides the measurement of the in-plane full-field displacements,  $u_x$  and  $u_y$ , by means of the analysis of the deformation of a grid, which is assumed to be perfectly bonded to the specimen surface. This grid consists of periodic bright and dark lines and is characterised by a spatial frequency vector  $\mathbf{F}$ . This vector is orthogonal to the grid lines, has an amplitude equal to the inverse of the pitch of the grid ( $p$ ) and its unit is lines/mm. Thus, for a grid made of vertical lines (parallel to the  $\mathbf{j}$  direction) the spatial frequency vector writes  $\mathbf{F}(1/p, 0)$  (Figure 3.2(a)), and, reversely, with a horizontal grid this vector writes  $\mathbf{F}(0, 1/p)$ . The component of the displacement along the direction defined by the spatial frequency vector is actually measured. Thus, a grid with vertical lines provides the measurement of  $u_x$ , whereas a horizontal one provides  $u_y$ . Both components of the displacement field must be measured if all the in-plane strain fields are to be derived. In this case, a crossed (horizontal and vertical) grid can be used and a digital filtering process applied afterwards in order to obtain two separate images of the grid with, respectively, vertical and horizontal lines (§ 3.4.1).

An electronic camera of  $H \times V$  pixel resolution is employed for image recording. The camera-lens optical system is set in order to face the plane of the grid and it is supposed to be motionless during the specimen deformation. Therefore, the pixels of the camera sensor represent a fixed spatial array imaging the grid, in such a way that a given pixel,  $M'(\xi, \eta)$ , will be sensitive to the light coming from its conjugate geometrical source point in the grid,  $M(x, y)$ , with  $(\xi, \eta)$  and  $(x, y)$  representing the cartesian coordinate systems associated to the sensor and grid planes, respectively (Figure 3.2(a)). Accordingly, the light intensity recorded by the image system is given by:

$$I(x_h, y_v) = I_0(x_h, y_v) \{1 + \gamma(x_h, y_v) f [2\pi \mathbf{F} \cdot \mathbf{R}(x_h, y_v)]\}, \quad (3.1)$$

where,

- $I_0(x_h, y_v)$  is the local intensity bias;
- $\gamma(x_h, y_v) \in [0, 1]$  is the local contrast of the grid pattern;
- $f$  a  $2\pi$ -periodic continuous function describing the light intensity (grid) pattern and

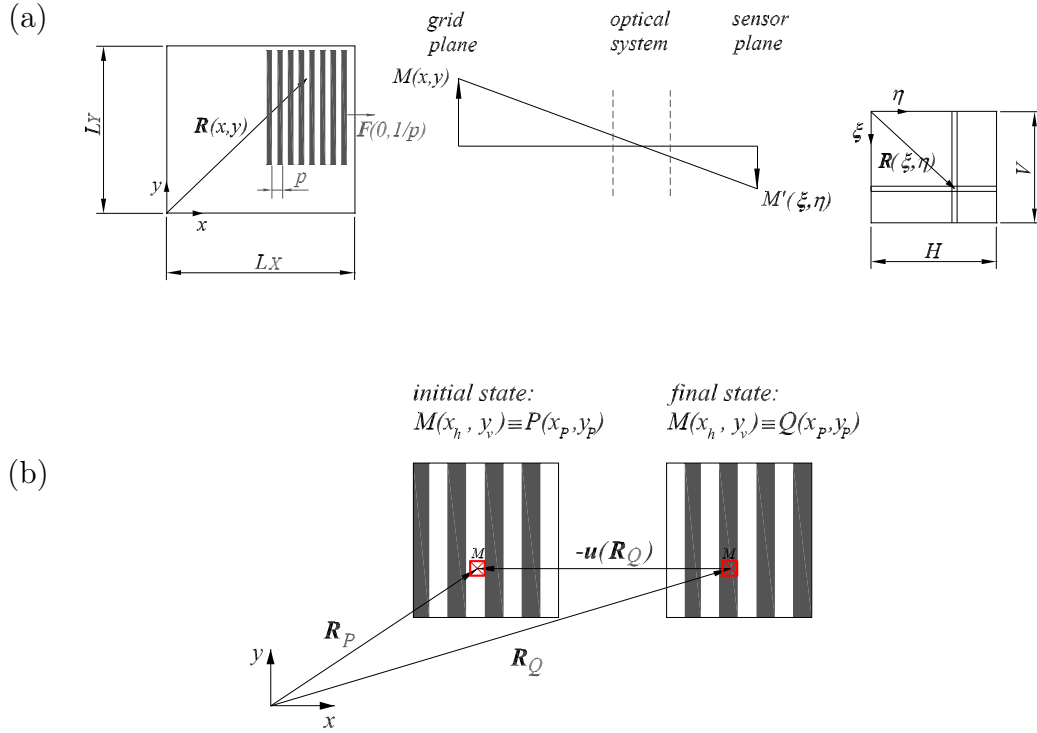


Figure 3.2: (a) Schematic representation of the grid principle: (a) imaging system (b) grid deformation.

whose argument is the optical phase,  $\phi(x_h, y_v) = 2\pi \mathbf{F} \cdot \mathbf{R}$ ;

- $\mathbf{R}(x_h, y_v)$  is the position vector of a given point of the grid, with  $0 \leq x_h \leq L_X$ ,  $0 \leq y_v \leq L_Y$ ,  $1 \leq h \leq H$ ,  $1 \leq v \leq V$  and where  $L_X \times L_Y$  (mm<sup>2</sup>) are the dimensions of the field of view (Figure 3.2(a));
- $(\cdot)$  denotes the scalar product of vectors.

At each state of the specimen, the phase field,  $\phi(x_h, y_v)$ , can be computed by solving Eq. (3.1) through a suitable phase-evaluation algorithm (§ 3.4.1). In Eq. (3.1), the invariability of the light intensity with time is assumed.

Let us now consider the problem of the grid deformation when the specimen is subjected to an external in-plane loading. First, two given points are defined, a fixed geometrical point  $M(x_h, y_v)$ , imaged by a given pixel of the camera sensor, and a physical point  $P(x_P, y_P)$  of the grid. These points are assumed to be coincident in the initial (undeformed) state of the specimen (Figure 3.2(b)). Owing to the application of the external load the grid/specimen will be deformed. Thus, in the final configuration of the specimen, the spatial point  $M(x_h, y_v)$  will now be coincident with a new point, say  $Q(x_Q, y_Q)$ , of the grid (Figure 3.2(b)). Therefore, due to the relative deformation between the final

and initial specimen configurations, a change of phase of the periodic function  $f$  at point  $M(x_h, y_v)$  is introduced equal to (Eq. 3.1):  $\Delta\phi(\mathbf{R}_M) = 2\pi\mathbf{F} \cdot (\mathbf{R}_P - \mathbf{R}_Q) = -2\pi\mathbf{F} \cdot \mathbf{u}(\mathbf{R}_Q)$ , where  $-\mathbf{u}(\mathbf{R}_Q)$  represents the inverse displacement of point  $Q$ . Furthermore, if the small perturbation assumption is valid, the inverse and direct displacement can be considered equivalent:  $\mathbf{u}(\mathbf{R}_Q) \simeq \mathbf{u}(\mathbf{R}_P)$ . The in-plane components of the displacement field can then be determined from the difference of phase, between undeformed and deformed states, according to the following relationship:

$$u_\beta(x_h, y_v) = -\frac{p}{2\pi}\Delta\phi_\beta(x_h, y_v), \quad (3.2)$$

where  $\beta = x$  or  $y$ , respectively for the horizontal (grid of vertical lines) or vertical (grid of horizontal lines) components of the displacement. The factor of proportionality in Eq. (3.2) represents the inverse of the sensitivity term:  $S = 2\pi/p$  (rad/mm) (§ 2.1.2). In the case of small displacements, parasitic effects on the measurement of the displacement fields introduced by geometric aberrations of the lens in the image formation, are automatically cancelled out by the subtraction of the two phase fields,  $\Delta\phi_\beta(x_h, y_v)$ , determined from the grid images before and after deformation.

## 3.4 Image processing

The phase and displacement fields have to be computed from the grid images recorded during the specimen deformation. Moreover, the strain field must be determined by numerical denoising and differentiation of the measured displacement field. This image processing scheme was performed following the flowchart presented in Figure 3.3, through in-house functions developed in Matlab®.

### 3.4.1 Phase-evaluation algorithm

In the first step of the image processing, the image of the crossed grid,  $[I(x, y)]$ , is separated into two different images, one with just the vertical lines of the grid,  $[I_x(x, y)]$ , and the other with the horizontal ones,  $[I_y(x, y)]$  (Figure 3.4). This is achieved by a filtering process, to be applied in the direction perpendicular to the lines to be suppressed, using a triangular windowed kernel of length equal to  $2N - 1$  pixels, where  $N$  is the integer number of pixels chosen for sampling one period of the grid (spatial phase-shifting method) (Surrel, 2004b). Any further processing is then separately performed with each set of images. This leads to the measurement of the  $u_x(x, y)$  and  $u_y(x, y)$  components of the displacement field through phase evaluation and scaling procedures.

In the grid method the kinematic quantity of interest (the displacement) is encoded in the change of phase of the periodic function describing the grid pattern (Eqs. 3.1 and

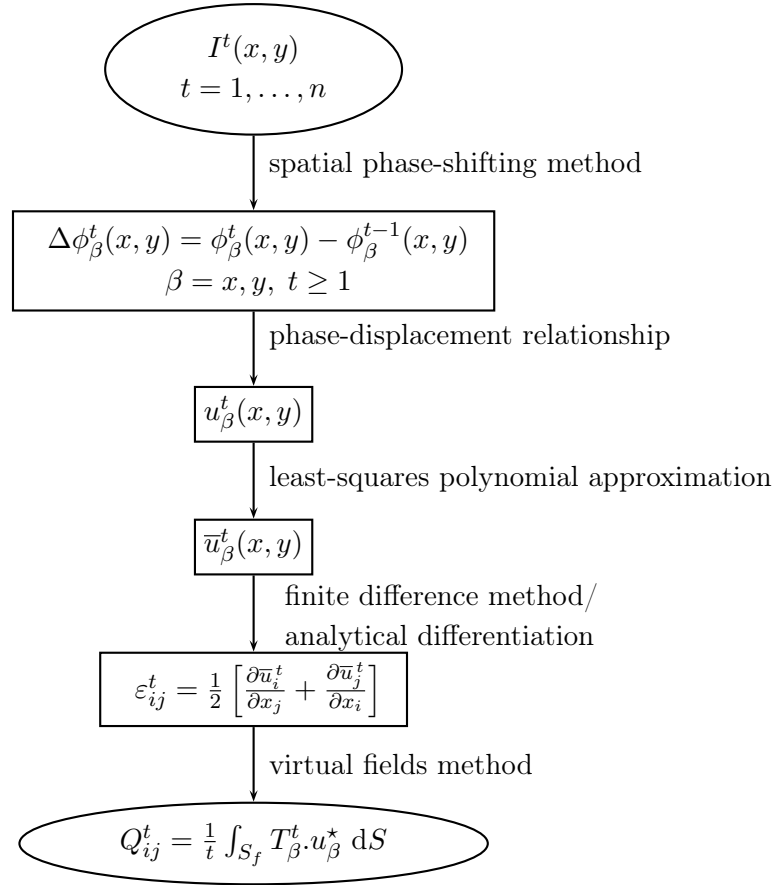


Figure 3.3: Image processing and identification flowchart.

3.2). Several algorithms have been proposed in the literature for the evaluation of the phase of fringes or grid images (Dorrío and Fernández, 1999). Among them, the spatial phase-shifting method with the windowed discrete Fourier transform (W-DFT) algorithm has been successfully applied to the phase evaluation from grid images (Surrel, 1996, 1999). In this technique a shift,  $\delta = 2\pi/N$ , is added to the phase map of a single image,  $\phi_\beta(x, y)$  ( $\beta = x, y$ ), in order to generate a sequence of  $M = 2N - 1$  intensity samples:  $I_{\beta_k} = I_\beta(\phi_\beta + k\delta)$ , where  $k \in \{0 \dots, M-1\}$ . This is achieved by shifting a reading window of one pixel in the appropriate direction (*i.e.*, by reading adjacent pixel intensities). For  $N = 4$ , the phase evaluation from the W-DFT algorithm is achieved by combining the set of intensity samples according to the following linear combination (Surrel, 1999, p. 66):

$$\phi_\beta(x, y) = \arctan \left[ \frac{(I_{\beta_0} - I_{\beta_6}) - 3(I_{\beta_2} - I_{\beta_4})}{2(I_{\beta_1} + I_{\beta_5}) - 4I_{\beta_3}} \right] \quad (\beta = x, y). \quad (3.3)$$

This algorithm has the advantage of cancelling or minimising some systematic errors introduced in the phase evaluation when using the grid method (Surrel, 1996, 1999):

- Although in the phase-evaluation method the periodic intensity profile of the grid

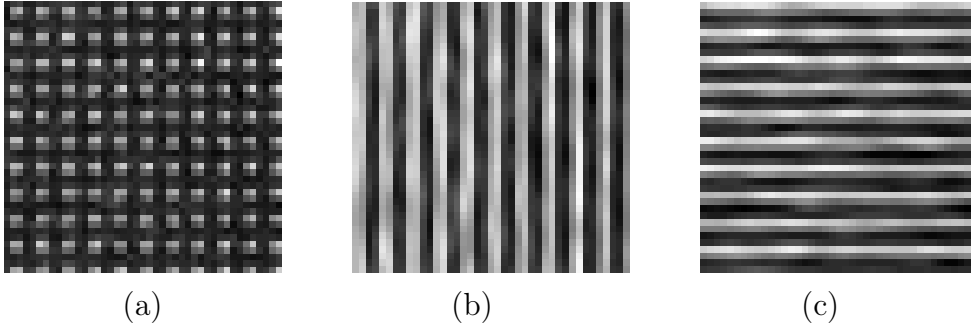


Figure 3.4: Images of the: (a) crossed grid,  $I(x, y)$ ; (b) vertical lines grid,  $I_x(x, y)$ ; (c) horizontal lines grid,  $I_y(x, y)$ .

is assumed to be sinusoidal, because of the abrupt transition between the bright and dark contrasted lines, its distribution can be rather close to a square signal. Accordingly, the function  $f$  in Eq. (3.1) can be described by a Fourier series that is not limited to its fundamental frequency term. High-order harmonics will be seen in the phase maps as parasitic waves, which can disturb the measurement of the displacement field. The presence of high-order harmonics is mainly dependent on the number of pixels ( $N$ ) chosen for sampling each period of the grid. However, in practice, several phenomena can introduce further deviations from a pure sinusoidal profile, for instance: (1) when using a highly contrasted image; (2) when reaching the saturation threshold of the CCD sensor at the pixels with maximum light intensity; (3) when imaging a grid that has a white and black unbalanced distributions within a period. Although the presence of high-order harmonics can disturb the phase field computation, the W-DFT algorithm filters out the harmonics up to the  $N - 2$  order;

- in practice, the sampling frequency requirement of an integer number of pixels ( $N$ ) per period cannot be kept exactly constant over the whole region covered by the grid because, for instance: (1) the geometrical aberrations of the lens; (2) the deformation of the grid during the test. Nevertheless, the W-DFT algorithm is insensitive to linear phase-step errors, hence “self-calibrated”;
- the background intensity ( $I_0$ ) and the contrast of the grid pattern ( $\gamma$ ) (Eq. 3.1) can vary across the region of interest, for instance, due to a non-uniform illumination or to the quality of the grid transfert. However, these effects are minimised when extracting the phase maps using the W-DFT algorithm because of its local operation.

One advantage of the spatial phase-shifting method is that a single image is required for the phase computation. In this case the spatial resolution can be considered equal to the pitch of the grid (sampled by  $N$  pixels) – it should be noticed that even if a total of  $2N - 1$  pixels are used for the phase evaluation with the W-DFT algorithm, a higher weight is given to the central pixels than the peripheral ones.

### 3.4.2 Strain field reconstruction

Since the grid method provides the measurement of the displacement fields, an additional numerical denoising and differentiation procedure is needed to calculate the corresponding strain field components (Figure 3.3), according to the well known strain-displacement relationship for small deformation:

$$\begin{aligned}\varepsilon_1(x_p, y_q) &= \frac{\partial \bar{u}_x(x_p, y_q)}{\partial x} \\ \varepsilon_2(x_p, y_q) &= \frac{\partial \bar{u}_y(x_p, y_q)}{\partial y} \\ \varepsilon_6(x_p, y_q) &= \frac{\partial \bar{u}_x(x_p, y_q)}{\partial y} + \frac{\partial \bar{u}_y(x_p, y_q)}{\partial x}\end{aligned}\quad (3.4)$$

where  $\varepsilon_\beta$  ( $\beta = 1, 2, 6$ ) are the engineering strain components,  $\bar{u}_x$  ( $\bar{u}_y$ ) is the approximated  $x$  ( $y$ ) component of the displacement field, and  $(x_p, y_q)$  represents the discrete coordinates over the gauge area where an independent measurement is performed. Several strategies can be used for the computational implementation of Eq. (3.4):

- the finite difference method: it consists of defining the derivative at a given point (*e.g.*, a pixel) as the slope of a line obtained by least-squares fitting over a length of  $2a + 1$  neighboring data points. In order to enhance the signal to noise ratio, the derivative can be calculated as the gradient of a plane adjusted over a kernel of  $2a + 1$  points in a convolution approach (Avril et al., 2004a; Kajberg and Lindkvist, 2004). This procedure is repeated in the relevant  $x$  (column) and  $y$  (row) directions of the field (matrix). The value of  $a$  determines the level of filtering of the experimental data. It should be chosen as a compromise between the resolution (large value of  $a$ ) and the spatial resolution (small value of  $a$ ), by taking into account the level of noise and displacement gradients expected over the region of interest;
- global 2D approximation: it consists in adjusting a generic function, *e.g.*, a polynomial, to the array (field) of raw (unfiltered) displacement data by a least-squares approximation scheme (Cordero and Roth, 2005; Pannier et al., 2006). The strain field can then be straightforwardly deduced by differentiating the basis functions;
- piecewise finite element approximation: it consists in determining the nodal displacements of a mesh defined over the region of interest by least-squares regression using a finite element shape functions as the basis functions (Avril and Pierron, 2007). The strain field can then be obtained from the nodal displacements by the derivatives of the shape functions.

### 3.4.2.1 Least-squares polynomial approximation

The global approximation using least-squares polynomial regression was hereafter chosen. Firstly, the experimental displacements,  $u_\beta(x_p, y_q)$ , were approximated by a 2D polynomial function,  $\bar{u}_\beta(x_p, y_q)$ , according to the following minimization problem (Figure 3.3):

$$\min_{\{a_{\beta_{ij}}\}} \sum_{p=1}^P \sum_{q=1}^Q w(x_p, y_q) [u_\beta(x_p, y_q) - \bar{u}_\beta(x_p, y_q)]^2 \quad (3.5a)$$

with

$$\bar{u}_\beta(x_p, y_q) = \sum_{i=0}^d \sum_{j=0}^d a_{\beta_{ij}} x_p^i y_q^j \quad (i + j < d) \quad (3.5b)$$

where  $P = H/N$  and  $Q = V/N$  are the total number of data points through, respectively, the  $x$  (column) and  $y$  (row) coordinates,  $w(x_p, y_q)$  represents a weighting mask (binary image) defining the validity of each pixels,  $a_{\beta_{ij}}$  ( $\beta = x, y$ ) are the unknown polynomial coefficients, and  $d$  is the degree of the polynomial (the same in  $x$  and  $y$ ). Using a matrix notation, a general solution of Eq. (3.5) can be written as:

$$[X]\{a_\beta\} = \{U_\beta\} \quad (3.6a)$$

where  $[X]_{[(P \times Q) \times ((d+1)(d+2)/2)]}$  is the Vandermonde matrix,  $\{a_\beta\}_{[((d+1)(d+2)/2) \times 1]}$  a vector listing the polynomial coefficients and  $\{U_\beta\}_{[(P \times Q) \times 1]}$  a vector listing the measured data points, *i.e.*:

$$\{a_\beta\} = \langle a_{\beta_{00}}, a_{\beta_{10}}, \dots, a_{\beta_{d0}}, a_{\beta_{01}}, a_{\beta_{11}}, \dots, a_{\beta_{d1}}, \dots, a_{\beta_{0d}}, a_{\beta_{1d}}, \dots, a_{\beta_{dd}} \rangle \quad (3.6b)$$

with,

$$[X] = \begin{bmatrix} 1 & x_1 & \cdots & x_1^d & y_1 & x_1 y_1 & \cdots & x_1^d y_1 & \cdots & y_1^d & x_1 y_1^d & \cdots & x_1^d y_1^d \\ 1 & x_1 & \cdots & x_1^d & y_2 & x_1 y_2 & \cdots & x_1^d y_2 & \cdots & y_2^d & x_1 y_2^d & \cdots & x_1^d y_2^d \\ \vdots & & & & & & & \vdots & & & & & \vdots \\ 1 & x_1 & \cdots & x_1^d & y_Q & x_1 y_Q & \cdots & x_1^d y_Q & \cdots & y_Q^d & x_1 y_Q^d & \cdots & x_1^d y_Q^d \\ \dots & \dots \\ 1 & x_P & \cdots & x_P^d & y_1 & x_P y_1 & \cdots & x_P^d y_1 & \cdots & y_1^d & x_P y_1^d & \cdots & x_P^d y_1^d \\ \vdots & & & & & & & \vdots & & & & & \vdots \\ 1 & x_P & \cdots & x_P^d & y_Q & x_P y_Q & \cdots & x_P^d y_Q & \cdots & y_Q^d & x_P y_Q^d & \cdots & x_P^d y_Q^d \end{bmatrix} \quad (3.6c)$$

and,

$$\{U\} = \langle u_\beta(x_1, y_1), u_\beta(x_1, y_2), \dots, u_\beta(x_1, y_Q), \dots, u_\beta(x_P, y_Q) \rangle^T \quad (3.6d)$$

The reliability of each datum point can be weighed by operating directly on the elements

of  $[X]$  and  $\{U_\beta\}$ .

The value of the polynomial degree ( $d$ ) affects directly the accuracy of the approximation and consequently the final results (the parameter identification). Two procedures may be used for choosing the degree of the polynomial. On the one hand, the residuals obtained from the difference between approximated and raw displacement fields can be evaluated for a given range of degrees. The best polynomial degree should eventually minimise the residual maps. This assumes that noise is uncorrelated from one pixel to another and the weighting function,  $w(x_p, y_q)$ , is set to one for all points where data are available. On the other hand, a study can be undertaken for evaluating directly the effect of the polynomial degree on the stiffness identification results.

For a given degree of the polynomial, the solution of the least-squares regression (Eq. 3.5) is affected both by the presence of noise in the measurements and by errors in the phase evaluation. In order to deal with this problem, a calibration procedure of the weighting matrix,  $w(x_p, y_q)$ , is proposed. Initially, this matrix is defined such that a uniform weight equal to one is prescribed to all pixels, excluding the ones outside the region of interest (crop operation) or associated to missing data (often due to locally non-transferred grid lines) (Figure 3.5(a)). A first approximation is then performed by solving Eq. (3.5). The residual matrix resulting from the difference between approximated and measured displacement fields is calculated, along with its standard deviation. A new mask is then defined such that all pixels whose absolute residual value exceeds twice the computed standard deviation are discarded by putting zero in the corresponding position of  $w(x_p, y_q)$  (Figure 3.5(b)). This procedure is efficient in getting rid of erroneous pixels, which appears namely at the edges of the grid image and at non-transferred grid regions where the phase is erroneously evaluated. In a second step, a new set of polynomial coefficients,  $a_{\beta_{ij}}$ , is determined using the updated weighting matrix. Finally, the in-plane strain field components are numerically determined from the approximated displacements either by analytical differentiation or by finite differences.

This approach is particularly suitable when the signal and noise frequencies are well separated, since it will work as a low-pass filter. Besides, it may be also efficient in eliminating some parasitic fringes associated with higher harmonics, which can be obtained in the phase-evaluation (§ 3.4.1). As far as derivatives are concerned, the polynomial approximation is better adapted when the spatial variation of the displacement data across the region of interest is relatively smooth. Indeed, in this case, a lower degree may be accurate (Moulart et al., 2006), avoiding the polynomial fluctuations around the original data points (namely at the edges) typically occurring when higher degrees are used (Bruno, 2007; Segall and Sipics, 2004). In summary, the main advantages of the least-squares polynomial approximation are: (1) the simplicity of the approach; (2) the possibility to give a different weight to each pixel value and therefore discarding erroneous pixels (where data are too noisy or missing); (3) the interpolation or extrapolation of

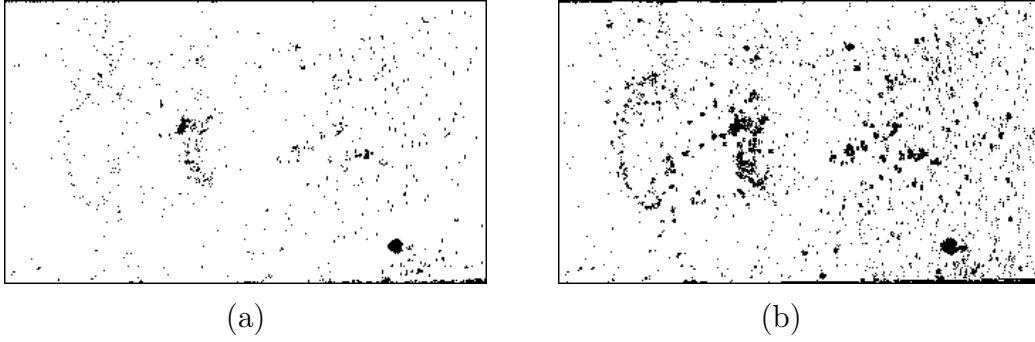


Figure 3.5: Weighting matrix: (a) first iteration (3.5% of invalid pixels over the region of interest); (b) second iteration (8.3% of invalid pixels over the region of interest).

the displacement value on pixels where no datum is initially available (*e.g.*, because of defects on the grid transfer). However, some drawbacks are: (1) the instability on the reconstruction of the strain fields, namely at the edges of the region of interest, when differentiating higher-degree polynomials; (2) the propagation of local errors over the whole field because of the global reconstruction scheme of the polynomial basic function.

## 3.5 Stiffness identification by the virtual fields method

### 3.5.1 Principle

Let us consider a rectangular plate submitted to the unnotched Iosipescu test depicted in Figure 3.6. The problem to be solved is the simultaneous identification of the unknown elastic parameters involved in the material mechanical response. It is assumed that both the resultant applied load ( $P$ ) – measured by the load cell of the testing machine – and the strain field across the surface of interest – *e.g.*, determined from the displacement field measured by the grid method – are known. Moreover, the specimen is assumed to be under a plane stress state.

The VFM is an identification strategy aimed at solving this inverse problem (§ 2.3.3). It is based on the principle of virtual work (PVW). For the plane stress problem and in absence of body forces, the PVW can be written as:

$$\int_S \sigma_i \varepsilon_i^* \, dS = \frac{1}{t} \int_{S_f} T_\beta(M, n_\beta) u_\beta^*(M) \, dS \quad (i = 1, 2, 6 \text{ and } \beta = x, y) \quad (3.7)$$

where  $\sigma_i$  is the stress field,  $\varepsilon_i^*$  the virtual strain field,  $S$  the exterior surface of interest of the plate,  $t$  the thickness of the plate,  $T_\beta(M, n_\beta)$  the distribution of external tractions applied over  $S_f$  ( $M$  is any point of this surface and  $n_\beta$  the outward normal vector at point  $M$ ) and  $u_\beta^*$  the virtual displacement field.

A macroscopic constitutive model of the material must be assumed at this stage. In

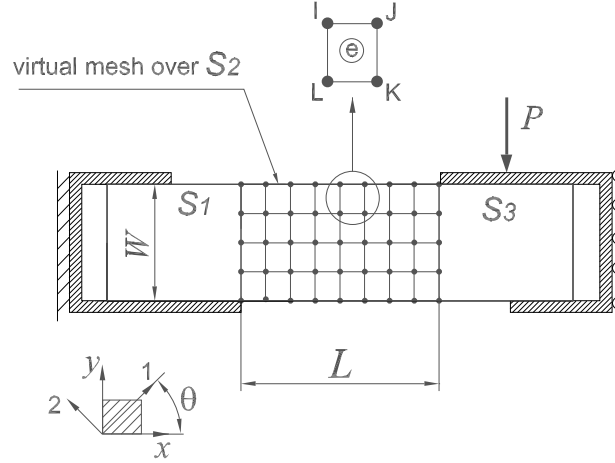


Figure 3.6: Schema of the unnotched Iosipescu test illustrating the application of the virtual fields method.  $x - y$  and  $1 - 2$  are the specimen and material coordinate systems, respectively.

this study, clear wood is modelled through an anisotropic linear elastic model (§ 1.2.2), which can be written in the  $(L, R) \equiv (1, 2)$  plane of symmetry as:

$$\begin{Bmatrix} \sigma_1 \\ \sigma_2 \\ \sigma_6 \end{Bmatrix} = \begin{bmatrix} Q_{11} & Q_{12} & 0 \\ Q_{12} & Q_{22} & 0 \\ 0 & 0 & Q_{66} \end{bmatrix} \begin{Bmatrix} \varepsilon_1 \\ \varepsilon_2 \\ \varepsilon_6 \end{Bmatrix} \quad (3.8a)$$

or, in contracted index notation,

$$\sigma_i = Q_{ij}\varepsilon_j \quad (3.8b)$$

where the four  $Q_{ij}$ 's are the material stiffness parameters. Substituting the constitutive equation (Eq. 3.8) into the PVW (Eq. 3.7), and assuming a macroscopically homogenous material, a new equation can be obtained:

$$Q_{ij} \int_S \varepsilon_j \varepsilon_i^* dS = \frac{1}{t} \int_{S_f} T_\beta(M, n_\beta) u_\beta^*(M) dS \quad (3.9)$$

involving the  $Q_{ij}$  unknown parameters, the  $\varepsilon_j$  actual strain components over  $S$ , the  $T_\beta$  applied tractions and the  $u_\beta^*$  and  $\varepsilon_i^*$  virtual fields. The above Eq. (3.9) is verified for any kinematically admissible (K.A.) virtual field  $(u_\beta^*, \varepsilon_i^*)$ , *i.e.*, continuous and differentiable. At this stage, Eq. (3.9) is rewritten with, at least, as many independent K.A. virtual fields as there are unknown parameters. This procedure yields a linear system of equations in the form of:

$$[P]\{Q\} = \{R\} \quad (3.10a)$$

where,

$$[P] = \begin{bmatrix} \int_S \varepsilon_1 \varepsilon_1^{*(1)} dS & \int_S \varepsilon_2 \varepsilon_2^{*(1)} dS & \int_S \left( \varepsilon_2 \varepsilon_1^{*(1)} + \varepsilon_1 \varepsilon_2^{*(1)} \right) dS & \int_S \varepsilon_6 \varepsilon_6^{*(1)} dS \\ \int_S \varepsilon_1 \varepsilon_1^{*(2)} dS & \int_S \varepsilon_2 \varepsilon_2^{*(2)} dS & \int_S \left( \varepsilon_2 \varepsilon_1^{*(2)} + \varepsilon_1 \varepsilon_2^{*(2)} \right) dS & \int_S \varepsilon_6 \varepsilon_6^{*(2)} dS \\ \int_S \varepsilon_1 \varepsilon_1^{*(3)} dS & \int_S \varepsilon_2 \varepsilon_2^{*(3)} dS & \int_S \left( \varepsilon_2 \varepsilon_1^{*(3)} + \varepsilon_1 \varepsilon_2^{*(3)} \right) dS & \int_S \varepsilon_6 \varepsilon_6^{*(3)} dS \\ \int_S \varepsilon_1 \varepsilon_1^{*(4)} dS & \int_S \varepsilon_2 \varepsilon_2^{*(4)} dS & \int_S \left( \varepsilon_2 \varepsilon_1^{*(4)} + \varepsilon_1 \varepsilon_2^{*(4)} \right) dS & \int_S \varepsilon_6 \varepsilon_6^{*(4)} dS \end{bmatrix} \quad (3.10b)$$

and,

$$\{Q\} = \langle Q_{11}, Q_{22}, Q_{12}, Q_{66} \rangle^T \quad (3.10c)$$

and,

$$\{R\} = \frac{1}{t} \langle \int_{S_f} T_\beta u_\beta^{*(1)} dS, \int_{S_f} T_\beta u_\beta^{*(2)} dS, \int_{S_f} T_\beta u_\beta^{*(3)} dS, \int_{S_f} T_\beta u_\beta^{*(4)} dS \rangle^T. \quad (3.10d)$$

where  $(u_\beta^{*(\alpha)}, \varepsilon_i^{*(\alpha)})$  with  $\alpha = 1, 2, 3$  and 4 are the four independent selected virtual fields. Finally, the system of equations (3.10) can be solved for the stiffness vector  $\{Q\}$ , providing that the virtual fields are selected so that  $[P]$  can be inverted and that all the unknowns are involved in the mechanical response. The latter requirement is fulfilled when the strain field is heterogeneous and their components smoothly balanced across the gauge area. Because of the integral form of the PVW, this method is well adapted for processing full-field measurement obtained by a suitable optical method.

A key issue of the VFM, however, is the selection of the four virtual fields, among a large set of possibilities, since they directly affect the degree of independence of the equations in the system (3.10) and therefore the invertibility of matrix  $[P]$ . Although these virtual fields can be selected by hand in a trial-and-error approach (Pierron and Grédiac, 2000), a general numerical procedure for their expression and selection was proposed by (Grédiac et al., 2002). The advantage is that a large domain of search of the virtual fields can be explored, enhancing the robustness of the method. Moreover, expressions for the direct identification of the stiffness parameters can be obtained because the virtual fields can be built up so that matrix  $[P]$ , in Eqs. (3.10), is reduced to the identity matrix  $[I]$ . Such virtual fields, called *special* virtual fields  $(\hat{u}_\beta^*, \hat{\varepsilon}_i^*)$ , can be expanded over a basis of functions (polynomials, for instance), either over the whole region of interest (Grédiac et al., 2002) or in a piecewise manner as in the finite element method (Toussaint et al., 2006). A constrained optimisation scheme was proposed by (Avril et al., 2004b) in order to select the special virtual fields that minimise the sensitivity of the VFM to noise (maximum likelihood solution). Such strategy was found to significantly improve the robustness of the method. The general procedure employed in this work for determining the special virtual fields is briefly described in the following.

### 3.5.2 Determination of the special virtual fields

#### 3.5.2.1 Piecewise expansion

According to the piecewise approach of the VFM (Toussaint et al., 2006), the special virtual fields are defined from the nodal displacements of a *virtual* mesh built in the region of interest ( $S_2$ ) as shown in Figure 3.6. In this case, over a given element ( $e$ ) of the virtual mesh, the  $x$  and  $y$  components of the virtual displacement field can be written as:

$$\begin{aligned}\widehat{u}_x^{*(e)}(x, y) &= \langle N_I(x, y) \ 0 \ N_J(x, y) \ 0 \ N_K(x, y) \ 0 \ N_L(x, y) \ 0 \rangle \{\widetilde{U}^{*(e)}\} \\ &= \langle N_x^{(e)}(x, y) \rangle \{\widetilde{U}^{*(e)}\} \\ \widehat{u}_y^{*(e)}(x, y) &= \langle 0 \ N_I(x, y) \ 0 \ N_J(x, y) \ 0 \ N_K(x, y) \ 0 \ N_L(x, y) \rangle \{\widetilde{U}^{*(e)}\} \\ &= \langle N_y^{(e)}(x, y) \rangle \{\widetilde{U}^{*(e)}\}\end{aligned}\quad (3.11)$$

with,

$$\{\widetilde{U}^{*(e)}\} = \langle \widetilde{u}_x^*(x_I, y_I), \widetilde{u}_y^*(x_I, y_I), \dots, \widetilde{u}_x^*(x_L, y_L), \widetilde{u}_y^*(x_L, y_L) \rangle^T$$

where  $\widetilde{u}_\beta^*(x_n, y_n)$  (with  $\beta = x, y$  and  $n = I, J, K, L$ ) are the nodal virtual displacements and  $N_n(x, y)$  are the classical 4-nodes bilinear shape functions of the quadrangular finite element:

$$N_n = \frac{1}{4}(1 + \xi_n \xi)(1 + \eta_n \eta) \quad (3.12)$$

in which  $\xi_n = \pm 1$  and  $\eta_n = \pm 1$  are the normalised coordinates at node  $n$ . Referring to Eqs. (3.4) and (3.11), the in-plane components of the strain field can be computed from the nodal displacements by:

$$\begin{aligned}\widehat{\varepsilon}_1^{*(e)}(x, y) &= \frac{\partial \langle N_x^{(e)}(x, y) \rangle}{\partial x} \{\widetilde{U}^{*(e)}\} = \langle B_1^{(e)}(x, y) \rangle \{\widetilde{U}^{*(e)}\}, \\ \widehat{\varepsilon}_2^{*(e)}(x, y) &= \frac{\partial \langle N_y^{(e)}(x, y) \rangle}{\partial y} \{\widetilde{U}^{*(e)}\} = \langle B_2^{(e)}(x, y) \rangle \{\widetilde{U}^{*(e)}\}, \\ \widehat{\varepsilon}_6^{*(e)}(x, y) &= \left( \frac{\partial \langle N_x^{(e)}(x, y) \rangle}{\partial y} + \frac{\partial \langle N_y^{(e)}(x, y) \rangle}{\partial x} \right) \{\widetilde{U}^{*(e)}\} \\ &= \langle B_6^{(e)}(x, y) \rangle \{\widetilde{U}^{*(e)}\}.\end{aligned}\quad (3.13)$$

According to this development and after assembling all the elementary matrices:

$$\langle B_i(x, y) \rangle = \sum_e \langle B_i^{(e)}(x, y) \rangle \quad (i = 1, 2, 6), \quad \{\tilde{U}^*\} = \sum_e \{\tilde{U}^{*(e)}\} \quad (3.14)$$

Eqs. (3.10) may be written as:

$$Q_{11}I_{11}^{(\alpha)} + Q_{22}I_{22}^{(\alpha)} + Q_{12}I_{12}^{(\alpha)} + Q_{66}I_{66}^{(\alpha)} = R^{(\alpha)} \quad (\alpha = 1, 2, 3 \text{ and } 4) \quad (3.15)$$

where,

$$\begin{aligned} I_{11}^{(\alpha)} &= \frac{S}{PQ} \sum_{p=1}^P \sum_{q=1}^Q \varepsilon_1(x_p, y_q) \langle B_1(x_p, y_q) \rangle \{\tilde{U}^{*(\alpha)}(x_p, y_q)\} \\ I_{22}^{(\alpha)} &= \frac{S}{PQ} \sum_{p=1}^P \sum_{q=1}^Q \varepsilon_2(x_p, y_q) \langle B_2(x_p, y_q) \rangle \{\tilde{U}^{*(\alpha)}(x_p, y_q)\} \\ I_{12}^{(\alpha)} &= \frac{S}{PQ} \sum_{p=1}^P \sum_{q=1}^Q (\varepsilon_1(x_p, y_q) \langle B_2(x_p, y_q) \rangle + \varepsilon_2(x_p, y_q) \langle B_1(x_p, y_q) \rangle) \{\tilde{U}^{*(\alpha)}(x_p, y_q)\} \\ I_{66}^{(\alpha)} &= \frac{S}{PQ} \sum_{p=1}^P \sum_{q=1}^Q \varepsilon_6(x_p, y_q) \langle B_6(x_p, y_q) \rangle \{\tilde{U}^{*(\alpha)}(x_p, y_q)\} \end{aligned}$$

and,

$$R^{(\alpha)} = \frac{1}{t} \sum_{a=1}^{n_f} \left( T_x(x_a, y_a) \cdot \tilde{U}_x^{*(\alpha)}(x_a, y_a) + T_y(x_a, y_a) \cdot \tilde{U}_y^{*(\alpha)}(x_a, y_a) \right).$$

### 3.5.2.2 Prescribed conditions

The special virtual fields must fulfilled some conditions (Grédiac et al., 2002). Generically, they must be K.A, *i.e.*, continuous and differentiable (the choice of the shape functions already ensures the continuity and differentiation requirements over the virtual mesh). Moreover, they must satisfy a condition which transforms matrix  $[P]$ , in system (3.10 or 3.15), into the identity matrix, *i.e.*:

$$\begin{bmatrix} I_{11}^{(1)} & I_{22}^{(1)} & I_{12}^{(1)} & I_{66}^{(1)} \\ I_{11}^{(2)} & I_{22}^{(2)} & I_{12}^{(2)} & I_{66}^{(2)} \\ I_{11}^{(3)} & I_{22}^{(3)} & I_{12}^{(3)} & I_{66}^{(3)} \\ I_{11}^{(4)} & I_{22}^{(4)} & I_{12}^{(4)} & I_{66}^{(4)} \end{bmatrix} = \begin{bmatrix} 1 & 0 & 0 & 0 \\ 0 & 1 & 0 & 0 \\ 0 & 0 & 1 & 0 \\ 0 & 0 & 0 & 1 \end{bmatrix} \quad (3.16)$$

As it can be noticed, this latter conditions has the advantage of yielding the direct identification of the unknown parameters, *i.e.*,  $\{Q\} = \{R\}$ .

When writing the special virtual fields for the case of the unnotched Iosipescu test further conditions must be fulfilled (Grédiac et al., 2002). The virtual fields over the  $S_1$  and  $S_3$  regions (Figure 3.6) must be rigid-body like, because the experimental strain

fields are only measured over the  $S_2$  region. Thus, the integrals  $\int_S \varepsilon_j \varepsilon_i^* dS$  in Eq. (3.10) become  $\int_{S_2} \varepsilon_j \varepsilon_i^* dS$ . Besides, the virtual displacements over the  $S_3$  region must be a vertical translation, because only the resulting force along the vertical direction is known experimentally (*i.e.*, the distribution of the applied load remains unknown). In addition, the virtual displacements within the  $S_1$  region must be zero, *i.e.* the left-hand side of the specimen must not virtually move. These conditions can be stated as follows:

$$\begin{aligned} - \widehat{\varepsilon}_1^*(M) &= \widehat{\varepsilon}_2^*(M) = \widehat{\varepsilon}_6^*(M) = 0; \quad \forall M \in S_3; \\ - \widehat{u}_x^*(M) &= 0; \widehat{u}_y^*(M) = c; \quad \forall M \in S_3 \text{ (where } c \text{ is a constant)}. \end{aligned}$$

Similarly, over the  $S_1$  region (Figure 3.6) one gets:

$$\begin{aligned} - \widehat{\varepsilon}_1^*(M) &= \widehat{\varepsilon}_2^*(M) = \widehat{\varepsilon}_6^*(M) = 0; \quad \forall M \in S_1; \\ - \widehat{u}_x^*(M) &= \widehat{u}_y^*(M) = 0; \quad \forall M \in S_1. \end{aligned}$$

Furthermore, the special virtual fields must be continuous between  $S_1$  and  $S_2$  and  $S_2$  and  $S_3$ :

$$\begin{aligned} - \widehat{u}_x^*(0, y) &= 0; \widehat{u}_y^*(0, y) = 0 \quad \forall y \in [0, W]; \\ - \widehat{u}_x^*(L, y) &= 0; \widehat{u}_y^*(L, y) = c \quad \forall y \in [0, W]. \end{aligned}$$

The above conditions illustrate the capability of the VFM to filter out unknown or unwanted quantities. In the piecewise approach, they can be written as independent linear constraints imposed to the unknown nodal displacement vector:

$$[C]\{\widetilde{U}^{*(\alpha)}\} = \{Z^{(\alpha)}\}. \quad (3.17)$$

By choosing four independent special virtual fields satisfying the above prescribed conditions (Eq. (3.17)), the development of Eq. (3.15) yields the following uncoupled system of equations for the identification of the stiffness parameters:

$$\begin{aligned} Q_{11} &= -\frac{P.\widetilde{U}_y^{*(1)}(L, y)}{t} \\ Q_{22} &= -\frac{P.\widetilde{U}_y^{*(2)}(L, y)}{t} \\ Q_{12} &= -\frac{P.\widetilde{U}_y^{*(3)}(L, y)}{t} \\ Q_{66} &= -\frac{P.\widetilde{U}_y^{*(4)}(L, y)}{t} \end{aligned} \quad (3.18)$$

where  $\{\tilde{U}_y^{*\alpha}(L)\}$ , with  $\alpha = 1, 2, 3$  and 4, are the vectors containing the virtual nodal displacements used, respectively, for the identification of  $Q_{11}$ ,  $Q_{22}$ ,  $Q_{12}$  and  $Q_{66}$ .

### 3.5.2.3 Optimal solution

For a given mesh with a sufficient number of elements, *i.e.* with significantly more degrees of freedom than unknown stiffness parameters, there is still an infinity of virtual fields that satisfy Eq. (3.18) under the conditions prescribed in Eq. (3.17). To overcome this selection issue, a procedure was proposed by Avril et al. (2004b). It consists in the selection of the virtual fields which minimises the sensitivity to a white noise. By considering unbiased measurements and adding a random noise to the actual strain fields:  $\varepsilon_i^t = \varepsilon_i^m - \gamma N_i$ , where  $\varepsilon_i^t$  represents the true strain,  $\varepsilon_i^m$  the measured strain,  $\gamma$  a strictly positive real number which represents a random intensity of the strain measurement (it is also interpreted as the uncertainty of the strain measurements) and  $N_i$  is a copy of a standard Gaussian white noise, the following cost function can be defined (Avril et al., 2004b):

$$(\eta_{ij})^2 = \frac{1}{2} \langle \tilde{U}^{*\alpha} \rangle [H] \{ \tilde{U}^{*\alpha} \} \quad (i, j = 1, 2, 6; \alpha = 1, 2, 3 \text{ and } 4) \quad (3.19a)$$

with,

$$\begin{aligned} 2[H] &= \frac{S_2}{PQ} \sum_{p=1}^P \sum_{q=1}^Q [ (Q_{11}^2 + Q_{12}^2) \{B_1(x_p, y_q)\} \langle B_1(x_p, y_q) \rangle + \\ &+ (Q_{22}^2 + Q_{12}^2) \{B_2(x_p, y_q)\} \langle B_2(x_p, y_q) \rangle + \\ &+ 2[Q_{12}(Q_{11} + Q_{22})] \{B_1(x_p, y_q)\} \langle B_2(x_p, y_q) \rangle + \\ &+ Q_{66}^2 \{B_6(x_p, y_q)\} \langle B_6(x_p, y_q) \rangle ]. \end{aligned} \quad (3.19b)$$

The value of  $\eta_{ij}$ , associated to each stiffness parameter  $Q_{ij}$ , provides a quantification of the sensitivity of the VFM to the presence of noise in the data. Hence, the vector  $\tilde{U}^{*\alpha}$  that minimises this cost function (Eq. 3.19) is the one leading to the most accurate identification of the stiffness parameters. The optimisation problem is a constrained one because  $\tilde{U}^{*\alpha}$  must verify Eq. (3.17). Thus, the following scalar-valued function of the Lagrangian of the constrained optimisation problem can be defined:

$$\mathcal{L}^{(\alpha)} = \frac{1}{2} \langle \tilde{U}^{*\alpha} \rangle [H] \{ \tilde{U}^{*\alpha} \} + \{ \lambda^{(\alpha)} \} \left[ [C] \{ \tilde{U}^{*\alpha} \} - \{ Z^{(\alpha)} \} \right] \quad (3.20)$$

where  $\{ \lambda^{(\alpha)} \}$  ( $\alpha = 1, 2, 3$  and 4) is the vector whose elements are the Lagrange multipliers. The minimisation of  $\mathcal{L}^{(\alpha)}$  (Eq. 3.20), with regard to  $\{ \tilde{U}^{*\alpha} \}$  and  $\{ \lambda^{(\alpha)} \}$ , leads to the following matrix system:

$$\begin{bmatrix} [H] & [C]^T \\ [C] & [0] \end{bmatrix} \begin{bmatrix} \{\tilde{U}^{*(\alpha)}\} \\ \{\lambda^{(\alpha)}\} \end{bmatrix} = \begin{bmatrix} \{0\} \\ \{Z^{(\alpha)}\} \end{bmatrix} \quad (3.21)$$

which can be solved for the unknown nodal displacements, defining the optimum virtual fields with regard to the sensitivity to noise criterion.

It was proved (Avril et al., 2004b) that the saddle point of the Lagrangian  $\mathcal{L}^{(\alpha)}$  (Eq. 3.20) exists and is unique, leading to the choice of the virtual fields which minimise the sensitivity to noisy data. However, the problem is implicit because the  $Q_{ij}$  unknowns are involved in the Lagrangian expression (Eq. 3.20). This issue can be solved by an iterative algorithm (Avril et al., 2004b). It has been found that the unknown parameters are identified in four iterations whatever the choice of the initial values used to initialise the iterative algorithm (one can start attributing a value of 1 GPa to all properties).

## 3.6 Conclusions

In this chapter the material characterisation approach used throughout this work was presented. Particularly, the unnotched Iosipescu test, consisting in loading a rectangular coupon in the Iosipescu fixture, was investigated. The in-plane displacements are provided by the grid method. The principle of the grid method along with the phase-evaluation method, used in the determination of the displacement fields from the grid images, were presented in the first part of the chapter. As the strain fields are required in the material characterisation, a least-squares polynomial regression scheme was proposed in order to filter out the raw displacement fields before numerical differentiation. These data, obtained from the unnotched Iosipescu test, must be processed by a suitable identification strategy yielding the identification of the whole set of in-plane material parameters. The proposed identification method is based on the development of the VFM for the case of in-plane stresses. The main features of this approach were also outlined.

In the following chapters, a numerical study followed by an experimental validation of the proposed approach will be presented.



# Chapter 4

## Characterisation of the longitudinal-radial stiffness of *P. pinaster* wood by a single test. I: Numerical study

### 4.1 Introduction

The aim of this chapter is to numerically validate the inverse identification approach proposed in Chapter 3, yielding the longitudinal-radial (*LR*) stiffness parameters of *P. pinaster* wood from a single test. The approach is based on the virtual fields method (VFM) coupled with full-field displacement measurements provided by the grid method.

### 4.2 0° configuration

For the purpose of validation, the actual experimental data (*i.e.*, the displacement fields provided by the grid method) were replaced by numerical data provided by finite element (FE) analyses.

The identification procedure can be separated into two parts (Figure 4.1):

- image processing: calculation of the strain fields by the numerical differentiation of the polynomial displacement fields;
- identification method: stiffness identification by the VFM from the measurement of the strain fields, specimen geometry and resultant load.

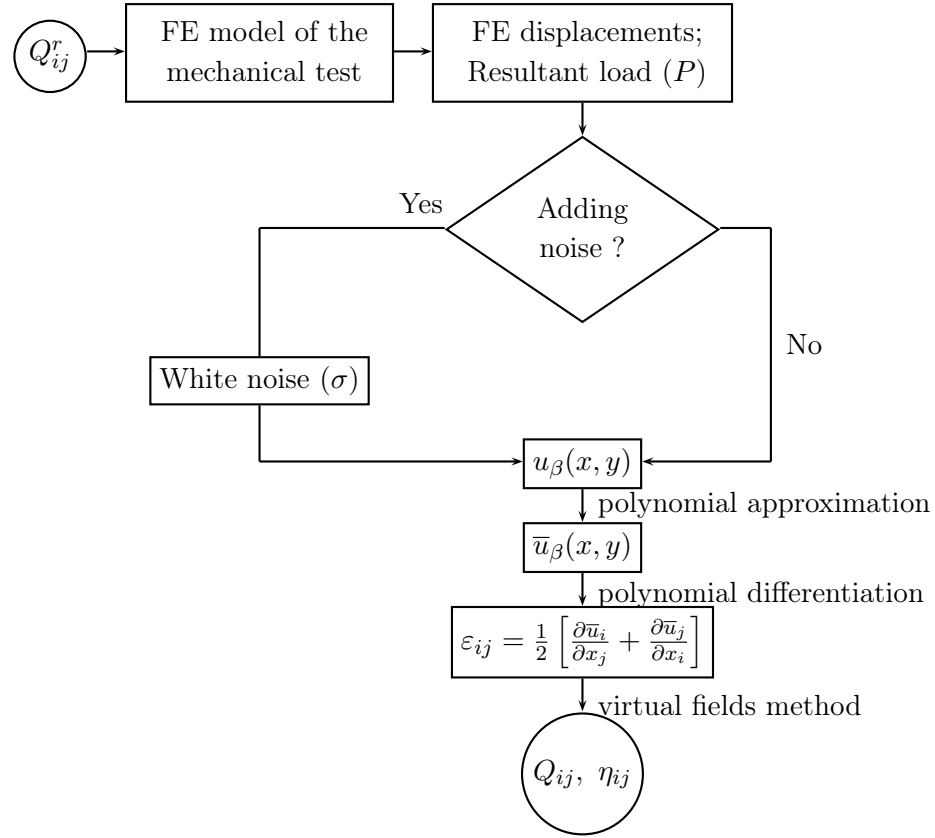


Figure 4.1: Algorithm implemented in the validation of the material characterisation approach ( $\beta = x, y, i, j = 1, 2, 6$ ).

## 4.2.1 Homogeneous material model

### 4.2.1.1 Finite element model

Assuming a plane stress state, a 2D FE model of the unnotched Iosipescu test was developed using the ANSYS 8.0<sup>®</sup> code. The geometrical model consists of a rectangular area of  $80 \times 20 \text{ mm}^2$ , corresponding to the dimensions of the tested specimens (§ 5.2.1). The material was assumed to be homogeneous with a linear elastic orthotropic behaviour. The  $x - y$  global coordinate system was considered oriented in the  $LR$  plane of symmetry.

The elastic properties of *P. pinaster* wood, input into the analyses, were taken from the literature (Table 4.1). The longitudinal ( $E_L$ ) and radial ( $E_R$ ) moduli, as well as Poisson's ratio ( $\nu_{LR}$ ), were measured by Pereira (2005) through tensile tests in the  $L$  and  $R$  directions of wood. The shear modulus ( $G_{LR}$ ) was determined by Xavier et al. (2004) carrying out Iosipescu shear tests onto notched specimens manufactured in the  $LR$  principal plane.

The specimen geometrical model was meshed using the quadrilateral isoparametric element PLANE182; this element has four nodes and a total of eight degrees of freedom,

Table 4.1: Reference elastic engineering properties of *P. pinaster* wood used in the finite element analyses (Pereira, 2005; Xavier et al., 2004) ( $1 - 2 \equiv L - R$ ).

$E_1$ (GPa)	$E_2$ (GPa)	$\nu_{12}$	$G_{12}$ (GPa)
15.1	1.91	0.471	1.41

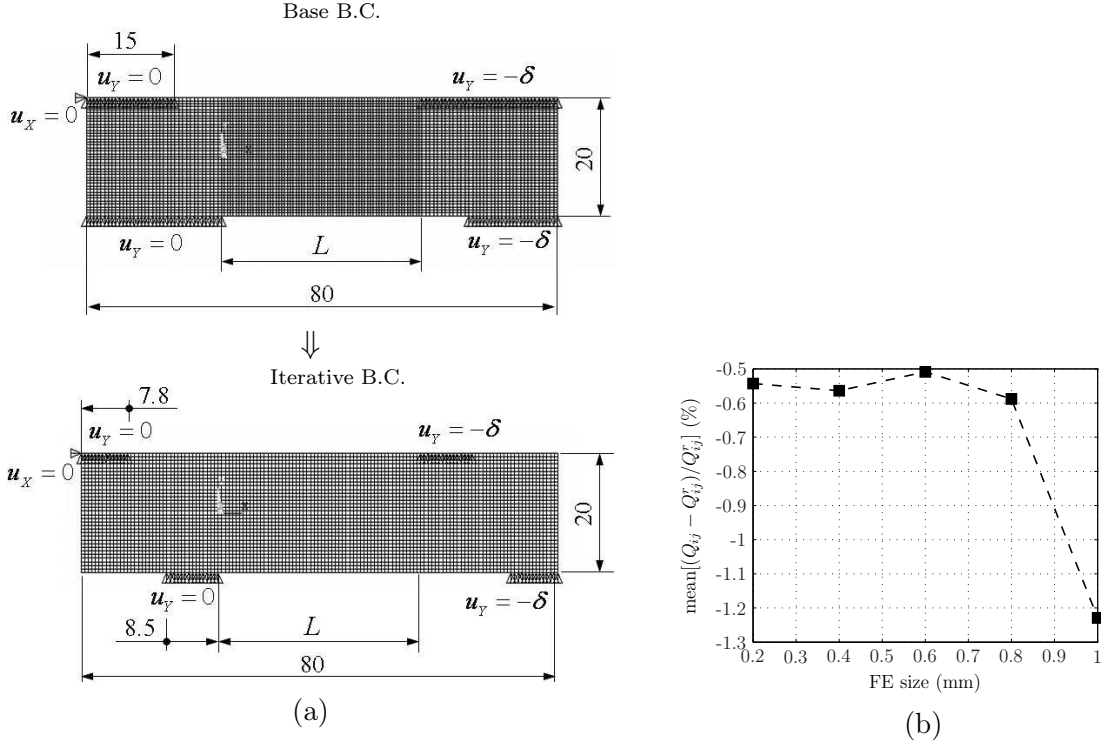


Figure 4.2: (a) Finite element model of the unnotched Iosipescu test, with  $L = 34$  mm ( $\delta = 0.4$  mm, FE size = 0.6 mm); (b) meshing refinement study –  $Q_{ij}^r$  and  $Q_{ij}$  are, respectively, the reference and identified stiffness parameters.

corresponding to two translations in the  $x$  and  $y$  directions per node. It is equivalent to PLANE42 but makes possible the input of the off-axis stiffness matrix, taking directly into account the actual orientation of the grain (fibre) with regard to the specimen global (ANSYS) coordinate system. Figure 4.2(a) shows the final mesh, reached after meshing refinement. In the convergence study, the average of the relative errors obtained among the reference ( $Q_{ij}^r$ ) and identified ( $Q_{ij}$ ) stiffness parameters was plotted versus the FE mesh size across the gauge area (the procedure for identifying the stiffness values is detailed further on, § 4.2.1.2.4). As it can be observed, the best agreement (minimum deviation from reference and identified stiffness values) is obtained for a mesh size of 0.6 mm. Actually, this element size is equal to six times the pitch of the grid ( $p = 0.1$  mm) used experimentally in the measurement of the displacements by the grid method (§ 5.2.2). The final model has a total number of 4389 elements and 4556 nodes.

In the literature different boundary conditions have been proposed to model the classical Iosipescu shear test (Adams and Walrath, 1987; Ho et al., 1993; Pierron and Vautrin,

1994; Xavier et al., 2003). Among them, the iterative procedure for defining the boundary conditions proposed by Ho et al. (1993) was employed here. Firstly, it consists in prescribing all vertical nodal displacements along the edges of the specimen initially in contact with the fixture (named Base B.C. in Figure 4.2(a)). The nodes on the left-hand part of the specimen (attached to the fixed part of the fixture) were prescribed to  $u_y = 0$ , whereas the ones on the right-hand part (attached to the movable part of the fixture) were set equal to  $u_y = -0.4$  mm. In addition, a zero horizontal displacement was prescribed at the upper-corner node in order to prevent the free rigid body motion of the specimen in the  $x$  direction. Then, iteratively, all nodes having tensile reaction forces are released (because in practice the specimen is loaded in compression) until convergence is reached (Iterative B.C. in Figure 4.2(a)). The convergence of these boundary conditions was reached after four iterations. Nevertheless, it may be worth saying that the actual boundary conditions, either Based or Iterative B.C., are expected to not significantly affect the identification by the VFM because of the filtering feature of the selected virtual fields concerning the actual (unknown) load distribution (§ 3.5.2.2); however, they can still have a slightly effect on the reconstruction of the strain fields from the numerical displacements.

Numerically, the global applied load was determined by the sum of all vertical reaction forces at the prescribed nodes in contact with the movable part of the fixture (the right-hand side of the specimen in Figure 4.2(a)).

The FE model of the unnotched Iosipescu test was set up using the ANSYS APDL language. The advantages is that automatic communication with Matlab can then be achieved. The parameters of the FE model (*e.g.*, geometric parameters, material properties, extension of boundary conditions, value of prescribed displacements) were input in a Matlab program. This writes a ASCII file that is read afterwards by the ANSYS finite element solver launched in batch mode. After running, the coordinates of the centroid of the finite elements over the gauge area and the corresponding numerical displacement (or strain) components, as well as the resultant of the reaction nodal forces, are stored into data files, which can then be read by Matlab. If necessary this routine can be run in a looping process.

#### 4.2.1.2 Numerical results

**4.2.1.2.1 Gauge length** The distribution of the strain field across the central region of the specimen, will be dependent on the free distance  $L$  between the inner loading points of the fixture (Figure. 3.6). Therefore, this distance must be calibrated in order to enhance the contribution of the whole set of stiffness components in the deformation of the specimen. Providing that all these parameters are involved in the material mechanical response, they can be identified afterwards by the VFM (Pierron and Grédiac, 2000). In practice, using the fixture presented in (Pierron, 1998), the distance  $L$  can be easily adjusted by moving the fixed part of the fixture with regard to the movable one, defining

the actual gauge area ( $S_2$  region in Figure. 3.6) over which the full-field displacements are to be measured. Hence, the aim is to find the appropriate length of the gauge area of the unnotched Iosipescu specimen that will lead to the reliable identification of the whole in-plane stiffness parameters of *P. pinaster* wood.

When using the VFM, the individual contribution of each material parameter on the global deformation of the specimen can be accessed by the sensitivity to noise relative terms defined as (Avril et al., 2004b):  $\xi_{11} = \eta_{11}/Q_{11}$ ,  $\xi_{22} = \eta_{22}/Q_{22}$ ,  $\xi_{12} = \eta_{12}/Q_{12}$  and  $\xi_{66} = \eta_{66}/Q_{66}$ . The lower  $\xi_{ij}$ , the more stable will be the identification of  $Q_{ij}$ . Thus, the minimisation of these coefficients can provide a criterion for test design.

Several FE models of the unnotched Iosipescu test (0° configuration) were tested with a length  $L$  varying from 15 mm up to 45 mm, with increments of 5 mm (Figure 4.2(a)). For each model, the displacement field was calculated in ANSYS and processed afterwards using the VFM (Matlab®). From the identification results, the variation of  $\xi_{ij}$  with regard to the gauge length  $L$  was analysed; these results are reported in Figure 4.3(a). On the one hand, lower values were obtained to  $\xi_{11}$  ( $Q_{11}$ ) and  $\xi_{66}$  ( $Q_{66}$ ), the former slightly decreasing with the increase of  $L$ . Moreover, the  $\xi_{66}$  coefficient is almost constant over the length  $L$ , showing that its associated  $Q_{66}$  stiffness is expected to be one of the best identified parameters. This result is not surprising if one bears in mind that the unnotched Iosipescu test is derived from the Iosipescu shear configuration. On the other hand, higher values of  $\xi_{22}$  ( $Q_{22}$ ) and  $\xi_{12}$  ( $Q_{12}$ ) were reached, increasing and decreasing, respectively, with the increase of  $L$ . Attending to the values of  $\xi_{ij}$ , for this test configuration, these observations mean that the  $Q_{11}$  and  $Q_{66}$  components are expected to be better identified than the  $Q_{22}$  and  $Q_{12}$  ones. For a gauge length larger than about 34 mm,  $\xi_{11}$ ,  $\xi_{12}$  and  $\xi_{66}$  are practically unchanged, although  $\xi_{22}$  continuously increases with  $L$ . This is consistent with the fact that a higher gauge length enhances the bending response of the specimen, and reduces the effect of transversal compression under the inner loading points. Therefore, a length larger than about 34 mm does not seem suitable for the purpose of identifying the whole set of stiffness components. Conversely, small gauge lengths penalise the identification of  $Q_{11}$  and particularly  $Q_{12}$ .

In order to balance out the identifiability of the stiffness components, the optimal gauge length  $L$  (the design variable) can be obtained as the solution of a minimisation problem whose objective function ( $\phi$ ) is given by (Pierron et al., 2007):

$$\phi(L) = \frac{(\xi_{11} - \xi_{22})^2 + (\xi_{11} - \xi_{66})^2 + (\xi_{22} - \xi_{66})^2}{(\xi_{11})^2 + (\xi_{22})^2 + (\xi_{66})^2}. \quad (4.1)$$

In this cost function the term  $\xi_{12}$  was not taken into account. This is because the  $Q_{12}$  parameter is linked to Poisson's ratio (Eq. 1.4), which typically has a low signal-to-noise ratio and therefore it is usually less identifiable with regard to the other components. In practice, this means that the term  $\xi_{12}$  is much larger than the other sensitivity coefficients,

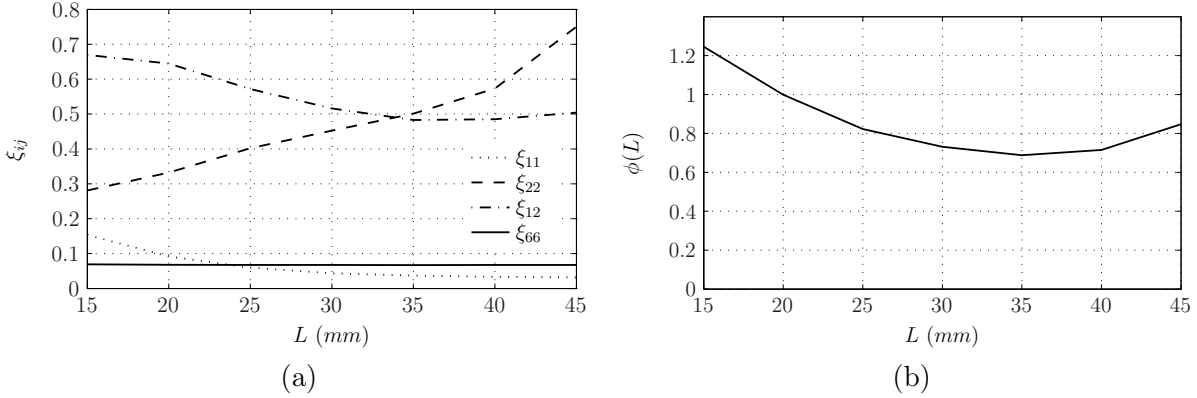


Figure 4.3: (a) Variation of the sensitivity coefficients,  $\xi_{ij} = \eta_{ij}/Q_{ij}$ , with regard to the gauge length  $L$ ; (b) evaluation of the objective function  $\phi(L)$ .

hiding their effect on the cost function value. To avoid this, the term  $\xi_{12}$  was not considered. Furthermore, the cost function was normalised by the sum of the squares of the sensitivity coefficients. It should be noticed that, for a given noise level, the coefficients  $\xi_{ij}$  increase with the strains values; thus, by normalising the cost function, its value will be insensitive to the strains magnitude, avoiding a premature convergence for the configuration ( $L$ ) of minimum stiffness or maximum strains (Pierron et al., 2007). The values taken by the cost function (Eq. 4.1) in the search space  $L = \{15, \dots, i-5, i, i+5, \dots, 45\}$  are plotted in Figure 4.3(b). It has a convex shape with a minimum around  $L = 35$  mm.

According to the previously analyses (Figure 4.3), a gauge length equal to  $L = 34$  mm was chosen thereafter.

**4.2.1.2.2 Polynomial degree** The FE mesh of the model has 1881 elements over the gauge area ( $L \times W = 34 \times 20$  mm<sup>2</sup>, see Figure 4.2(a)), respectively, 57 and 33 elements along the  $x$  and  $y$  directions. The  $x$  and  $y$  displacement components at the centroid of these elements were exported from ANSYS to Matlab for further processing. An independent measurement of the displacement by the grid method (spatial resolution) was assumed to be performed over a window of adjacent pixels (spatial phase-shifting method) imaging a whole period of the grid. Therefore, the original FE displacements were firstly interpolated, using Delaunay triangle-based linear interpolation, on a regular array of coordinates  $(X, Y)$ , where  $p/2 \leq X \leq (L - p/2)$  and  $(W/2 - p/2) \leq Y \leq (-W/2 + p/2)$ , *i.e.*, over a total of 68000 independent points, respectively 340 and 200 along the  $x$  and  $y$  directions. Thus, the experimental data is equivalently replaced by a numerical one in terms of spatial resolution. The  $x$  and  $y$  components of the simulated (interpolated) displacement field,  $u_x(X, Y)$  and  $u_y(X, Y)$ , are shown respectively in Figure 4.4(a) and Figure 4.5(a) (without noise). Because in practice the displacements are always measured with some amount of noise, these numerical fields were corrupted by adding a Gaussian white noise, having a zero mean and a standard deviation  $\sigma_u = 2$   $\mu\text{m}$ :  $u_\beta^n = u_\beta + \sigma_u r$

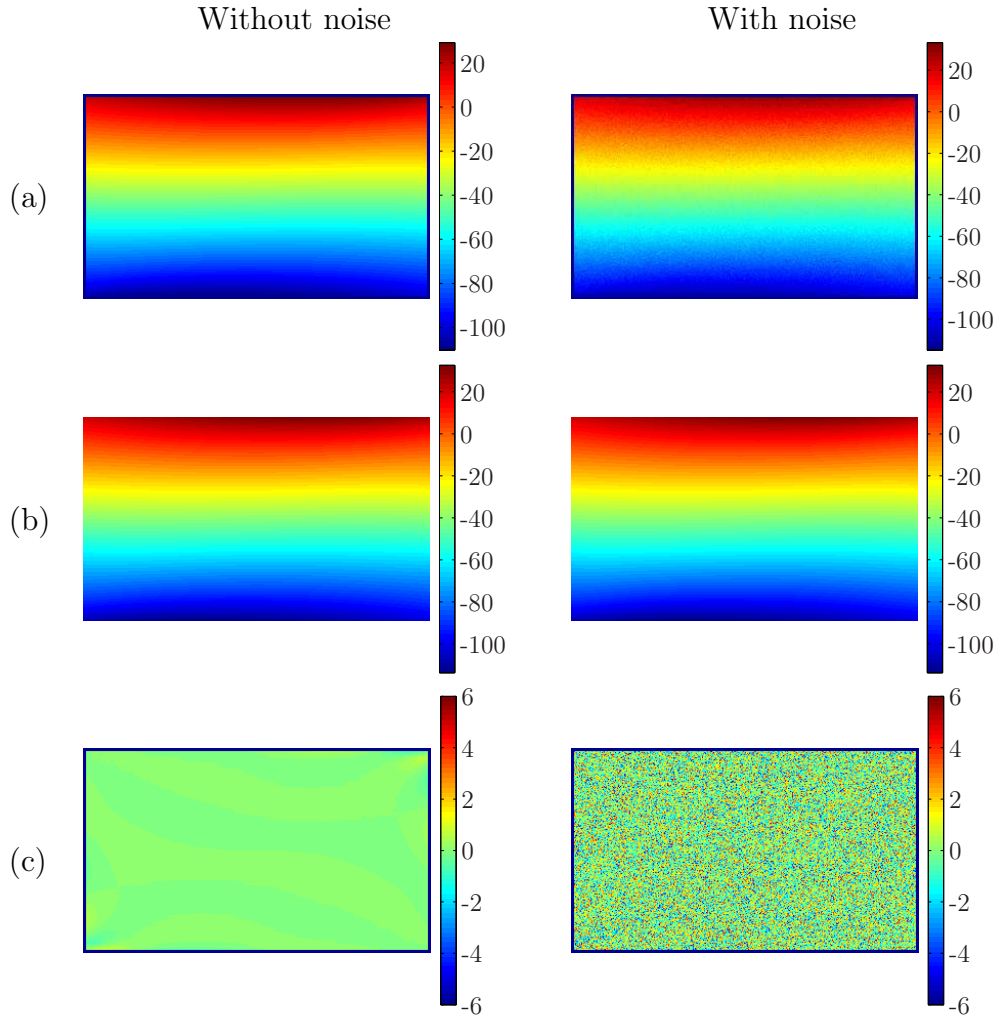


Figure 4.4: (a) Simulated, (b) approximated (7th-degree polynomial) and (c) residual  $u_x$  displacement component obtained for the 0° specimen (without and with adding a Gaussian white noise with  $\sigma_u = 2 \mu\text{m}$ ) (unit:  $\mu\text{m}$ ).

( $\beta = x, y$ ), where  $u_\beta^n$  is the noisy displacement field,  $u_\beta$  the displacement field without noise and  $r$  a normally distributed random number (with zero mean value). The  $\sigma_u$  value is about twice of the displacement resolution reached experimentally with the grid method (§ 5.2.3). The resulting  $x$  and  $y$  components of the noisy displacement fields are shown, respectively, in Figure 4.4(a) and Figure 4.5(a) (with noise).

The simulated displacement fields (without and with noise) were then approximated by a 2D polynomial using the least-squares approximation scheme (§ 3.4.2.1). In order to select the appropriate polynomial degree, the difference between simulated and approximated displacements was analysed with respect to a set of degrees ranging from 5 to 11. This search domain was selected because a lower-degree polynomial may not follow accurately the displacement gradients and a higher-degree one may be prone to fluctuations around the data points, especially at the edges. The results of this study are shown

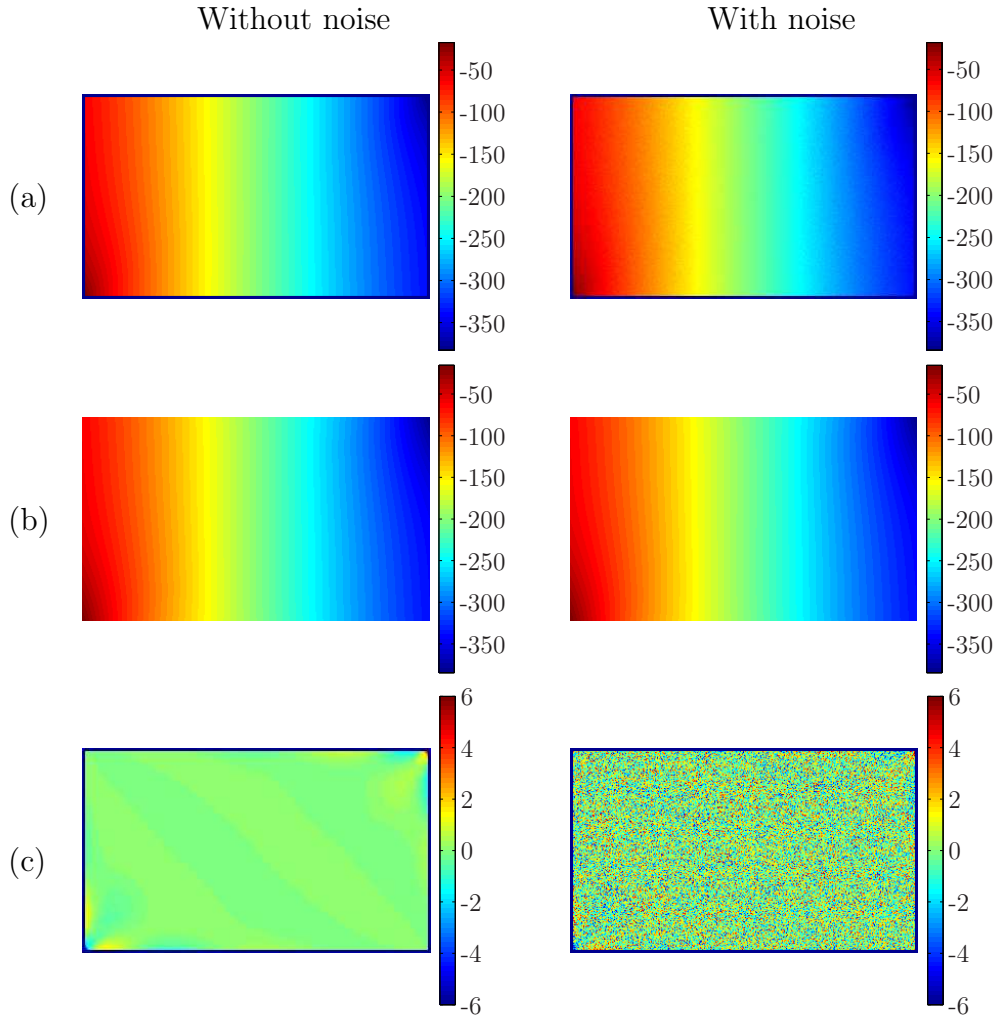


Figure 4.5: (a) Simulated, (b) approximated (7th-degree polynomial) and (c) residual  $u_y$  displacement component obtained for the  $0^\circ$  specimen (without and with adding a Gaussian white noise with  $\sigma_u = 2 \mu\text{m}$ ) (unit:  $\mu\text{m}$ ).

in Figure 4.6, where the average of the residual ( $\Delta u_\beta$ ,  $\beta = x, y$ ) between simulated ( $u_\beta$ ) and approximated ( $\bar{u}_\beta$ ) displacement fields are plotted over the set of polynomial degrees. Since noisy data were used, these results were obtained as the average among 30 iterative analyses, where, at each step, a new different white noise was added to the simulated displacements. As it can be observed (Figure 4.6) the variation of the (mean) residual, between simulated and approximated displacements, does not significantly change for a polynomial degree higher than 7 for both  $x$  and  $y$  components. The strain components ( $\varepsilon_1$ ,  $\varepsilon_2$  and  $\varepsilon_6$ ), obtained by differentiating (using the finite difference scheme) the 2D polynomial displacements with degrees ranging from 5 to 11, are shown in Figure 4.7. It can be noticed from these maps that the utilisation of large polynomial degrees tend to increase the strain values at the edges of the gauge area. Consequently, when processing strain maps obtained from the differentiation of high degree polynomials, the identified

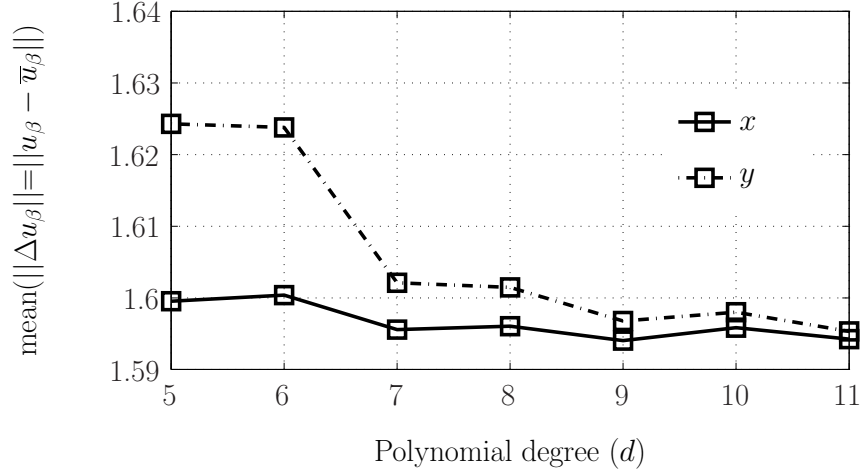


Figure 4.6: Evaluation of the residual ( $\Delta u_\beta$ ,  $\beta = x, y$ ) of the difference between simulated ( $u_\beta$ ) and approximated ( $\bar{u}_\beta$ ) displacement fields, with the increase of the degree ( $d$ ) of the fitting polynomial (unit:  $\mu\text{m}$ ).

stiffness components may be somewhat underestimated. On the basis of these numerical results, the 7th-degree polynomial was judged to be a good compromise. The resulting  $x$  and  $y$  approximated displacement maps (without and with noise) are shown, respectively, in Figure 4.4(b) and Figure 4.5(b). The  $x$  and  $y$  residual difference between simulated and approximated displacements (without and with noise) is also shown in Figure 4.4(c) and Figure 4.5(c), respectively. A small residual difference can be observed, showing that a suitable polynomial approximation is obtained from a degree equal to 7.

**4.2.1.2.3 Virtual mesh size** In order to develop the piecewise virtual fields, a mesh with  $N_X$  and  $N_Y$  elements, respectively, along the  $x$  and  $y$  directions, is generated across the gauge area, as illustrated in Figure 3.6 (§ 3.5). Similarly to the FE method, the effect of the mesh refinement on the identified stiffnesses was studied by comparing their values to reference ones when the number of elements varies over  $N_X = \{2, \dots, i-1, i, i+1, \dots, 14\}$  and  $N_Y = \{2, \dots, i-1, i, i+1, \dots, 8\}$ . Contrarily to FE analyses, rather coarse meshes are usually suitable for developing the piecewise virtual fields (Toussaint et al., 2006), so this number of elements was assumed suitable for the analysis. This study is summarised in Figure 4.8, for which the relative differences (dif., %) between identified (using a 7th-degree polynomial displacement without noise) and reference values are plotted against the number of  $N_X$  elements (where  $N_Y$  is set as parametric datum). It can be concluded that the number of elements of the mesh does not affect significantly the identification of  $Q_{66}$  (Figure 4.8(d)), especially if a coarse mesh is used (*i.e.*,  $N_X < 12$  and  $N_Y < 5$ ). For  $Q_{11}$  (Figure 4.8(a)), a stable value is reached with  $N_X \geq 8$ ; moreover, the solution approaches the reference if a higher number of elements is used in the  $y$  direction ( $N_Y \geq 4$ ). The number of elements of the mesh has a more significant effect on the identification of

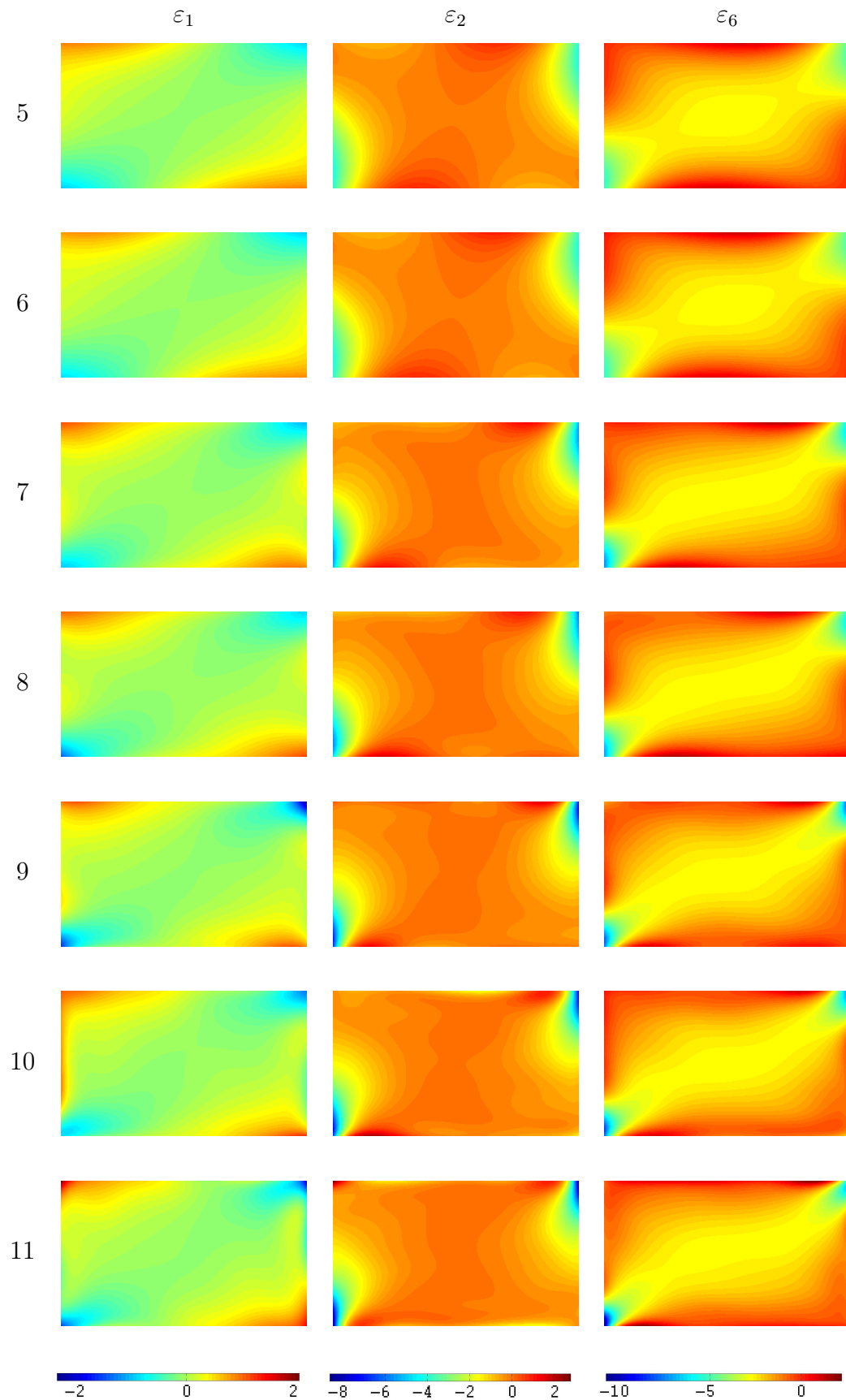


Figure 4.7: Typical strain fields ( $P = -261.8 \text{ N}$ ): (a)  $\varepsilon_1$ , (b)  $\varepsilon_2$ , (b)  $\varepsilon_6$ , obtained for the  $0^\circ$  specimen by differentiating (finite difference scheme) 2D polynomial displacements with degrees ( $d$ ) ranging from 5 to 11 (unit:  $\times 10^{-3}$ ).

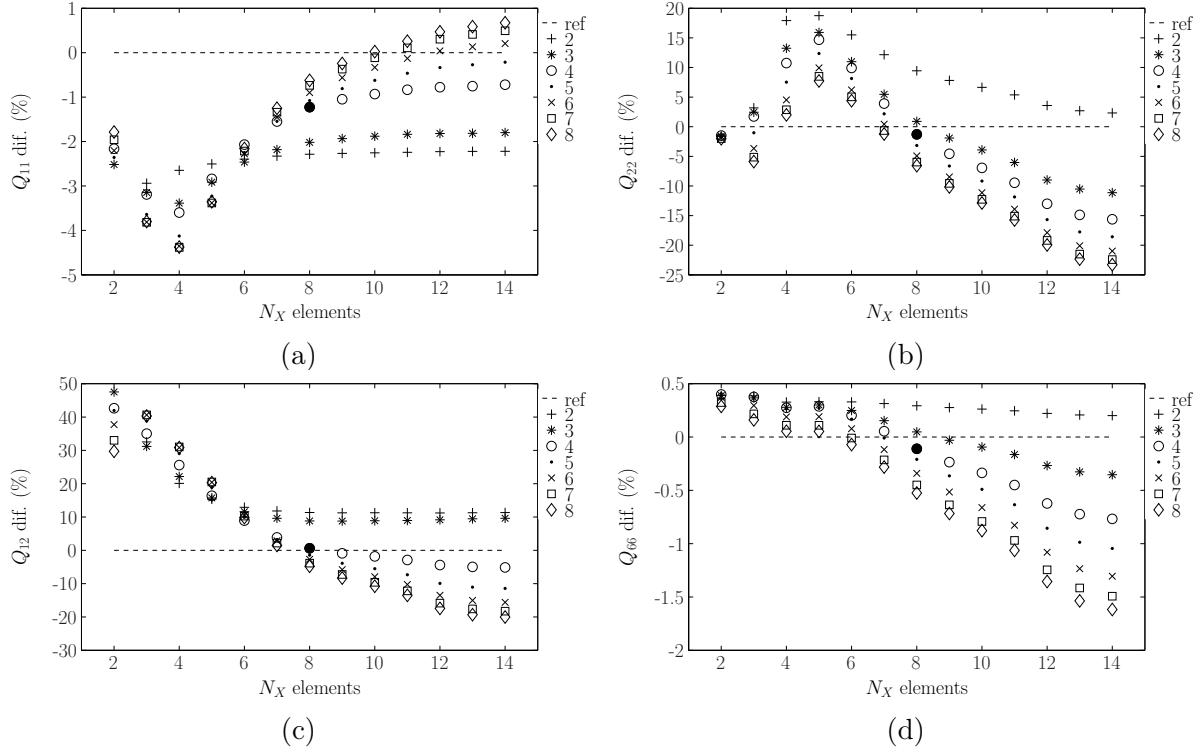


Figure 4.8: Relative differences of the (a)  $Q_{11}$ , (b)  $Q_{22}$ , (c)  $Q_{12}$  and (d)  $Q_{66}$  stiffness components, with regard to reference values, identified using piecewise virtual fields defined over a mesh of  $N_X = \{2, 3, \dots, 14\}$  and  $N_Y = \{2, 3, \dots, 8\}$  elements (using a 7th-degree polynomial displacement without noise).

both  $Q_{22}$  (Figure 4.8(b)) and  $Q_{12}$  (Figure 4.8(c)). From these results, a *virtual* mesh of  $8 \times 4$  elements over the  $x$  and  $y$  directions, respectively, was chosen. A graphical display of the mesh deformation corresponding to each optimised special virtual field used in the identification of the stiffness parameters is shown in Figure 4.9.

**4.2.1.2.4 Stiffness identification** The stiffness values identified by the VFM – using a polynomial degree equal to 7 and a virtual mesh of  $8(x) \times 4(y)$  elements – are reported in Table 4.2. These results were obtained considering different cases where the identification was performed from: (1) the FE strains (Ident. 1); (2) the FE strains corrupted by adding a Gaussian white noise (the mean and the coefficient of variation (C.V.) values were determined among 30 iterations, where, in each step, a new Gaussian white noise with standard deviation of  $\sigma_\varepsilon = 10^{-4}$  was added to the original strain maps) (Ident. 2); (3) the FE displacements without noise (Ident. 3); (4) the FE displacements disturbed by a white noise (the values of mean and coefficient of variation were determined among 30 iterations using a standard deviation of  $\sigma_u = 2 \mu m$ ) (Ident. 4). When processing the strain fields retrieved directly from the FE analysis (Ident. 1 and 2), all stiffness are identified with differences, with regard to reference values, less than 1.0%. Besides, the scatter quantified

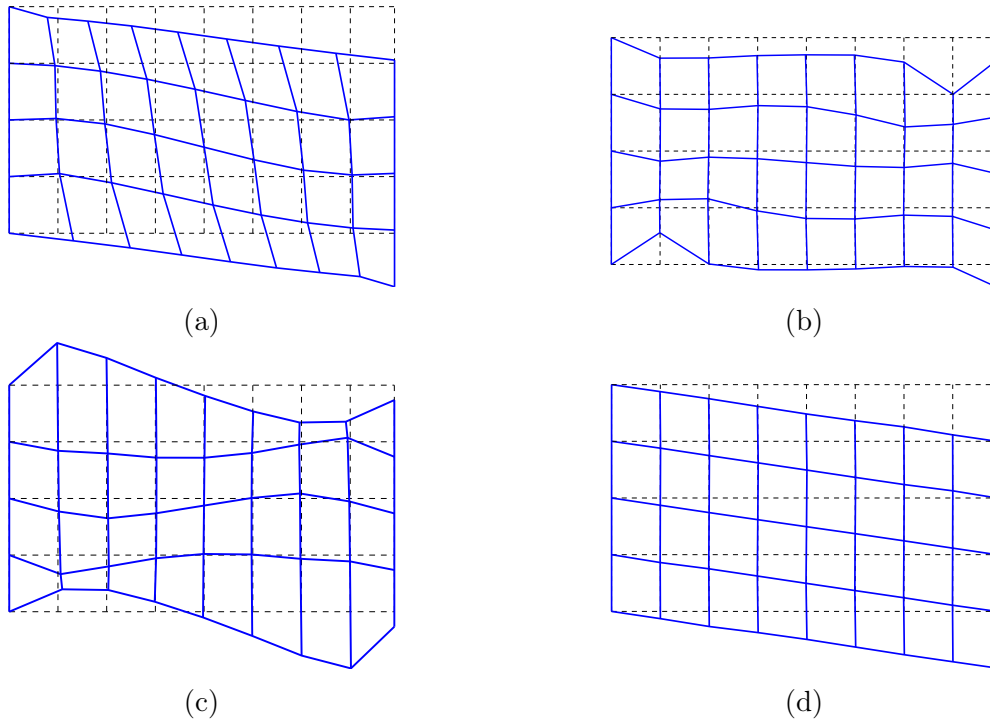


Figure 4.9: Graphical display of the mesh deformation corresponding to each optimised special virtual field used in the identification of: (a)  $Q_{11}$ ; (b)  $Q_{22}$ ; (c)  $Q_{12}$ ; (d)  $Q_{66}$ .

by the coefficients of variation associated to the stiffness values, determined from the noisy strain fields (Ident. 2), are always less than 0.5%. This proves that the VFM routine can lead to the correct identification of all the material parameters using the unnotched Iosipescu test. Moreover, it can be said that a high level of agreement is also found by processing polynomial displacement fields (Ident. 3 and 4). In this case, slightly higher differences are obtained for  $Q_{11}$  and  $Q_{22}$  (although less than 2.0%), but  $Q_{12}$  and  $Q_{66}$  are determined with differences less than 1.0%. When processing noisy displacement fields, however, high coefficients of variation are determined for both the  $Q_{22}$  (2.7%) and the  $Q_{12}$  (6.7%) parameters (Table 4.2). In this case, the polynomials provide a reconstruction of the actual fields that may induce a bias in the identified values.

### 4.2.2 Layered material model

The VFM procedure presented in § 3.5 assumes that the material is homogeneous. A direct consequence is that the stiffness parameters,  $Q_{ij}$ , could be factorised out of the integrals in Eq. (3.9) before further developments. In clear wood specimens, this assumption is equivalent to assuming that the material elementary representative volume integrates along the radial direction the local heterogeneity due to earlywood and latewood constituents. However, because of the relatively small size of the rectangular specimen used in the unnotched Iosipescu test (the width, along the radial direction, is equal to

Table 4.2: Stiffness parameters identified by the virtual fields method (with a mesh of  $8(x) \times 4(y)$  elements) from the finite element strains, without (Ident. 1) and with (Ident. 2) noise ( $\sigma_\varepsilon = 10^{-4}$ , 30 iterations), and from the finite element displacements, without (Ident. 3) and with (Ident. 4) noise ( $\sigma_u = 2 \mu m$ , 30 iterations) (unit: GPa) ( $1-2 \equiv L-R$ ).

		$Q_{11}$	$Q_{22}$	$Q_{12}$	$Q_{66}$
Reference		15.57	1.967	0.927	1.410
Strain					
Ident. 1: Without noise		15.61	1.953	0.918	1.412
	dif. (%)	0.26	-0.73	-0.89	0.11
Ident. 2: With noise	Mean	15.61	1.953	0.918	1.411
	C.V. (%)	0.14	0.11	0.36	0.03
	dif. (%)	0.24	-0.73	-0.88	0.11
Displacement (7th-degree polynomial)					
Ident. 3: Without noise		15.38	1.942	0.932	1.408
	dif. (%)	-1.23	-1.29	0.63	-0.11
Ident. 4: With noise	Mean	15.33	1.930	0.922	1.409
	C.V. (%)	1.80	2.68	6.68	0.31
	dif. (%)	-1.52	-1.90	-0.46	-0.04

about 20 mm), with regard to the size of the annual rings (a few millimeters), checking the relevance of the homogeneity assumption is required. This is the purpose of the present section.

#### 4.2.2.1 Finite element model

Assuming a plane stress approach, a 2D layered material FE model of the unnotched Iosipescu wood specimen was set up using ANSYS 8.0. Both linear elasticity and orthotropy were assumed. The global dimensions of the specimen were those used in the experimental work. Moreover, the same element type, mesh refinement and boundary conditions used in the homogeneous model of the unnotched Iosipescu specimen (§ 4.2.1.1), were kept here.

The geometrical model of the specimen was built up by stacking successive layers of earlywood and latewood, as shown in Figure (4.10). Two geometric parameters of this model were considered to be relevant: (1) the total number of annual growth rings ( $n$ ) along the width of the specimen; (2) the volume fractions of the earlywood ( $w^e$ ) and latewood ( $w^l$ ) layers within a given annual ring. The former parameter takes into account the radial variation of the width of the individual annual rings (typically, these are wider in the centre of the stem and thinner at the periphery). The latter parameter considers

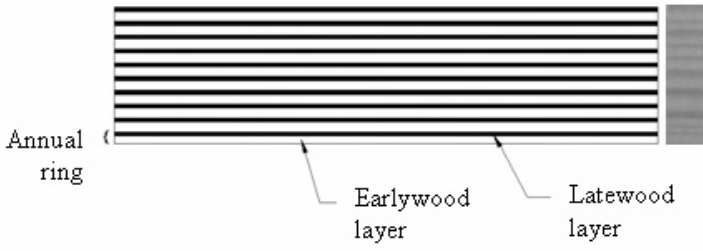


Figure 4.10: Layered material model of the unnotched Iosipescu wood specimen.

the relative percentage of the early and late woods formed within each annual ring (the width of the earlywood layer is greater than the latewood one, moreover the latter tends to be constant across the annual rings).

Using the procedure described in (Lousada, 2000), X-ray densitometry measurements were carried out on unnotched Iosipescu wood specimens. From these measurements, it was determined that the width of the latewood layer ( $w^l$ ), with regard to the annual ring width, was about 30%-40%. Moreover, the ratio between latewood and earlywood densities ( $k = \rho^l/\rho^e$ ) was found to lie within the range of 1.5 and 2. Besides, from the manufactured specimens, the variation of the total number of annual rings was counted between 6 and 10. These measurements were used here as input in the FE analyses, aiming at verifying if effective elastic properties are indeed identified by the VFM from the layered material model.

Because of the lack of available data in the literature, the elastic engineering properties of the earlywood and latewood layers of *P. pinaster* wood were assessed from reference values for this species determined at the macroscopic scale (Table 4.1). For the sake of simplicity, Poisson's ratio was considered to be constant in both layers:  $\nu_{12} = \nu_{12}^e = \nu_{12}^l$  ( $1-2 \equiv L-R$ ). Moreover, the elastic properties of the earlywood and latewood layers were considered to be related to their relative densities according to the following equalities:

$$\frac{E_1^l}{E_1^e} = \frac{E_2^l}{E_2^e} = \frac{G_{12}^l}{G_{12}^e} = \frac{\rho^l}{\rho^e} = k \quad (4.2)$$

where  $k = 1.5$  or  $2$ . For deriving the effective properties, the law of mixtures was assumed (Jones, 1999, Chapter 3):

$$E_1 = (1 - w^l)E_1^e + w^lE_1^l \quad (4.3a)$$

$$E_2 = \frac{1}{(1 - w^l)/E_2^e + w^l/E_2^l} \quad (4.3b)$$

$$G_{12} = \frac{1}{(1 - w^l)/G_{12}^e + w^l/G_{12}^l} \quad (4.3c)$$

where  $w^l = 0.3$  or  $0.4$ . An estimation of the individual elastic engineering properties of both earlywood and latewood could then be determined from the above equations (4.2)

Table 4.3: Earlywood and latewood elastic engineering properties used in the finite element analyses ( $k = 2$ ,  $w^l = 0.4$ ) ( $1 - 2 \equiv L - R$ ).

	$E_1$ (GPa)	$E_2$ (GPa)	$\nu_{12}$ –	$G_{12}$ (GPa)
earlywood	10.8	1.53	0.47	1.13
latewood	21.6	3.06	0.47	2.26

and (4.3). As an example, Table 4.3 reports the elastic properties associated to earlywood and latewood constituents, used in the layered material FE model, for the case of  $k = 2$  and  $w^l = 0.4$ .

#### 4.2.2.2 Numerical results

Twenty FE analyses were performed by varying the number of annual rings over the width of the specimen ( $n = \{6, 7, 8, 9, 10\}$ ), the percentage of latewood within the annual rings ( $w^l = \{0.3, 0.4\}$ ) and the ratio between latewood and earlywood densities ( $k = \{1.5, 2.0\}$ ). From each FE analysis, the  $u_x$  and  $u_y$  numerical displacements over the gauge area were processed using the algorithm described previously in § 4.2.1.2.4 (without noise), *i.e.*, assuming an homogeneous material. An example of the numerical displacement fields, obtained for a material model with  $n = 10$ ,  $w^l = 0.4$  and  $k = 2$ , is shown in Figure 4.11(a). These displacement fields were then approximated by a 7th-degree polynomial (Figure 4.11(b)). The residual differences between the simulated and approximated displacements are shown in Figure 4.11(c). Periodic gradients can be observed from these residual maps, corresponding to the loci of the earlywood and latewood layers, that have been filtered out in the polynomial approximation scheme. However, their magnitude still remains in the order of the displacement resolution of the grid method, used experimentally in the measurement of the displacement fields (§ 5.2.3). The strain field components were then computed by numerical differentiation of these polynomial displacement fields. These strain fields (corresponding to the layered material model with  $n = 10$ ,  $w^l = 0.4$  and  $k = 2$ ) are presented in Figure 4.12, along with the FE strain maps directly obtained from ANSYS.

The strain fields were then processed by the VFM. The stiffness components obtained as output in the VFM were converted into the corresponding engineering properties, according to Eq. (1.4). The evaluation of these properties as function of the number of layers ( $n$ ) (where ( $w^l, k$ ) were set as parametric data) is shown in Figure 4.13. As it can be seen, the number of layers have a major effect on the identified values; these become closer to the reference properties when the number of layers is higher. The values of the elastic engineering constants identified by the VFM, among the whole set of material models, are reported in Table 4.4, along with the reference effective properties. Two set of results are reported: (1) the values identified directly from the finite element strain fields without noise (Ident. 1); (2) the values identified from the finite element displacement

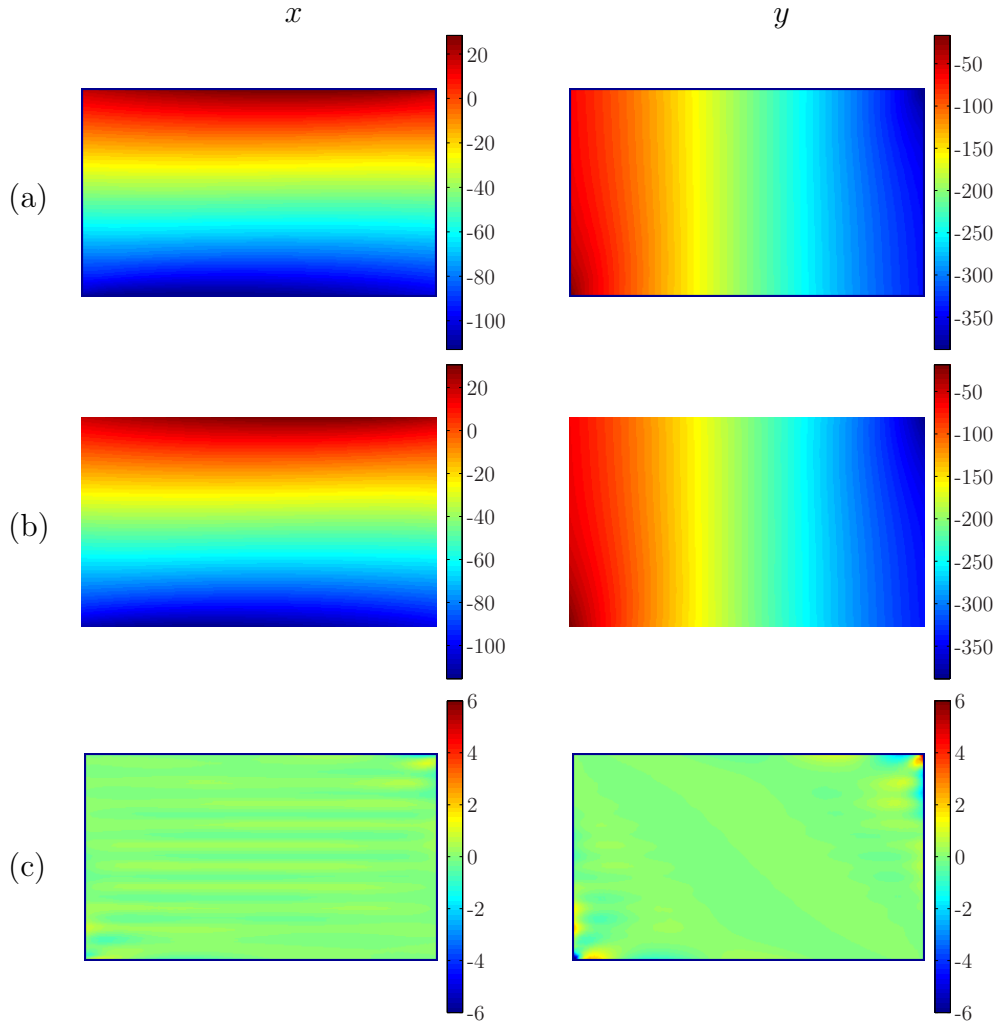


Figure 4.11: (a) Simulated, (b) approximated (7th-degree polynomial) and (c) residual  $x$  and  $y$  displacement components obtained for the layered material model ( $n = 10$ ,  $w^l = 0.4$  and  $k = 2$ ) (unit:  $\mu\text{m}$ ).

maps without noise (Ident. 2). The interest is that the homogenisation effect of the identification by the VFM and the smoothness effect of the polynomial approximation can be separated. Hence, in Ident. 1 only the homogenisation effect is analysed, whereas in Ident. 2 both effects are presented. In addition, for the sake of results interpretation, the identification results obtained from the homogeneous material model using strain fields without noise (Ident. 1 in Table 4.2) are also reported in Table 4.4 (Ident. 3).

When processing the strain fields, larger differences are obtained for  $E_2$  (-4.3%) and  $\nu_{12}$  (3.0%) with regard to the reference values, although a close estimation is obtained for both  $E_1$  and  $G_{12}$  (both less than 0.5%) (Table 4.4). Besides, these differences, especially for  $E_2$  and  $\nu_{12}$ , are higher than the ones obtained from the homogenous material model (Ident. 3), which may be explained by the geometry of the problem in terms of load direction and arrangement of the layers. Furthermore, the coefficients of variation about

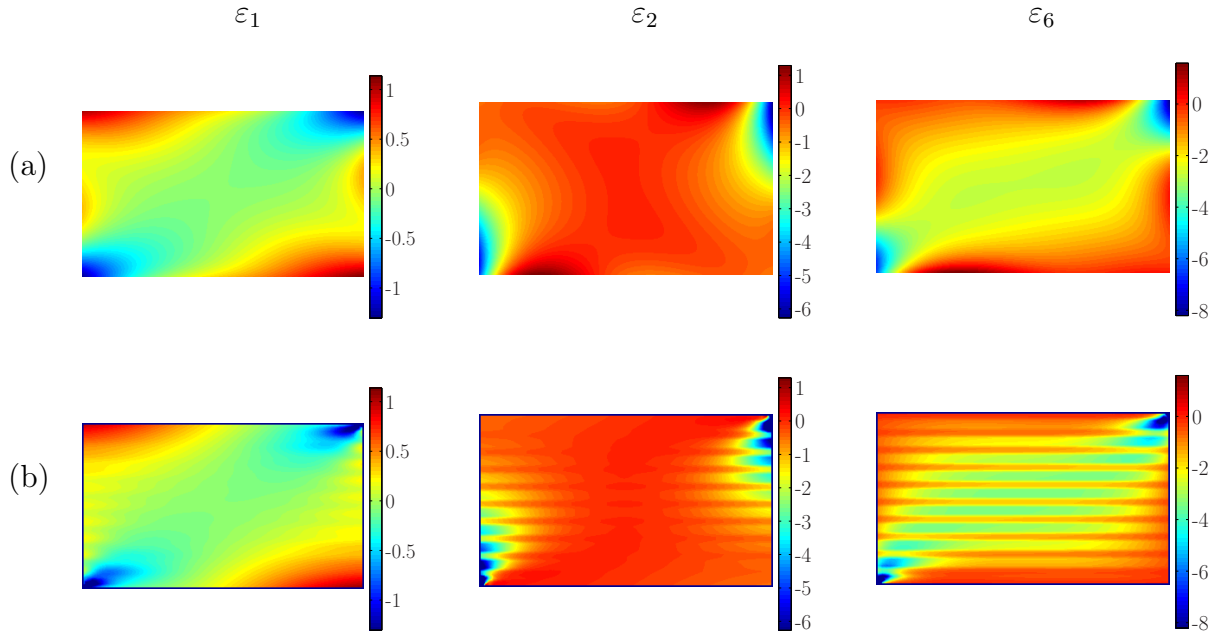


Figure 4.12: Strain field components ( $\varepsilon_1$ ,  $\varepsilon_2$  and  $\varepsilon_6$ ) of the layered material model ( $P = -261.2$  N): (a) obtained from numerical differentiation of the polynomial displacement fields; (b) delivered directly from ANSYS (unit:  $\times 10^{-3}$ ).

the mean values are low (less than 2.0%), particularly for  $E_1$  and  $G_{12}$ . Considering that the scatter of the identified homogeneous engineering properties is lower than the dispersion usually reported due to the inherent material variability of wood when experimental tests are carried out (see [Green et al., 1999](#), p. 4.23), it can be concluded that the VFM can actually retrieve the effective properties of the unnotched specimen. In other words, the elastic properties identified by the VFM are in good agreement with the moduli obtained using the law of mixtures (Eq. 4.3).

When processing the displacement fields, a higher scatter is obtained for  $E_2$  (C.V. = 2.3%) and  $\nu_{12}$  (C.V. = 3.8%), in relation to the one reached by processing directly the strain fields (Table 4.4). The differences between the mean and the reference values of the elastic constants are, in absolute value, about 4.0%, except for  $G_{12}$  which remains lower than 1%. Although  $E_2$  and  $\nu_{12}$  are identified with a larger scatter than the one obtained from the strain fields, a good agreement can still be found between reference and homogenised elastic constants obtained using the classical homogenisation laws. However, it should be noticed that when processing experimental data, the scatter generated by noisy measurements can be larger than the one due to the layered structure of the wood specimens. Therefore, it was concluded that the characterisation of the elastic properties of *P. pinaster* wood by the unnotched Iosipescu test and the VFM provides a relevant estimate of the homogenised stiffness properties of wood.

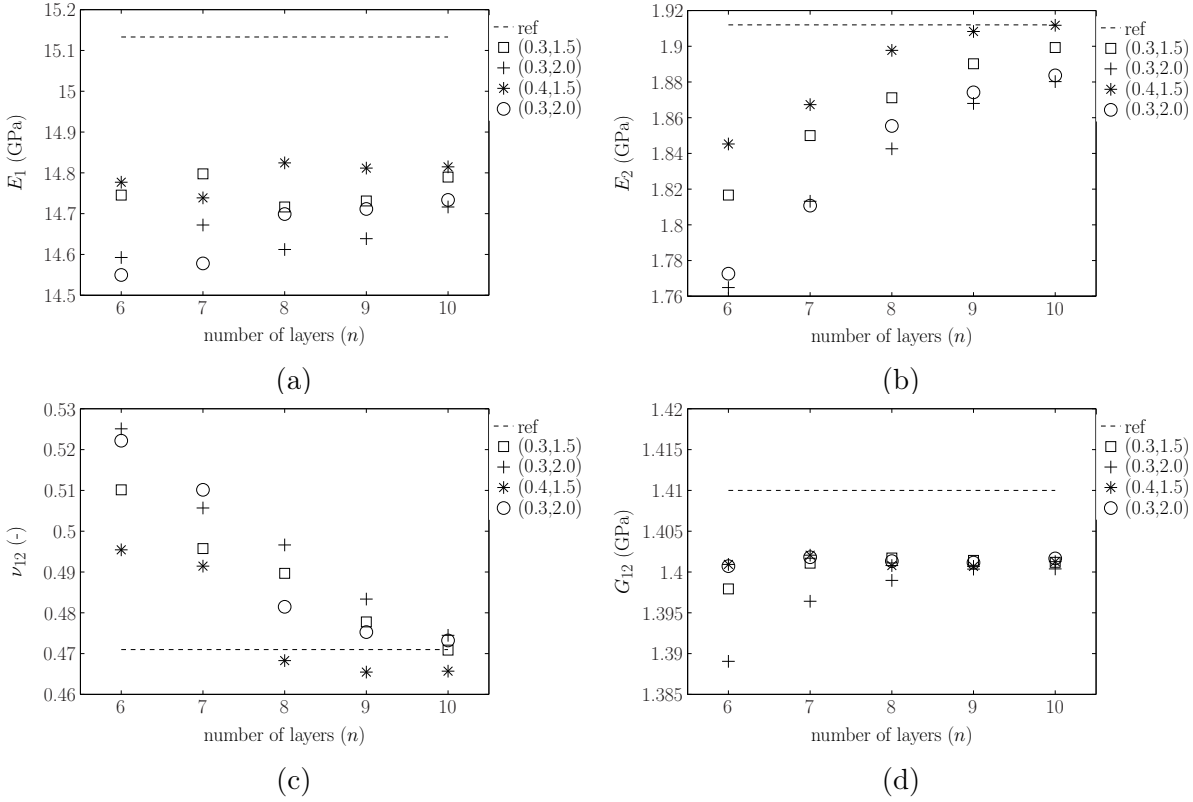


Figure 4.13: Elastic constants: (a)  $E_1$ , (b)  $E_2$ , (c)  $\nu_{12}$  and (d)  $G_{12}$ , identified from the layered material models by the virtual fields method (parametric data:  $(w^l, k)$ ).

## 4.3 Optimal specimen configuration: sensitivity study

### 4.3.1 Optimisation scheme

The identification of the stiffness components using the VFM has already led to satisfactory results, by processing numerical displacement fields obtained from the  $0^\circ$  configuration of the unnotched Iosipescu test (§ 4.2). However, it was found that for this configuration both the  $Q_{22}$  and the  $Q_{12}$  stiffness components are identified with less confidence than the  $Q_{11}$  and  $Q_{66}$  ones (§ 4.2.1.2.1). This can partly be explained by the fact that the transverse strain ( $\varepsilon_2$ ) is almost zero over a large part of the gauge section, excepting under the inner loading points where the specimen is submitted to a local compression (*e.g.*, see Figure 4.7). Moreover, the shear strain component ( $\varepsilon_6$ ) is higher and more evenly spread over the active gauge area than the other two components. Therefore, the test can be improved to a configuration where the whole set of stiffness properties may be identified with the same confidence.

For the purpose of the study, an optimisation scheme was defined as presented in Figure 4.14. Generically, both the shape of the specimen and loading arrangement can be optimised; however, the rectangular geometry of the unnotched specimen and the

Table 4.4: Identification of homogenised elastic engineering properties of the layered material model of the unnotched Iosipescu wood specimen by the virtual fields method: (1) directly from the finite element strain fields without noise (Ident. 1); (2) from the finite element displacement maps without noise (Ident. 2). Ident. 3: identification results obtained from the homogeneous material model (from Ident. 1 in Table 4.2) ( $1 - 2 \equiv L - R$ ).

		$E_1$	$E_2$	$\nu_{12}$	$G_{12}$
		(GPa)	(GPa)	–	(GPa)
Reference		15.13	1.912	0.471	1.410
Ident. 1: Strain	Mean	15.08	1.830	0.485	1.404
	C.V. (%)	0.58	1.91	2.01	0.76
	dif. (%)	-0.34	-4.29	2.97	-0.43
Ident. 2: Displacement (7th-degree polynomial)	Mean	14.71	1.856	0.489	1.400
	C.V. (%)	0.56	2.27	3.77	0.21
	dif. (%)	-2.78	-2.93	3.82	-0.71
Ident. 3: Homogeneous model (strain fields without noise)	Mean	15.18	1.899	0.470	1.412
	dif. (%)	0.30	-0.69	-0.16	0.11

Iosipescu fixture are restrictive conditions. In practice, two parameters can easily be varied to affect the strain distribution in the centre of the specimen (Figure 3.6): (1) the length of the active gauge area ( $L$ ), which can be conveniently adjusted by the fixture; (2) the angle ( $\theta$ ) defining the orientation of the grain (fibre) with respect to the specimen longitudinal direction. Hence,  $L$  and  $\theta$  were set as design variables. The design space for these parameters was chosen, respectively, within the range of:

$$\begin{cases} L \text{ (mm)} \in \{14, \dots, i-4, i, i+4, \dots, 46\} \\ \theta \text{ (}^\circ\text{)} \in \{0, \dots, i-2, i, i+2, \dots, 50\} \end{cases}.$$

On the one hand, a gauge length lower than about 14 mm may generate high strain gradients in the specimen that will hardly be represented because of the smoothness process in the differentiation of the measured displacements. On the other hand, for a length value higher than about 46 mm, the width-to-length ratio of the gauge area becomes too different from the 2/3" (11.14 mm) sensor format of typical digital cameras (*e.g.*, 1376(H) $\times$ 1040(V) for the PCO Sencam camera used experimentally), resulting in a degradation of the spatial resolution. Furthermore, in order to avoid the configurations for which the directions of the applied load and grain are too close, angles higher than 50° were not considered in the search domain. The justification is that for these configurations (the 90° configuration being the worst) the condition of constant strain through the thickness of the specimen is more difficult to achieve in practice, because of the end-effects generated at the vicinity of the inner loading points (Melin and Neumeister, 2006; Morton et al.,

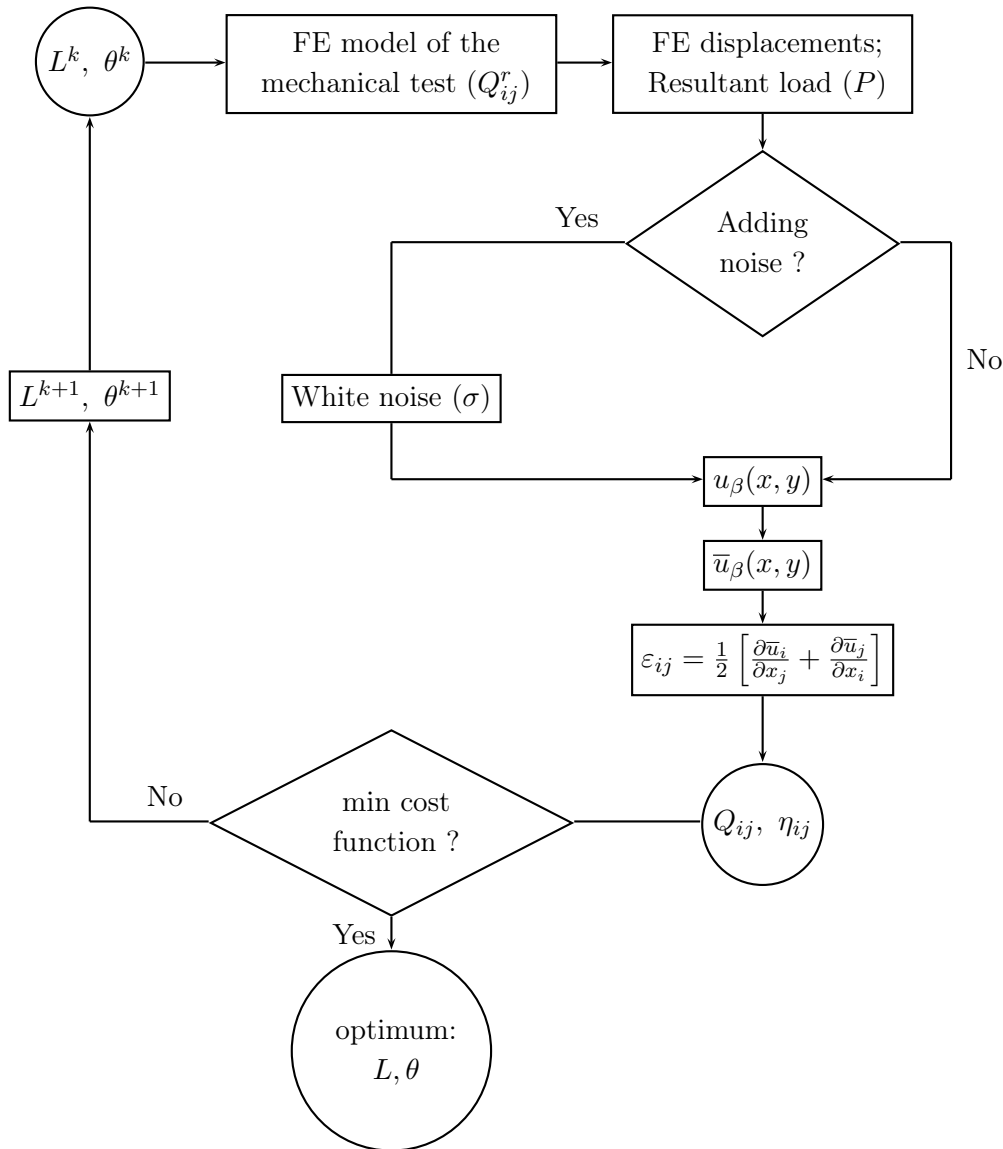


Figure 4.14: Algorithm used in the optimisation scheme of the configuration of the unnotched Iosipescu specimen.

1992; Pierron, 1998). In this case, an additional scatter can be obtained in the stiffness results, especially if the measurements are performed over only one face of the specimen.

In this study, the displacement fields (without noise) were obtained numerically, using the homogeneous 2D FE model of the unnotched Iosipescu test (§ 4.2.1). A first set of design parameters ( $L = 30$  mm and  $\theta = 0^\circ$ ) was arbitrarily chosen to initiate the iterative routine from Matlab. Each set of parameters was updated in an ASCII file and read afterwards by the FE code, written in the APDL language of ANSYS. The reference elastic properties used throughout the analyses are reported in Table 4.1. The isoparametric finite element PLANE184 (4 nodes, 8 degrees of freedom) was used. The same

mesh refinement and boundary conditions detailed for the  $0^\circ$  configuration (Figure 4.2) were kept here. The finite element analyses in ANSYS were launched in batch mode. Both coordinates and displacements at the centroid of the elements across the gauge area resulting from the analyses, as well as the resultant reaction force at the prescribed nodes in the right-hand side of the specimen (Figure 4.2(a)), were written in output ASCII files afterwards. The results were read by the Matlab routine. For all configurations, the simulated displacements were interpolated, using Delaunay triangulation, at an array of points covering the actual gauge section and spaced by  $p$  mm, where  $p$  represent the actual pitch of the grid, which is recalculated (as described later in § 5.2.2) in each analysis for the new value of  $L$ , *i.e.*, taking into account the actual dimensions of the gauge section. These interpolated displacement fields were then approximated by a 7th-degree polynomial and numerically differentiated to compute the in-plane strain field components over the gauge section (§ 4.2.1.2.4). The strain fields, the thickness of the specimen, the dimensions of the gauge area, the grain angle, the resultant reaction force and the number of elements to be used in the piecewise special virtual fields were then input into the VFM algorithm. For all configurations, a *virtual* mesh of  $8 \times 4$  elements through the  $x$  and  $y$  directions, respectively, used previously for the  $0^\circ$  configuration, was conserved here. From the output in the VFM routine, the relative sensitivity to noise terms,  $\xi_{ij} = \eta_{ij}/Q_{ij}$ , were analysed.

The minimisation of the cost function,  $\phi(L, \theta)$ , chosen throughout the optimisation problem should yield a configuration for which the strain components are balanced out and evenly spread across the gauge section. As mentioned above, the sensitivity to noise terms provided in the VFM,  $\xi_{ij}$ , can be employed in this analysis since, for a given uncertainty of the input strain fields, they quantify the identifiability of each parameter in terms of the uncertainty in the identification process. Hence, the following cost function can be defined (Pierron et al., 2007):

$$\phi(L, \theta) = \frac{(\xi_{11} - \xi_{22})^2 + (\xi_{11} - \xi_{66})^2 + (\xi_{22} - \xi_{66})^2}{(\xi_{11}^2 + \xi_{22}^2 + \xi_{66}^2)^2}. \quad (4.4)$$

The lower the value of  $\xi_{ij}$  the better the identification of the corresponding  $Q_{ij}$  component.

The evaluation of the cost function (Eq. 4.4) was iteratively repeated until a minimum value was eventually reached. In each iteration a new set of design parameters was introduced and the cost function was evaluated from the VFM results until convergence was reached (Figure 4.14).

### 4.3.2 Numerical results

The evolution of the cost function within the search domain of the design variables is presented in Figure 4.15. As it can be seen, the cost function varies more significantly with the variation of the grain angle than with the gauge length. This pattern is directly related to the anisotropy of the material. It is clear that, according to the sensitivity

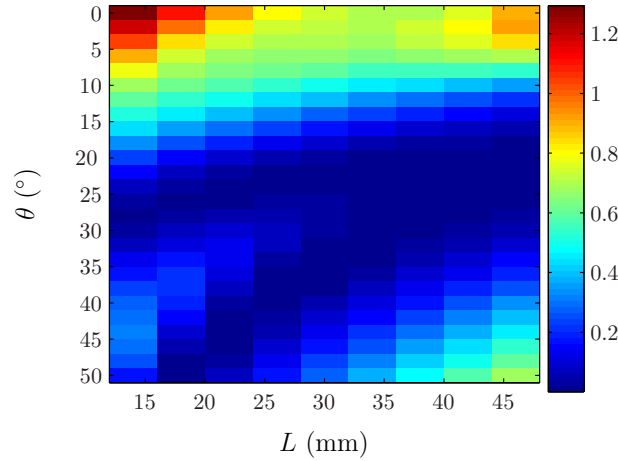


Figure 4.15: The cost function pattern as function of the  $L$  and  $\theta$  design variables.

to noise criterion, the global identifiability can be improved by rotating the grain angle. Grain angles between  $20^\circ$  and  $35^\circ$  and gauge lengths ranging from 30 mm to 40 mm, are located in a valley of the cost function distribution. The best configuration was found at  $L = 35$  mm and  $\theta = 30^\circ$ .

In order to compare the  $0^\circ$  and  $30^\circ$  configurations, the strain field components calculated from the displacement fields (without noise) simulated for both cases are shown in Figure 4.16 ( $L = 35$  mm). It can be observed that indeed, in the material coordinate system, a more evenly spread distribution of both  $\varepsilon_1$  and  $\varepsilon_2$  strain components is reached for the  $30^\circ$  configuration. This can also be clearly observed from the corresponding histogram plots. However, the shear strain component remains evenly distributed for both configurations. Thus, it can be concluded that a better identification can be expected from the  $30^\circ$  configuration.

## 4.4 Conclusions

In this chapter the proposed inverse identification approach, yielding the four  $LR$  stiffness components of *P. pinaster* wood from full-field displacements obtained in a single test, was numerically tested. From the analyses, the following conclusions can be drawn.

- (i) When processing numerical displacement fields obtained for the  $0^\circ$  configuration, a gauge length equal to 34 mm was found suitable for the stiffness identification. In this case, all the in-plane stiffness parameters  $Q_{ij}$  could be identified with relative differences with regard to reference values lower than 3.3%. However, when using the sensitivity to noise coefficients provided by the VFM, it was shown that the mechanical response of the  $0^\circ$  configuration is more significantly affected by the  $Q_{11}$  and  $Q_{66}$  stiffness components than by the  $Q_{22}$  and the  $Q_{12}$  ones.

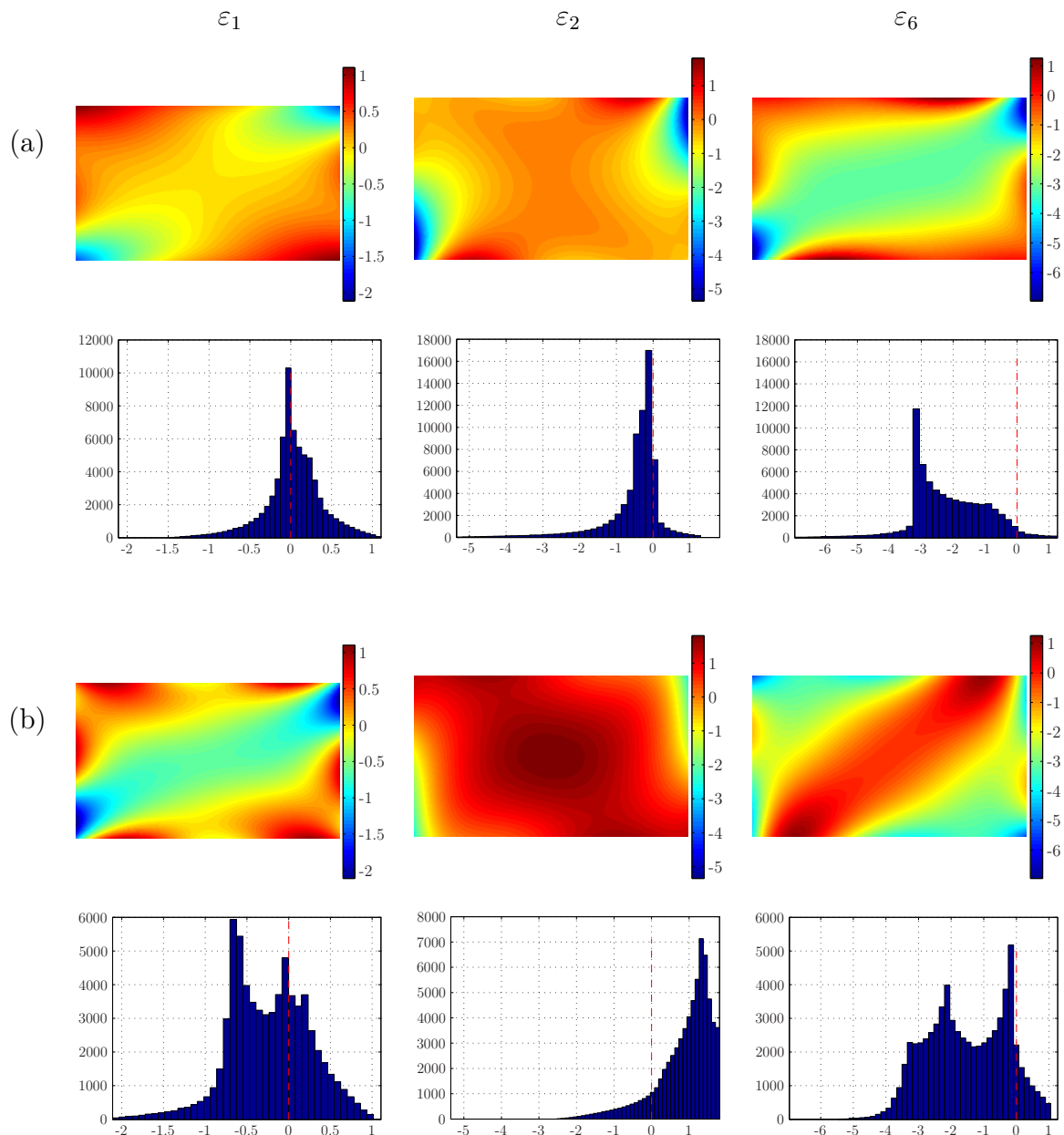


Figure 4.16: Strain field maps ( $\varepsilon_1$ ,  $\varepsilon_2$  and  $\varepsilon_6$ ), along with their histograms plots, obtained for the ( $L = 35$  mm): (a)  $0^\circ$  configuration, (b)  $30^\circ$  configuration (unit:  $\times 10^{-3}$ ).

- (ii) A study was lead in order to calibrate the polynomial degree to be used in the strain reconstruction scheme. It was shown for the  $0^\circ$  configuration that a 7th-degree polynomial was a good compromise between the efficiency of noise filtering and the faithfulness of the reconstruction.
- (iii) Piecewise special virtual fields were used in the study. For the  $0^\circ$  configuration, it was found that the effect of the number of elements of the mesh, used to define the virtual fields, was less significant for both  $Q_{11}$  and  $Q_{66}$  parameters than for the

$Q_{22}$  and  $Q_{12}$  ones. Nevertheless, a good compromise was reached for a mesh of  $8(x) \times 4(y)$  elements.

- (iii) In working out the VFM, the homogeneity assumption of the material was assumed. This assumption was checked by building up a layered material model, consisting of several successive earlywood and latewood layers, with different volume fractions, number of layers and elastic engineering properties. Different geometrical models were considered in order to study the inherent variability associated to the specimen composition. From these material models, the effective properties provided by the law of mixtures could be recovered by the VFM, proving the relevance of the homogeneity assumption.
- (iv) It was found that the rotation of the grain angle ( $\theta > 0$ ) enhances the stiffness parameter identifiability by improving the contribution of both  $\varepsilon_1$  and  $\varepsilon_2$  strains, still keeping the influence of the shear strain component,  $\varepsilon_6$ . Thus, for a gauge length of 35 mm, a grain angle of  $30^\circ$  was found to maximise the global identifiability of the stiffness parameters.

# Chapter 5

## Characterisation of the longitudinal-radial stiffness of *P. pinaster* wood by a single test. II: Experimental validation

### 5.1 Introduction

The aim of this chapter is to validate, from an experimental point of view, the material characterisation approach presented in Chapter 3.

### 5.2 Experimental work

#### 5.2.1 Tree and specimens

The specimens used in this work were manufactured from wood coming from a single *P. pinaster* tree, aged of 74 years and selected in the district of Viseu (Portugal) (Figure 5.1). For reasons of availability, the specimens were cut in the outer part of quarter-sawn and plain-sawn boards taken at about eight meters from the basal plane of the tree. These boards were previously dried in a kiln to a moisture content of about 10–12%.

The specimen consisted in a straight rectangular coupon oriented in the longitudinal-radial (*LR*) principal plane with nominal dimensions of  $80(L) \times 20(R) \times 5(T)$  mm<sup>3</sup>. The surface of  $80(L) \times 20(R)$  mm<sup>2</sup> was chosen in order to fit the Iosipescu fixture used in the experimental work. The specimen thickness was set to 5 mm as a compromise to ensure both material representativeness and plane stress assumption. It may be worth saying that a thicker specimen is expected to be more prone to non-uniform load distributions through the thickness, which can result in different deformations measured at the front and back



Figure 5.1: *P. pinaster* tree from where the specimens were manufactured.

surfaces of the specimen (Pierron, 1998; Xavier et al., 2004). Consequently, this can yield an additional dispersion on the identification results due to the test itself, especially if the measurements are performed over only one face of the specimen. Besides, the relatively small size of the specimen, with regard to the local curvature of the annual growth rings, has justified the approximation of cylindrical anisotropy of wood by a rhombic orthotropy. In average, the width of the annual rings covered by the specimens was about 2 mm.

In the previous numerical study (§ 4.2 and 4.3), it was shown that the stiffness identifiability could be improved by adjusting the off-axis angle of the specimen. Accordingly, different specimen configurations were proposed to be investigated here, having the grain oriented at  $0^\circ$ ,  $30^\circ$  and  $45^\circ$  (see Figure 5.2(d)), with regard to the specimen longitudinal axis.

Several specimens were prepared for repeatability quantification purposes. The samples were free from visible structural defects. They were kept into the laboratory in order to reach their equilibrium state before grid transfer and testing. The oven-dry density of the specimens (determined as the ratio between the oven-dry weight and green volume) was found to range between  $0.505$  and  $0.559 \text{ g.cm}^{-3}$ . Using the oven-dry method (§ 1.4.3.1), the moisture content of the specimens during testing was determined to be around 9–10%.

The wood samples are assumed here as being completely damage free prior to their mechanical testing. Although convenient, this assumption can be questionable because wood within the stem may be damaged due to the growth stresses and environmental loads; besides, harvesting, transportation and handling can cause further damage. Any inherent pre-damage may be responsible for further variability of the mechanical properties of wood.

### 5.2.2 Pitch evaluation and grid transfer

The pitch of the grid ( $p$ ) was chosen considering the following specifications.

- A gauge section of  $34(L) \times 20(W)$  mm<sup>2</sup> (see Figure 3.6).
- A 12 bit PCO SenSicam CCD Camera with  $1376(H) \times 1040(V)$  pixels resolution and  $6.45 \mu\text{m}$  pixel size.
- A number of pixels per period ( $N$ ) equal to 4.  $N$  has to be chosen as a compromise between resolution and spatial resolution. On the one hand, a high value of  $N$  will improve the resolution of the method (which is proportional to  $1/\sqrt{N}$ ), as more pixels are used for sampling a whole period of the grid. On the other hand, a small value of  $N$  ( $N \geq 3$ ) will favour the spatial resolution, as an independent phase evaluation is performed over about one period of the grid. Here, the choice was to maximise the spatial resolution of the method.

A pitch of  $98.8 \mu\text{m}$  was then assessed for fulfilling the previous requirements according to the following equation:  $p = \max\{\frac{LN}{H}, \frac{WN}{V}\}$ . This value was rounded up to a pitch of  $100 \mu\text{m}$ , corresponding to a spatial frequency of 10 lines/mm (low-frequency grating), because it must be a multiple of  $20 \mu\text{m}$  due to printing requirements.

In our experiments the grid was transferred according to the procedure proposed by (Piro and Grédiac, 2004). The first step consists in printing the network of crossed lines onto a photographic film (Ferrania photographic film AI PO-50<sup>®</sup>) made of a polymeric transparent support and a photosensitive emulsion coating (a Heidelberg Recorder 3030 plotter set to a resolution of 2540 dpi was used). The pattern of lines was printed from a Postscript file within which the grid parameters (*i.e.*, the pitch, the relative size of the bright and dark distribution and the paper size) can be accurately and easily adjusted. As both components of the displacement field are needed to compute the in-plane strain fields (Eq. 3.4), a 2D grid (*i.e.*, with horizontal and vertical superimposed orthogonal lines, with equal pitch in both directions) was bonded onto the specimens as follows.

- After manufacturing, each specimen was polished (by hand, with low pressure and working over a glass surface) using several grits of sandpaper ranged from P240 up to P800. Particular care was given to the parallelism of the loading faces of the specimen and their perpendicularity to the front and back surfaces. The final dimensions of the specimens (length, width and thickness) as well as their grain orientation, were then determined as the mean value of at least three independent measurements, using, respectively, a micrometer (resolution of  $0.02 \text{ mm}$ ) and a goniometer (resolution of about  $0.5^\circ$ ). The gauge area at the centre of the specimens was delimited afterwards (Figure 5.2(a)). The specimens were protected all around

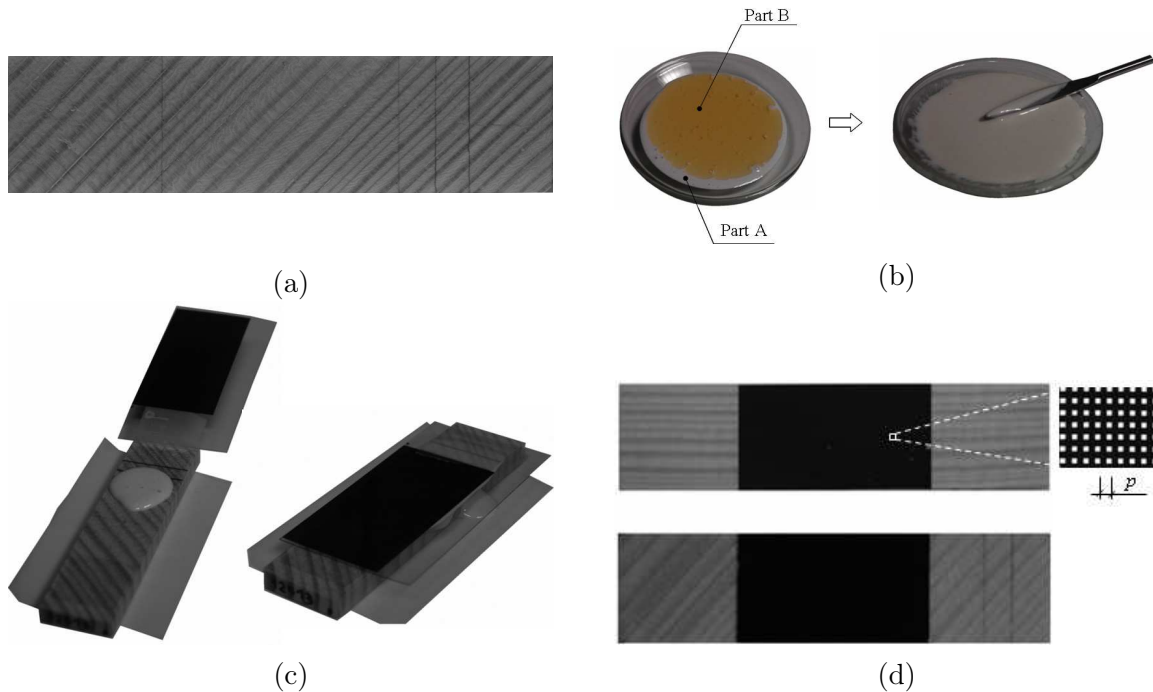


Figure 5.2: Illustration of the steps in the grid transfer ( $p = 0.1$  mm).

this region using low-medium masking or sticky tape. This protection is helpful because it will avoid the direct contact of the glue, used in the grid transfer, with other surfaces of the specimen. The gauge region was cleaned up using a cleaning agent (*e.g.*, acetone or alcohol) followed by M-Pre Neutralisant 5A (Vishey Measurement), as recommended in strain gauges bonding.

- From the printed photographic film (size A4) a piece with dimensions slightly higher than the gauge area was carefully cut (over the non printed face of the film). Its printed face was then cleaned (spreading a cleaning agent all around the surface without using a gauze). After drying, the piece of film was placed over the region of interest of the specimen using a Sellotape bonded to one end. Special care must be taken to guarantee that the printed lines will be well oriented with regard to the specimen directions. To clarify this point, let us consider a grid consisting of vertical lines characterised by a spatial frequency vector  $\mathbf{F}(0, 1/p)$ . Ideally, the correct orientation of the grid must satisfy the condition  $\mathbf{F} \cdot \mathbf{i} = 0$  (where “ $\cdot$ ” represents scalar product between two vectors); thus, any rotational misalignment  $\delta\theta$  between the grid and specimen axes will be proportional to  $\cos(\delta\theta)$ . If  $\delta\theta$  remains small, errors on the positioning of the grid can be neglected; for instance, a deviation of  $1^\circ$  introduces an error of 0.02% in the phase evaluation.
- The film was bonded onto the specimen using the Epotechny E504<sup>®</sup> epoxy resin (Figure 5.2(b)). After mixing its components, this glue has a white colour, which

increases the final optical contrast of the grid pattern. For the preparation of the resin, two components, part  $A$  (the resin) and part  $B$  (the hardener), need to be mixed in the relative proportion of  $B/A = 1/5 \pm 10\%$  (Figure 5.2(b)). The weight measurements were performed using an analytical balance (Ohaus Explorer Pro) with a resolution of 0.001 g (for the surface of  $34 \times 20 \text{ mm}^2$ , 1 g of part A per specimen may be sufficient). The two components must be carefully and slowly mixed using a spatula and left at rest a few minutes to release air bubbles.

- A sufficient quantity of resin was poured at the base of the gauge region in the edge where the film is fixed to the specimen (with Sellotape) (Figure 5.2(c)). While maintaining the film under an angle of about  $30^\circ$ , the glue is spread all over the extension of the gauge area by progressively laying the film, with low pressure and with the help of a gauze. All spilt resin was removed afterwards.
- The grid (film+resin) was then covered with silicone rubber and subjected, during cure, to a small mass of about 50 g in order to create an even and thin layer with a thickness of about 0.1 mm. The resin was then cured during a week at a constant temperature of  $23^\circ\text{C}$ .
- After the polymerisation of the resin, the backing of the photographic film was carefully removed pulling the film slowly and all in one go. Doing so, the coating of the film remains bonded to the glue defining a periodic bright and dark grating over the gauge area (Figure 5.2(d)).

### 5.2.3 Photomechanical set-up and measurement details

A PCO SenSicam CCD Camera connected to a PC, along with a Nikon AF Zoom–Nikkor 28–105mm f/3.5–4.5D IF lens and a 15 mm extension tube were used for image grabbing (Figure 5.3(a)). The camera-lens system was mounted on a tripod and positioned in front of the specimen, with special attention paid to the alignment of the CCD sensor and grid planes. The image acquisition was performed with the software CamWare v2.03<sup>®</sup> supplied with the CCD camera (Figure. 5.4(a)). The focal length, the aperture of the lens and the exposure time, along with the working distance (defined as the distance between the object and the front of the camera) and light source intensity were carefully selected in order to achieve a grid image of good quality. In this context, this means a contrasted image of the grid lines (*i.e.*, with a histogram showing a relatively high ratio of maximum to minimum brightness, within the dynamic range of the camera sensor, over the region covered by the grid) and a magnification leading to approximately 4 pixels/period. More precisely, the calibration of the camera-lens optical system was performed as follows.

- Positioning and alignment of the optical system: after setting up the specimen into the fixture, the CCD camera was aligned with respect to the grid plane. Since only

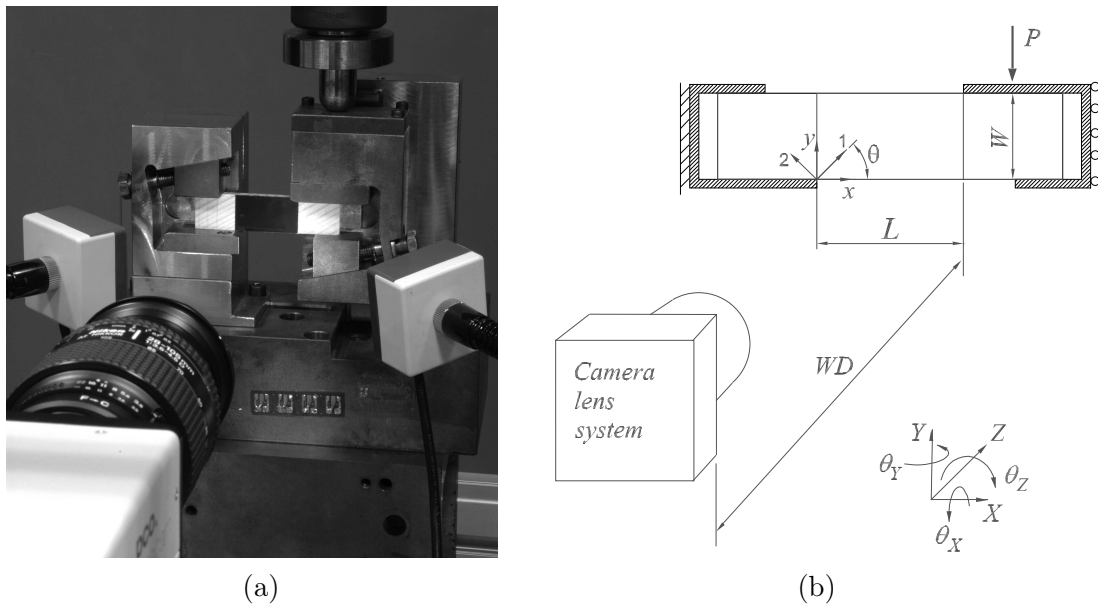


Figure 5.3: (a) Photo and (b) schematic of the mechanical set-up ( $WD$  (working distance)  $\sim 450$  mm).

one camera is used, this adjustment is important to guarantee a constant value of magnification of the grid image (non-perspective effect). In practice, the translations ( $X, Y, Z$ ) and all possible rotations ( $\theta_X, \theta_Y, \theta_Z$ ) of the optical system need to be adjusted (Figure 5.3(b)). The  $X$  and  $Y$  spatial positions of the optical system are simply set in order that the imaged field of view will cover the whole gauge region (area delimited by the grid) throughout testing. The rotations about these axes,  $\theta_X$  and  $\theta_Y$ , can be adjusted by a ruler (*e.g.*, a laser ruler) to achieve a correct parallelism between the camera sensor and grid planes. The rotation  $\theta_Z$  can be set using a moiré effect, providing the sub-sampling image  $I(x, y)/N$  (in our case  $N = 4$ ) can be monitored in real time. In such image, when the system parameters (*e.g.*, the focal length or the working distance) are adjusted so that each period of the grid is imaged by approximately  $N$  pixels, bi-dimensional crossed fringes will be seen. Namely, this occurs because the periods are not imaged by an exact integer number of pixels, so a bias is progressively introduced across the grid image, generating low-frequency fringes (like in moiré) instead of a pure black or white image (depending if the imaged regions within the periods of the grid cover the dark or the bright lines, respectively). Provided that some fringes are visible across the region of interest (*i.e.*, no perfect match of  $N$  pixels per period exists), they can be used to align the sensor array with respect to the grid lines. This is fulfilled when parallel fringes, in both horizontal and vertical directions, are imaged. Finally, the distance  $Z$  is adjusted, coupled with both the focal length of the lens and the sensitivity to out-of-plane displacements, in order to calibrate the magnification of the optical system

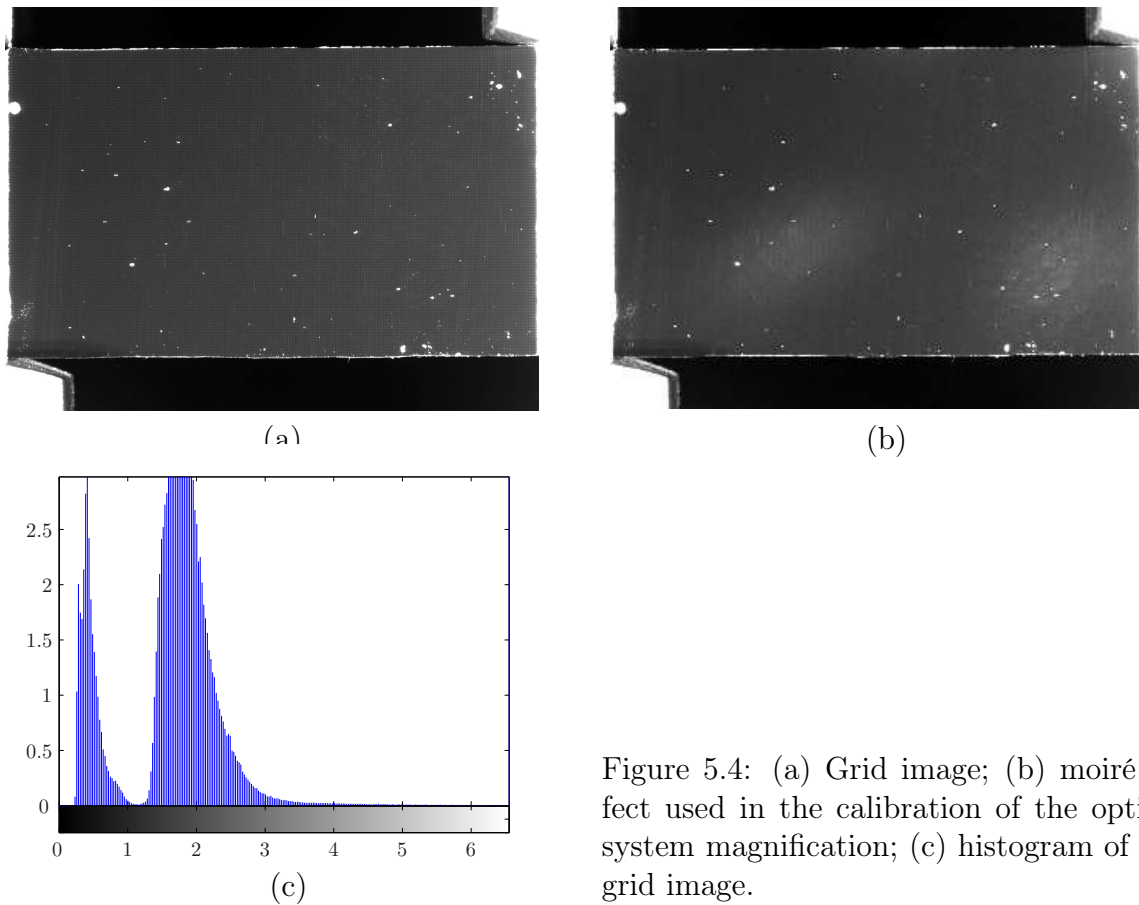


Figure 5.4: (a) Grid image; (b) moiré effect used in the calibration of the optical system magnification; (c) histogram of the grid image.

as explained next.

- Calibration of the magnification ( $m$ ) of the imaging system: the magnification is determined as:  $m = p_{s_i}/p_{s_o}$ , where  $p_{s_i}$  is the pixel size at the image plane whilst  $p_{s_o}$  is the pixel size at the object plane, determined in the grid method by  $p_{s_o} = p/N$ . In our experiments,  $m = \frac{6.45\mu m}{25\mu m} = 0.258$  (1:3.9). In practice, the calibration of the optical system for this magnification can be achieved in two ways. On the one hand, a scale is fixed in the same plane as the grid. The calibration here consists in setting an exact number of pixels over a known distance. As an example and for a grid pitch of 0.1 mm, a total of 40 pixels must image a distance of 1 mm in order to fulfil the sampling requirement of 4 pixels/period. On the other hand, the sub-sampling image (moiré effect described previously) can also be efficiently used for this purpose. In this case, in order to approximate the exact integer number of pixels per period, the total number of fringes in the sub-sampling image ( $I(x, y)/N$ ) must converge to zero (Figure 5.4(b)). In the ideal situation, no bias is introduced (by an incorrect sampling) so the moiré fringes in the image will completely lose their contrast since only 1 among  $N$  pixels over the periods will be imaged across the field of view, all corresponding to the same position in the grid periods. As an

example, over the specimen width of 20 mm there are theoretically 200 periods, so exactly 800 pixels must cover this distance in a error-free calibration. In practice, however, namely because of lens aberrations, only a close approximation is possible. Experimentally, the number of fringes in the sub-sampling image is proportional to the sampling error, *i.e.*, it corresponds to the number of periods that deviates from the ideal case. Thus, if there is one fringe across the width of the specimen in the sub-sampling image, for instance, that means that a sampling error of 1 over 200 periods is obtained, corresponding to a calibration error of 0.05%. In practice, the magnification can be controlled either by the distance  $Z$  or by the focal length of the lens. In addition, the distance  $Z$  must be chosen taking into account the coupling effect between in-plane and out-of-plane displacements existing in monocular techniques (this will be detailed later). In our experiments, the working distance was set to about 450 mm, and the focal length to 100 mm. A 15 mm extension tube was mounted between the camera and the lens which, for the same magnification, allows imaging the grid/specimen to a further distance (Figure. 5.3).

- Exposure time: the value of the exposure time is selected as a compromise between two conditions. On the one hand, throughout the exposure time, the specimen must not significantly move with regard to the CCD sensor, *i.e.*, the global rigid-body motion of the specimen ( $d$ ) must remain small when compared to the pixel size in the object plane ( $p_{s_o}$ ). The time ( $t$ ) fulfilling this condition can be evaluated from the kinematic expression:  $t = d/v$ , where  $v$  is the cross-head displacement rate of the testing machine. The exposure time can then be defined such that:  $t \ll p_{s_o}/v$ . On the other hand, the integration time should be long enough to insure a high signal-to-noise ratio of the light signal magnitude compared to the measurement (intensity) uncertainty. Furthermore, the selection of this parameter is intrinsically related to the amount of light reflected by the specimen (which can be controlled by the aperture of the lens or directly by the potentiometer of the light source projected over the specimen), since both the duration and the intensity quantify the actual amount of light reaching the photosensitive areas (photodiodes) of the camera and therefore the amount of electronic signal generated by the sensor. Therefore, as a compromise, an exposure time of  $1/8 = 0.125$  s ( $p_{s_o} = 25 \mu\text{m}$ ,  $v = 1$  mm/min) was chosen here.
- Sharpness of the grid image: the image was carefully focused at the grid plane setting the lens aperture at  $f/2.3$ . For a given focal length and working distance, this maximum aperture (minimum  $f$ -number) corresponds to minimum depth of field (it represents the distance by which the object may be shifted back or forward still remaining in acceptable focus) in the image formation, which can be helpful in focusing exactly onto the plane of interest. However, before testing, the  $f$ -number

was changed to a value of  $f/8$  in order to improve the depth of field such that, throughout the test, even if the specimen is subjected to an out-of-plane motion (a few tenth of  $\mu\text{m}$ ) the grid image will still remain in focus, *i.e.*, keeping its contrast. In order to avoid pixel saturation in the image when changing the lens aperture, the light source must be properly adjusted afterwards since the exposure time is kept constant (during either calibration or testing). The histogram of the grid image is also helpful in this step of the calibration, since the pixels distribution, over the dynamic range of the light intensity image, gives insight into the contrast of the grid image (as a function of the maximum and minimum intensity values) (Figure. 5.4(c)).

During the tests, both load ( $P^t$ ) and grid images ( $I^t(x, y)$ ) were automatically recorded at intervals of 1 s ( $t = 0, 1, \dots, n$ ) (see Figure 3.3). From the grid images, the phase difference was afterwards evaluated for each pair of consecutive measurements ( $\Delta\phi_\beta^t(x, y) = \phi_\beta^t(x, y) - \phi_\beta^{t-1}(x, y)$ ;  $\beta = x, y$ ;  $t \geq 1$ ). One advantage of this approach is that the phase difference between two consecutive acquisitions is not wrapped, *i.e.*, it is always obtained within the interval  $[-\pi, \pi]$  because the undergoing displacements between the two consecutive states does not exceeds the pitch of the grid. Therefore, the usual phase unwrapping process (Surrel, 1999) in data processing is avoided (this approach for avoiding phase jumps is usually called temporal unwrapping (Huntley and Saldner, 1993)). For a given load level, the corresponding continuous displacement fields were subsequently determined by summing up the contributions of all previous incremental displacement fields:

$$\bar{u}_\beta^t(x, y) = \sum_{t=1}^n \bar{u}_\beta^{t-1}(x, y) + \frac{p}{2\pi} \Delta\phi_\beta^t(x, y) \quad (t = 1, \dots, n). \quad (5.1)$$

In the grid method, the measurement of the in-plane displacement field is coupled to the out-of-plane motion of the specimen ( $\Delta Z$ ) because only one camera is used (monocular vision). If the specimen undergoes a given out-of-plane displacement during the test, the magnification of the optical system will be consequently changed ( $\Delta m$ ). This induces a parasitic effect that is equivalent to an apparent uniform pitch variation. It is similar to submit the specimen to a tension ( $-\Delta Z$ ) or compression ( $+\Delta Z$ ) load in the direction perpendicular to the grid lines. Hence, a non negligible apparent linear deformation of the grid can occur, being approximated by (thin-lens model):  $\varepsilon_\beta^a = \Delta m/m = -\Delta Z/Z$ , where  $\beta = 1$  or  $2$  for a grid with vertical or horizontal lines, respectively, and  $Z$  is the distance between the object and the lens centre. In our experiments,  $Z$  was around 350 mm, so if a strain resolution of  $10^{-4}$  is targeted, it can be calculated that a  $\Delta Z$  of about 35  $\mu\text{m}$  can disturb the measurements. Therefore, in order to monitor the magnitude of  $\Delta Z$ , a LVDT was placed on the back surface of the specimen during the experiments.

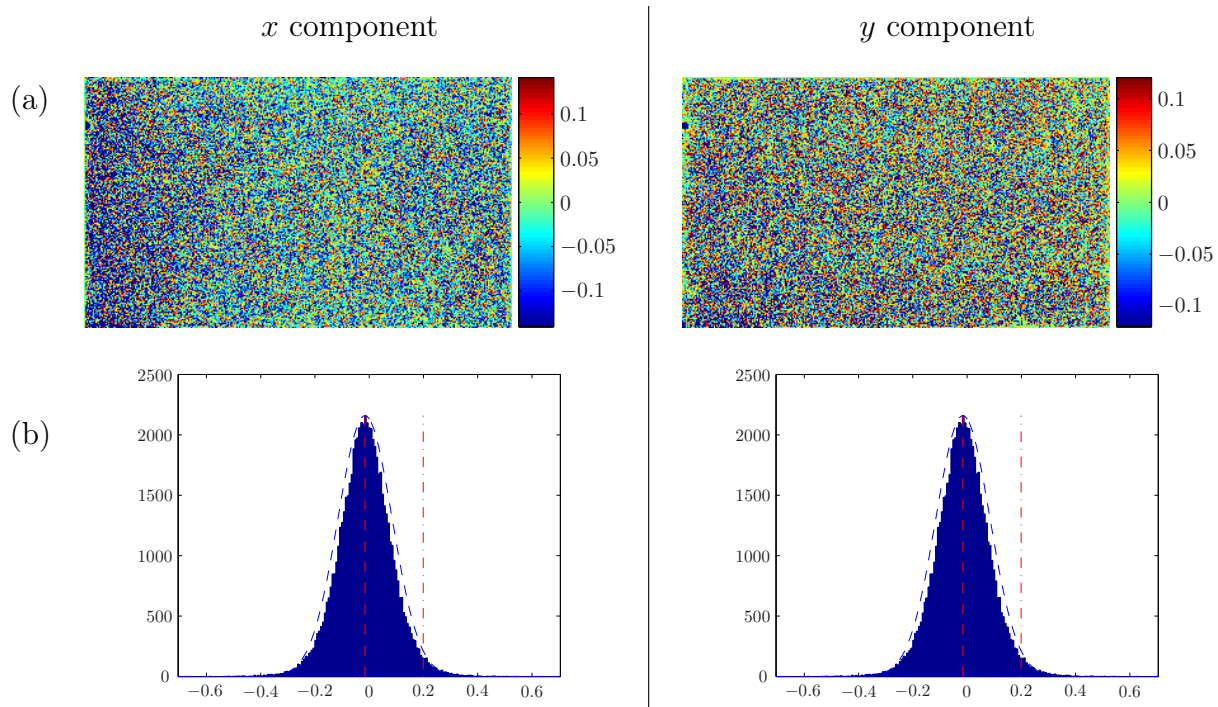


Figure 5.5: (a) Residual maps of the displacement typically obtained from experimental measurements; (b) Verification of the Gaussian distribution of the residual values of the displacement ( $-\cdot-\cdot-$ :  $2\sigma$ ) (unit:  $\mu m$ ).

The spatial resolution of the grid method (*i.e.*, the smallest distance separating two independent measurements) is about the pitch of the grid, *i.e.*, 0.1 mm (gauge area of  $34 \times 20 \text{ mm}^2$ ). After the calibration of the optical system and before testing, the resolution (*i.e.*, the smallest value that can be detected or measured) associated to the phase measurements was globally evaluated by the standard deviation of the residual maps, resulting from the difference of phase fields of the same undeformed state of the grid/specimen. In practice, 7 images of the grid at rest were taken at intervals of 10 s and their phase evaluated. From the residual maps obtained by subtracting pairs of successive phase fields, a standard deviation vector was calculated (spatial uncorrelated measurements were assumed). The phase resolution ( $\sigma_\phi$ ) was then determined as the mean of the standard deviations. In our experiments,  $\sigma_\phi$  was found between  $2\pi/160$  and  $2\pi/115$  radians (*i.e.*, between 2.2 and 3.1 degrees). The displacement resolution ( $\sigma_u$ ) was determined afterwards according to:  $\sigma_u = \sigma_{\Delta\phi}/S$ , where  $S = 2\pi/p = 62.8 \text{ rad/mm}$  (§ 2.1.2). The residual displacement maps (both  $x$  and  $y$  components) typically obtained from experimental measurements are shown in Figure 5.5(a). As it can be seen in Figure 5.5(b), the residual values follow relatively well a Gaussian distribution with a mean of almost zero, which confirms the relevance of evaluating the resolution as a function of the standard deviation of the residual maps.  $\sigma_u$  was determined to range between  $p/90$  and  $p/120$  (*i.e.*, between 0.9 and 1.2  $\mu m$ ). In the calibration process, these values of resolution can give an indication of the setting

quality in the optical system (*i.e.*, magnification and contrast). Moreover, it may be worth mentioning that the scatter of the resolution obtained here was strongly related to the quality of the grid transfer achieved in each specimen.

The tests were carried out using the Iosipescu fixture proposed in (Pierron, 1998) mounted in an Instron 5582 universal testing machine (Figure 5.3). The relative positions of the motionless and sliding parts of the Iosipescu fixture were adjusted in order to obtain a length of 34 mm between the inner loading supports. The specimens were set up into the fixture through sliding wedges, tightened up with a torque of about 0.5 Nm. The load was applied at a controlled displacement rate of 1 mm/min and measured with a 100 kN load cell.

## 5.3 Results and discussion

The image processing and identification procedures were performed using Matlab functions (in house developed) according to the flowchart presented in Figure 3.3 (§ 3.4).

As both loads and grid images were simultaneously measured during the tests at an acquisition rate of 1 per second, the stiffness components could be identified at different levels of load (or strain) below the elastic limit. Thus, for stability reasons, the stiffness components were systematically determined as the mean of the set of all identified results obtained within a pre-selected range of loads.

Owing to the relatively small levels of load reached during the tests (less than about 300 N), the out-of-plane displacement of the specimen, as measured by a LVDT positioned at the centre of the back face of the specimen, was always inferior to about 30  $\mu\text{m}$ . According to the thin-lens model, this out-of-plane displacement can generate, in the measurement of the undergoing in-plane deformation, an additional apparent strain component of  $8.6 \times 10^{-5}$ , which can be assumed negligible compared to the typical strain resolution of about  $10^{-4}$ . Therefore, no correction of the linear strain components, due to artifacts introduced by a given out-of-plane motion of the specimen, was required.

### 5.3.1 0° configuration

Throughout data processing, some parameters must be carefully chosen since they can significantly affect the parameter identification. First the degree of the 2D polynomial, used to filter out the measured displacement fields before spatial numerical differentiation, must be chosen (§ 3.4.2). These polynomial displacement fields are to be processed afterwards in the identification of the material stiffness components. The quality of the approximation (and consequently the accuracy of the identification results) depends to a great extent on the choice of the polynomial degree. Thus, a preliminary study was undertaken for assessing its influence on the stiffness results. For a given degree, both mean

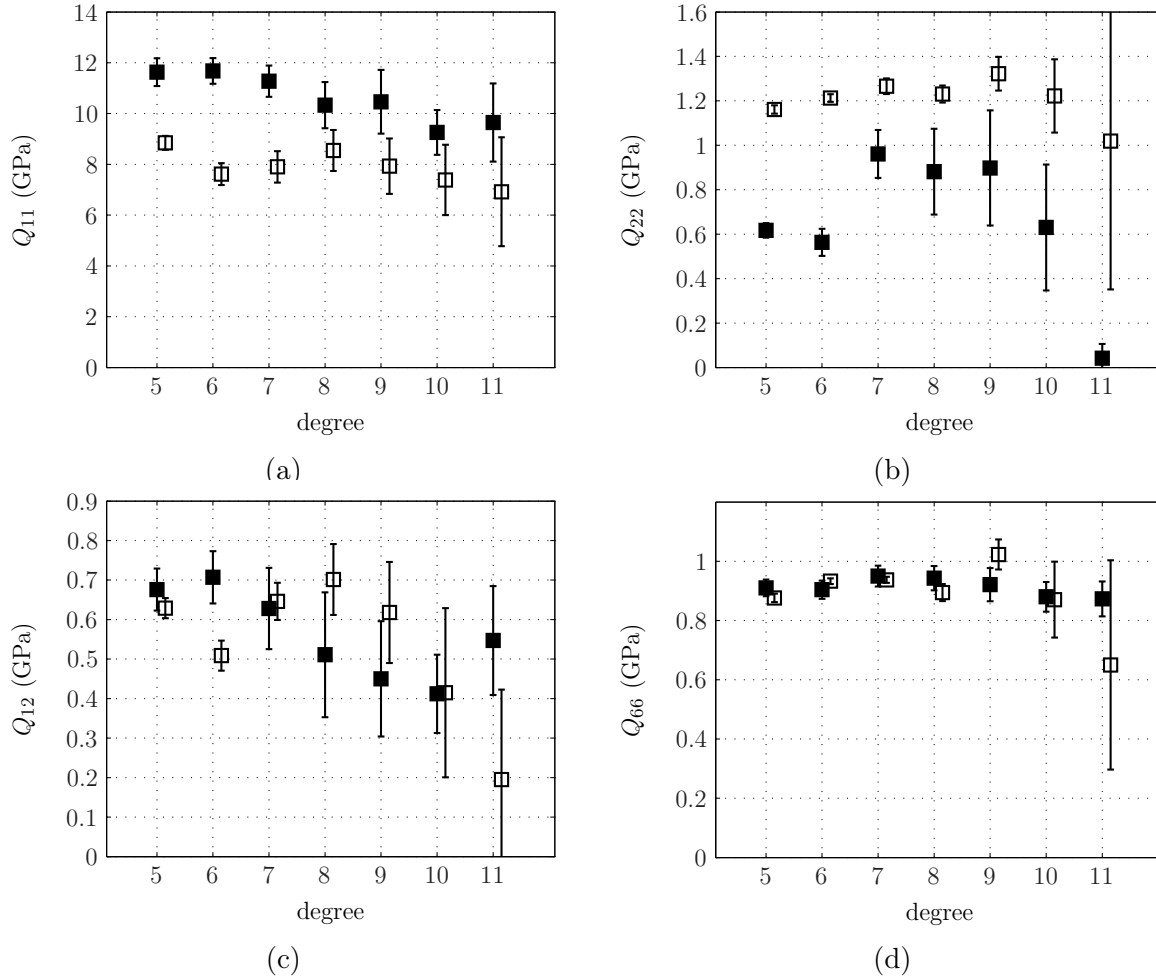


Figure 5.6: Variation of the stiffness parameters with respect to the degree of the fitting polynomial for 0° (■) and 45° (□) specimens: (a)  $Q_{11}$ , (b)  $Q_{22}$ , (c)  $Q_{12}$ , (d)  $Q_{66}$ .

and dispersion (quantified by the standard deviation  $\sigma$ ) values of the stiffness components, determined from all the results identified within a selected range of measurements, were evaluated. Results from this study are reported in Figure 5.6 for a 0° specimen, where the mean values of  $Q_{11}$ ,  $Q_{22}$ ,  $Q_{12}$  and  $Q_{66}$  are plotted versus the polynomial degree, ranging between 5 and 11 with increments of 1; error bars are also plotted corresponding to  $\pm 1 \sigma$ . In this example, 27 measurements were used, corresponding to loads ranging from 73 to 140 N. As it can be observed, all stiffnesses tend to decrease for higher degrees. This result is due to erroneous values reached at the edges of the reconstructed strain fields of higher-degree polynomials. This is consistent with the results shown in (§ 4.2.1.2.4) by processing simulated displacement fields (see Figure 4.7). Moreover, the scatter on the mean stiffness values generally increases for higher degrees (Figure 5.6), suggesting that higher-degree polynomials are more sensitive to noisy measurements. Besides, the processing time significantly increases for higher degrees (*e.g.*, the least-squares approximation for a 7th-degree and 11th-degree polynomial takes 49.2 s and 150.6 s, respectively

with a PC HP Intel Xeo CPU 2.80 GHz, *i.e.*, about three times higher for degree 11). Hence, a degree equal to 7 was chosen as a compromise between accuracy and processing time.

An example for the  $0^\circ$  specimen of the measured ( $u_\beta$ ) and approximated ( $\bar{u}_\beta$ ) (7th-degree polynomial) displacement fields ( $200(y) \times 340(x)$  matrices), together with the residual maps resulting from the difference  $u_\beta - \bar{u}_\beta$ , is shown in Figure 5.7. It can be observed that both  $x$  and  $y$  components of  $u_\beta$  and  $\bar{u}_\beta$  are similar and missing data have been interpolated at “points” where no initial information was available. From the residual maps (Figure 5.7(c)) it can be seen that some high-frequency fringes have been filtered out of the signal.

Typical strain fields obtained by finite differences from the polynomial displacement fields for a  $0^\circ$  specimen are shown in Figure 5.8(I). It can be seen that all in-plane strain components exist, although with different intensities and distributions across the region of interest. The  $\varepsilon_1$  field (Figure 5.8(I.a)) corresponds to a double cantilever bending field with compression near the inner loading points, tension at the opposite sides and almost zero across the centre of the gauge area. The  $\varepsilon_2$  field (Figure 5.8(I.b)) has compression zones concentrated near the inner supports and vanishes elsewhere. Finally, the  $\varepsilon_6$  field (Figure 5.8(I.c)) shows a predominant shear spread across the centre of the region of interest. These strain fields (Figure 5.8(I)) can be compared to numerical counterparts (Figure 5.8(II)) computed from a finite element analysis (§ 4.2.1.1), using elastic properties identified by the VFM from these actual experimental strain fields. As it can be seen, a close match is obtained between the experimental and numerical fields. Nevertheless, it is interesting to remark that the most significant differences between these fields occur near the edges of the region of interest, which reveals that the least-squares polynomial approach used here may induce some systematic errors in the strain computation in these areas. Moreover, the approximation will be affected by the quality of the grid transfer achieved in the specimens.

The strain fields computed from the experiments were then processed by the VFM, with optimised piecewise special virtual fields. From the parametric study shown in Figure 5.9, it can be concluded that the identification results are not significantly affected by the number of elements used to define the mesh along the  $x$  direction ( $N_X$ ), especially for the  $Q_{11}$  and the  $Q_{66}$  stiffness parameters. However, the increase of the number of elements along the  $y$  direction ( $N_Y$ ) tends to significantly underestimate the  $Q_{22}$  and the  $Q_{12}$  components. Hence, for the  $0^\circ$  specimen, a *virtual* mesh of  $8(x) \times 4(y)$  elements (45 nodes) was defined over the gauge area (§ 4.2.1.2.4).

As both grid images and loads were recorded simultaneously during the tests, the stiffness components were systematically identified for each load level. The identification results obtained for a  $0^\circ$  specimen are presented in Figure 5.10. It can be seen that the data converge to a reasonably stable value for both  $Q_{11}$  and  $Q_{66}$ . However, within the

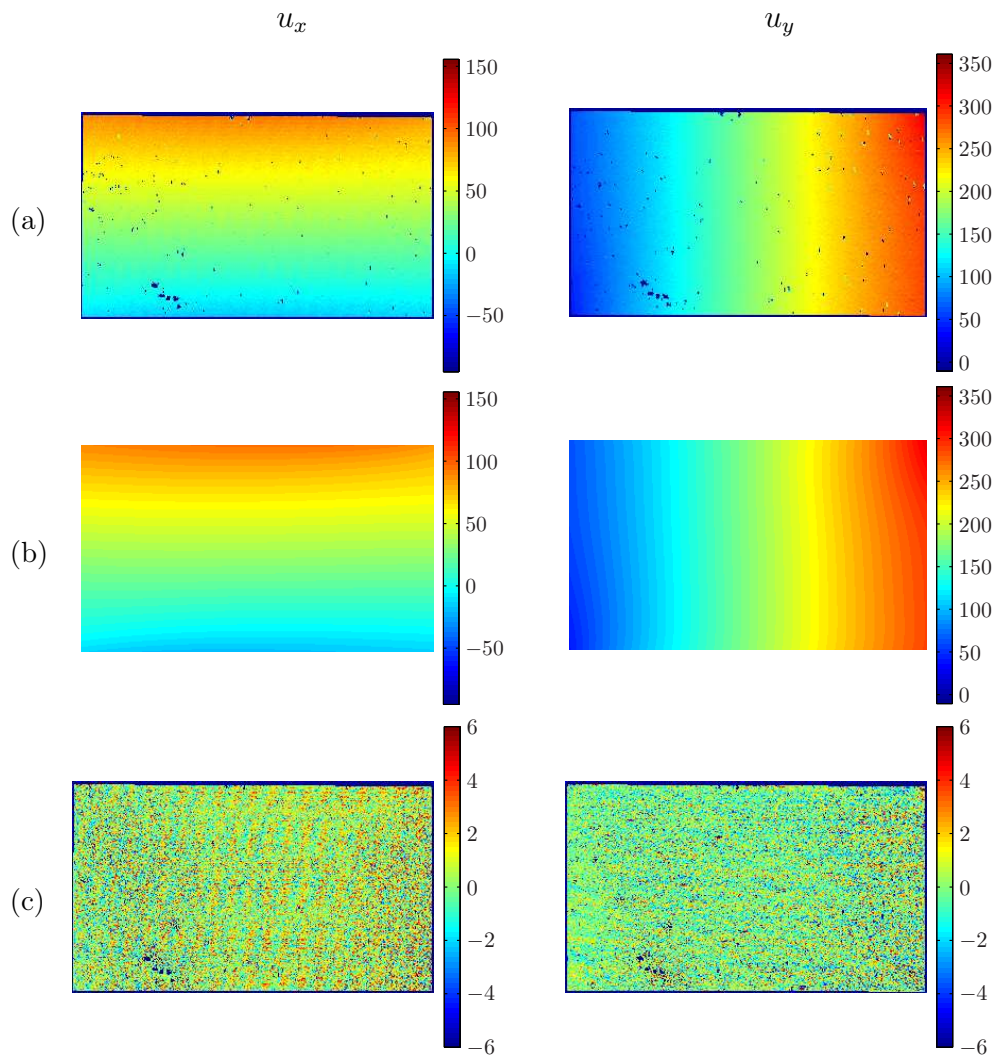


Figure 5.7: (a) Measured, (b) approximated (7th-degree polynomial) and (c) residual for  $u_x$  and  $u_y$  obtained for a  $0^\circ$  specimen ( $P = -139.4 \text{ N}$ ) (unit:  $\mu\text{m}$ ).

range of loads, scattered data are obtained for both  $Q_{22}$  and  $Q_{12}$ , which disturbs their convergence to a possible identifiable value. This result is a first indicator pointing out that the  $0^\circ$  configuration may not be suitable for the correct identification of these two parameters. As the parameter identification can be somewhat scattered (Figure 5.10), the values of the stiffness parameters were determined as the mean of the stiffness values identified within a pre-defined interval of applied loads:  $Q_{ij} = Q_{ij}^k/m$  ( $k = 1, 2, \dots, m$ ). This range of loads, within which the  $Q_{ij}$  stiffness parameters are evaluated, was selected individually for each specimen in order to eliminate outlying results. It systematically excludes low levels of load, for which the signal-to-noise ratio is still too low, and high levels of load, where the non-linear response of the material may have been already reached (typically characterised by a decrease in the stiffness parameters). Accordingly and for the stiffness components which are reliably identified, the stiffness mean values can be

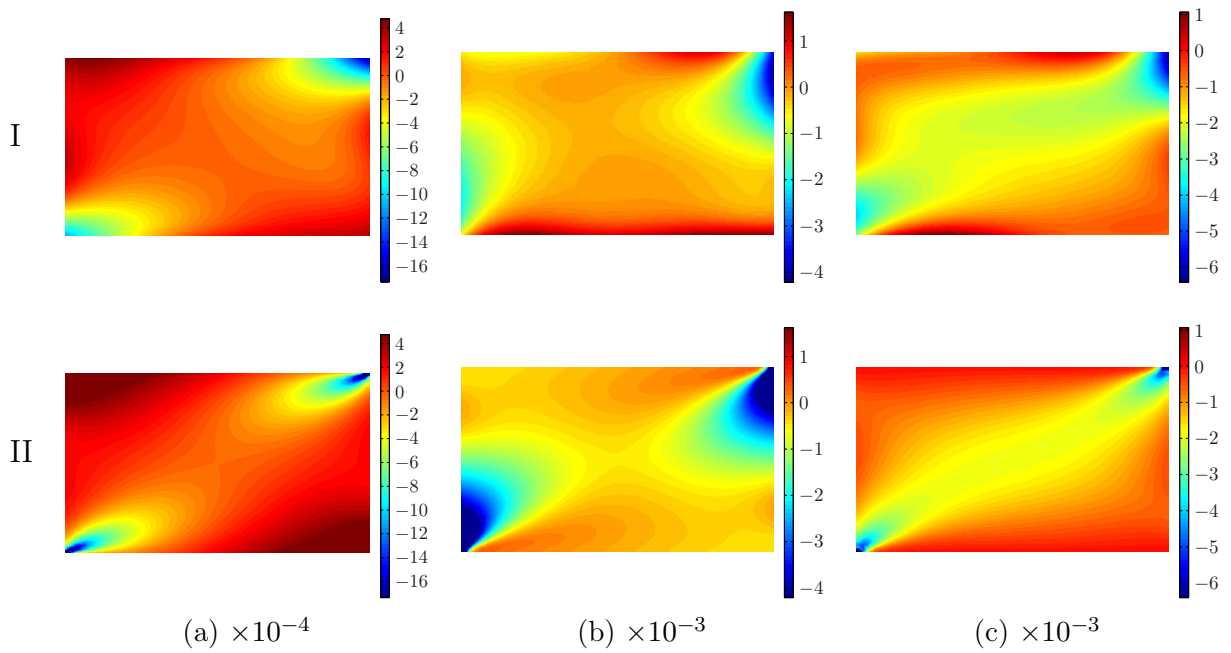


Figure 5.8: Typical (I) experimental and (II) numerical strain fields obtained for a  $0^\circ$  specimen ( $P = -139.4 \text{ N}$ ): (a)  $\varepsilon_1$ , (b)  $\varepsilon_2$ , (b)  $\varepsilon_6$ .

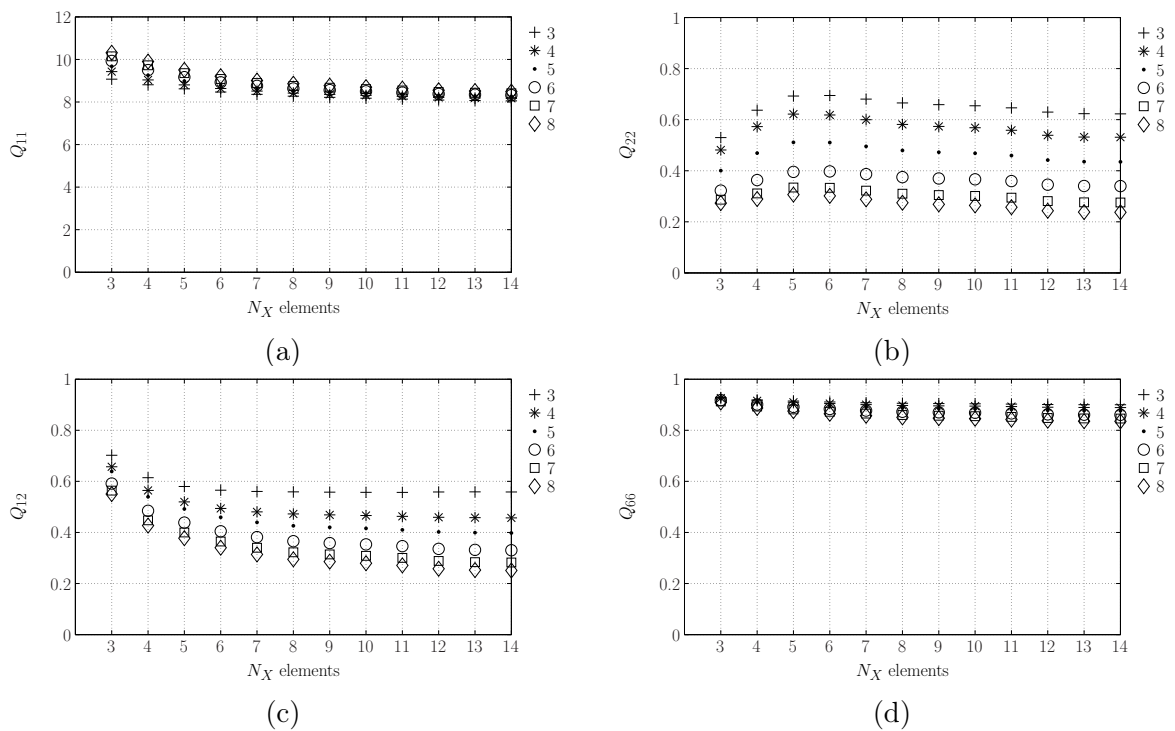


Figure 5.9: Variation of the identified stiffness components with respect to the number of elements used to set up the *virtual* mesh of the  $0^\circ$  specimen: (a)  $Q_{11}$ , (b)  $Q_{12}$ , (c)  $Q_{22}$ , (d)  $Q_{66}$ .

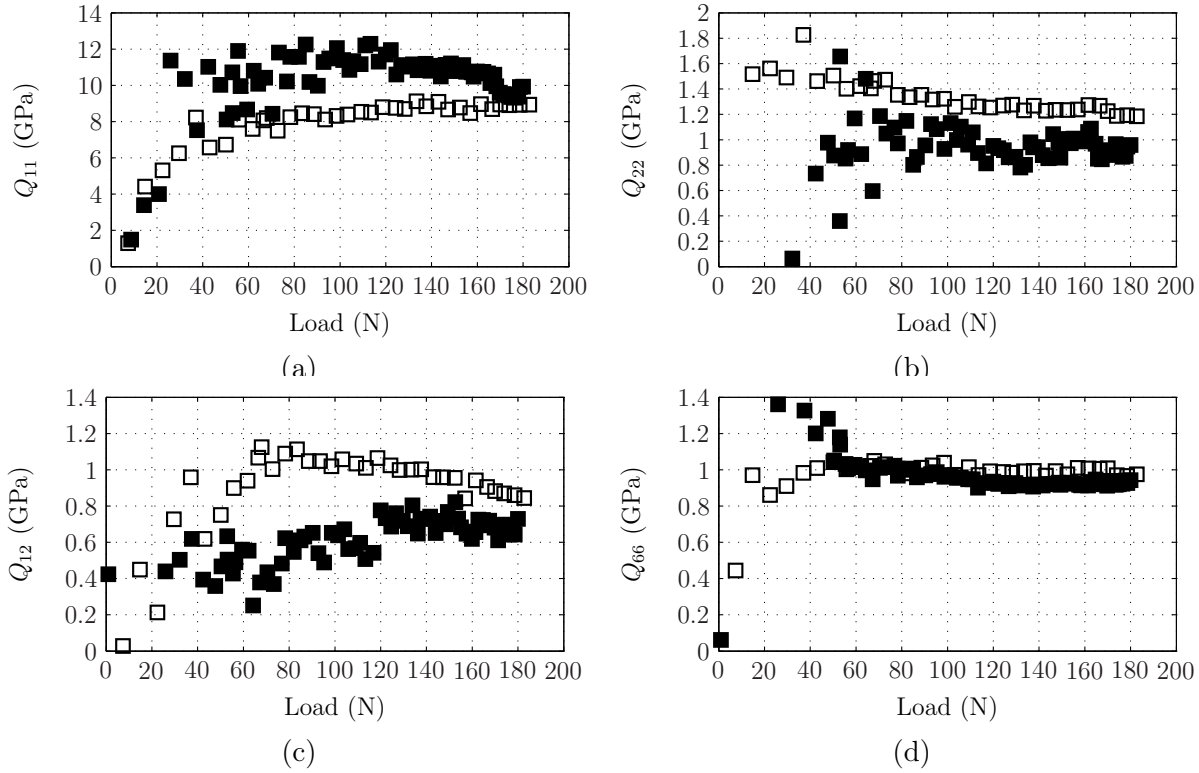


Figure 5.10: Identified stiffness parameters as a function of the applied load for a  $0^\circ$  (■) and  $45^\circ$  (□) specimens: (a)  $Q_{11}$ , (b)  $Q_{22}$ , (c)  $Q_{12}$ , (d)  $Q_{66}$ .

Table 5.1: Reference stiffness values of *P. pinaster* wood identified using standard tests (moisture content of about 11%) (Pereira, 2005; Xavier et al., 2004) ( $1 - 2 \equiv L - R$ ).

	(L) tensile test			(R) tensile test		(LR) Iosipescu test	
	$\rho$	$Q_{11}$	$Q_{12}$	$\rho$	$Q_{22}$	$\rho$	$Q_{66}$
	(g.cm <sup>-3</sup> )	(GPa)	(GPa)	(g.cm <sup>-3</sup> )	(GPa)	(g.cm <sup>-3</sup> )	(GPa)
Mean	0.616	15.5	0.920	0.696	1.97	0.589	1.41
C.I. <sup>a</sup>		±0.580	±0.055		±0.089		±0.112
C.V. <sup>b</sup>	2.0	7.00	10.8	0.9	8.18	5.6	10.3

(<sup>a</sup>) Confidence intervals at 95% confidence level;

(<sup>b</sup>) Coefficient of variation (%).

Table 5.2: Stiffness properties of *P. pinaster* wood identified by the virtual fields method (*virtual* mesh of  $8(x) \times 4(y)$  elements) from the  $0^\circ$  specimens (moisture content about 9–10%) ( $1 - 2 \equiv L - R$ ).

	$\rho$ ( $\text{g}\cdot\text{cm}^{-3}$ )	$Q_{11}$ (GPa)	$Q_{22}$ (GPa)	$Q_{12}$ (GPa)	$Q_{66}$ (GPa)
1	0.508	10.0	0.916	0.351	0.777
2	0.505	11.0	1.03	0.589	0.985
3	0.522	9.73	0.763	0.551	0.835
4	0.509	10.3	0.303	0.294	0.992
5	0.531	10.3	0.605	0.558	0.948
6	0.537	10.5	0.256	0.335	1.07
7	0.534	10.1	0.417	0.209	0.963
Mean	0.521	10.3	0.613	0.412	0.939
C.I. <sup>a</sup>		$\pm 0.388$	$\pm 0.280$	$\pm 0.140$	$\pm 0.092$
C.V. <sup>b</sup>	2.6	4.09	49.4	36.6	10.6
Ref.		15.6	1.97	0.926	1.41
Dif.(%)		34	69	55	33

<sup>(a)</sup> Confidence intervals at 95% confidence level;

<sup>(b)</sup> Coefficient of variation (%).

determined with a coefficient of variation that is reasonably low (*i.e.*, a few percents).

The identification results obtained in this study were compared with stiffness values of *P. pinaster* wood reported in the literature (Table 5.1). These reference stiffness parameters were calculated, using the relationships given in Eq. (1.4), from the engineering constants determined experimentally by carrying out three independent tests using strain-gauge measurements ( $1 - 2 \equiv L - R$ ):  $E_1$  and  $\nu_{12}$ , from a tensile test along the longitudinal direction (Pereira, 2005);  $E_2$ , from a tensile test along the radial direction (Pereira, 2005);  $G_{12}$ , from the classical Iosipescu shear test on specimens oriented in the (1, 2) principal plane (Xavier et al., 2004). The specimens used in this work were manufactured from the same tree used to provide the material for those conventional tests. Nevertheless, for reasons of availability, the specimens used here were cut from a higher location (of about six meters) than the reference ones. As a result, no matched specimens could be prepared in relation to those previous studies. Even so, these references were reported here in order to comment our results.

The  $Q_{11}$ ,  $Q_{22}$ ,  $Q_{12}$  and  $Q_{66}$  stiffness parameters of *P. pinaster* wood identified by the VFM for the  $0^\circ$  specimens, along with their densities ( $\rho$ ), are reported in Table 5.2. After checking the normality of the distributions of the stiffness values by the Shapiro-Wilk test (Neully, 1999, p. 87), the 95% confidence intervals on the mean of each parameter were determined from the *t*-distribution (Table 5.2). It can be concluded from these results that

$Q_{22}$  and  $Q_{12}$  are identified with a very large scatter, confirming that the  $0^\circ$  configuration is not suitable for their accurate identification. Similar results were also obtained for a unidirectional glass/epoxy composite material (Chalal et al., 2006). Particularly, this result can be understood from the  $\varepsilon_2$  strain field since both  $Q_{22}$  and  $Q_{12}$  parameters are strongly tied to this strain component through Eq. (3.9). It was shown above that the level of the  $\varepsilon_2$  strain is only significant in concentrated zones near the inner loading points (Figure 5.8(b)). Hence, the low identifiability of these parameters is supported by the fact that the spatial resolution, associated to the experimental data, is not sufficient for the accurate representation of the high concentrated gradients of  $\varepsilon_2$ . This observation leads to the conclusion that, generally, high concentrated strain gradients are not favourable to the identification purpose, strongly depending either on the performance of the optical method or on the filtering process. This can also be analysed in terms of the sensitivity to noise coefficients ( $\xi_{ij} = \eta_{ij}/Q_{ij}$ ) provided by the VFM routine (§ 3.5.2.3). It was shown by processing numerical displacement data that for  $Q_{22}$  and  $Q_{12}$ , these coefficients are much higher than for  $Q_{11}$  and  $Q_{66}$  (§ 4.2.1.2.1). This is confirmed by the low scatter associated to the  $Q_{11}$  and  $Q_{66}$  parameters (Table 5.2), which is in the order of magnitude of the one reached in the reference tests (Table 5.1). Moreover, the anisotropic ratio  $Q_{11}/Q_{66}$  determined from the present results and the references is, respectively, 10.9 and 11.0. However, the mean values of  $Q_{11}$  and  $Q_{66}$  are lower than the reference values by 34% and 33%, respectively. Besides, the mean density of the specimens used in this work (Table 5.2) are lower than the ones of the references (Table 5.1). Nevertheless, the density variation among specimens can not alone explain the stiffness differences obtained here. Instead, the underestimation of both  $Q_{11}$  and  $Q_{66}$  is understood as a result of vertical spatial variation of the wood mechanical properties within the stem. A recent study (Machado and Cruz, 2005) has shown that for this species, a decrease in the elastic modulus parallel to grain ( $E_1$ ) between 29% and 35% – depending on the radial location of the specimens – can be obtained from specimens taken at different vertical locations within the stem, separated by a distance of about 65% of the total height of the tree. The authors justified this vertical decrease of the longitudinal modulus by the greater percentage of juvenile wood on the specimens coming from the higher positions within the stem.

### 5.3.2 $45^\circ$ configuration

In order to find a more suitable configuration for the reliable identification of the whole set of stiffness parameters, specimens with a grain at  $45^\circ$  with respect to its longitudinal axis were tested (Figure 5.3(a)). The same procedure used previously to analyse the results of the  $0^\circ$  specimens was applied here.

Firstly, a study was undertaken regarding the choice of the polynomial degree to be used for the  $45^\circ$  configuration. As outlined above, the lowest possible polynomial

degree that would adequately describe the data will be the best choice. The evaluation of the stiffness parameters (*i.e.*, both mean and standard deviation determined from the set of identification results obtained for load levels ranging from 109 N to 193 N) with respect to the set of polynomial degrees (ranging between 5 and 11), used in the least-squares approximation of the measured displacement fields, of a  $45^\circ$  specimen is reported in Figure 5.6. The following conclusions can be highlighted: (1) lower values of the stiffness components are identified from higher-degree polynomials; (2) the dispersion on the stiffness values increases with the increase of the polynomial degree. Thus, similarly to the  $0^\circ$  specimen, a polynomial degree equal to 7 was deemed suitable for the approximation scheme with the  $45^\circ$  configuration.

Figure 5.11 shows an example of the  $x$  and  $y$  components of the (a) raw and (b) 7th-degree polynomial displacement fields, along with (c) the maps resulting from their subtraction, obtained for a  $45^\circ$  specimen. As it can be noticed, missing data have been interpolated and some noise filtered out from the measured displacement fields.

The heterogeneous strain fields, plotted in the  $(1, 2)$  material coordinate system, typically obtained for the  $45^\circ$  specimen are shown in Figure 5.12(I). From the analysis of Figure 5.12(I.b), it can be pointed out that the  $\varepsilon_2$  strain component is more evenly distributed across the gauge area than the one obtained by the  $0^\circ$  configuration (Figure 5.8(I.b)). Moreover, the magnitude of the  $\varepsilon_1$  strain component (Figure 5.12(I.a)) is closer to that of the other two components. Hence, the following conclusion can be drawn: the rotation of the grain of the specimen clearly yielded a more balanced contribution of the strain components over the gauge area. Consequently, the stiffness parameters can be expected to be more confidently identified with the  $45^\circ$  configuration. As a qualitative criterion, the experimental strain fields (Figure 5.12(I)) are compared to simulated ones (Figure 5.12(II)) computed from a finite element analysis. In spite of the similarity between these fields, some differences exist, particularly near the edges, induced by the least-squares polynomial approximation scheme.

For the  $45^\circ$  specimen, the special virtual fields were defined over a virtual mesh of  $5(x) \times 3(y)$  elements (24 nodes) (see Figure 3.6). For this configuration, it has been shown (Figure 5.13) that an increase of the number of elements in the  $x$  direction yields a significant underestimation of both  $Q_{11}$  and  $Q_{12}$  stiffness parameters (when compared to the counterpart values obtained for the  $0^\circ$  configuration reported in Table 5.2), although it had a less effect on the other two components. It appears that local errors on  $\varepsilon_1$  near the edges of the gauge area (Figure 5.12(I.a)) are averaged and thus minimised when large *virtual* finite elements are used. However, the refinement of the mesh along the  $y$  direction was found to have a minor effect on the stiffness identification (Figure 5.13).

An example of the stiffness parameters as a function of the applied load obtained for a  $45^\circ$  specimen is plotted in Figure 5.10. A good convergence (*i.e.*, without highly scattered values) to a stable value is reached for the  $Q_{11}$ ,  $Q_{22}$  and  $Q_{66}$  parameters with the increase

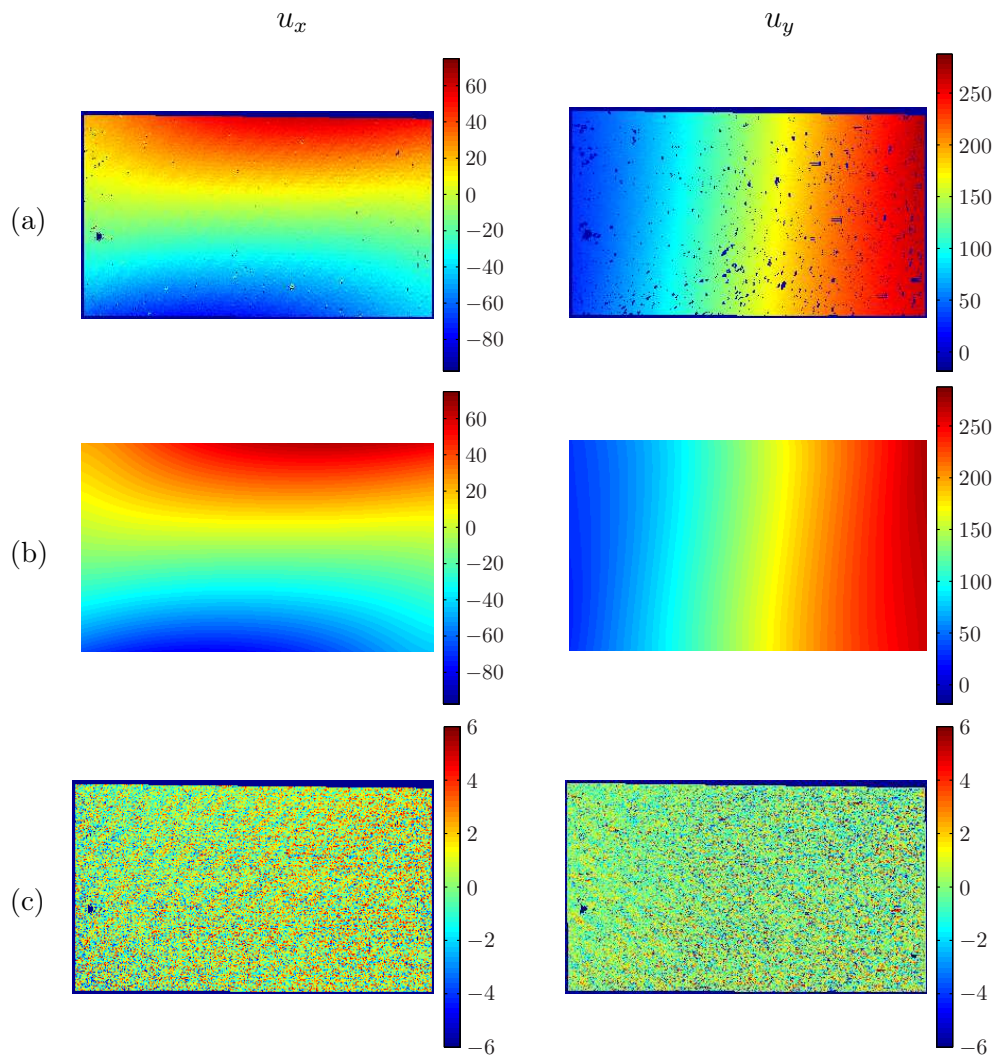


Figure 5.11: (a) Measured, (b) approximated (7th-degree polynomial) and (c) residual for  $u_x$  and  $u_y$  obtained for a  $45^\circ$  specimen ( $P = -143.0\text{ N}$ ) (unit:  $\mu\text{m}$ ).

of load. However, the identification of the  $Q_{12}$  stiffness still remains difficult. This result could be expected because this parameter involves Poisson's effect which is usually small and therefore more difficult to detect and measure.

The  $LR$  stiffness parameters of *P. pinaster* wood identified by the VFM with the  $45^\circ$  specimens, along with the specimen densities, are reported in Table 5.3. The 95% confidence intervals on the mean values of the stiffness parameters were determined from the  $t$ -distribution, after checking the normality of the data by the Shapiro-Wilk test (Table 5.3). For this configuration, both  $Q_{22}$  and  $Q_{66}$  parameters are identified with a scatter of the same order of magnitude as that of the reference tests. However, a higher dispersion is obtained for  $Q_{11}$  and  $Q_{12}$ . Because of the issue of identifiability, only the  $Q_{11}$  and  $Q_{66}$  stiffness can be compared between the  $0^\circ$  (Table 5.2) and  $45^\circ$  (Table 5.3) configurations. As it can be seen, almost the same mean value is identified from both

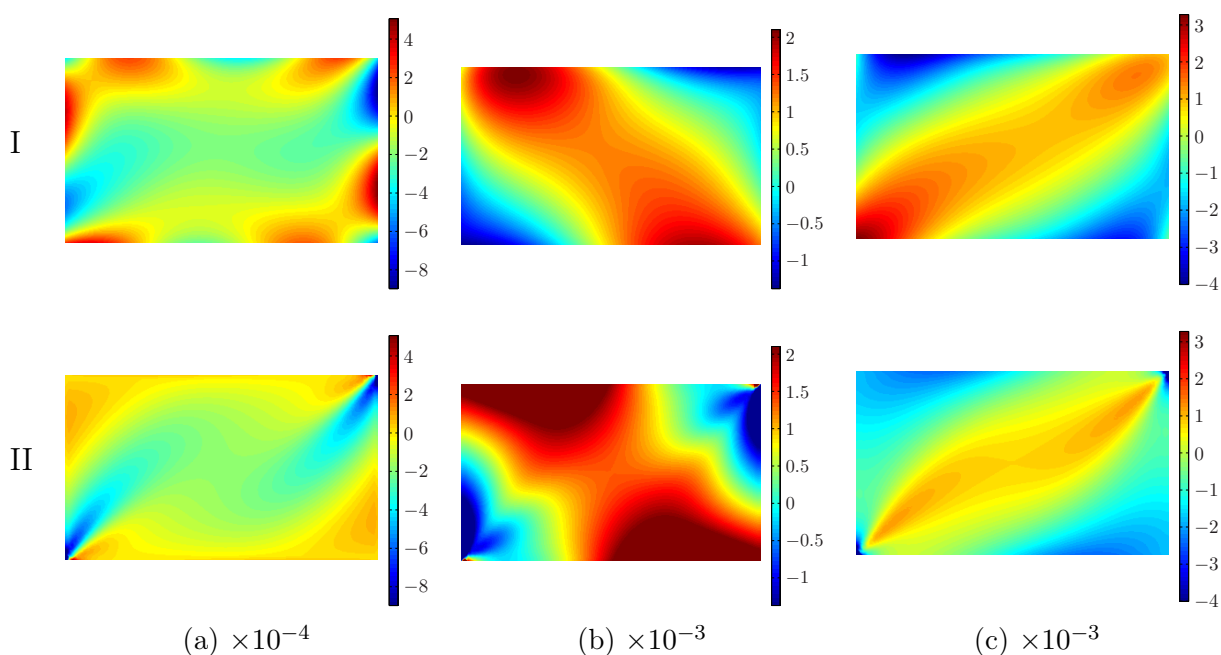


Figure 5.12: Typical (I) experimental and (II) numerical strain fields obtained for a  $45^\circ$  specimen ( $P = -143.0\text{ N}$ ): (a)  $\varepsilon_1$ , (b)  $\varepsilon_2$ , (b)  $\varepsilon_6$ .

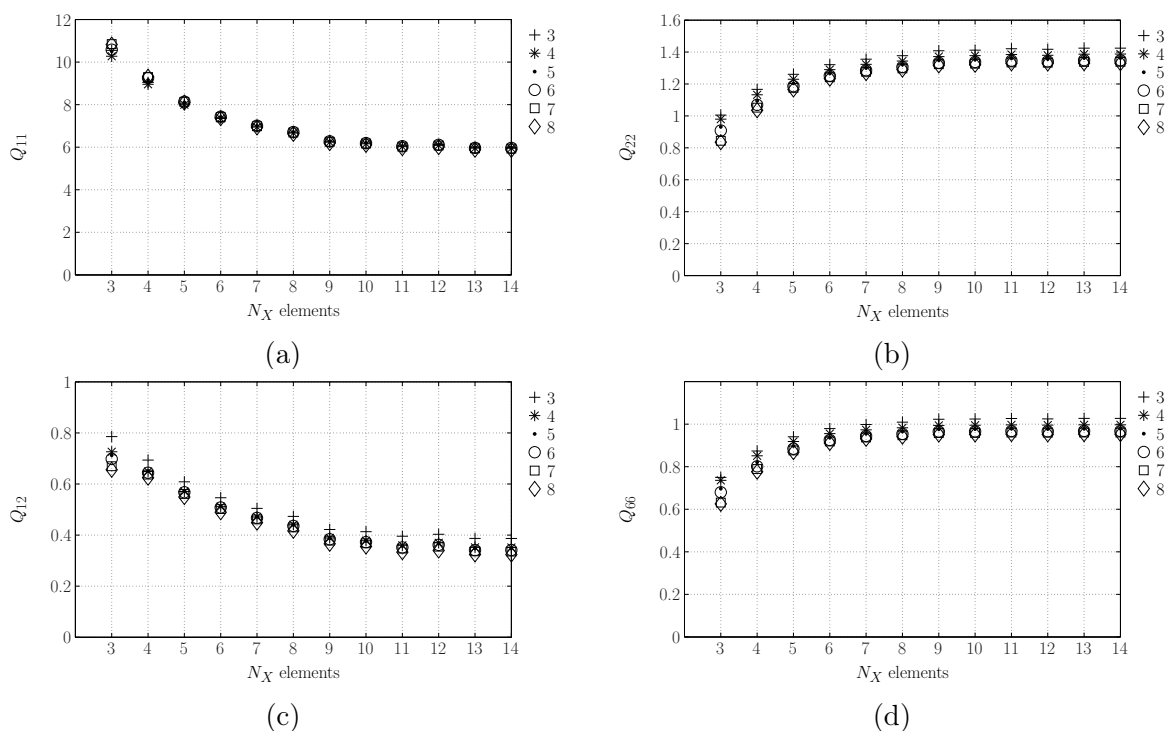


Figure 5.13: Variation of the identified stiffness components with regard to the number of elements used to set up the *virtual* mesh of the  $45^\circ$  specimen: (a)  $Q_{11}$ , (b)  $Q_{12}$ , (c)  $Q_{22}$ , (d)  $Q_{66}$ .

Table 5.3: Stiffness properties of *P. pinaster* wood identified by the virtual fields method (*virtual* mesh of  $5(x) \times 3(y)$  elements) from the  $45^\circ$  specimens (moisture content about 9–10%) ( $1 - 2 \equiv L - R$ ).

	$\rho$ (g.cm <sup>-3</sup> )	$Q_{11}$ (GPa)	$Q_{22}$ (GPa)	$Q_{12}$ (GPa)	$Q_{66}$ (GPa)
1	0.559	8.11	1.29	0.624	0.925
2	0.537	8.69	1.28	0.954	1.00
3	0.557	8.45	1.24	0.363	1.01
4	0.542	11.6	1.17	0.702	0.928
5	0.540	10.7	1.26	0.667	1.03
6	0.544	11.8	1.16	0.591	0.856
7	0.539	11.7	1.26	0.730	0.905
Mean	0.545	10.2	1.24	0.661	0.950
C.I. <sup>a</sup>		$\pm 1.552$	$\pm 0.048$	$\pm 0.163$	$\pm 0.059$
C.V. <sup>b</sup>	1.6	16.5	4.22	26.7	6.67
Ref.		15.6	1.97	0.926	1.41
Dif.(%)		35	37	29	33

<sup>(a)</sup> Confidence intervals at 95% confidence level;

<sup>(b)</sup> Coefficient of variation (%).

configurations. This is statistically confirmed with the *t*-test for equality of the means at a 95% of confidence level. Moreover, similar anisotropic ratios are obtained between the  $45^\circ$  configuration and the reference results: 8.2 and 7.9 for  $Q_{11}/Q_{22}$  and 10.7 and 11.0 for  $Q_{11}/Q_{66}$ , respectively. Nevertheless, when comparing the mean results, a lower estimation is again observed for the  $45^\circ$  specimens of the order of 35%, 37%, 29% and 33%, respectively, for  $Q_{11}$ ,  $Q_{22}$ ,  $Q_{12}$  and  $Q_{66}$  (Tables 5.1 and 5.3). As already stated above, the vertical spatial variation of the wood mechanical properties within the stem (Machado and Cruz, 2005) is believed to be the major reason for this systematic underestimation of the stiffness values.

As general conclusions at this stage, we can say that from the  $0^\circ$  configuration, only the  $Q_{11}$  and  $Q_{66}$  parameters could be correctly identified with coefficients of variation of the same order of the reference ones. It was pointed out that the difficult representation (using least-squares polynomial approximation) of the high gradient distribution of the  $\varepsilon_2$  strain component reached for this configuration (Figure 5.8(I.b)), was the major reason why both  $Q_{22}$  and  $Q_{12}$  components had a low identifiability. For the  $45^\circ$  configuration, the  $Q_{22}$  and  $Q_{66}$  parameters were identified with low scatter when compared to the reference one; however, a slightly higher coefficient of variation was still obtained for  $Q_{11}$  and especially for  $Q_{12}$ . It is important to highlight that the grain rotation from  $0^\circ$  to  $45^\circ$  has generated a redistribution of the strain fields such that the  $\varepsilon_2$  strain is, in the  $45^\circ$  configuration,

more balanced with respect to the  $\varepsilon_6$  shear strain (*i.e.*, smoother and more evenly spread over the gauge area with comparable magnitudes). Therefore, the reliable identification of the  $Q_{22}$  stiffness was possible for this latter configuration. However, a more difficult representation of the  $\varepsilon_1$  strain component for the  $45^\circ$  specimens was obtained because some artifacts are introduced at the edges of this field by the polynomial reconstruction (Figure 5.12(I.a)). Hence, the reliability in the identification of the  $Q_{11}$  component was found to be lower for the  $45^\circ$  configuration than for the  $0^\circ$  one.

### 5.3.3 $30^\circ$ configuration

Specimens with grain at an angle of  $30^\circ$  were finally tested. From the optimisation problem analysed in § 4.3 by processing numerical displacement fields, according to the criterion of minimisation the sensitivity to noise coefficients (Figure 4.15), the off-axis angle of  $30^\circ$  was found to correspond to the best test configuration for parameter identification. The same procedure as described above for the other configurations was used here. However, in practice, unstable identification results were systematically obtained for this configuration. In particular, this instability came from the fact that the accurate representation of the strain fields could not be achieved in this case, as can be noticed from the experimental and numerical strain fields plotted in Figure 5.15. At it can be seen, highly erroneous strain values at the edges of the region of interest are introduced by the numerical differentiation of the polynomial fields (7th-degree polynomial) used to approximate the measured displacement fields. The variation of the identified stiffness parameters as a function of the applied load obtained for a  $30^\circ$  specimen is shown in Figure 5.15. As it can be noticed, scatter results are typically obtained for all stiffness parameters. Moreover, the values of  $Q_{22}$ ,  $Q_{12}$  and  $Q_{66}$  tend to be lower and the values of  $Q_{11}$  higher than their counterpart results obtained from both the  $0^\circ$  (Figure 5.10) and the  $45^\circ$  (Figure 5.10) configurations. It should be noticed that the quality of the grid transfert achieved for the  $30^\circ$  specimens was similar to the one obtained for both the  $0^\circ$  and  $45^\circ$  specimens.

It seems that these results are directly related to the lack of correct representation of the strain fields for this configuration. As a result from these remarks, the  $30^\circ$  configuration was experimentally judged inappropriate, but further analyses are required. Particularly, a local reconstruction approach of the strain fields, such as the piecewise finite element approximation scheme (§ 3.4.2), can be tested. Nevertheless, whatever the reasons of this paradox, it was found pragmatically reasonable to disqualify the  $30^\circ$  configuration for further experiments.

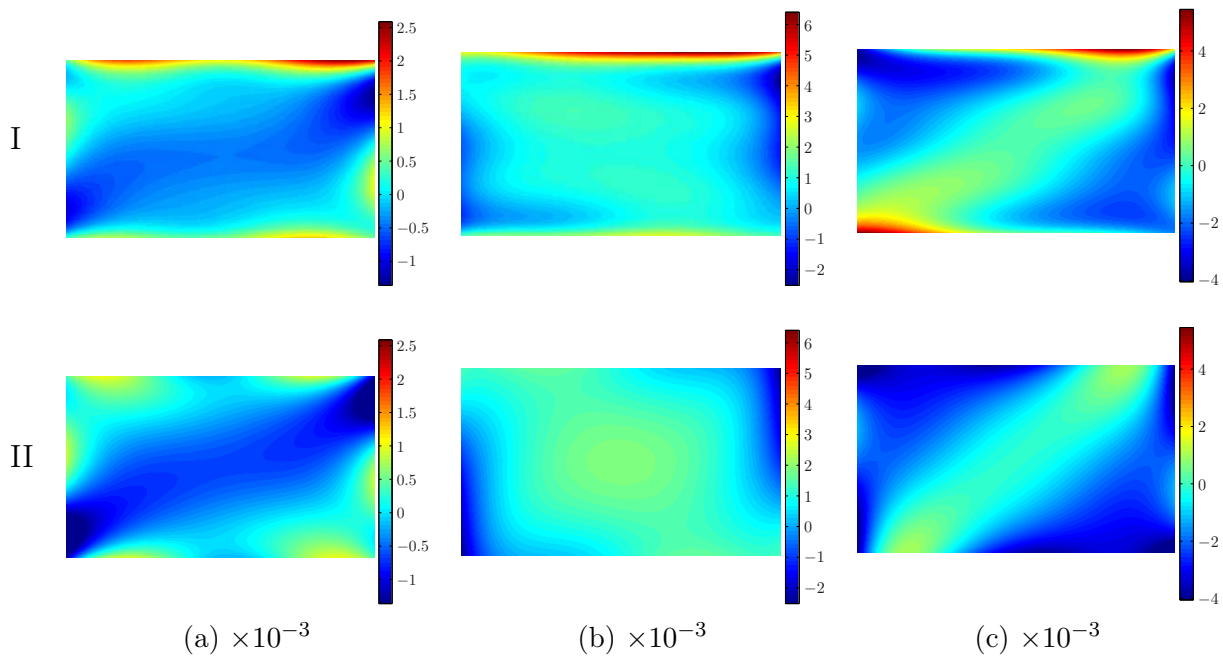


Figure 5.14: Typical (I) experimental and (II) numerical strain fields obtained for a  $30^\circ$  specimen ( $P = -176.5 \text{ N}$ ): (a)  $\varepsilon_1$ , (b)  $\varepsilon_2$ , (c)  $\varepsilon_6$ .

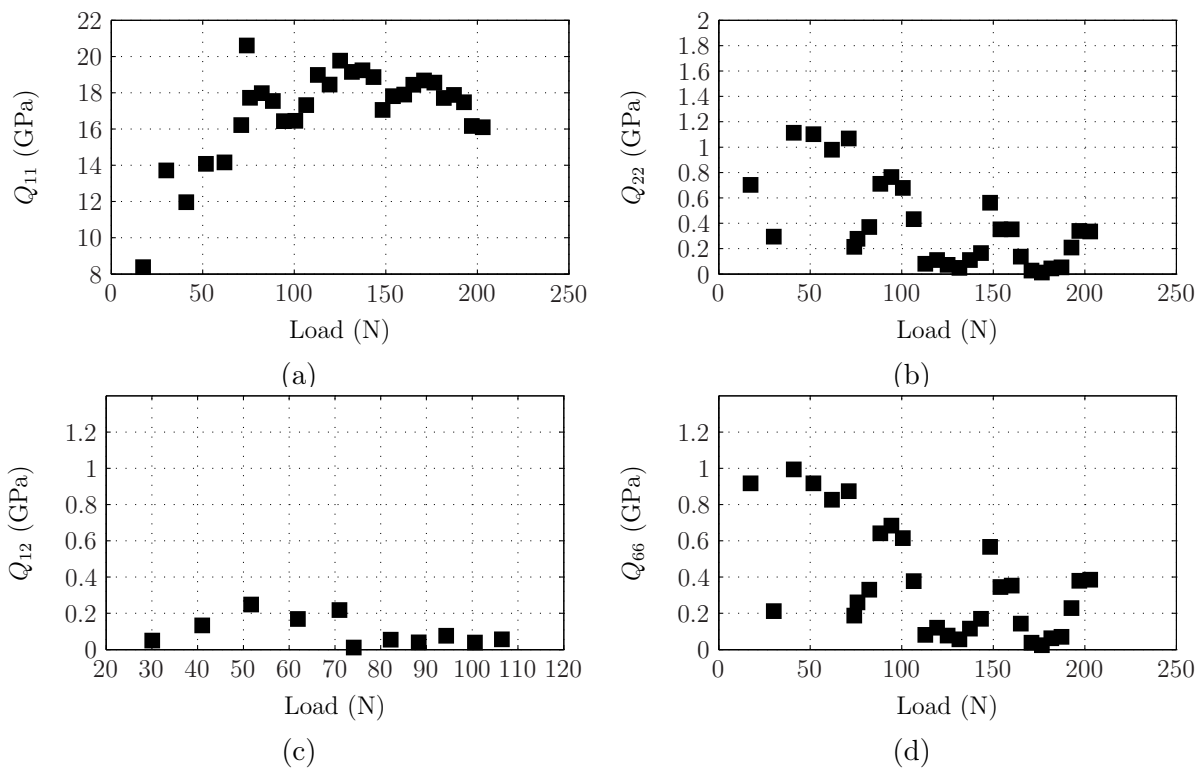


Figure 5.15: Identified stiffness parameters as function of the applied load for a  $30^\circ$  specimen: (a)  $Q_{11}$ , (b)  $Q_{22}$ , (c)  $Q_{12}$ , (d)  $Q_{66}$ .

## 5.4 Conclusions

The inverse identification approach based on the application of the VFM to a rectangular coupon loaded with the Iosipescu fixture has been experimentally investigated in this chapter. The aim of the study was to determine a suitable configuration yielding the most robust characterisation of the  $LR$  stiffness parameters of *P. pinaster* wood. The following points can be summarised.

- (i) From the  $0^\circ$  configuration, only the  $Q_{11}$  and  $Q_{66}$  parameters could be correctly identified with coefficients of variation of the same order of magnitude as reference values for this species.
- (ii) In spite of the identifiability of the  $Q_{12}$  parameter still remained low, the  $45^\circ$  configuration has led to some improvements in the results, especially for the identification of the  $Q_{22}$  component. Accordingly, the grain rotation from  $0^\circ$  to  $45^\circ$  allowed more balanced strain fields and thus improved the parameter identification.
- (iii) The mean values of the identified stiffness parameters were systematically lower than the reference ones. Our explanation is that experimental inadequacies are probably responsible for this, since the specimens used in this work and the ones in the references were taken from different heights within the stem. Indeed, the vertical spatial variation of the mechanical properties of *P. pinaster* wood within the stem can be high (in the range of 30-35%) as reported in (Machado and Cruz, 2005). This assumption, however, has to be confirmed by further tests.
- (iv) Although it has been shown numerically in § 4.3 that the best configuration should correspond to a grain angle of  $30^\circ$ , experimentally, unstable identification results were systematically obtained due to a not faithful reconstruction of the strain fields. Therefore, the  $30^\circ$  configuration was disqualified for further experiments.
- (v) Experimentally, difficulties have been found in transferring the grid to the wood surface. Consequently, small areas of non-transferred grid were often observed from where no measurements could be provided. Although the spatial resolution requirement had led to the choice of the grid method, these observations may suggest that optical techniques for which no specifications in terms of specimen preparation (*e.g.*, digital image correlation or speckle interferometry techniques) may be preferable to a natural material like wood. Furthermore, because of the use of 2D polynomials for reconstructing the strain fields, local areas of corrupted data can have a global effect on the actual reconstruction of the strain fields. Hence, a more local reconstruction approach, such as the piecewise finite element approximation scheme (Avril and Pierron, 2007), is recommended for further studies.



# Chapter 6

## On the spatial variability of the longitudinal-radial stiffness of *P. pinaster* wood within the stem

### 6.1 Introduction

It is well accepted that the physical and the mechanical properties of wood vary within the stem, both radially (horizontal spatial variation) and longitudinally (vertical spatial variation) (§ 1.4.4). Moreover, it has been pointed out (*e.g.*, Machado and Cruz, 2005) that the spatial variation of the mechanical properties of wood is more significant along the radial direction than along the longitudinal one. However, contrarily to physical properties of wood such as the density, experimental studies for accessing the spatial variability of the mechanical properties of wood within the stem are scarce. Hence, the aim of this chapter is to apply the procedure presented and validated in the former chapters to investigate the spatial variability of the longitudinal-radial stiffness parameters of *P. pinaster* wood within the stem. For this purpose the radial variation of the stiffness parameters are to be investigated at two different vertical locations.

From the experimental validation reported in Chapter 5, a 45° configuration was chosen for the present study. For this configuration it was shown that both the  $Q_{22}$  and the  $Q_{66}$  stiffness parameters were well identified, although more scattered results were obtained for  $Q_{12}$  and, to a lesser extent, for  $Q_{11}$ . The robustness of the proposed identification approach for identifying  $Q_{22}$  and  $Q_{66}$  is timely since there has been a lack of information in the literature about the spatial distribution of these parameters. Indeed, the experimental studies, in terms of elastic properties of wood, have always targeted the longitudinal elastic modulus (which is proportional to  $Q_{11}$  through Eq. 1.4) (*e.g.*, Machado and Cruz, 2005). Thus, a contribution regarding the radial variation of the  $Q_{22}$  and  $Q_{66}$  parameters at two distinct longitudinal locations is eventually sought here.

## 6.2 Experimental work

The wood material used in this study was manufactured from a single *P. pinaster* tree, aged of 64 years and selected in the district of Viseu (Portugal). After the felling, the tree was cut into several logs with a length of 2.5 m (Figure 6.1(a)). As no information about the cardinal points of the location of the tree (North–South orientation) was available, the logs were longitudinally cut at an arbitrary orientation into quarter–sawn and plain–sawn boards (Figure 6.1(a)). Nevertheless, it has been pointed out that the stem orientation has no significant effect on the mechanical properties of wood (Machado and Cruz, 2005). The boards were dried in a kiln during several weeks afterwards in order to reach a moisture content of about 12%.

In order to study the radial variations of the stiffness parameters, two groups of specimens were cut along the radius of the stem at two distinct vertical locations as schematised in Figure 6.1(b). The first group was manufactured from log 1 at vertical location 1 ( $l_1$ ), whereas the second one was cut from log 3 at vertical location 2 ( $l_2$ ). Both locations are separated by a distance of about 4 m. All the specimens were taken from the central board of the logs, which contained the pith of the stem. For each vertical location in the stem, rectangular specimens with nominal dimensions  $80(L) \times 20(R) \times 5(T)$  mm<sup>3</sup> and grain at 45°, with respect to the specimen longitudinal axis, were sampled along the radial direction from the pith to the outer part of the board as shown in Figure 6.1(b). Because of some eccentricity and taper shape of the stem, the specimens were cut at four ( $r_1$ ,  $r_2$ ,  $r_3$  and  $r_4$ ) and three ( $r_1$ ,  $r_2$  and  $r_3$ ) radial positions at the first ( $l_1$ ) and second ( $l_2$ ) vertical locations, respectively. The radial positions were measured and referenced with regard to the geometrical centre of the specimens (Figure 6.1(b)). At vertical location 1, in average, radial positions  $r_1$ ,  $r_2$ ,  $r_3$  and  $r_4$  corresponded to 29% (13th annual ring), 46% (19th annual ring), 64% (29th annual ring) and 81% (43th annual ring) of the total length from pith to end; whilst at vertical location 2, the radial positions  $r_1$ ,  $r_2$  and  $r_3$  were at 30% (7th annual ring), 54% (54th annual ring) and 76% (30th annual ring) of the local radius of the board. For repeatability quantification, at location 1, nine specimens per radial position were machined, *i.e.*, a total of thirty-six specimens; whereas, at location 2, eight specimens per radial position were prepared, *i.e.*, a total of twenty-four specimens. All specimens were free from visible defects and contained a few annual rings over the region of interest.

The preparation of the surface of the specimens, the grid transfer, the calibration of the optical system and the tests were achieved as described in § (5.2). The tests were carried out using an Instron 5582 universal testing machine and the grid images were recorded by a 12 bit PCO SenSicam CCD Camera system. The load was measured by a 5 kN load cell. It was applied at a constant cross-head displacement rate of 1 mm/min. The load and grid images were recorded automatically during the tests with an acquisition



frequency of 2 Hz. Among all tested specimens, the values of the phase and displacement resolutions associated to the grid method were determined in the range of  $3.05 \pm 0.5^\circ$  and  $1.20 \pm 0.2 \mu\text{m}$ , respectively. The tests were carried out at a room temperature of  $23.2 \pm 1.2^\circ\text{C}$  and at a relative humidity of  $42.7 \pm 4.9\%$ . After the tests, the specimens were dried and their moisture content during the tests was estimated, according to the oven-dry method (§ 1.4.3.1), equal to  $10.3 \pm 0.5\%$ .

## 6.3 Results and discussion

### 6.3.1 Stiffness variation along the radial direction

The curves of the applied load (N) against the cross-head displacement (mm) (measured by the Instron machine), obtained from the set of specimens located at vertical location 1 in the stem (Figure 6.1(b)), are shown in Figure 6.2, for the radial positions (a)  $r_1$ , (b)  $r_2$ , (c)  $r_3$  and (d)  $r_4$ , whereas the mean curves are plotted together in (e). In turn, Figure 6.3 shows the curves of the load versus the cross-head displacements for the specimens at vertical location 2 within the stem. These curves show some dispersion which is, however, in a range that is typically observed when testing wood, owing to the inherent variability among specimens. The variation of the oven-dry density of the specimens across the radial direction at the vertical locations 1 and 2 is shown together in Figure 6.4. The normality of the densities distribution was verified by the Shapiro-Wilk test (Neuilly, 1999, p. 87). As it can be observed, at location 1, the density decreases gradually by 12.3% between the radial positions  $r_1$  ( $r/R = 29\%$ ),  $r_2$  ( $r/R = 46\%$ ) and  $r_3$  ( $r/R = 64\%$ ) and slightly increases afterwards at the outermost position  $r_4$  ( $r/R = 81\%$ ) by 1.6%. Besides, from the Student's  $t$ -test of equality of means between two samples, the hypothesis that the two means are equal is rejected for densities at radial positions  $r_2$  ( $0.638 \pm 0.007$ ) and  $r_4$  ( $0.626 \pm 0.009$ ), and accepted, only at a 99% confidence level, between densities at  $r_3$  ( $0.616 \pm 0.009$ ) and  $r_4$ . At location 2, the density decreases from the innermost position  $r_1$  ( $r/R = 30\%$ ) to position  $r_2$  ( $r/R = 54\%$ ) by 4.4% and increases afterwards to the outmost position  $r_3$  ( $r/R = 76\%$ ) by 1.8%. The densities between the radial positions  $r_1$  ( $0.641 \pm 0.006$ ) and  $r_3$  ( $0.625 \pm 0.010$ ) represent different mean values, whereas the densities between  $r_2$  ( $0.614 \pm 0.010$ ) and  $r_3$  have equal means only at a 99% confidence level, according to the  $t$ -test of equality of means.

In the identification of the stiffness parameters by the virtual fields method (VFM), the same procedure as described in § (5.3.2) was followed here. The measured displacement fields were filtered by a 7th-degree polynomial using the least-squares regression scheme. The strain fields were then determined by finite differences from the polynomial displacement fields. Piecewise optimised virtual fields were defined over a mesh of  $5(x) \times 3(y)$  elements (see Figure 3.6). Both the computed strain fields and the applied

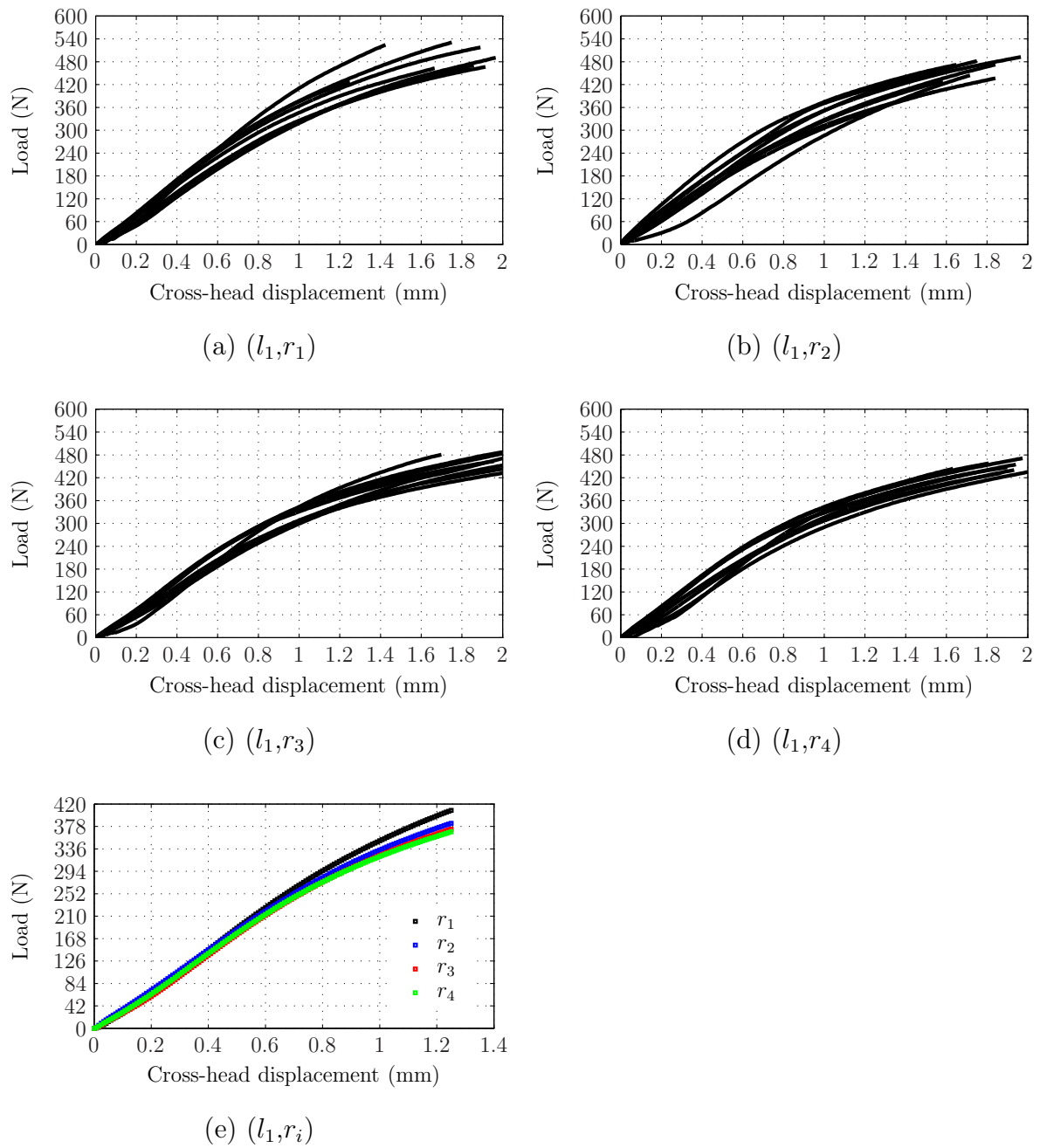


Figure 6.2: Curves of load versus cross-head displacement obtained at vertical location 1 for the radial positions : (a)  $r_1$ ; (b)  $r_2$ ; (c)  $r_3$ ; (d)  $r_4$ ; (e) average curves (displacement rate of 1 mm/min).

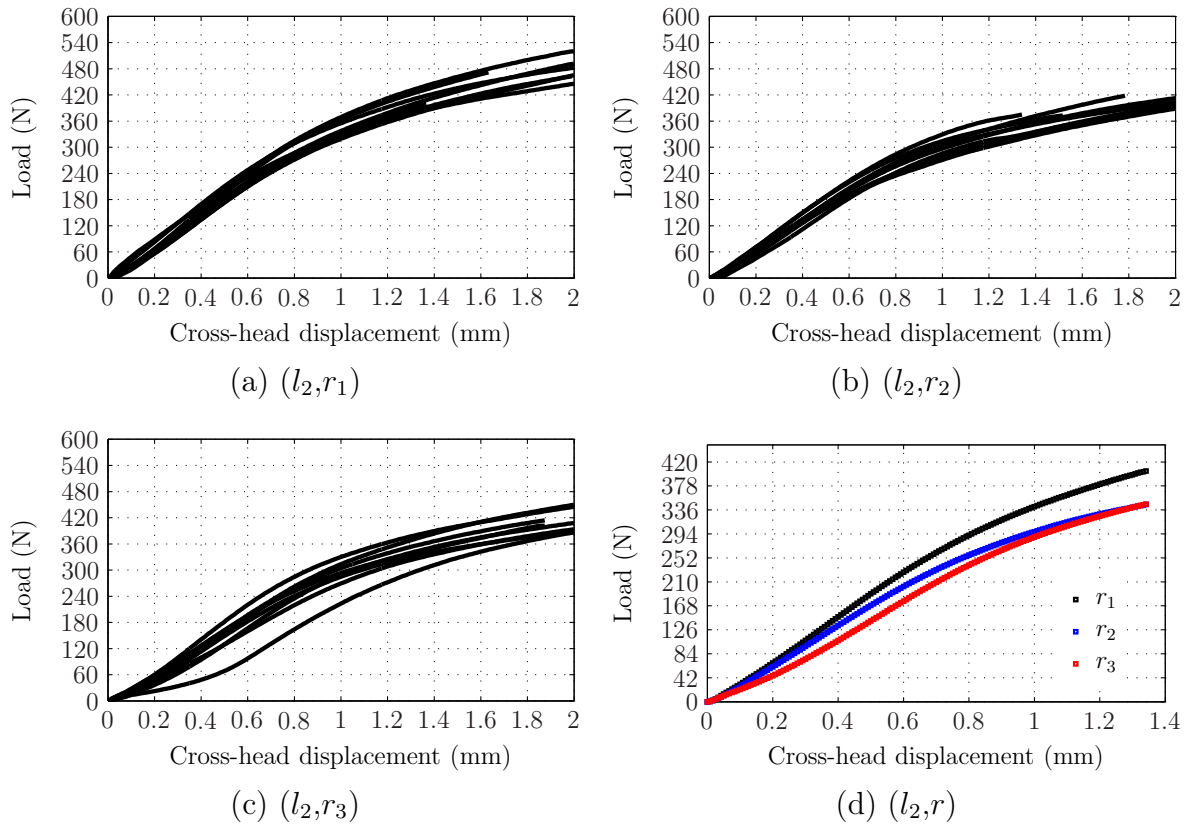


Figure 6.3: Curves of load versus cross-head displacement obtained at vertical location 2 for the radial positions: (a)  $r_1$ ; (b)  $r_2$ ; (c)  $r_3$ ; (d) average curves (displacement rate of 1 mm/min).

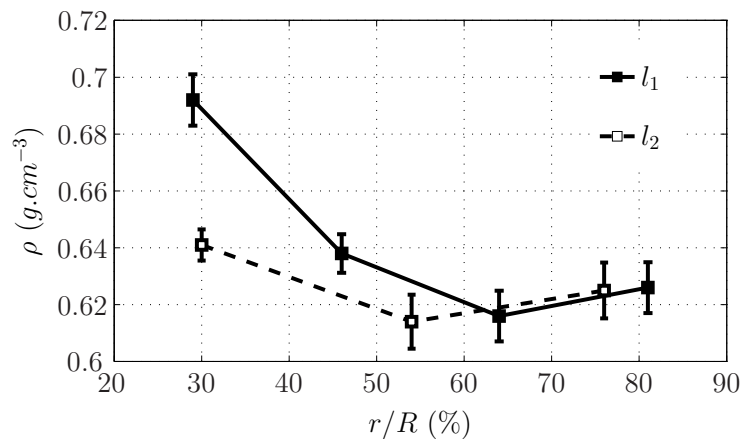


Figure 6.4: Variation of the oven-dry density ( $\rho$ ) at vertical locations 1 (■) and 2 (□) with the radial positions.

load, corresponding to different acquisition times, were input into the VFM routine for the identification of the stiffness parameters. For filtering purposes, the parameters were determined as the mean of a set of identified values obtained within a specified range of loads. For choosing this range of loads, a first parameter identification was performed between 100 N and 300 N. If the results have a coefficient of variation larger than 10%, then the data, corresponding to the identified stiffness values that are higher than  $\pm 2\sigma$  about the mean, are systematically removed in further reevaluations until convergence is eventually reached.

As expected from the experimental validation reported in § 5.3.2, the results for  $Q_{11}$  and  $Q_{12}$  were highly dispersed and consequently no exploitable variability patterns could be clearly determined. Therefore, only the results for  $Q_{22}$  and  $Q_{66}$  are reported below.

An example of the identified  $Q_{22}$  and  $Q_{66}$  stiffness values, at the different radial positions, versus the applied load is plotted in Figures 6.5 and 6.6, respectively, for the vertical locations 1 and 2. As it can be seen, reasonable stable results are obtained to these properties within the selected levels of load. Moreover, some contrast can be observed between values identified at different radial positions, *e.g.*, between the radial positions  $r_2$  and  $r_4$  at vertical location 1, and between the radial positions  $r_2$  and  $r_3$  at vertical location 2.

The identified stiffness values at vertical location 1 as well as their mean and error bars (95% confidence intervals about the mean value), are plotted as a function of the radial positions in Figure 6.7: (a)  $Q_{22}$ ; (b)  $Q_{66}$ . As it can be noticed (Figure 6.7(a)), the  $Q_{22}$  parameter decreases between the radial positions  $r_1$  and  $r_2$  by 36.5%, and a progressive increase of 23.7% and 49.0% is observed afterwards between  $r_2$  and  $r_3$  and from  $r_2$  up to  $r_4$ , respectively. A great contrast arises between positions  $r_2$  and  $r_4$ , which corresponds to a radial distance from about the 19th annual ring to about the 43th annual ring of the stem (Figure 6.1(b)). The mean values of  $Q_{22}$  at the different radial positions were compared, using the *t*-test for equality of means of two samples (same variance) at a 95% confidence level (Table 6.1). Accordingly,  $Q_{22}(l_1, r_2)$  represents a different mean value when compared to the values at the other radial positions. This confirms that an effective decrease of  $Q_{22}$  is observed along the radial direction around 46% of the radius of the stem. Furthermore,  $Q_{22}(l_1, r_1)$  has the same mean value as  $Q_{22}(l_1, r_3)$  and  $Q_{22}(l_1, r_4)$ . Between the two outmost positions,  $r_3$  and  $r_4$ ,  $Q_{22}(l_1, r_3)$  was lower than  $Q_{22}(l_1, r_4)$  by 20.4%, and they represent a different mean value according to the *t*-test at a 95% confidence level. The same pattern of spatial variation along the radial direction was also observed for  $Q_{66}$ , although with a lower contrast (Figure 6.7(b)):  $Q_{66}$  decreases from  $r_1$  to  $r_2$  by 20.9%, and increases within the outmost positions by 12.9% and 17.7% between  $r_2$  and  $r_3$  and between  $r_2$  and  $r_4$ , respectively. The mean values of  $Q_{66}$  at the different radial positions were compared by the *t*-test of equality of means at a 95% confidence level (Table 6.1). A different mean values is confirmed to  $Q_{66}(l_1, r_2)$  with regard to the values at the other radial positions, showing that a decrease of the  $Q_{66}$  parameter is obtained

around 46% of the radius of the stem. Besides,  $Q_{66}(l_1, r_1)$ ,  $Q_{66}(l_1, r_3)$  and  $Q_{66}(l_1, r_4)$  all represent the same mean value. Thus, more stable properties were obtained between  $r_3$  and  $r_4$  with a difference between  $Q_{66}(l_1, r_3)$  and  $Q_{66}(l_1, r_4)$  of 4.3%. Moreover, it can be noticed from the values reported in the tables accompanying Figure 6.7, that the dispersion (coefficients of variation) associated to the identified stiffness results, for both  $Q_{22}$  and  $Q_{66}$ , are of the same order of magnitude as reference ones determined from conventional tests (Table 5.1). The radial variation of the stiffness parameters (Figure 6.7) does not follow the same pattern as the oven-dry density of the specimens (Figure 6.4), and the variation of the former is more important than the latter. These observations suggest that other structure features (*e.g.*, microfibril angle, percentage of juvenile and mature wood of the specimens,...) are to be considered in order to understand the origin of the radial variation of the elastic properties of the clear wood specimens. This issue may be regarded as a perspective study.

The identification results along with error bars of mean and 95% confidence intervals obtained from the specimens at vertical location 2 are plotted in Figure 6.8: (a)  $Q_{22}$  and (b)  $Q_{66}$ . As it can be noticed (Figure 6.8(a)), the  $Q_{22}$  parameter decreases between  $r_1$  and  $r_2$  by 62.4% and increases afterwards from  $r_2$  up to  $r_3$  by 71.7%. The mean values of  $Q_{22}$  are compared in Table 6.2. The  $Q_{22}(l_2, r_2)$  clearly represent a different mean value with regard to both  $Q_{22}(l_2, r_1)$  and  $Q_{22}(l_2, r_3)$ , which have been confirmed equal means. Thus, a significant decrease of  $Q_{22}$  around 54% of the radius of the stem was observed. Regarding  $Q_{66}$ , the same radial distribution was observed, although again with a lower spatial variability: the  $Q_{66}$  parameter decreases by 21.2% between  $r_1$  and  $r_2$ , and increases afterwards by 26.6% from  $r_2$  up to  $r_3$ . The hypothesis of equal means among the values of  $Q_{66}$  was checked (Table 6.2). It was confirmed by the *t*-test of equality of means at 95% confidence level that  $Q_{22}(l_2, r_2)$  is a different mean when compared to both  $Q_{22}(l_2, r_1)$  and  $Q_{22}(l_2, r_3)$ , which, in their turn, represent the same mean value. Furthermore, the dispersion of the stiffness values identified at vertical location 2 for both  $Q_{22}$  and  $Q_{66}$ , reported in the tables within Figure 6.8, are of the same order of magnitude as reference ones reported from conventional tests on clear wood specimens (Table 5.1). Particularly, the stiffness radial distribution (Figure 6.8) follows the general pattern of the density variation along the radial direction (Figure 6.4), although the former with a high contrast than the latter.

### 6.3.2 Stiffness variation along the longitudinal direction

The identification results for the different radial and vertical locations within the stem are plotted in Figure 6.9. As it can be noticed, no significant vertical variation exists for analogous radial positions. By comparing the  $Q_{22}$  and the  $Q_{66}$  stiffness values for the outmost specimens taken at the two vertical locations, *i.e.*,  $r_4$  and  $r_3$  for vertical locations

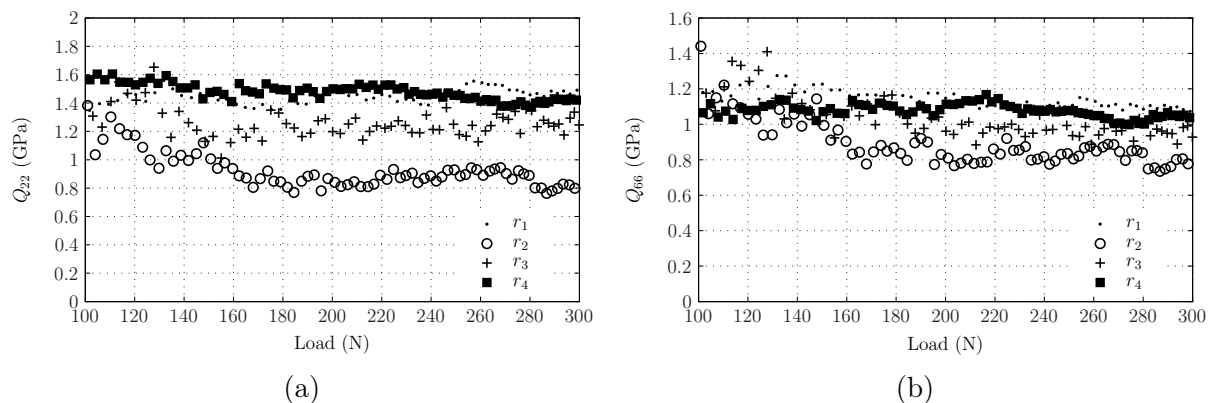


Figure 6.5: Identified stiffness parameters at vertical location 1 as a function of the applied load: (a)  $Q_{22}$ ; (b)  $Q_{66}$ .

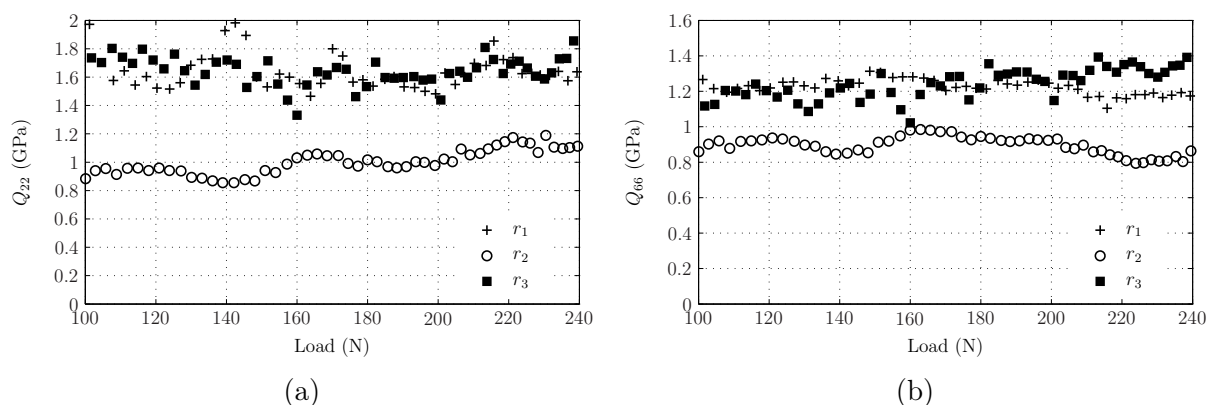


Figure 6.6: Identified stiffness parameters at vertical location 2 as a function of the applied load: (a)  $Q_{22}$ ; (b)  $Q_{66}$ .

1 and 2, respectively, using the  $t$ -test for equality of the means at a 95% confidence level, it is concluded that the two properties are both equal at the two vertical locations. A comparison of these values with regard to reference ones for the *P. pinaster* wood (Table 5.1) is presented in Figure 6.10. As it can be noticed, lower values were identified here although with differences, ranging from 12.6% to 18.0%, which can be assumed to be dissolved within the typical dispersion associated with mechanical properties of wood. Besides, the variation of the oven-dry density of the specimens along the longitudinal direction can be compared directly from Figure 6.4. Excluding the innermost radial positions within the stem for where a decrease of density is observed along the vertical direction, the density at analogous positions higher than about 50% of the radius stem is rather stable.

Although these observations are not consistent with our assumption at Chapter 5 concerning the vertical spatial variation of the stiffness properties, it should be noticed that the distance between vertical locations 1 and 2 (about 4 m) is shorter than the

Table 6.1: Comparison of mean values between the different radial positions at vertical location 1 by the Student's  $t$ -test of equality of means of two samples at a 95% of confidence level ( $1 - 2 \equiv L - R$ ).

$Q_{22}$		$Q_{66}$	
Two-samples	null hypothesis: means are equal	Two-samples	null hypothesis: means are equal
$(l_1, r_1)$ vs $(l_1, r_2)$ :	rejected	$(l_1, r_1)$ vs $(l_1, r_2)$ :	rejected
$(l_1, r_1)$ vs $(l_1, r_3)$ :	accepted	$(l_1, r_1)$ vs $(l_1, r_3)$ :	accepted
$(l_1, r_1)$ vs $(l_1, r_4)$ :	accepted	$(l_1, r_1)$ vs $(l_1, r_4)$ :	accepted
$(l_1, r_2)$ vs $(l_1, r_3)$ :	rejected	$(l_1, r_2)$ vs $(l_1, r_3)$ :	rejected
$(l_1, r_2)$ vs $(l_1, r_4)$ :	rejected	$(l_1, r_2)$ vs $(l_1, r_4)$ :	rejected
$(l_1, r_3)$ vs $(l_1, r_4)$ :	rejected	$(l_1, r_3)$ vs $(l_1, r_4)$ :	accepted

Table 6.2: Comparison of mean values between the different radial positions at vertical location 2 by the Student's  $t$ -test of equality of means of two samples at a 95% of confidence level ( $1 - 2 \equiv L - R$ ).

$Q_{22}$		$Q_{66}$	
Two-samples	null hypothesis: means are equal	Two-samples	null hypothesis: means are equal
$(l_2, r_1)$ vs $(l_2, r_2)$ :	rejected	$(l_2, r_1)$ vs $(l_2, r_2)$ :	rejected
$(l_2, r_1)$ vs $(l_2, r_3)$ :	accepted	$(l_2, r_1)$ vs $(l_2, r_3)$ :	accepted
$(l_2, r_2)$ vs $(l_2, r_3)$ :	rejected	$(l_2, r_2)$ vs $(l_2, r_3)$ :	rejected

one between the specimens compared in the discussion of results in § 5.3 (about 6 m). Furthermore, from the study by (Machado and Cruz, 2005), the authors have observed that along the stem, from specimens taken radially at 10% (DP10), 50% (DP50) and 90% (DP90) of the radius of the stem, the longitudinal elastic modulus ( $E_1$ ) slightly decreases for DP10 and strongly decreases for DP50 and DP90, but only with a more visible pattern between 35% and 65% of the total height of the trees (*i.e.*, for distances higher up than about 5.6–7 m from the tree bottom). The authors have explained these decrease on the  $E_1$  parameters due to the juvenile/mature wood transition observed along the stem.

It follows that, in order to push forward the investigations about the longitudinal variation of the stiffness parameters, tests should be carried out on specimens cut from other vertical locations within the stem. Indeed, the data provided here from only two vertical locations may not be sufficient to supply a relevant pattern of the longitudinal variations of the stiffness parameters.

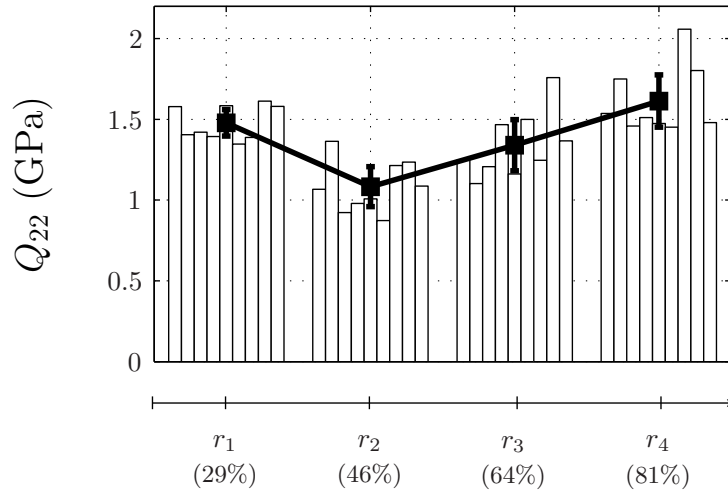
## 6.4 Conclusions

This chapter aimed at giving a contribution to the spatial variability of the longitudinal-radial,  $(L, R) \equiv (1, 2)$ , stiffness parameters of clear wood of *P. pinaster* within the stem. For this target, the radial variation of the stiffness parameters were investigated at two distinct vertical locations. In this study, unnotched specimens with grain at  $45^\circ$  were tested using the Iosipescu fixture. The virtual fields method (VFM) was used to the identification of the stiffness parameters from the displacement fields measured by the grid method. From the identification results, the interpretation of both the  $Q_{11}$  and the  $Q_{12}$  parameters was difficult because of the scattered values reached – this was somewhat expected from the experimental validation reported in § 5.3. Consequently, no exploitable patterns could be clearly determined to these two parameters. Hence, only the identification results corresponding to the  $Q_{22}$  and the  $Q_{66}$  parameters were analysed. The following conclusions were drawn.

- (i) It was found that along the radial direction both the  $Q_{22}$  and the  $Q_{66}$  parameters decrease from the pith to about the middle radius of the stem and increase afterwards to the outmost positions. Besides, the radial spatial variability of  $Q_{22}$  was found higher than the one obtained for  $Q_{66}$ , *i.e.*, with a contrast ranging between 49%-72% and 18%-27% (depending on the location within the stem), respectively.
- (ii) No significant longitudinal variation was observed for both  $Q_{22}$  and  $Q_{66}$  parameters within the two studied vertical locations at the different radial positions. However, the data provided here from only two vertical locations may not be sufficient to supply a relevant pattern of the longitudinal variations of the stiffness parameters.
- (iii) The density variation of the specimens along the radial direction did not explained by itself the pattern of the stiffnesses variation. This supports the point that other structure features (*e.g.*, microfibril angle, percentage of juvenile and mature wood of the specimens...) are to be considered in order to understand the causes in the origin of the radial variation of the elastic properties. This issue may be regarded as perspectives, where the data provided from the methodology presented here could be tied to studies focused on the material structure, similarly to the one presented in (Xu et al., 2004).

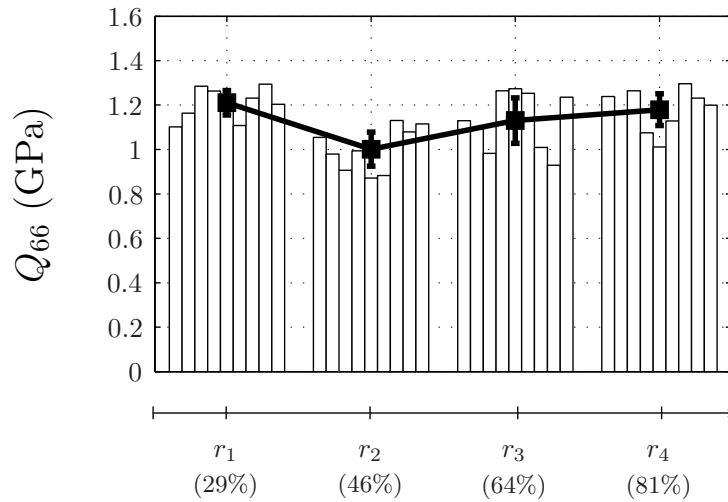
At this stage, a further improvement of this approach can be foreseen. The idea is to capture directly the radial variability from a single test. The approach can be extended to bending tests using plates taken from the pith to the bark of the stem. The radial variability of the stiffness parameters can be parameterised using a polynomial basis function, for instance. A similar procedure of the VFM has already been developed for the identification of the local stiffness reduction on damaged composite plates (Kim et al., 2007).

(a)  $(l_1, r_i)$



	$r_1$		$r_2$		$r_3$		$r_4$	
	$\rho$	$Q_{22}$	$\rho$	$Q_{22}$	$\rho$	$Q_{22}$	$\rho$	$Q_{22}$
Mean	0.692	1.48	0.638	1.08	0.616	1.34	0.626	1.61
C.I. <sup>a</sup>		$\pm 0.082$		$\pm 0.123$		$\pm 0.158$		$\pm 0.162$
C.V. <sup>b</sup> (%)	1.30	7.21	1.06	14.8	1.45	15.4	1.43	13.1

(b)  $(l_1, r_i)$

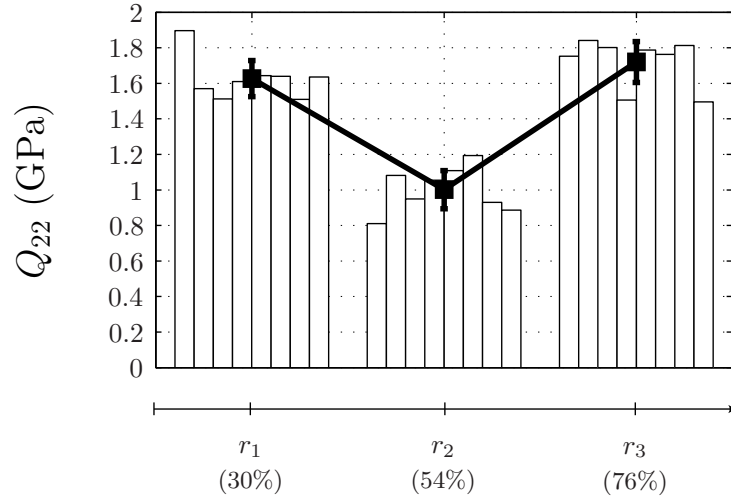


	$r_1$		$r_2$		$r_3$		$r_4$	
	$\rho$	$Q_{66}$	$\rho$	$Q_{66}$	$\rho$	$Q_{66}$	$\rho$	$Q_{66}$
Mean	0.692	1.21	0.638	1.00	0.616	1.13	0.626	1.18
C.I. <sup>a</sup>		$\pm 0.055$		$\pm 0.077$		$\pm 0.103$		$\pm 0.072$
C.V. <sup>b</sup> (%)	1.30	5.93	1.06	9.94	1.45	11.8	1.43	7.89

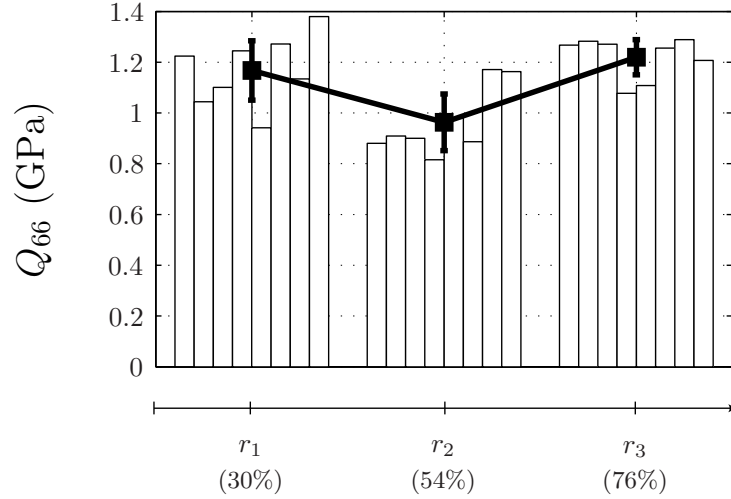
<sup>(a)</sup> Confidence intervals at 95% confidence level;

<sup>(b)</sup> Coefficient of variation (%).

Figure 6.7: Stiffness values: (a)  $Q_{22}$ ; (b)  $Q_{66}$ , identified at vertical position 1 for the radial positions  $r_1, r_2, r_3$  and  $r_4$  (unit:  $\rho$  -  $\text{g}\cdot\text{cm}^{-3}$ ;  $Q_{ij}$  - GPa).

(a)  $(l_2, r_i)$ 

	$r_1$		$r_2$		$r_3$	
	$\rho$	$Q_{22}$	$\rho$	$Q_{22}$	$\rho$	$Q_{22}$
Mean	0.641	1.63	0.614	1.00	0.625	1.72
C.I. <sup>a</sup>		$\pm 0.102$		$\pm 0.107$		$\pm 0.115$
C.V. <sup>b</sup> (%)	0.86	7.47	1.55	12.8	1.56	8.02

(b)  $(l_2, r_i)$ 

	$r_1$		$r_2$		$r_3$	
	$\rho$	$Q_{66}$	$\rho$	$Q_{66}$	$\rho$	$Q_{66}$
Mean	0.641	1.17	0.614	0.963	0.625	1.22
C.I. <sup>a</sup>		$\pm 0.117$		$\pm 0.112$		$\pm 0.069$
C.V. <sup>b</sup> (%)	0.86	12.0	1.55	13.9	1.56	6.79

<sup>(a)</sup> Confidence intervals at 95% confidence level;<sup>(b)</sup> Coefficient of variation (%).Figure 6.8: Stiffness values: (a)  $Q_{22}$ ; (b)  $Q_{66}$ , identified at vertical position 2 the radial positions  $r_1$ ,  $r_2$  and  $r_3$  (unit:  $\rho$  -  $\text{g.cm}^{-3}$ ;  $Q_{ij}$  - GPa).

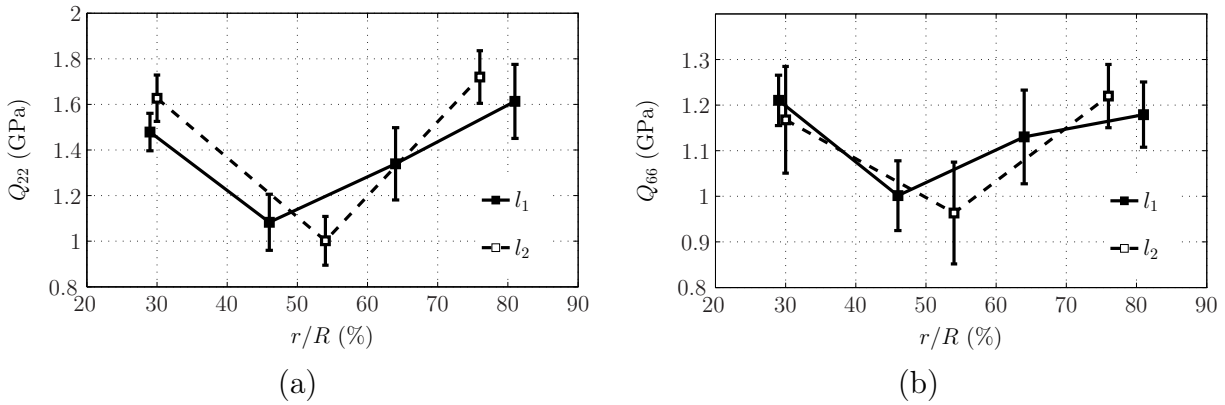


Figure 6.9: Variation of the stiffness parameters: (a)  $Q_{22}$ ; (b)  $Q_{66}$ , identified at the two vertical locations 1 (■) and 2 (□) as a function of the radial position ( $r/R$ ).

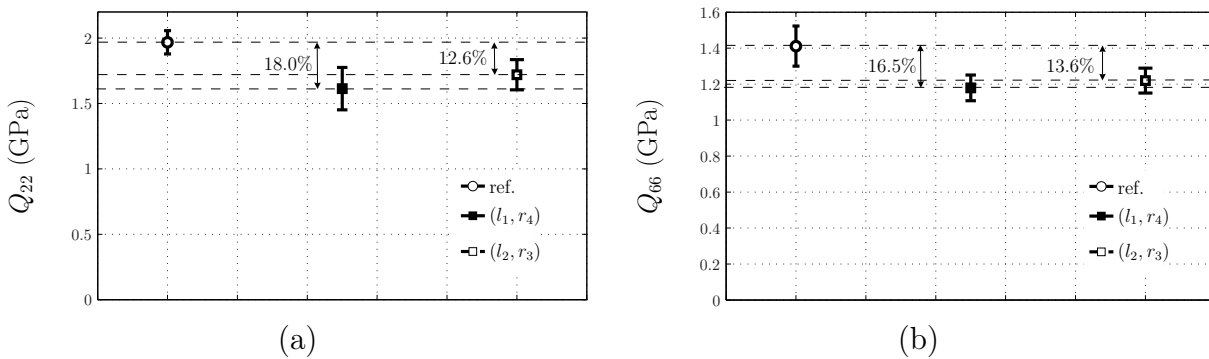


Figure 6.10: Comparison of the stiffness parameters: (a)  $Q_{22}$ ; (b)  $Q_{66}$ , identified at the two vertical locations 1 (■) and 2 (□) at the outmost radial position,  $r_4$  and  $r_3$ , respectively, with regard to reference values (○).

# General conclusions and future work

This work has investigated a material characterisation approach for the identification of the longitudinal-radial ( $LR$ ) stiffness parameters of maritime pine (*Pinus pinaster* Ait.) wood. The approach is based on the application of the virtual fields method (VFM) to the Iosipescu test with an unnotched specimen. This method relies on the fundamental equations of solid mechanics: the principle of the virtual work (PVW) (which describes the global equilibrium of a body) and the constitutive equations (which states the stress and strain relationship at each point within a body). Optimised (with regard to a sensitivity to noise criterion) piecewise special virtual fields were used. The unnotched Iosipescu test has been designed in such a way that heterogeneous strain fields were reached in the central part of the unnotched specimen (*i.e.*, between the inner loading points). These kinematic fields, needed in the material characterisation problem, were derived from the displacement fields measured by the grid method, through a least-squares regression and finite difference scheme. The strain fields and resultant applied load (measured by a universal testing machine) were processed by the VFM routine, yielding the direct identification of the four effective stiffness components of clear wood in the  $(L, R) \equiv (1, 2)$  plane of symmetry:  $Q_{11}$ ,  $Q_{22}$ ,  $Q_{12}$  and  $Q_{66}$ . The following general conclusions can be drawn from this work.

- (i) The proposed inverse identification approach was firstly validated from a numerical point of view. The experimental data were replaced by simulated displacement fields obtained from a finite element model of the mechanical test developed in the ANSYS code. Reference elastic properties of *P. pinaster* wood taken from the literature were used in the numerical analyses. For the  $0^\circ$  specimen configuration, a study was undertaken for calibrating the gauge length, defined as the distance between the inner loading points. A free length of 34 mm was chosen according to the criterion of minimisation of the sensitivity to noise coefficients provided by the VFM routine. Moreover, a study was performed in order to calibrate the polynomial degree to be used in the least-squares regression scheme for the strain reconstruction. It was found that a 7th-degree polynomial was a good compromise between the efficiency of noise filtering and the faithfulness of the reconstruction. Besides, a parametric study was achieved for choosing the *virtual* mesh, over which the piecewise virtual fields are defined. It was shown that stable results are obtained for a mesh of  $8(x) \times 4(y)$

elements, even when processing displacement fields corrupted by a Gaussian white noise.

- (ii) In the VFM, the material parameters were assumed to be constant across the region of interest of the specimen. However, owing to the small size of this region (with a width of 20 mm along the radial direction), the annual rings structure of the specimens may contradict this assumption. Consequently, it was checked, by building up a layered material model, if the VFM can provide homogenised values of the stiffness parameters. Different geometrical models were analysed by changing the volume fractions, number of layers and elastic engineering properties of the two layers, in order to access the inherent variability associated to the specimen composition. From these material models, the effective properties provided by the law of mixtures could be recovered by the VFM, proving the relevance of the homogeneity assumption.
- (iii) According to the sensitivity to noise coefficients given by the VFM, it was found that the mechanical response of the  $0^\circ$  configuration favours the identifiability of both the  $Q_{11}$  and  $Q_{66}$  stiffness parameters to the detriment of the  $Q_{22}$  and  $Q_{12}$  components. This led to an optimisation study aimed at determining the best configuration for which an evenly balanced contribution of the stiffness components could be eventually reached. The gauge length and the grain angle were taken as design variables. A cost function was built up from the sensitivity to noise terms of the VFM. It was found that the rotation of the grain angle ( $\theta > 0$ ) enhances the robustness of the identification by improving the contribution of both  $\varepsilon_1$  and  $\varepsilon_2$  strains, still keeping some influence of the shear strain component,  $\varepsilon_6$ . A gauge length of 35 mm and a grain angle of  $30^\circ$  were found to maximise the whole identifiability of the stiffness parameters.
- (iv) The inverse identification approach was then validated from an experimental point of view. The displacement fields were provided by the grid method. Three configurations were tested with grain angles of  $0^\circ$ ,  $45^\circ$  and  $30^\circ$ . The gauge length was set to 34 mm, so a region of interest of  $34 \times 20 \text{ mm}^2$  was used. The spatial resolution of the method was about the pitch of the grid, *i.e.*, 0.1 mm. The displacement resolution was found between 0.9 and 1.2  $\mu\text{m}$ , strongly depending on the quality of the grid transfer.
- (v) Experimentally, for the  $0^\circ$  configuration, only the  $Q_{11}$  and  $Q_{66}$  parameters could be correctly identified with reasonable dispersion. The  $45^\circ$  configuration led to some improvements in the results, especially in the identification of the  $Q_{22}$  parameter. However, the identifiability of the  $Q_{12}$  parameter still remained low. Although it has been shown numerically that the best configuration should correspond to a grain

angle of  $30^\circ$ , experimentally, unstable results were systematically obtained due to an unfaithful reconstruction of the strain fields. Therefore, the  $30^\circ$  configuration was disqualified for further experiments.

- (vi) The stiffness parameters identified from the inverse approach were systematically lower than reference properties for the *P. pinaster* species by about 30-35%. As the specimens used here and the reference ones were taken from different heights within the same tree (separated by about 6 m), these differences were interpreted as due to the spatial variability of the mechanical properties of wood within the stem. Indeed, a recent study (Machado and Cruz, 2005) has shown that for this species a decrease in the elastic modulus parallel to grain ( $E_1$ ) between 29% and 35% can be observed for specimens taken at different vertical locations within the stem separated by about 65% of the total height of the tree.
- (vii) The  $45^\circ$  configuration was used in a subsequent study for investigating the spatial variability of the *LR* stiffness parameters of *P. pinaster* wood within the stem. As expected, results for  $Q_{11}$  and  $Q_{12}$  were largely scattered, preventing any exploitation for commenting their spatial variability. Nevertheless, interesting results were found for  $Q_{22}$  and  $Q_{66}$ . It was found that both parameters decrease from the pith to about the middle radius of the stem and increase afterwards to the outmost positions. The radial variability of  $Q_{22}$  is, however, higher than the one obtained for  $Q_{66}$ , *i.e.*, with a contrast ranging between 49%-72% and 18%-27% respectively (depending on the location within the stem). Nevertheless, no significant longitudinal variation was observed for both  $Q_{22}$  and  $Q_{66}$  components within the two studied vertical locations separated by about 4 m. However, the data provided here from only two vertical locations may not be sufficient to supply a relevant pattern of the longitudinal variations of the stiffness parameters.

The following points can be highlighted for improving the approach proposed in this thesis and investigate with more insight the spatial variability of the wood mechanical properties.

- Experimentally, difficulties have been found in transferring the grid to the wood surface. Consequently, small areas of non-transferred grid were often observed from which no measurements could be provided. Although the spatial resolution requirement had led to the choice of the grid method, these observations may suggest that optical techniques in which no specifications in terms of specimen preparation (*e.g.*, digital image correlation or speckle interferometry techniques) may be preferable for a natural material like wood.
- Since a least-squares regression scheme using 2D polynomials was employed, local areas of corrupted data (*e.g.*, non-transferred grid) can have a global effect on the ac-

tual reconstruction of the strain fields. Hence, a more local reconstruction approach, such as the piecewise finite element approximation scheme ([Avril and Pierron, 2007](#)), is recommended for further studies.

- The methodology proposed in this work could be tied to studies focused on the material structure (*e.g.*, microfibril angle, percentage of juvenile and mature wood of the specimens...), in order to provide relevant information concerning the causes in the origin of the spatial variation of the stiffness properties of wood. In the literature only a few studies have addressed this issue (*e.g.*, [Xu et al., 2004](#)).
- It would be interesting to propose non-standard tests (either in-plane or bending tests) allowing the identification of all the stiffness components of clear wood from a reduced number of tests; *i.e.*, the identification of the nine stiffness parameters (in the material coordinate system) from only three tests instead of six independent tests usually employed (*e.g.*, tension/compression and shear tests).
- The utilisation of, for instance, bending tests on wood plates taken from the pith to the periphery of the stem, could be set up to directly identify from a single test the radial variability within the plate. A similar procedure of the VFM has already been developed for the identification of the local stiffness reduction on damaged composite plates ([Kim et al., 2007](#)).
- At the meso scale of observation, the identification of ratios of properties between latewood and earlywood could be implemented using the VFM.
- The VFM could be extended to more complex constitutive equations, *e.g.*, viscoelasticity, by using complex special virtual fields ([Giraudeau et al., 2006](#)).

# References

- D.F. Adams and D.E. Walrath. Current status of the Iosipescu shear test method. *Journal of Composite Materials*, 21(6):494–507, 1987.
- S. Aicher, G. Dill-Langer, and L. Höfflin. Effet of polar anisotropy of wood loaded perpendicular to grain. *Journal of Materials in Civil Engineering*, 13(1):2–9, 2001.
- E.I. Alloba. *Extensométrie optique: Aspects métrologiques et application à la mécanique expérimentale des composites*. PhD thesis, Univeristé Claude Bernard - Lyon I, 1997.
- M. Arcan, Z. Hashin, and A. Voloshin. A method to produce uniform plane-stress states with applications to fiber-reinforced materials. *Experimental Mechanics*, 18(4):141–146, 1976.
- ASTM D143. *Standard methods of testing small clear specimens of timber*. American Society for Testing and Materials, Philadelphia, PA, USA, 1994.
- ASTM D198. *Standard methods of static tests of lumber in structural sizes*. American Society for Testing and Materials, Philadelphia, PA, USA, 1994.
- ASTM D3044. *Test method for shear modulus of wood-based structural panels*. American Society for Testing and Materials, Philadelphia, PA, USA, 1994.
- ASTM D4442. *Standard test methods for direct moisture content measurement of wood and wood-base materials*. American Society for Testing and Materials, Philadelphia, PA, USA, 2003.
- ASTM D5379. *Test method for shear properties of composite materials by the V-notched beam method*. American Society for Testing and Materials, Philadelphia, PA, USA, 1993.
- S. Avril and F. Pierron. General framework for the identification of constitutive parameters from full-field measurements in linear elasticity. *International Journal of Solids and Structures*, 44(14-15):4978–5002, 2007.
- S. Avril, E. Ferrier, A. Vautrin, P. Hamelin, and Y. Surrél. A full-field optical method for the experimental analysis of reinforced concrete beams repaired with composites. *Composites Part A: Applied Science and Manufacturing*, 35(7-8):873–884, 2004a.
- S. Avril, M. Grédiac, and F. Pierron. Sensitivity of the virtual fields method to noisy data. *Computational Mechanics*, 34(6):439–452, 2004b.
- E. Badel and P. Perré. Using a digital X-ray imaging device to measure the swelling coefficients of a group of wood cells. *NDT and E International*, 34(5):345–353, 2001.
- J. Bodig and R. Goodman. Prediction of elastic parameters for wood. *Wood Science*, 5(4):249–264, 1973.

- L. Boström. Determination of the modulus of elasticity in bending of structural timber - comparison of two methods. *Holz als Roh - und Werkstoff*, 57(2):145–149, 1999.
- T. Bothe, J. Burke, and H. Helmers. Spatial phase shifting in electronic speckle pattern interferometry: Minimization of phase reconstruction errors. *Applied Optics*, 36(22):5310–5316, 1997.
- J. Brillaud and F. Lagattu. Limits and possibilities of laser speckle and white-light image-correlation methods: Theory and experiments. *Applied Optics*, 41(31):6603–6613, 2002.
- L. Bruno. Global approach for fitting 2D interferometric data. *Optics Express*, 15(8):4835–4847, 2007.
- L. Bruno, F.M. Furgiuele, L. Pagnotta, and A. Poggialini. A full-field approach for the elastic characterization of anisotropic materials. *Optics and Lasers in Engineering*, 37(4):417–431, 2002.
- J.F. Cárdenas-García, S. Ekwaro-Osire, J.M. Berg, and W.H. Wilson. Non-linear least-squares solution to the moiré hole method problem in orthotropic materials. Part II: Material elastic constants. *Experimental Mechanics*, 45(4):314–324, 2005.
- P. Castéra and P. Morlier. Variability of the mechanical properties of wood: Randomness and determinism. In *Probabilities and materials. Test models and applications*, volume NATO ASI Series E: Appl Sci 269, pages 109–118. Kluwer Academic Publishers, London, 1993.
- H. Chalal, S. Avril, F. Pierron, and F. Meraghni. Experimental identification of a nonlinear model for composites using the grid technique coupled to the virtual fields method. *Composites Part A: Applied Science and Manufacturing*, 37(2):315–325, 2006.
- C.C. Chamis and J.H. Sinclair. Ten degree off-axis test for shear properties in fiber composites. *Experimental Mechanics*, 17(9):339–346, 1977.
- D. Choi, J.L. Thorpe, W.A. Jr. Côté, and R.B. Hanna. Quantification of compression failure propagation in wood using digital image pattern recognition. *Forest Products Journal*, 46(10):87–91, 1996.
- G.L. Cloud. Optical methods in experimental mechanics. Part 23: Reflection moiré. *Experimental Techniques*, 30(5):19–22, 2006.
- G.L. Cloud. *Optical methods of engineering analysis*. Cambridge University Press, New York, 1995.
- T.E. Connors and P.J. Medvecz. Wood as a bimodular material. *Wood and Fiber Science*, 24(4):413–423, 1992.
- R.R. Cordero and P. Roth. On two methods to evaluate the uncertainty of derivatives calculated from polynomials fitted to experimental data. *Metrologia*, 42(1):39–44, 2005.
- K. Creath. Phase-shifting speckle interferometry. *Applied Optics*, 24(18):3053–3058, 1985.
- J.W. Dally and F.R. William. *Experimental stress analysis*. McGraw-Hill International Editions, 3rd edition, 1991.
- F. De Magistris and L. Salmén. Combined shear and compression analysis using the Iosipescu device: Analytical and experimental studies of medium density fiberboard. *Wood Science and Technology*, 37(6):509–521, 2004.

- F. De Magistris and L. Salmén. Combined shear and compression analysis using a modified Iosipescu shear test device. Experimental studies on dry wood. *Holzforschung*, 59(5): 539–545, 2005.
- DGF. *Inventário Florestal Nacional*. Direcção-Geral das Florestas, Lisboa, Portugal, 2007.
- J.M. Dinwoodie. *Timber: Its nature and behaviour*. Van Nostrand Reinhold, 2000.
- B.V. Dorrió and J.L. Fernández. Phase-evaluation methods in whole-field optical measurement techniques. *Measurement Science and Technology*, 10(3):R33–R55, 1999.
- P. Doumalin. *Microextensométrie Locale par Corrélation d’Images Numériques*. PhD thesis, Ecole Polytechnique, 2000.
- J.-F. Dumail and L. Salmén. Intra-ring variations in the rolling shear modulus of spruce wood. *Holzforschung*, 55(5):549–553, 2001.
- J.-F. Dumail, K. Olofsson, and L. Salmén. An analysis of rolling shear of spruce wood by the Iosipescu method. *Holzforschung*, 54(4):420–426, 2000.
- J. Eberhardsteiner. Biaxial testing of orthotropic materials using electronic speckle pattern interferometry. *Measurement: Journal of the International Measurement Confederation*, 16(3):139–148, 1995.
- G. Ebrahimi and S. Sliker. Measurement of shear modulus in wood by a tension test. *Wood Science*, 13(3):171–176, 1981.
- R. El-Hajjar and R. Haj-Ali. In-plane shear testing of thick-section pultruded FRP composites using a modified Arcan fixture. *Composites Part B: Engineering*, 35(5):421–428, 2004.
- EN 408. *Timber structures. Structural timber and glued laminated timber – Determination of some physical and mechanical properties*. European Committee for Standardization, Office for Official Publications of the European Communities, Luxembourg, 2002.
- A. Foudjet, C. Surry, and J.F. Jullien. Indirect identification methods for the elastic constants of orthotropic materials and their application to wood. *Wood Science and Technology*, 16(3):215–222, 1982.
- D. Garcia, J.J. Orteu, and L. Penazzi. A combined temporal tracking and stereo-correlation technique for accurate measurement of 3D displacements: Application to sheet metal forming. *Journal of Materials Processing Technology*, 125-126:736–742, 2002.
- K.J. Gåsvik. *Optical metrology*. John Wiley and Sons, 3rd edition, 2002.
- L.J. Gibson and M.F. Ashby. *Cellular solids. Structure and properties*. Cambridge University Press, 2nd edition, 1997.
- A. Giraudeau, B. Guo, and F. Pierron. Stiffness and damping identification from full field measurements on vibrating plates. *Experimental Mechanics*, 46(6):777–787, 2006.
- N. Goldenberg, M. Arcan, and E. Nicolau. On the most suitable specimen shape for testing shear strength of plastics. In *International Symposium on Plastics Testing and Standardization, ASTM STP 247*, pages 115–121, 1958.
- M. Grédiac. Principe des travaux virtuels et identification. *Comptes Rendus de l’Académie*

- des Sciences*, 309(2):1–5, 1989.
- M. Grédiac. The use of heterogeneous strain fields for the characterization of composite materials. *Composites Science and Technology*, 56(7):841–846, 1996.
- M. Grédiac. The use of full-field measurement methods in composite material characterization: Interest and limitations. *Composites Part A: Applied Science and Manufacturing*, 35(7-8):751–761, 2004.
- M. Grédiac, E. Toussaint, and F. Pierron. Special virtual fields for the direct determination of material parameters with the virtual fields method. 2- Application to in-plane properties. *International Journal of Solids and Structures*, 39(10):2707–2730, 2002.
- M. Grédiac, F. Pierron, S. Avril, and E. Toussaint. The virtual fields method for extracting constitutive parameters from full-field measurements: A review. *Strain*, 42(4):233–253, 2006.
- D.W. Green, J.E. Winandy, and D.E. Kretschmann. Mechanical properties of wood. In *Wood handbook: Wood as an engineering material*. Madison, WI: USDA Forest Service, Forest Products Laboratory, General technical report FPL; GTR-113: Pages 4.1-4.45, 1999.
- D. Guitard. *Mécanique du matériau bois et composites*. Cepaduès-Éditions, Collection Nabla, 1987.
- R. Hernandez. Analysis of strain in finger-jointed lumber. In *5<sup>th</sup> World Conference on Timber Engineering*, volume 1, Montreux, Switzerland, August 17-20 1998.
- F. Hild, B. Raka, M. Baudequin, S. Roux, and F. Cantelaube. Multiscale displacement field measurements of compressed mineral wool samples by digital image correlation. *Applied Optics*, 41(32):6815–6828, 2002.
- H. Ho, M.Y. Tsai, J. Morton, and G.L. Farley. Numerical analysis of the Iosipescu specimen for composite materials. *Composite Science and Technology*, 46(2):115–128, 1993.
- S. Holmberg, K. Persson, and H. Petersson. Nonlinear mechanical behaviour and analysis of wood and fibre materials. *Computers and Structures*, 72(4-5):459–480, 1999.
- S.-C. Hung and K.M. Liechi. An evaluation of the Arcan specimen for determining the shear moduli of fiber-reinforced composites. *Experimental Mechanics*, 37(4):460–468, 1997.
- Y.Y. Hung and H.P. Ho. Shearography: An optical measurement technique and applications. *Materials Science and Engineering*, 49(3):61–87, 2005.
- J.M. Huntley and H. Saldner. Temporal phase-unwrapping algorithm for automated interferogram analysis. *Applied Optics*, 32(17):3047–3052, 1993.
- P.G. Ifju. The shear gage: For reliable shear modulus measurements of composite materials. *Experimental Mechanics*, 34(4):369–378, 1994.
- ISO 15310. *Fibre-reinforced plastic composites - Determination of the in-plane shear modulus by the plate twist method*. 1999.
- J.J. Janowiak and R.F. Pellerin. Shear moduli determination using torsional stiffness measurements. *Wood and Fiber Science*, 24(4):392–400, 1992.
- L.O. Jernkvist and F. Thuvander. Experimental determination of stiffness variation across

- growth rings in *Picea abies*. *Holzforschung*, 55(3):309–317, 2001.
- R. M. Jones. *Mechanics of composite materials*. Taylor and Francis, 2nd edition, 1999.
- J. Kajberg and G. Lindkvist. Characterisation of materials subjected to large strains by inverse modelling based on in-plane displacement fields. *International Journal of Solids and Structures*, 41(13):3439–3459, 2004.
- C.-. Kao, G.-. Yeh, S.-S. Lee, C.-K. Lee, C.-S. Yang, and K.-C. Wu. Phase-shifting algorithms for electronic speckle pattern interferometry. *Applied Optics*, 41(1):46–54, 2002.
- M. Kawai, M. Morishita, H. Satoh, S. Tomura, and K. Kemmochi. Effects of end-tab shape on strain field of unidirectional carbon/epoxy composite specimens subjected to off-axis tension. *Composites Part A: Applied Science and Manufacturing*, 28(3):267–275, 1997.
- J.-H. Kim, F. Pierron, M.R. Wisnom, and K. Syed-Muhamad. Identification of the local stiffness reduction of a damaged composite plate using the virtual fields method. *Composites Part A: Applied Science and Manufacturing*, 38(9):2065–2075, 2007.
- R. Kligler, M. Perstorper, and G. Johansson. Stiffness in structural timber - Effect according to position in the stem. In *IUFRO/S5.02 Timber Engineering Meeting*, Bordeaux, France, 1992.
- R. Kligler, M. Perstorper, and G. Johansson. Bending properties of Norway spruce timber. Comparasion between fast- and slow- grown stands and influence of radial position of sawn timber. *Annual Science Forest*, 55(3):349–358, 1998.
- F.P.F. Kollman and W.A. Côté Jr. *Principles of wood science and technology – Solid wood*. Springer-Verlag, Berlin, 1984.
- J. Konnerth, A. Valla, W. Gindl, and U. Müller. Measurement of strain distribution in timber finger joints. *Wood Science and Technology*, 40(8):631–636, 2006.
- L. Le Magorou, F. Bos, and F. Rouger. Identification of constitutive laws for wood-based panels by means of an inverse method. *Composite Science and Technology*, 62(4):591–596, 2002.
- D. Lecompte. *Elastic and elasto-plastic material parameter identification by inverse modeling of static tests using digital image correlation*. PhD thesis, Vrije Universiteit Brussel, 2007.
- J.-R. Lee, J. Molimard, A. Vautrin, and Y. Surrel. Digital phase-shifting grating shearography for experimental analysis of fabric composites under tension. *Composites Part A: Applied Science and Manufacturing*, 35(7-8):849–859, 2004a.
- J.-R. Lee, J. Molimard, A. Vautrin, and Y. Surrel. Application of grating shearography and speckle shearography to mechanical analysis of composite material. *Composites Part A: Applied Science and Manufacturing*, 35(7-8):965–976, 2004b.
- H. Lindström, P. Harris, and R. Nakada. Methods for measuring stiffness of young trees. *Holz als Roh - und Werkstoff*, 60(3):165–174, 2002.
- J.Y. Liu. Effects of shear coupling on shear properties of wood. *Wood and Fiber Science*, 32(4):458–465, 2000.
- J.Y. Liu. Analysis of off-axis tension test of wood specimens. *Wood and Fiber Science*, 34

- (2):205–211, 2002.
- J.Y. Liu and R.J. Ross. Relationship between radial compressive modulus of elasticity and shear modulus of wood. *Wood and Fiber Science*, 37(2):201–206, 2005.
- J. Ljungdahl, L.A. Berglund, and M. Burman. Transverse anisotropy of compressive failure in european oak - A digital speckle photography study. *Holzforschung*, 60(2):190–195, 2006.
- J.L. Lousada. *Variação fenotípica e genética em características estruturais na madeira de Pinus pinaster Ait.* PhD thesis, Universidade de Trás-os-Montes e Alto Douro, Vila Real, Portugal, 2000.
- J.S. Machado and H.P. Cruz. Within stem variation of Maritime Pine timber mechanical properties. *Holz als Roh - und Werkstoff*, 63(2):154–159, 2005.
- S. Mamada, J. Yamada, and S. Hirai. Shearing moduli of plywood, hardboard and particle board. *Mokuzai Gakkaishi*, 5(4):127–130, 1959.
- L.N. Melin and J.M. Neumeister. Measuring constitutive shear behavior of orthotropic composites and evaluation of the modified iosipescu test. *Composite Structures*, 76(1-2):106–115, 2006.
- M.H.H. Meuwissen, C.W.J. Oomens, F.P.T. Baaijens, R. Petterson, and J.D. Janssen. Determination of the elasto-plastic properties of aluminium using a mixed numerical-experimental method. *Journal of Materials Processing Technology*, 75(1-3):204–211, 1998.
- D. Mohr and M. Doyoyo. A new method for the biaxial testing of cellular solids. *Experimental Mechanics*, 43(2):173–182, 2003.
- J. Molimard, R. Le Riche, A. Vautrin, and J.-R. Lee. Identification of the four orthotropic plate stiffnesses using a single open-hole tensile test. *Experimental Mechanics*, 45(5):404–411, 2005.
- J. Morton, H. Ho, M.Y. Tsai, and G.L. Farley. An evaluation of the Iosipescu specimen for composite materials shear property measurement. *Journal of Composite Materials*, 26(5):708–750, 1992.
- R. Moulart, S. Avril, and F. Pierron. Identification of the through-thickness rigidities of a thick laminated composite tube. *Composites Part A: Applied Science and Manufacturing*, 37(2):326–336, 2006.
- L. Muszyński. Empirical data for modeling: Methodological aspects in experimentation involving hygromechanical characteristics of wood. *Drying Technology*, 24(9):1115–1120, 2006.
- L. Muszyński, R. Lagana, and S.M. Shaler. An optical method for characterization of basic hygro-mechanical properties of solid wood in tension. In *8th International IUFRO Wood Drying Conference*, pages 77–82, Brasov, Romania, August 24-29 2003.
- L. Muszyński, R. Lagana, S.M. Shaler, and W. Davids. Comments on the experimental methodology for determination of the hygro-mechanical properties of wood. *Holzforschung*, 59(2):232–239, 2005.
- J.A. Nairn. A numerical study of the transverse modulus of wood as a function of grain

- orientation and properties. *Holzforschung*, 61(4):406–413, 2007.
- K. Naruse. Estimation of shear moduli of wood by quasi-simple shear tests. *Journal of Wood Science*, 49(6):479–484, 2003.
- M. Neuilly. *Modelling and estimation of measurement errors*. Lavoisier Publishing, 1999.
- J.M. Oliveira. Caracterização do comportamento ao corte da madeira usando o ensaio de Arcan. Master’s thesis, Universidade de Trás-os-Montes e Alto Douro, Vila Real, Portugal, 2004.
- S. Ormarsson, O. Dahlblom, and K. Persson. Influence of varying growth characteristics on stiffness grading of structural timber. In *Meeting 31 of CIB-W18, Document CIB-W18/31-5-1*, Savonlinna, 1998.
- Y. Pannier, S. Avril, R. Rotinat, and F. Pierron. Identification of the elastic-plastic constitutive parameters from statically undetermined tests using the Virtual Fields Method. *Experimental Mechanics*, 46(6):735–755, 2006.
- V.J. Parks. Geometric moiré. In A. Kobayashi, editor, *Handbook on Experimental Mechanics*, chapter 6, pages 267–296. Society for Experimental Mechanics, 2nd edition, 1993.
- E. Parsons, M.C. Boyce, and D.M. Parks. An experimental investigation of the large-strain tensile behavior of neat and rubber-toughened polycarbonate. *Polymer*, 45(8):2665–2684, 2004.
- R.G. Pearson and R.C. Gilmore. Effect of fast growth rate on the mechanical properties of loblolly pine. *Forest Products Journal*, 30(5):47–54, 1980.
- M.U. Pedersen, C.O. Clorius, L. Damkilde, and P. Hoffmeyer. A simple size effect model for tension perpendicular to the grain. *Wood Science and Technology*, 37(2):125–140, 2003.
- J.L. Pereira. Comportamento mecânico da madeira em tracção nas direcções de simetria material. Master’s thesis, Universidade de Trás-os-Montes e Alto Douro, Vila Real, Portugal, 2005.
- K. Persson. *Micromechanical modelling of wood and fibre properties*. PhD thesis, Division of Structural Mechanics, Lund Institute of Technology, Lund, Sweden, 2000.
- F. Pierron. Saint-Venant effects in the Iosipescu specimen. *Journal of Composite Materials*, 32(22):1986–2015, 1998.
- F. Pierron and M. Grédiac. Identification of the through-thickness moduli of thick composites from whole-field measurements using the Iosipescu fixture: Theory and simulations. *Composites Part A: Applied Science and Manufacturing*, 31(4):309–318, 2000.
- F. Pierron and A. Vautrin. Accurate comparative determination of the in-plane shear modulus of T300/914 by the Iosipescu and 45° off-axis tests. *Composite Science and Technology*, 51(1):61–72, 1994.
- F. Pierron and A. Vautrin. The 10° off-axis tensile test: A critical approach. *Composites Science and Technology*, 56(4):483–488, 1996.
- F. Pierron, E. Alloba, Y. Surrel, and A. Vautrin. Whole-field assessment of the effects of boundary conditions on the strain field in off-axis tensile testing of unidirectional

- composites. *Composites Science and Technology*, 58(12):1939–1947, 1998.
- F. Pierron, G. Vert, R. Burguete, S. Avril, R. Rotinat, and M. R. Wisnom. Identification of the orthotropic elastic stiffnesses of composites with the virtual fields method: Sensitivity study and experimental validation. *Strain*, 43(3):250–259, 2007.
- M.-J. Pindera and C.T. Herakovick. Shear characterization of unidirectional composites with the off-axis tension test. *Experimental Mechanics*, 26(1):103–112, 1986.
- M.-J. Pindera, G. Choksi, J.S. Hidde, and C.T. Herakovich. A methodology for accurate shear characterization of unidirectional composites. *Journal of Composite Materials*, 21(12):1164–1184, 1987.
- M.-J. Pindera, P. Ifju, and D. Post. Iosipescu shear characterization of polymeric and metal matrix composites. *Experimental Mechanics*, 30(1):101–108, 1990.
- J.-L. Piro and M. Grédiac. Producing and transferring low-spatial-frequency grids for measuring displacement fields with moiré and grid methods. *Experimental Techniques*, 28(4):23–26, 2004.
- D. Post, G. Han, and P. Ifju. *High sensitivity moiré*. Springer Verlag, New York, 1994.
- J.S. Poulsen, P.M. Moran, C.F. Shih, and E. Byskov. Kink band initiation and band broadening in clear wood under compressive loading. *Mechanics of Materials*, 25(1):67–77, 1997.
- A.K. Prasad and K. Jensen. Scheimpflug stereocamera for particle image velocimetry in liquid flows. *Applied Optics*, 34(30):7092–7099, 1995.
- D. R. Rammer and R. Hernandez. Moiré analysis of the modified Arcan shear specimen. In J. Natterer and J.-L. Sandoz, editors, *5th World Conference on Timber Engineering*, volume 2, Montreux, Switzerland, 17-20 August 1988.
- A. Reiterer and S.E. Stanzl-Tschegg. Compressive behaviour of softwood under uniaxial loading at different orientations to the grain. *Mechanics of Materials*, 33(12):705–715, 2001.
- F. Rouger. *Application des méthodes numériques aux problèmes d’identification des lois de comportement du matériaux bois*. PhD thesis, Université de Technologie de Compiègne, 1988.
- S. Samarasinghe and G.D. Kulasiri. Displacement fields of wood in tension based on image processing. Part 1: Tension parallel- and perpendicular-to-grain and comparisons with isotropic behaviour. *Silva Fennica*, 34(3):251–259, 2000.
- S. Samarasinghe and G.D. Kulasiri. Stress intensity factor of wood from crack-tip displacement fields obtained from digital image processing. *Silva Fennica*, 38(3):267–278, 2004.
- A. E. Segall and M. J. Sipics. The influence of interpolation errors on finite-element calculations involving stress-curvature proportionalities. *Finite Elements in Analysis and Design*, 40(13-14):1873–1884, 2004.
- E. Serrano and B. Enquist. Contact-free measurement and non-linear finite element analyses of strain distribution along wood adhesive bonds. *Holzforschung*, 59(6):641–646, 2005.

- A. Shipsha and L.A. Berglund. Shear coupling effects on stress and strain distributions in wood subjected to transverse compression. *Composites Science and Technology*, 67(7-8):1362–1369, 2007.
- M. Sjö Dahl. Accuracy in electronic speckle photography. *Applied Optics*, 36(13):2875–2885, 1997.
- M. Sjö Dahl. Some recent advances in electronic speckle photography. *Optics and Lasers in Engineering*, 29(2-3):125–144, 1998.
- M. Sjö Dahl and L.R. Benckert. Systematic and random errors in electronic speckle photography. *Applied Optics*, 33(31):7461–7471, 1994.
- A. Sliker. Orthotropic strains in compression parallel to grain tests. *Forest Products Journal*, 35(11-12):19–26, 1985.
- A. Sliker. A method for predicting non-shear compliances in the RT plane of wood. *Wood and Fiber Science*, 20(1):19–26, 1988.
- A. Sliker and Y. Yu. Elastic constant for hardwoods measured from plate and tension tests. *Wood Fiber Science*, 25(1):8–22, 1993.
- I. Smith, E. Landis, and M. Gong. *Fracture and fatigue in wood*. John Wiley and Sons, 2003.
- W. J. Smith. *Modern Optical Engineering - The Design of Optical Systems*. McGraw-Hill, 3rd edition, 2000.
- STEP. *Structures en bois aux états limites. Tome 1: Introduction à l'Eurocode 5, Matériaux et bases de calcul*. Eyrolles, 1996.
- STEP. *Structures en bois aux états limites. Tome 2: Introduction à l'Eurocode 5, Calcul de structure*. Eyrolles, 1997.
- C.T. Sun and S.P. Berreth. A new end tab design for off-axis tension test of composite materials. *Journal of Composite Materials*, 22(8):766–779, 1998.
- C.T. Sun and I. Chung. An oblique end-tab design for testing off-axis composite specimens. *Composites*, 24(8):619–623, 1993.
- Y. Surrel. Design of algorithms for phase measurements by the use of phase stepping. *Applied Optics*, 35(1):51–60, 1996.
- Y. Surrel. Fringe analysis. In P.K. Rastogi, editor, *Photomechanics (Topics in Applied Physics)*, pages 57–104. Springer Verlag, 1999.
- Y. Surrel. Some metrological issues in optical full-field techniques. *Proceedings of SPIE*, 4777:220–231, 2002.
- Y. Surrel. Les techniques optiques de mesures de champ: Essai de classification. *Instrumentation, Mesure, Métrologie*, 4(3-4):11–42, 2004a.
- Y. Surrel. La technique de la grille pour la mesure de champs de déplacements et ses applications. *Instrumentation, Mesure, Métrologie*, 4(3-4):193–216, 2004b.
- Y. Surrel. Deflectometry: A simple and efficient noninterferometric method for slope measurement. In *Xth SEM International Congress on Experimental Mechanics*. Society for Experimental Mechanics, 7-10 June in Costa Mesa, California, USA, 2004c.

- M.A. Sutton, S.R. McNeill, J.D. Helm, and Y.J. Chao. Advances in two-dimensional and three-dimensional computer vision. In P.K. Rastogi, editor, *Photomechanics (Topics in Applied Physics)*, pages 323–372. Springer Verlag, 1999.
- P. Synnergren and M. Sjö Dahl. A stereoscopic digital speckle photography system for 3D displacement field measurements. *Optics and Lasers in Engineering*, 31(6):425–443, 1999.
- N. Takeda. Evaluation of microscopic deformation in cfrp laminates with delamination by micro-grid methods. *Journal of Composite Materials*, 32(1):83–100, 1998.
- Yu.M. Tarnopol'skii and V.L. Kulakov. Mechanical tests. In S.T. Peters, editor, *Handbook of Composites*, volume 34, pages 779–793. Springer-Verlag, 2nd edition, 1998.
- F. Thuvander, M. Sjö Dahl, and L.A. Berglund. Measurements of crack tip strain field in wood at the scale of growth rings. *Journal of Materials Science*, 35(24):6267–6275, 2000.
- E. Toussaint, M. Grédiac, and F. Pierron. The virtual fields method with piecewise virtual fields. *International Journal of Mechanical Sciences*, 48(3):256–264, 2006.
- A. Tsehaye, A.H. Buchanan, and J.C.F. Walker. Stiffness and tensile strength variation within and between radiata pine trees. *Journal of the Institute of Wood Science*, 13(5): 513–518, 1995.
- A. Voloshin and M. Arcan. Pure shear moduli of unidirectional fibre-reinforced materials. *Fibre Science and Technology*, 13(2):125–134, 1980.
- H.A. Vrooman and A.A.M. Maas. Image processing algorithms for the analysis of phase-shifted speckle interference patterns. *Applied Optics*, 30(13):1636–1641, 1991.
- D.E. Walrath and D.F. Adams. The Iosipescu shear test as applied to composite materials. *Experimental Mechanics*, 23(1):105–110, 1983.
- D.R. Walton and J.P. Armstrong. Taxonomic and gross anatomical influences on specific gravity - mechanical property relationships. *Wood and Fiber Science*, 18(3):413–420, 1986.
- S. Widehammar. Stress-strain relationships for spruce wood: Influence of strain rate, moisture content and loading direction. *Experimental Mechanics*, 44(1):44–48, 2006.
- T.G. Williamson. *APA Engineered Wood Handbook*. McGraw-Hill, 2002.
- R. W. Wolfe, R. Rowlands, and C.H. Lin. Full field stress/strain analysis: Use of moiré and TSA for wood structural assemblies. In *Experimental Mechanics Plenary Session at the Forest Products Research Society Annual Meeting*, Portland, ME, June 29, 1994.
- J. Xavier, J. Oliveira, J. Morais, P. Camanho, and F. Pierron. Measurement of the shear modulus of wood *pinus pinaster* Ait. by the Iosipescu test. In *Livro de Actas do VII Congresso Nacional de Mecânica Aplicada e Computacional*, Universidade de Évora, Portugal, 14 a 16 de Abril, 2003.
- J. Xavier, N.M. Garrido, J. Oliveira, J.L. Morais, P.P. Camanho, and F. Pierron. A comparison between the Iosipescu and off-axis shear test methods for the characterization of *pinus pinaster* Ait. *Composites Part A: Applied Science and Manufacturing*, 35(7-8): 827–840, 2004.

- P. Xu, L. Donaldson, J. Walker, R. Evans, and G. Downes. Effects of density and microfibril orientation on the vertical variation of low-stiffness wood in radiata pine butt logs. *Holzforschung*, 58(6):673–677, 2004.
- H. Yoshihara and A. Matsumoto. Measurement of the shearing properties of wood by in-plane shear test using a thin specimen. *Wood Science and Technology*, 39(2):141–152, 2005.
- H. Yoshihara and Y. Sawamura. Measurement of the shear modulus of wood by the square-plate twist method. *Holzforschung*, 60(5):543–548, 2006.
- H. Yoshihara, H. Ohsaki, Y. Hubojima, and M. Ohta. Applicability of the Iosipescu shear test on the measurement of the shear properties of wood. *Journal of Wood Science*, 45(1):24–29, 1999.
- W. Zhang and A. Sliker. Measuring shear moduli in wood with small tension and compression samples. *Wood Fiber Science*, 23(1):58–68, 1991.
- A.G. Zink, R.W. Davidson, and R.B. Hanna. Strain measurement in wood using a digital image correlation technique. *Wood and Fiber Science*, 27(4):346–359, 1995.
- B.J. Zobel and J.P. Van Buijtenen. *Wood variation: Its causes and control*. Springer Series in Wood Science, Ed: Timell, T.E., Springer-Verlag, 1989.

## CHARACTERISATION OF THE WOOD STIFFNESS VARIABILITY WITHIN THE STEM BY THE VIRTUAL FIELDS METHOD: APPLICATION TO *P. PINASTER* IN THE *LR* PLANE

**ABSTRACT:** In this work, an inverse approach for the identification of the *LR* stiffness parameters of maritime pine (*P. pinaster*) wood within the stem has been investigated. It is based on the application of the virtual fields method (VFM) to a rectangular specimen loaded with the Iosipescu fixture. This test has been designed in order to involve several in-plane stiffness components. The displacement fields have been measured by the grid method. The strain fields have been reconstructed from the measured displacement fields using a polynomial approximation scheme. The approach has been validated both numerically and experimentally. Two specimen configurations with grain at  $0^\circ$  and  $45^\circ$  have been compared. With the  $0^\circ$  configuration, only the  $Q_{11}$  and  $Q_{66}$  (longitudinal and shear stiffnesses) parameters have been identified with acceptable dispersion. The grain rotation of  $45^\circ$  has generated a redistribution of the strain fields allowing a better identification, namely for the  $Q_{22}$  (radial or transverse stiffness) parameter. The latter has been used in a subsequent study aiming at investigating the radial variability of the stiffnesses within the stem. It has been found that both  $Q_{22}$  and  $Q_{66}$  decrease from the pith to about the middle radius of the stem and increase afterwards to the outmost positions.

**Key-words:** *full-field measurements; parameter identification; Iosipescu test; virtual fields method; wood*

## IDENTIFICATION DE LA VARIABILITÉ DES RIGIDITÉS DU BOIS À L'INTÉRIEUR DE L'ARBRE PAR LA MÉTHODE DES CHAMPS VIRTUELS: APPLICATION AU *P. PINASTER* DANS LE PLAN *LR*

**RÉSUMÉ :** Dans ce travail, une méthode d'identification des paramètres de rigidité du bois a été étudiée et appliquée à l'essence pin maritime (*P. pinaster*) dans le plan *LR*. Cette approche est basée sur la méthode de champs virtuels (MCV) et sur la mesure de champs de déplacements sur une éprouvette parallélépipédique chargée avec le montage de cisaillement d'Iosipescu. Cet essai a été conçu afin d'activer plusieurs rigidités, générant des champs de déformation non homogènes. Ces champs ont été déduits à l'aide d'une méthode d'approximation polynomiale des champs de déplacement mesurés par la méthode de la grille. Les paramètres constitutifs ont ensuite été déterminés par la MCV. L'approche a été validée numériquement et expérimentalement. Deux configurations d'éprouvette avec le fil du bois orienté à  $0^\circ$  et à  $45^\circ$  ont été comparées. Avec la configuration à  $0^\circ$ , seuls les paramètres  $Q_{11}$  et  $Q_{66}$  (rigidités longitudinale et de cisaillement) ont été identifiés avec une dispersion acceptable. L'orientation à  $45^\circ$  a introduit une redistribution des champs de déformation permettant notamment une meilleure identification du paramètre  $Q_{22}$  (rigidité radiale ou transverse). Cette dernière configuration a été employée dans une étude concernant la variabilité radiale des rigidités à l'intérieur de la grume de l'arbre. Il a été constaté que  $Q_{22}$  et  $Q_{66}$  diminuent du centre à la moitié du rayon de la grume et augmentent après jusqu'à la périphérie.

**Mots-clés :** *bois, essais d'Iosipescu, identification, mesure de champs, méthode des champs virtuels*